

**IDENTIFICATION AND ATTENUATION OF  
LOSSES IN THERMOACOUSTICS: ISSUES  
ARISING IN THE MINIATURIZATION OF  
THERMOACOUSTIC DEVICES**

by

**Florian Zink**

Dipl.-Ing (M.S.) in Mechanical Engineering, RWTH Aachen,  
Germany, 2005

Submitted to the Graduate Faculty of  
the Swanson School of Engineering in partial fulfillment  
of the requirements for the degree of  
Ph.D. in Mechanical Engineering

University of Pittsburgh

2009

UNIVERSITY OF PITTSBURGH  
SWANSON SCHOOL OF ENGINEERING

This dissertation was presented

by

Florian Zink

It was defended on

May 26, 2009

and approved by

Laura A. Schaefer, Ph. D., Professor

Jeffrey S. Vipperman, Ph. D., Professor

Sung Kwon Cho, Ph. D., Professor

Andrew J. Schaefer, Ph. D., Professor

Dissertation Director: Laura A. Schaefer, Ph. D., Professor

Copyright © by Florian Zink

2009

# IDENTIFICATION AND ATTENUATION OF LOSSES IN THERMOACOUSTICS: ISSUES ARISING IN THE MINIATURIZATION OF THERMOACOUSTIC DEVICES

Florian Zink, PhD

University of Pittsburgh, 2009

Thermoacoustic energy conversion is based on the Stirling cycle and uses sound waves to displace and compress the working gas. When this process occurs inside a porous medium that is subject to a temperature gradient, a thermoacoustic engine creates intense sound. Conversely, when strong sound waves interact with a porous medium, a temperature gradient can be imposed through the attenuation of the pressure amplitude, creating a thermoacoustic refrigerator. The device size is a limiting factor to widespread use. This work investigates issues arising in their miniaturization in three separate ways.

To date, the thermal properties of the driving components are largely ignored during the design phase, partially because the traditional design “works,” and partially because of a lack of understanding of the thermal energy fluxes that occur during operation. First, a direct quantification of the influence of the thermal conductivity of the driving components on the performance of a thermoacoustic engine and refrigerator is performed. It is shown that materials with low thermal conductivity yield the highest sound output and cooling performance, respectively.

As a second approach to decreasing the footprint of a thermoacoustic system, the introduction of curvature to the resonator tube was investigated. A CFD analysis of a whole thermoacoustic engine was performed, and the influence of the stack assembly on the flow behavior was investigated. Nonlinearities in the temperature behavior and vortices in the flow close to the stack ends were identified. Resonator curvature prompts a decrease in the

amplitude of the pressure, velocity, and temperature oscillations. Furthermore, the total energy transfer from the stack to the fluid is also reduced.

Finally, through combining the aforementioned investigations, an optimization scheme is applied to a standing wave engine. A black box solver was used to find the optimal combination of the design parameters subject to four objectives. When focusing solely on acoustic power, for example, the device should be designed to be as large as possible. On the other hand, when attempting to minimize thermal losses, the stack should be designed as small as possible.

## TABLE OF CONTENTS

<b>1.0</b>	<b>INTRODUCTION</b>	1
1.1	Background	1
1.1.1	Stirling Cycle	2
1.1.2	Thermoacoustics	4
1.1.3	Standing Wave Engine	7
1.1.4	Traveling Wave Engine	8
1.2	Application: Thermoacoustic Refrigeration	10
1.3	Motivation	13
1.3.1	Environmental Motivation	13
1.3.2	Technological Motivation	14
1.4	Solution Approach	16
<b>2.0</b>	<b>REFRIGERATION TECHNOLOGY</b>	18
2.1	Background	18
2.2	Science of Refrigeration	19
2.2.1	Global Warming and Ozone Depletion Potential	19
2.2.2	Properties of commonly used Refrigerants	20
2.3	Refrigerants Use in Cooling applications	21
2.4	Other Refrigeration Technologies	22
2.4.1	Absorption Refrigeration	22
2.4.2	Adsorption Refrigeration	23
2.4.3	Thermoelectric Refrigeration	23
2.4.4	Thermoacoustic Refrigeration	24

2.5	Total Equivalent Warming Impact (TEWI) . . . . .	24
2.6	Requirements for a Successful Transition . . . . .	25
2.7	Comparison between VC and TA Refrigeration in Vehicles . . . . .	27
	2.7.1 Fuel Usage for Air Conditioning . . . . .	28
	2.7.2 COP Comparison between Technologies . . . . .	29
2.8	Calculation of Emissions . . . . .	29
2.9	Other Potential Application Areas for TARs . . . . .	32
<b>3.0</b>	<b>LOSS MECHANISMS OF THERMOACOUSTIC DEVICES . . . . .</b>	<b>33</b>
3.1	Streaming Losses . . . . .	34
	3.1.1 Gedeon Streaming . . . . .	34
	3.1.2 Rayleigh Streaming . . . . .	36
3.2	Acoustic Losses . . . . .	38
3.3	Viscous Losses . . . . .	39
3.4	Parasitic Heat Flux in a Thermoacoustic Regenerator . . . . .	40
<b>4.0</b>	<b>EXPERIMENTAL INVESTIGATIONS . . . . .</b>	<b>46</b>
4.1	Thermal Loss Mechanisms . . . . .	46
4.2	Thermoacoustic Engines . . . . .	48
	4.2.1 Design . . . . .	48
	4.2.1.1 Hot Side Heat Exchanger . . . . .	48
	4.2.1.2 Cold Side Heat Exchanger . . . . .	48
	4.2.1.3 Fabrication of the Stack . . . . .	48
	4.2.1.4 Final Assembly . . . . .	50
	4.2.2 Data Acquisition . . . . .	52
	4.2.3 Uncertainties in the Data Acquisition . . . . .	52
4.3	Results, Thermoacoustic Engine . . . . .	54
	4.3.1 Temperature Behavior of Stacks . . . . .	54
	4.3.2 Thermoacoustic Behavior of Different Stacks . . . . .	57
	4.3.3 Thermoacoustic Similarity of Stacks . . . . .	59
	4.3.4 Heat Flux Investigation . . . . .	62
4.4	Thermoacoustic Refrigerators . . . . .	65

4.4.1	Design . . . . .	66
4.4.2	Data Acquisition . . . . .	68
4.5	Initial Thermoacoustic Refrigerator Results . . . . .	69
4.5.1	SPL as a Function of Driving Frequency . . . . .	69
4.5.2	Temperature Behavior as a Function of Driving Frequency . . . . .	71
4.5.3	Varying the Regenerator Location . . . . .	73
4.5.4	Varying the Inertance Dimensions . . . . .	75
4.6	Screen Density Variation . . . . .	80
4.6.1	Theoretical Considerations for Screen Density . . . . .	80
4.6.2	Experimental Investigation of Screen Spacing . . . . .	84
4.7	Results from the Screen Density Variation . . . . .	85
4.7.1	105 $\mu\text{m}$ Nylon Screen . . . . .	85
4.7.2	200 $\mu\text{m}$ Nylon Screen . . . . .	87
4.7.3	100 $\mu\text{m}$ Stainless Steel Screen . . . . .	92
4.7.4	Comparing Temperature Levels and Temperature Differences . . . . .	95
4.7.5	Uncertainties in the Temperature Measurements . . . . .	96
4.8	Conclusions . . . . .	98
4.8.1	Engines . . . . .	98
4.8.2	Refrigerators . . . . .	99
<b>5.0</b>	<b>THERMAL/FLUID SIMULATION . . . . .</b>	<b>101</b>
5.1	CFD Modeling . . . . .	101
5.1.1	Background of CFD Modeling . . . . .	101
5.1.2	Previous CFD Modeling in Thermoacoustics . . . . .	104
5.1.3	Motivation for CFD Modeling . . . . .	108
5.1.4	Losses due to Resonator Geometry-Curvature . . . . .	109
5.2	Development of the CFD Model . . . . .	110
5.2.1	Mesh . . . . .	110
5.2.2	Boundary Conditions . . . . .	112
5.2.3	Simulation Settings . . . . .	115
5.2.4	Modeling Turbulence . . . . .	115

5.2.5	Summary of Simulation Settings . . . . .	118
5.2.5.1	Steady Simulation: Initializing the Pressure Disturbance . . . . .	118
5.2.5.2	Transient Simulation: Transition to Sustained Oscillations . . . . .	122
5.3	Sensitivity Analysis . . . . .	126
5.3.1	Solution Dependence on the Grid Properties . . . . .	126
5.3.2	Solution Dependence on the Temperature Boundary Conditions . . . . .	127
5.3.3	Solution Dependence on the Heat Transfer Coefficient . . . . .	128
5.3.4	Solution Dependence on the Initial Pressure Disturbance . . . . .	129
<b>6.0</b>	<b>RESULTS OF THE CFD ANALYSIS . . . . .</b>	<b>133</b>
6.1	Visualization Methodology . . . . .	133
6.2	Investigating the Thermoacoustic Effect . . . . .	135
6.2.1	Individual Data Plots . . . . .	135
6.2.2	Direct Comparison of Velocity, Temperature, Pressure, and Wall Heat Transfer . . . . .	138
6.2.3	Comparing Flow Variables between Channel Center and Wall . . . . .	142
6.3	The Effect of Resonator Curvature . . . . .	144
6.3.1	Development of new Grids . . . . .	144
6.3.2	Pressure . . . . .	146
6.3.3	Velocity . . . . .	148
6.3.4	Eulerian and Lagrangian Point of View . . . . .	151
6.3.5	Reynolds Number . . . . .	152
6.3.6	Temperature . . . . .	154
6.3.7	Heat Transfer between Solid and Gas . . . . .	155
6.4	Visualization of the Flow Variables . . . . .	160
6.4.1	Visualizing Entry and Exit Effects . . . . .	160
6.4.2	Visualizing the Velocity by Vectors . . . . .	166
6.4.3	Visualizing Vortices with Stream Traces . . . . .	170
6.5	Visualizing the Influence of Curvature . . . . .	173
6.5.1	Visualizing the Pressure Field . . . . .	173
6.5.2	Visualizing the Velocity Field . . . . .	174

6.5.3	Visualizing the Turbulence Intensity . . . . .	176
6.5.4	Discussion of the Flow Field Visualization . . . . .	177
6.6	Comparison of Simulation Data with the Free Field Pressure Distribution	177
6.7	Discussion of Results . . . . .	178
<b>7.0</b>	<b>EFFECT OF THE THERMAL PENETRATION DEPTH . . . . .</b>	<b>183</b>
7.1	Variation of the Thermal Conductivity . . . . .	184
7.2	Phaseshifts as a Result of the Variation of the Prandtl Number . . . . .	191
7.3	The Stability Limit . . . . .	193
7.4	Variation of the Specific Heat . . . . .	193
7.5	Conclusions from the Prandtl Number Variation . . . . .	196
<b>8.0</b>	<b>OPTIMIZATION APPLIED TO THERMOACOUSTICS . . . . .</b>	<b>198</b>
8.1	Motivation for Optimization . . . . .	198
8.2	Introduction to Optimization and Previous Efforts . . . . .	199
8.2.1	Previous Optimization Efforts . . . . .	199
8.2.2	Motivation . . . . .	200
8.3	Model Development . . . . .	200
8.3.1	Computational Domain . . . . .	200
8.3.2	Boundary Conditions . . . . .	202
8.3.3	Anisotropic Thermal Conductivity . . . . .	203
8.4	Objective Functions . . . . .	204
8.4.1	Convective and Radiative Heat Flux . . . . .	204
8.4.2	Conductive Heat Flux . . . . .	206
8.4.3	Acoustic Power . . . . .	206
8.4.4	Viscous Resistance . . . . .	208
8.5	Solution Strategy . . . . .	208
8.5.1	Normalizing Objective Functions . . . . .	209
8.5.2	Penalty Functions . . . . .	210
8.5.3	The Optimization Method: Nelder-Mead Simplex . . . . .	211
8.6	Implemented Optimization Routine . . . . .	212
8.6.1	Mesh Dependence of the Solution . . . . .	213

8.6.2	Pre-Processing Accuracy . . . . .	213
8.7	Results . . . . .	216
8.7.1	Shape of the Objective Function . . . . .	216
8.7.2	Optimization Behavior . . . . .	217
8.7.3	Varying the Weights . . . . .	218
8.7.4	Interpretation of the Results . . . . .	219
8.7.5	Discussion of the Solution Strategy . . . . .	221
<b>9.0</b>	<b>CONCLUSIONS . . . . .</b>	<b>223</b>
9.1	Summary . . . . .	223
9.2	Summary of the Experimentation . . . . .	223
9.3	Summary of the CFD Analysis . . . . .	225
9.4	Summary of the Optimization . . . . .	227
9.5	Outlook . . . . .	228
9.5.1	Advanced Experimentation . . . . .	228
9.5.2	Advanced Modeling . . . . .	228
<b>APPENDIX A. ADDITIONAL PLOTS: STACK MATERIAL VARIATION</b>		<b>231</b>
A.1	Temperature Data (Cold and Hot) Stack Material Variation . . . . .	231
A.2	Temperature Difference of Different Stack Materials . . . . .	233
A.3	Sound Pressure Level as a Function of Temperature Difference . . . . .	235
A.4	Sound Pressure Level as a Function of Input Power . . . . .	237
A.5	Thermal Penetration Depth as a Function of Input Power . . . . .	239
A.6	Ratio of Channel Size and Thermal Penetration Depth as a Function of Input Power . . . . .	241
<b>APPENDIX B. ADDITIONAL PLOTS, OPTIMIZATION . . . . .</b>		<b>243</b>
B.1	Temperature Distributions for Different Element Types . . . . .	243
B.2	Plots corresponding to the Material Variation . . . . .	245
B.3	Plots showing the Behavior of “fminsearch” . . . . .	247
B.4	Variation of the Weights for each Objective . . . . .	249
<b>BIBLIOGRAPHY . . . . .</b>		<b>251</b>

## LIST OF TABLES

1	Material properties of several relevant refrigerants adapted from Kim et al. and DOE Building Energy Data Handbook 2007 for R-134 . . . . .	20
2	Material properties of potential stack and regenerator materials . . . . .	50
3	Results from the variation of the size of the feedback inertance. . . . .	76
4	Ideal design parameters, to be applied to the screen variation investigation. . . . .	79
5	Different regenerators using variable screen counts and regenerator lengths ( $L_R$ ), resulting in a variation of the regenerator density. The ranges used in the experiments are shown. . . . .	84
6	Choices of simulation controls for the steady simulation: Solver . . . . .	119
7	Choices of simulation controls for the steady simulation: Solution Controls . . . . .	119
8	Choices of simulation controls for the steady simulation: Discretization . . . . .	120
9	Choices of simulation controls for the steady simulation: Initialization (all areas) . . . . .	120
10	Extension of solution controls for steady solution to include controls for the transient simulation. . . . .	123
11	Frequency $f$ and final pressure amplitude $\Delta p$ depending on grid properties, for a straight resonator . . . . .	127
12	Maximum pressure amplitude achieved and deviation from the standard case ( $h = 50 W/m^2K$ ) as a function of the heat transfer coefficient between the gas and wall in the stack . . . . .	130
13	Final state of oscillations, frequency $f$ , final pressure amplitude $\Delta p$ , as a result of various initial pressure disturbances $\Delta p_0$ . . . . .	131
14	Number of cells and nodes for each of the simulated cases of curvature. . . . .	145

15	Pressure evaluation for four different cases of resonator curvature (data corresponds with plots shown in Figure 70) . . . . .	147
16	Values of the velocity at negative and positive peaks (basis for functional correlation between velocity amplitude and curvature) . . . . .	148
17	Derivation of the timestep for TecPlot data . . . . .	173
18	Maximum and minimum values for all variables discussed above, with dependence on curvature. . . . .	180
19	Same data as in Table 18, but normalized with respect to maximum value (if normalizing maxima) and minimum value (if normalizing minima). . . . .	181
20	Variation of $\alpha = k/k^*$ and results from the simulation . . . . .	186
21	Variation of $\beta = c_p^*/c_p$ and results from the simulation . . . . .	195
22	Sensitivity analysis for the grid size during the calculations of maximum values of heat fluxes . . . . .	216
23	Properties (density, specific heat, and thermal conductivity) of the materials used in the material variation. . . . .	218
24	Weight distribution (in %) for all objectives (acoustic work $W$ , viscous resistance $R_\nu$ , convective and conductive heat fluxes $Q$ ) . . . . .	220

## LIST OF FIGURES

1	Schematic of Stirling Engine . . . . .	2
2	T-s Diagram for Stirling Cycle . . . . .	3
3	The four sections of the thermoacoustic cycle, heat transfer via the “bucket brigade” . . . . .	5
4	Simple standing wave engine demonstrator, built with Pyrex tubing, and a 600cpi ceramic monolith stack. . . . .	8
5	Two different configurations to achieve traveling wave phasing in thermoacoustic engines: (a) using a looped gas exchange path and (b) using a direct pressure exchange (feedback) between the two heat exchangers. The latter is much more compact. . . . .	9
6	Illustration of three main thermoacoustic refrigerator types . . . . .	10
7	Illustration of the additional energy required to drive a thermoacoustic refrigeration system when it replaces a vapor compression refrigeration system . . . . .	30
8	Illustration of drift (Gedeon streaming) resulting from variations in viscosity in the working gas in a pulse tube refrigerator . . . . .	35
9	Illustration of flow behavior of a gas flowing leaving a small (a) tube as opposed to entering it (b) . . . . .	36
10	Vortex formed by streaming inside the resonator of a thermoacoustic engine . . . . .	37
11	Illustration of heat driven refrigeration: Cooling at onset of oscillation (80 seconds) and subsequent heating of the cold side because of addition of heat from driving stack via unchecked streaming . . . . .	38

12	Temperatures on both ends of the stack in a standing wave engine. The heating of the ambient side is apparent . . . . .	41
13	Energy balance of a thermoacoustic engine as a function of heat input . . . . .	44
14	Hot side heat exchanger, ceramic frame with NiCr wire woven through it . . . . .	49
15	Exploded view of the engine components: resonator, cold side heat exchanger, stacks, hot side heat exchanger, and compliance . . . . .	51
16	Assembled TAE test bed. . . . .	51
17	Placement of thermocouples near the hot side heat exchanger as a source of inconsistent measurements . . . . .	53
18	Hot side and cold side temperature across the ceramic stack. . . . .	55
19	Curve fits of the temperature behaviors depending on stack material . . . . .	55
20	Temperature difference across the ceramic stack. . . . .	57
21	Illustration of the achieved sound pressure level as a function of electrical input power and temperature difference $\Delta T$ . . . . .	58
22	Thermal penetration depth $\delta_\kappa$ as a function of temperature . . . . .	60
23	Thermal penetration depth as a function of input power (solid symbols: hot side, outlined symbols: cold side) for the ceramic stack. . . . .	60
24	Ratio of channel size and thermal penetration as a function of input power (solid symbols: hot side, outlined symbols: cold side), for the ceramic stack. . . . .	62
25	The heat transfer coefficient and its curve fit over the relevant range of temperatures . . . . .	64
26	Estimates of the convective and radiative heat flux around the stack assembly . . . . .	65
27	Schematic view of the TAR setup . . . . .	67
28	Illustration of the TAR regenerator, individual components, and fully assembled . . . . .	68
29	Sound pressure level as a function of driving frequency. . . . .	70
30	Illustration of the SPL achieved in the regenerator housing empty, and with the regenerator assembly in place. . . . .	71
31	Illustration of the temperature difference across the regenerator as a function of driving frequency. . . . .	72

32	Temperature difference as a function of regenerator location relative to the closed end (measurement locations are spaced 25 <i>mm</i> apart) . . . . .	74
33	Temperature distribution along the regenerator as a result of the variation of the feedback inertance size (refer to Table 3 for the dimension of each case) .	77
34	Temperature difference between hot and cold end for all five cases. . . . .	78
35	Direct comparison between each case and measurement location, for two different times: initial distribution and an established case (after $\approx 10$ minutes). .	79
36	Three ratios of displacement to screen spacing: Case 1 is $d/\delta s < 1$ , Case 2 $d/\delta s = 1$ , Case 3 $d/\delta s > 1$ . . . . .	81
37	Plots showing all data for 105 $\mu m$ Nylon, for the whole range of the number of screens and regenerator length . . . . .	85
38	105 $\mu m$ Nylon, temperature data separated by screen count, as a function of regenerator length, part 1: 20-60 screens . . . . .	87
39	105 $\mu m$ Nylon, temperature data separated by screen count, as a function of regenerator length, part 2: 80-160 screens . . . . .	88
40	Plots showing all data for 200 $\mu m$ Nylon, for the whole range of number of screens and regenerator length . . . . .	89
41	200 $\mu m$ Nylon, temperature data separated by screen count, as a function of regenerator length, part 1: 20-80 screens. . . . .	90
42	200 $\mu m$ Nylon, temperature data separated by screen count, as a function of regenerator length, part 2: 100-200 screens . . . . .	91
43	Plots showing all data for 100 $\mu m$ stainless steel, whole range of number of screens and regenerator length . . . . .	92
44	100 $\mu m$ stainless steel, temperature data separated by screen count, as a function of regenerator length, part 1: 20-80 screens. . . . .	93
45	100 $\mu m$ stainless steel, temperature data separated by screen count, as a function of regenerator length, part 2: 100-200 screens . . . . .	94
46	Plots showing the temperature levels (maximum $T_{hot}$ and minimum $T_{cold}$ ) for each material and screen count. . . . .	95

47	Illustration of the displacement throughout the regenerator housing: measurement position 2 is located at 50 <i>mm</i> , and each subsequent position an additional 50 <i>mm</i> further away. . . . .	98
48	Rijke tube as modeled by Hanschk et al. . . . .	105
49	Traveling wave engine, basis for CFD model by Nijholt et al. . . . .	105
50	Illustration of computational model used extensively in numerical investigations as well as CFD study by Zoontjens . . . . .	107
51	Suggested resonator tube design (solid line), curled around the traveling wave loop rather than the traditional straight design (dashed line) . . . . .	108
52	Suggested resonator curvatures . . . . .	109
53	Dimensions of the computational domain for the TAE . . . . .	111
54	Section of the CFD grid, developed in Gambit . . . . .	111
55	Heat transfer behavior of tube flow subject to oscillations, compared to laminar, transitional, and turbulent heat transfer correlations. . . . .	114
56	Initial Condition, Pressure [ <i>Pa</i> ], 0° bending case . . . . .	121
57	Initial Condition, Temperature [ <i>K</i> ], 0° bending case . . . . .	121
58	Initial Condition, Velocity [ <i>m/s</i> ], 0° bending case . . . . .	122
59	First replication of thermoacoustic oscillations, transitioning from amplification to approaching a steady state (called the limit cycle by Hanschke et al.) . . . . .	125
60	Temperature contours in the compliance and stack (ranging from 700 <i>K</i> to 300 <i>K</i> ). The hot gas is streaming through the stack into the compliance. . . . .	125
61	Illustration of the difference in pressure amplitude between the various curved resonator geometries. . . . .	128
62	Sensitivity of the solution to the prescribed temperature profile, hot side temperatures of 800 <i>K</i> , 700 <i>K</i> , and 600 <i>K</i> . The cold side is constant at 300 <i>K</i> . . . . .	129
63	Transition behavior as a result of different initial pressure disturbances . . . . .	131
64	Illustration of the probe points along the stack. 10 points are located along the interior of the stack, 4 points outside the stack towards the compliance and 4 points outside of the stack towards the open end. Half of the points are located along the center of a channel, the other half are located near the wall. . . . .	134

65	Pressure, velocity, and temperature measured in the center/stream location, straight resonator. . . . .	136
66	Normalized Pressure, Velocity, Temperature, and Heat Flux (stream probes 3, 5, and 7) . . . . .	140
67	Comparison between free stream and wall temperature, pressure, and velocity behavior at the hot end of the stack revealing the influence of pressure on the temperature change. . . . .	143
68	Illustration of the differently bent resonators (0°, 30°, 60°, 90°) . . . . .	145
69	Illustration of the collection of data relative to the minimum of the compliance pressure (after 30000 timesteps) . . . . .	146
70	Comparison of pressure behavior under the influence of different degrees of resonator curvature. . . . .	147
71	Comparison of velocity behavior under the influence of different degrees of resonator curvature. . . . .	149
72	Comparison of velocity behavior in the stack and the outlet for the straight resonator (velocity antinode). . . . .	150
73	Reynolds number for probes 1, 3, 5, 7, and 9, center of the channel. . . . .	152
74	Comparison of the Reynolds number behavior under the influence of different degrees of resonator curvature. . . . .	153
75	Comparison between wall and free stream temperature behavior. . . . .	155
76	Comparison of temperature behavior under the influence of different degrees of resonator curvature. . . . .	156
77	The integrated heat flux ( $Q_{int}$ , as derived in Equation 6.7) over the horizontal stack surfaces, comparing four different resonator shapes (0°, 30°, 60°, 90°). . . . .	157
78	Energy transferred ( $\Delta E$ ) for the horizontal stack surface. Comparing four different resonator shapes (0°, 30°, 60°, 90°). . . . .	158
79	Effect of the curvature on energy transfer and sound pressure level . . . . .	159
80	Entry/exit effects on the hot side of the stack, part 1 . . . . .	161
81	Entry/exit effects on the hot side of the stack, part 2 . . . . .	162
82	Entry/exit effects on the cold side of the stack, part 1 . . . . .	164

83	Entry/exit effects on the cold side of the stack, part 2 . . . . .	165
84	Velocity vectors at the hot side . . . . .	168
85	Velocity vectors at the cold side . . . . .	169
86	Velocity vectors as a result from PIV investigation of the thermoacoustic effect as published by Berson et al. . . . .	170
87	Vortex structure at the stack outlet, as measured through PIV by Mao et al.	171
88	Instantaneous stream traces for times with strong vortex generation (high ve- locity magnitude and flow reversal). . . . .	172
89	Pressure distribution for the whole domain for four cases of resonator curvature.	174
90	Velocity field for the entire domain for four cases of resonator curvature. . . .	175
91	Turbulence generation for the whole domain for four cases of resonator curvature.	176
92	Pressure peaks throughout the stack, and comparison with the free field pres- sure distribution of a standing wave. . . . .	179
93	Illustration of the dependence of pressure, velocity, temperature, heat transfer and energy transfer on resonator curvature (normalized). . . . .	182
94	Pressure behavior for four values of $\alpha$ (1, 1.5, 2, and 3), compared to the physical case. . . . .	187
95	Pressure behavior for three values of $\alpha$ (4,6, and 8), compared to the physical case. . . . .	187
96	Pressure behavior for three values of $\alpha$ (4,6, and 8), compared to the physical case. . . . .	188
97	Pressure behavior for three different Prandtl numbers (physical, $\times 2$ , and $\times 4$ ) by variation of the thermal conductivity. . . . .	188
98	Change in operating frequency (normalized with respect to physical case) and its inverse (as used in Equation 7.3) as the thermal conductivity is increased.	189
99	Change in thermal penetration depth as the thermal conductivity is increased.	190
100	Change in pressure amplitude as the thermal conductivity is increased, shown as a function of $\alpha$ directly and as a function of (normalized) thermal penetra- tion depth. . . . .	190

101	Change in phase shift between pressure and velocity as the thermal conductivity of the gas is increased. . . . .	192
102	Phase difference between pressure and heat transfer as the thermal conductivity of the gas is increased. . . . .	192
103	Phase difference between pressure and heat transfer and quadratic curve fits, omitting either $\alpha = 6$ or $\alpha = 8$ . . . . .	194
104	Illustration of the approaching stability limit, where an amplification of the pressure amplitude does not occur, $\alpha = 4$ , $\alpha = 1$ and $\alpha = 0.75$ shown. . . . .	195
105	Illustration of the difference in oscillation behavior for a Prandtl number variation as a result of changing $c_p$ and $k$ . . . . .	197
106	Illustration of computational domain and implemented boundary conditions .	201
107	Error in the temperature distribution resulting from use of quadratic mesh elements . . . . .	202
108	Temperature differences between isotropic and anisotropic thermal conductivity for Copper and PMMA, $L \times H = 0.4 \times 0.2$ . . . . .	204
109	Flow diagram of the optimization routine, including the preprocessor . . . . .	214
110	Illustration of the error resulting from using a coarse mesh rather than a refined mesh in COMSOL. The error is less than 2% and not expected to rise further with increasing cell count. . . . .	215
111	Objective function as a function of domain dimensions for PMMA . . . . .	217
112	Behavior of the optimization as a function of initial guess . . . . .	219
113	Contours for Case 5: emphasis on the heat flux objectives (convection and conduction) . . . . .	221
114	Hot side and cold side temperature, including linear curve fits, for various stack materials ranging from low thermal conductivity (a) to high thermal conductivity (e) . . . . .	232
115	Temperature difference across the stack ranging from materials with low thermal conductivity (a) to high thermal conductivity (e) . . . . .	234

116	Sound pressure level achieved by each stack as a function of temperature difference, ranging from materials with low thermal conductivity (a) to high thermal conductivity (e) . . . . .	236
117	Sound pressure level achieved by each stack as a function of input power, ranging from materials with low thermal conductivity (a) to high thermal conductivity (e) . . . . .	238
118	Thermal penetration depth as a function of input power for each stack material, ranging from materials with low thermal conductivity (a) to high thermal conductivity (e) . . . . .	240
119	Ratio of the channel size and thermal penetration depth as a function of input power for each stack material, ranging from materials with low thermal conductivity (a) to high thermal conductivity (e) . . . . .	242
120	Illustration of the surface temperature distribution for a fixed domain size as a function of element type (Linear through quintic). Higher order elements minimize errors. . . . .	244
121	Variation of the stack material . . . . .	246
122	Variation of the starting points for constant L each (PMMA). . . . .	248
123	Variation of the Weights for each Objective, with case numbers corresponding to Table 24 . . . . .	250

## 1.0 INTRODUCTION

### 1.1 BACKGROUND

Modern societies rely heavily on the conversion of thermal energy into mechanical energy and vice versa. For this conversion, turbines and combustion engines are generally utilized. The latter can be subdivided into internal and external combustion engines (ICE and ECE, respectively). Internal combustion engines were discovered at the end of the 19<sup>th</sup> century and are in widespread use today. There are numerous types of ICEs, most commonly the Otto engine and the Diesel engine, named after their inventors Gustav Otto and Rudolf Diesel. Most ICEs run on fossil fuel because of its high energy density and ease of storage. To extract work from an ICE, air and the fuel are supplied to the combustion chamber, ignited, and the reaction products are expelled from the engine at the end of one work cycle. The ECE, on the other hand, uses the same working gas for each cycle, so there is no mass exchange with its environment during its working cycle. Over the course of this cycle, the gas is heated, it performs work, releases heat and is returned to its original state. The external addition of heat enables the ECE to be run on different fuels than fossil fuels, such as solar energy or waste heat from other processes. The Stirling engine is a well established external combustion engine.

This work will focus on the Stirling cycle and its application to *thermoacoustic heat engines* (TAEs) and ultimately *thermoacoustic refrigerators* (TARs). More specifically, the miniaturization of current designs will be discussed. Miniaturization, particularly of TARs, is necessary in order to expand the use of the technology into wider markets and utilize their inherent benefits. Of course, there are limitations to the operation and implementation of thermoacoustic engines and refrigerators. During their operation, they exhibit certain

unique loss mechanisms. As a system based on acoustic phenomena, there are acoustic losses resulting from the properties of the waveguide as well as gas streaming losses that are a unwanted byproduct of the gas oscillations in confined spaces. Both acoustic and streaming losses and their impact on miniaturization are well understood. However, the losses contributed by the thermal properties of the driving components as well as the housing have not been studied in detail and remain a largely unknown influence on engine and refrigerator performance. It is the goal of this work to determine the effect of these thermal properties, and whether they pose a practical limit on miniaturization.

### 1.1.1 Stirling Cycle

The first Stirling engine was developed in 1816 by Robert Stirling. It was the first engine that operated without a high-pressure steam boiler (1). It utilizes two pistons and a regenerative heat exchanger.

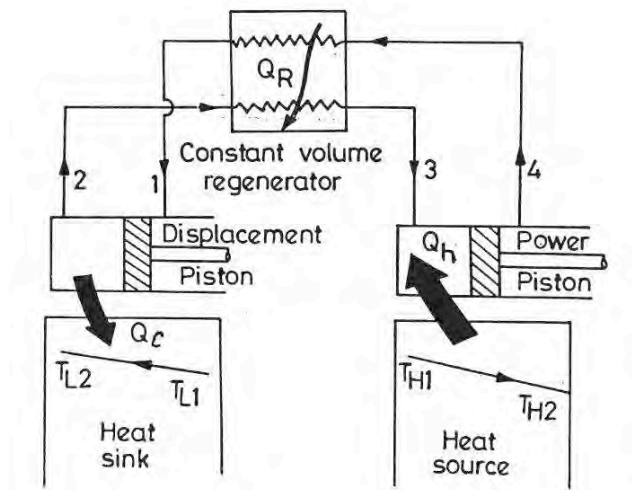


Figure 1: Schematic of Stirling Engine

Figure 1 shows such an engine (2). There is a heat sink and a heat source with the displacement piston and power piston, respectively. The working gas is compressed between states 1 and 2, and heat is given off to the heat sink. Between states 2 and 3, the gas is heated at constant volume and is then heated isothermally to reach state 4. The simultaneous

expansion drives the power piston. The remaining heat is given off in the regenerator to return to state 1 (the gas is *regenerated* to its original state). Figure 2 illustrates this process with a T-s diagram (2).

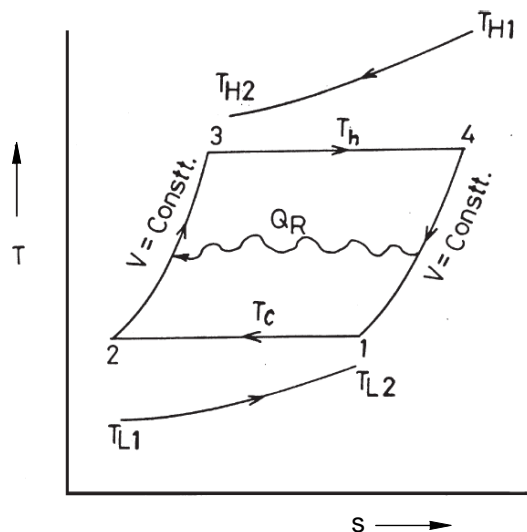


Figure 2: T-s Diagram for Stirling Cycle

The classic Stirling engine employs two pistons that are connected with a rod. The pistons illustrated in Figure 1 are connected and are forced to move together. An improvement over this engine is the free piston Stirling engine, which eliminates the need for this rod. The pistons are synchronized based solely on the pressures in the compression chamber and piston backspace. This coupling reduces the need for sealing and fewer mechanical components, which could reduce production costs and maintenance (3). The logical progression from this improvement was to eliminate all moving, mechanical parts altogether (4). In thermoacoustics, this feat is accomplished by replacing the pistons with sound waves. The idea of generating mechanical work with no moving parts sounds almost like an attempt to build a perpetual motion machine. In fact, Sir Arthur Clarke’s third law seems to offer a good explanation for this phenomenon: “Any sufficiently advanced technology is indistinguishable from magic” (5). However, there is a very realistic approach to realizing this type of engine design; an approach which uses sound waves instead of pistons to displace and compress the

working gas. As it is a combination of a thermodynamic cycle and acoustics, this has been known as thermoacoustics.

In the earliest stages, the thermoacoustic effect was not known as a means to extract power, but rather was a physical phenomenon discovered by chance. The earliest mention of the thermoacoustic effect was when glass blowers noticed that glass pipes emitted a noise during production when one end was hot and the other had cooled. A similar effect was noted by workers who worked with liquid Helium (at a temperature of  $4K$ ). Again, when a temperature gradient was imposed on a pipe (room temperature at the closed end and in contact with the Helium at the open end), spontaneous oscillations could be observed (6). This was later described as “thermoacoustics” by Rott (7), and was initially only an interesting phenomenon and not subject to detailed research. It was not until Ceperley connected the thermoacoustic effect with the Stirling cycle that modern thermoacoustics, as it exists now, was initiated. He built the first *traveling wave heat engine* (without actually calling it a “thermoacoustic engine”) in 1978 (8). The first application of this cycle as a thermoacoustic technology occurred when Ceperley recognized that sound waves could replace pistons for gas compression and displacement (9).

### 1.1.2 Thermoacoustics

In thermoacoustic engines (TAEs), the compression and expansion is prompted by the sound waves maintained in the resonator instead of pistons. The velocity component of the sound waves causes the displacement of the working gas, so that the gas is transported from a hot environment to a colder environment. As illustrated with the (ideal gas) isentropic relationship between a change in temperature and a change in pressure, the gas is heated and cooled during compression and expansion, as shown in Equation 1.1:

$$\left(\frac{T_1}{T_2}\right) = \left(\frac{p_1}{p_2}\right)^{\frac{\gamma-1}{\gamma}} \quad (1.1)$$

where  $\gamma$  is the ratio of constant pressure and constant volume specific heats. This change in temperature occurs in all pressure waves. In order to illustrate this, consider the following,

simple example. In a normal conversation, the sound pressure level (SPL) is approximately 60 *dB*. The correlation between SPL and pressure amplitude is:

$$SPL = 20 \cdot \log \left( \frac{p_{rms}}{20 \mu Pa} \right) \quad (1.2)$$

where 20  $\mu Pa$  is the commonly used reference pressure for determination of the SPL. With a SPL of 60 *dB* the resulting pressure amplitude is 0.2 *Pa*. Using the isentropic relationship between  $\Delta T$  and  $\Delta p$ , the temperature difference occurring in the gas during that conversation is on the order of  $\mu K$ . Of course, in free air, this heat is dissipated with no usable benefit. If a solid wall is introduced in the vicinity of this sound wave, we can use the thermoacoustic effect in a useful way. Figure 3 illustrates this so-called “bucket brigade” of heat transfer that occurs in a thermoacoustic stack (or regenerator). Note that the solid wall here is subject to a temperature gradient from right to left (high to low) and the gas is subject to a standing wave. Considering now the central gas parcel denoted by state 1 at location *a*, we can follow it through one cycle that is caused by the velocity component of the standing wave. Figure 3 illustrates this process.

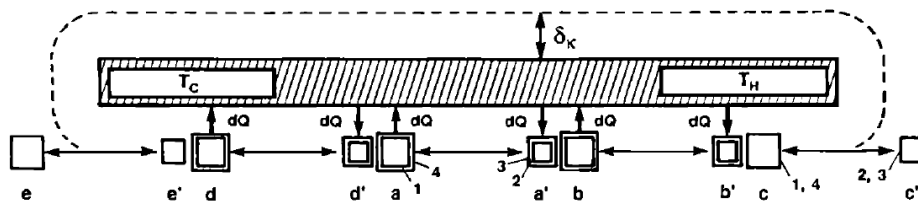


Figure 3: The four sections of the thermoacoustic cycle, heat transfer via the “bucket brigade”

First, the gas parcel is displaced to location *a'*. At the same time, the gas is compressed by the pressure wave (as indicated by the decrease in the parcel’s size). As a result of the displacement, the parcel is located near a part of the solid wall that is now hotter than the gas. As a result, heat is transferred from the wall to the gas; the gas parcel expands to reach state 3. Then, the parcel is returned to position *a* and expanded by the pressure component

of the wave to reach state 4. At this state and location, the gas is now hotter than the surrounding wall. By giving off its excess heat content in order to re-establish equilibrium with the wall, the parcel returns to state 1. Essentially, this process is a superposition of an isentropic temperature change in the gas and a heat transfer between that wall/gas and gas/wall, respectively. The difference in heat addition at high pressure versus heat removal at low pressure is responsible for the amplification of this pressure change between cycle halves.

The isentropic gas behavior is of importance here, but this temperature change alone is not responsible for driving the thermoacoustic effect. Only if the temperature gradient in the wall is sufficiently large relative to the gas' displacement is the net amplification of the pressure amplitude possible. This idea has been developed in detail by Swift (10). In order for amplification to occur, the walls have to exhibit a temperature gradient that at least equals the “critical temperature gradient,” which is, again, derived from the temperature gradient a gas experiences under the influence of a sound wave in adiabatic conditions. The expression for this critical temperature gradient, as derived by Swift (10) is given in Equation 1.3:

$$\nabla T_{crit} = \frac{\omega p_1^s}{\rho_m c_p u_1^s} \quad (1.3)$$

The critical temperature gradient depends on the operating frequency  $\omega$ , and the first order pressure and velocity in the standing wave  $p_1^s$  and  $u_1^s$ , as well as the mean gas density  $\rho_m$  and specific heat  $c_p$ . Depending on the ratio of the temperature gradient and critical temperature gradient, acoustic work is created (a thermoacoustic engine) when  $\frac{dT/dx}{dT/dx|_{crit}} > 1$ . If we allow sound waves to interact with a porous medium, the sound waves are attenuated and create a temperature gradient across this stack that is smaller than the critical temperature gradient  $\frac{dT/dx}{dT/dx|_{crit}} < 1$ . This derivation is outlined in detail by Xiao et al. (11–13).

There are two fundamental modes of operation of thermoacoustic engines, resulting in standing wave and traveling wave devices. The difference lies in the phasing between the pressure and velocity components of the acoustic wave. This results in subtle but important differences in the design of the regenerative unit and major differences in performance parameters, such as efficiency.

### 1.1.3 Standing Wave Engine

Most commonly, standing wave devices use a quarter wavelength ( $\lambda/4$ ) resonator, which allows for a pressure antinode (location of maximum change in pressure) to be located at the closed end and a pressure node (zero change in pressure with respect to time) to be located at the opening. The velocity is phase shifted with respect to pressure (between  $0^\circ$  and  $90^\circ$ ). A velocity node is located at the closed end and a velocity antinode at the opening. Considering this behavior, it becomes obvious why the stack is to be placed close to the closed end: the engine is driven based on pressure oscillations and requires gas displacement, and thus the stack cannot be located at either end of the resonator. The stack is usually placed closer to the velocity node than the pressure node, as with increasing gas displacement, the viscous losses increase which can disable the engine. The particular phasing of pressure and velocity in a standing wave engine results in compression followed by the displacement. This requires a delay in the heat exchange if the gas is to be heated when it is most compressed or if it is to reject heat at the point of expansion. For this reason, the flow channels for the gas are larger than the thermal penetration depth  $\delta_\kappa$  of the gas. This is the distance heat can diffuse through the gas in a given time and is governed by the frequency of oscillation and the gas properties as illustrated in Equation 1.4 (10):

$$\delta_\kappa = \sqrt{\frac{2k}{\omega \rho c_p}} = \sqrt{\frac{k}{\pi f \rho c_p}} \quad (1.4)$$

The artificial delay of heat transfer results in the addition of irreversibility and thus a relatively poor performance (14) with a thermal efficiency of around 20% (15). Figure 4 shows a simple demonstration engine. It is constructed using Pyrex tubing (25 mm inner diameter) and a 600 cells per square inch (cpi) ceramic monolith shaped to fit inside the resonator. Heat is supplied with 22WG NiCr wire corrugated through one end of the ceramic material. The opposite end does not require cooling because of the low thermal conductivity of the ceramic. When heated to  $\approx 300^\circ\text{C}$ , the engine is capable of creating soundwaves of approximately 120dB. An alternative to the standing wave engine is the inherently more efficient traveling wave engine.

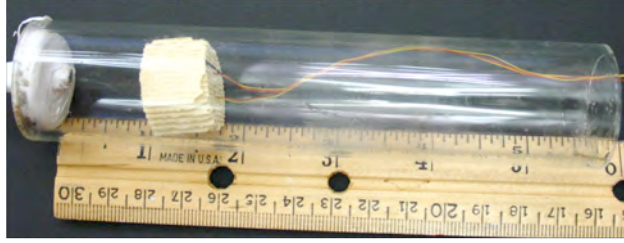


Figure 4: Simple standing wave engine demonstrator, built with Pyrex tubing, and a 600cpi ceramic monolith stack.

#### 1.1.4 Traveling Wave Engine

As opposed to the standing wave engine, the traveling wave engine exhibits pressure and velocity oscillations that are in phase. Thus, when the gas is at a peak of its displacement (i.e. zero velocity) the gas also experiences its maximum compression or expansion. This change in pressure/velocity phasing is achieved by utilizing a looped compliance (first mentioned by Ceperley in (16) and also considered by Backhaus et al. (17) and Ueda et al. (18)) or a feedback inertance around the regenerator, introduced by deBlok (19) and used in a very compact demonstration device by Bastyr et al. (20). Both types of traveling wave designs are illustrated in Figure 5 (19). Note that deBlok used this design with a mechanical driver as a refrigerator, and Bastyr used his design as a heat engine. The effect of the feedback inertance is the same for both configurations.

As a result of this more ideal pressure-velocity phasing, the regenerator can be designed differently than the stack of a standing wave engine. The walls can be spaced much closer together; specifically, they are spaced smaller than the thermal penetration depth. This results in improved heat transfer and fewer losses (10). The regenerator-based thermoacoustic engine can theoretically reach the Carnot efficiency, which the standing wave engine cannot (21).

Backhaus et al. claim that the first engines of this type were only theoretically able to amplify acoustic power (15). Yazaki et al. were the first to actually measure this amplifica-

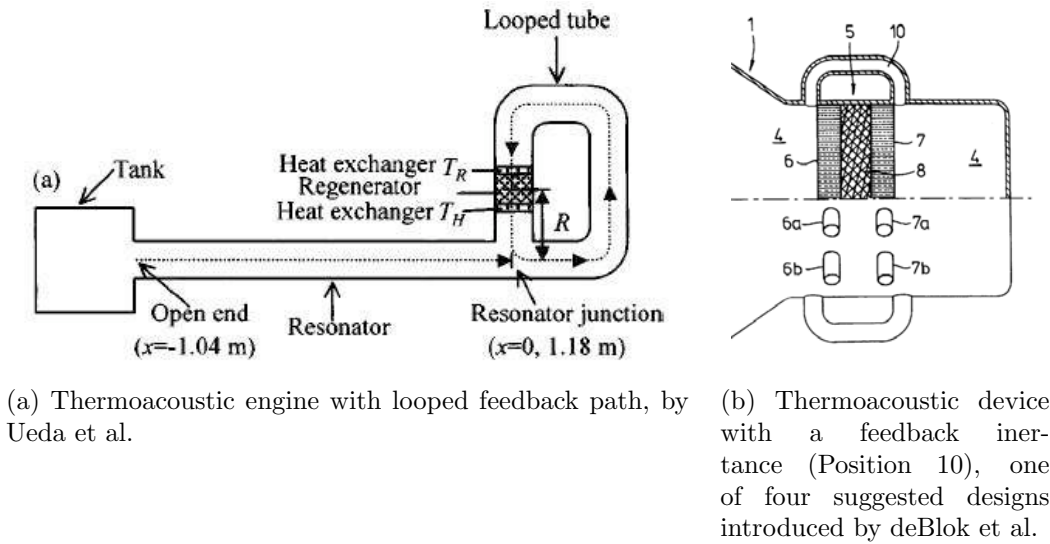


Figure 5: Two different configurations to achieve traveling wave phasing in thermoacoustic engines: (a) using a looped gas exchange path and (b) using a direct pressure exchange (feedback) between the two heat exchangers. The latter is much more compact.

tion (22). The basic configuration for powerful large scale models has remained unchanged. The common design used in today's applications of thermoacoustic engines utilize the looped design shown in Figure 5 (a) because their nature is well understood. Smaller devices are also being developed which utilize the feedback inductance around the regenerator and heat exchangers to create traveling wave phasing, as shown in Figure 5 (b). Although they are traveling wave engines, both designs use a resonator just like the standing wave engines. This is where acoustic loads are attached to withdraw acoustic power (18). In addition to simple single stage engines, Gardener et al. have demonstrated the feasibility of multistage TAEs, combining standing wave and traveling wave engines to reach an acoustic power to heater power ratio of about 20% (23).

## 1.2 APPLICATION: THERMOACOUSTIC REFRIGERATION

Aside from a use as an emergency siren, or for electricity generation (6; 24) and dehumidification (25), thermoacoustic devices have almost exclusively been applied to refrigeration as a replacement for vapor compression (VC) refrigerators. The heat driven system is mostly noted for its complete lack of moving parts (as shown by Yazaki et al. (26)), which is convenient because there are no sliding seals. These seals create the biggest problems in mechanical reciprocating engines. In regard to refrigeration, this is beneficial as sealing at cryogenic temperatures is extremely difficult. Below, the three most prevalent types of thermoacoustic refrigerators (TARs) will be described, as shown in Figure 6 (27).

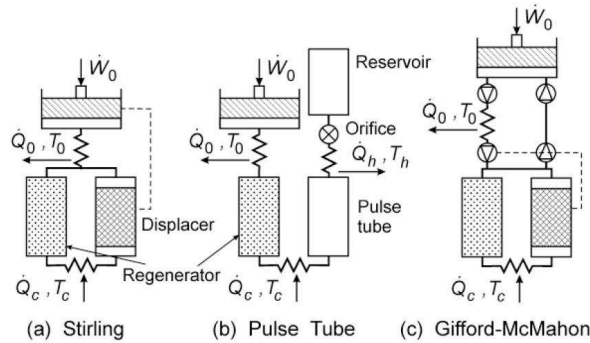


Figure 6: Illustration of three main thermoacoustic refrigerator types

Both the Stirling and Gifford-McMahon refrigerators use a piston to generate pressure oscillations. Since the operating temperatures of these devices can be extremely low (covering the cryogenic region between  $120\text{ K}$  and  $2\text{ K}$ ), the life span of the moving parts is very short. Presently, this has hindered commercial use of these devices (27). The (resonant) pulse tube refrigerator works without any moving parts, making it much more feasible to operate at cryogenic temperatures, and it can also be driven by a TAE (3). Similar to the very simple demonstration device for sound creation as introduced above, it is also possible to prove the reverse cycle. This is outlined by Russell et al. (28), and this design serves as the basis for many of the experiments that were conducted as part of this work.

While vapor compression coolers can reach about 230  $K$  in a single stage, TARs can achieve much lower temperatures. This makes the technology very attractive as a replacement for VC refrigeration. Several research groups have reported on the successful design of thermoacoustically driven cryocoolers and chillers. Jin et al. achieved a temperature of about 120  $K$ , making their device a cryocooler (29). Other thermoacoustic cryocooler designs achieved temperatures as low as 75  $K$  (30) and 60  $K$  (3; 31). A cryocooler capable of reaching 50  $K$  was demonstrated by Vanapelli et al. (32). The largest example to date has been developed by Praxair, which is a cryocooler that is capable of liquefying natural gas at a rate of  $\approx 2,000$   $l/day$  (33). An everyday application of thermoacoustic refrigeration was introduced by Pennsylvania State University with their development of a loudspeaker driven chiller that was able to achieve 120  $W$  of cooling power at  $-25^\circ C$ . The design was patented by Smith (34) and elaborated on in a second patent (35). It was used to cool ice cream (36).

The efficiency of the refrigeration unit has been found to be the same as that of conventional Stirling cycle refrigerators, which is simply the ratio of the cold side to hot side temperatures across the regenerator,  $\eta_{th} = T_c/T_h$  (37). These examples prove a (admittedly small) market for TARs; however, the need for gas-liquefaction and general cooling at cryogenic temperatures has risen in recent years (27). We must expect a sharp increase in this need if cars and trucks begin utilizing supercooled gases as fuel as a replacement for current fossil fuels, and thus developing a cost effective way to create large amounts of supercooled liquids will become increasingly important. In addition to mobile refrigeration and cryogenics, thermoacoustics has also been proposed as the basis for a cogeneration system for power and heating or cooling for buildings (24; 38). For an additional overview of the literature on thermoacoustics, refer to (39).

An advantage of thermoacoustic refrigeration is the fact that it is not based on the Rankine cycle. Wheatley et al. illustrate the source of losses in refrigeration cycles and their effect on the coefficient of performance (COP). The COP is the ratio of cooling capacity over work added to achieve this capacity. Note that the COP can also be used to quantify heating performance, and that it is not an efficiency in the classical sense and is not bounded by 1. Using an air-to-air heat pump based on the Rankine cycle as an example, the COP is less than that of the ideal Carnot cycle due to irreversibilities and compressor losses (40). The

Carnot cycle is an idealization of a power cycle that is not subject to entropy generation and thus poses the theoretical limit of efficiency for any non-ideal cycle. The Stirling cycle can be compared directly to the Carnot cycle, rather than the Rankine cycle (41), thus the COP of the *refrigeration cycle* of TARs is very good compared to other refrigeration technologies.

In reality, however, there are some drawbacks to thermoacoustic refrigeration. Its largest problem is that its actual COP is smaller (less than 1) than that of conventional vapor compression systems (ranging from 2 to 6), as demonstrated by Herman et al. (42) and Phelan et al. (43). The reason for this inherent drawback is that we have to consider the system as a whole and realize that the whole cycle takes place in the gaseous phase of the working fluid. In VC refrigeration, the working gas is condensed before it is compressed. This compressed liquid is then evaporated at high pressure. The compression work is significantly smaller than the work required to compress a gas. Also, there is a limit to which the gas can be compressed by a sound wave, a limit which does not exist in a mechanical compressor. The highest sound pressure level reported in the literature is 190 *dB* (1) which results in a pressure amplitude of

$$10^{\left(\frac{190\text{dB}}{20}\right)} \cdot 20\mu\text{Pa} \cdot \sqrt{2} \approx 90,000 \text{ Pa}. \quad (1.5)$$

Thus the compression ratio, defined as  $\Pi$ , is only 1.2, which is low compared to conventional pumps. However, even for that compression ratio, the sound level is very dangerous (the threshold for pain inflicted by noise is roughly 140 *dB*). For atmospheric conditions, it is also close to the highest achievable sound pressure level, as the maximum amplitude cannot exceed 1 atmosphere (or 101,325 *Pa*). It must be kept in mind that this sound pressure level occurs within the device in the vicinity of the regenerator. The surrounding area is not exposed to dangerously high sound levels. Since the engine is operated at primarily one frequency (higher harmonics exist but do not show as high an intensity as the first harmonic), we can isolate this frequency and ensure safe operation of engines and refrigerators. In case of leaks of the resonator system, the operating conditions are changed in such a way that safety is not of concern.

## 1.3 MOTIVATION

History has shown that in certain technologies, a small change in a component’s design, a new idea, can revolutionize that device’s utility. Consider, for example, the computer during the transition from room sized systems using vacuum tubes to now ubiquitous calculators and computers using (microfabricated) transistors. A significant decrease in size and power consumption, opened the door to a wide market penetration. Today, of course, computer technology is an integral part of daily life. Current thermoacoustic refrigeration systems are also room sized, and have limited efficiency. It is because of their size that these promising systems are not visible to the public. Thermoacoustics can be considered as being in the “tube” stage. In order to create widespread interest in this environmentally sound technology (i.e. advance it to the ubiquitous state), we must increase the efficiency (or COP) and also decrease the footprint.

### 1.3.1 Environmental Motivation

Thermoacoustic refrigerators can provide cooling without environmentally harmful refrigerants. In addition, the system design is extremely simple, which allows for very good “cradle to grave” performance as well. Using TARs instead of conventional VC driven cycles can significantly reduce the global warming potential of refrigeration and air conditioning. This is especially true in locations where waste heat can be used for the necessary heat input. In cases where such a system cannot provide sufficient cooling, it could be used as a supplement to a conventional refrigeration system. Since thermoacoustic refrigeration is inherently less efficient than conventional technologies, the use of waste heat is a key factor in the implementation of this alternative refrigeration technology. The potential savings of environmentally harmful materials in cases where waste heat is available in abundance can be significant enough to justify a push in the use of TARs in the long term. Primarily, the efficiency and refrigeration capacity has to be increased in order for TARs to become a feasible replacement for current technology. Thus, a detailed understanding of inherent loss mechanisms is important. In addition, we also have to consider overall dimensions of thermoacoustic devices.

If we cannot decrease the size of current large scale examples, or decrease the cost of current laboratory examples on the small scale and microscale, it will prove to be very difficult for thermoacoustics to find its way into broad acceptance.

### 1.3.2 Technological Motivation

It must be assumed that both the decrease in size as well as the introduction of curvature for a more compact footprint will be responsible for a relative amplification of all inherent losses during operation of the refrigeration system. Benavides attempted to determine a theoretical lower limit for miniaturization of thermoacoustic devices. He developed an analytical model of a thermoacoustic engine (44) and then applied it to a model for determination of a low feasibility limit. His work resulted in a concise description of the size limits in both the axial and lateral direction, as well as maximum operating frequency (45):

$$\begin{aligned} \text{Min. longitudinal size: } L_c &= \frac{2\pi 2\Gamma}{a} \\ \text{Min. transversal size: } l_c &= \pi \frac{\sqrt{2\nu\Gamma}}{a} \\ \text{Max. frequency: } f_c &= \frac{a^2}{2\pi 2\Gamma} \end{aligned}$$

These limits depend on the speed of sound in the gas  $a$ , and the parameter  $\Gamma$ , which depends on kinematic viscosity  $\delta$ , kinematic bulk viscosity  $\nu$ , thermal diffusivity  $\alpha$ , and the ratio of the constant pressure/constant volume specific heats  $\gamma$ :  $\Gamma = \delta + 4/3\nu + \alpha(\gamma - 1)$ . Assuming that a continuum description is valid, and not accounting for the effect of the walls on fluid flow, the minimum sizes are determined to be on the order of single micrometers and  $\frac{1}{10}\mu m$  longitudinally and transversally, respectively, when operating at atmospheric pressure. The maximum operating frequency is determined to be on the order of 100  $MHz$ . These results are provided for a range of inert working gases as well as air at a temperature of 300K (45). It is not conclusive whether this limit is an absolute value, but it is a first reasonable estimate.

There are several physical examples of developments towards small scale devices. Nika et al. provided a detailed insight into the development of a thermoacoustic engine and

pulse tube refrigerator. They utilize microfabrication for the regenerative units and heat exchangers. They illustrate the range of possibilities at the small scale in both manufacturing (46; 47) and modeling (48). Also, Symko et al. illustrated a miniature thermoacoustic cooling system as an application for electronics cooling (49; 50). It is obvious that the manufacturing of system components can become difficult as microfabrication techniques are implemented, (46; 51). These efforts prove that thermoacoustics can be applied on the small scale, albeit in a laboratory setting. With this proof in place, this work aims to develop means that allow us to further understand issues arising in the miniaturization.

As a consequence of past research efforts, it was found that there is significant potential to improve thermoacoustic devices on all scales, but especially on the small scale. To date, the materials used in the construction of thermoacoustic engines and refrigerators has been driven by convenience and availability. It is understood that the regenerator should have a high heat capacity as its temperature should not to be influenced by the temperature of the oscillating gas. However, the thermal behavior of device components has largely been overlooked as a contributor to overall system performance. Any time heat is transferred across a temperature difference, entropy is generated. This is synonymous with energy loss. In addition, there will be energy loss to the surroundings via device boundaries. This energy is lost without having contributed to the thermoacoustic effect. It is intuitive that a decrease in size will increase the importance of thermal losses, as the surface-to-volume ratio increases. Here, surface refers to the outer surface of the device, and volume refers to the thermoacoustically active volume of the device.

As an alternative to general scaling of the device, it is also possible to introduce curvature to the resonator tubes of a TAR. This approach as a means to reduce the device footprint has also not been considered. Again, intuition leads us to assume that the introduction of curvature to a wave guide is responsible for losses. In order to verify that curving the resonator is a useful way to advance thermoacoustic devices, these losses have to be quantified. It is neither understood nor investigated whether a limit of curvature (where the “straight” assumption loses validity) exists, or what that limit is. It is one of the goals of this work to understand the losses that are created by the curvature of the resonators.

## 1.4 SOLUTION APPROACH

As outlined above, this work aims to investigate thermoacoustics in three areas, all under the umbrella of furthering this environmentally sound technology by decreasing device components and the entire system. The lack of understanding of the thermal losses that occur during operation is a large obstacle that hinders progress in this direction. Thus this work can be divided into the following parts:

1. Prove the validity of a thermoacoustics refrigerator as a replacement for conventional refrigeration (vapor compression),
2. Investigate the influence of the thermal properties (specific heat, thermal conductivity, and density) of device components, and
3. Consider resonator curvature as a means to decrease the device footprint.

These main goals will be targeted by utilizing the following tools:

1. A detailed case study on replacing vapor compression mobile air conditioning by a thermoacoustically driven system.
2. An experimental analysis to investigate the influence of thermal properties in a thermoacoustic engine and refrigerator.
3. A CFD analysis to investigate curvature effects as well as furthering the field of CFD analysis in thermoacoustics and thermoacoustics itself through a better understanding of fluid behavior around the stack.
4. Numerical optimization techniques as a design tool for thermoacoustic devices.

First, in order to justify further efforts, the case study will discuss mobile air conditioning as a major target area of thermoacoustics. This choice is based on the ample availability of waste heat in vehicle's engine compartments as well as the resulting dimensions of a thermoacoustic replacement. It will be shown that the temperature level of waste heat available in vehicles is sufficiently high to drive a thermoacoustic refrigerator. Also, the resulting size of the device is sufficiently small to fit into an engine compartment. Finally, the environmental impact of this hypothetical replacement will be estimated.

Next, the effect of the thermal properties of the driving components on the performance of thermoacoustic devices will be quantified. This influence will be investigated in both an engine as well as a refrigerator through a material variation of the stack and the regenerator, respectively. We will illustrate that it is important to consider thermal losses. Results from the engine will highlight the tradeoff between conductive heat transfer through the stack assembly and the convective and radiative heat transfer to the surroundings.

In order to investigate the effect of resonator curvature on the thermoacoustic effect, a CFD study was developed, because it allows insights into the detailed processes that experimental work cannot uncover. Through this means, it is possible to illustrate the minute effects of curvature on the ability to sustain a standing wave and on the heat transfer between the solid walls and the gas. Also, this investigation will be used to highlight the effect of the working gas' thermal penetration depth on performance by means of a variation of the Prandtl number. Equally as important as understanding these phenomena better, the development of the CFD study is in itself a significant contribution to the field of thermoacoustics. Previous examples are few. The presented efforts should lead to an increased utilization of simulation-based investigation for future system designs.

Finally, as a combination of findings from the experimental work as well as the numerical thermal/fluid simulation, optimization will be introduced as an additional design tool. Again, previous examples are rare. An approach to account for thermal losses based on design choices that can be made for a stack of a thermoacoustic engine will be shown. Modeling for this section involved a finite element solver to account for the temperature distribution throughout the stack. In conjunction with a numerical optimization algorithm, results show an influence of the material choice and an estimate of an optimal stack geometry.

## 2.0 REFRIGERATION TECHNOLOGY

### 2.1 BACKGROUND

Mechanical refrigerators were developed close to 250 years ago, when William Cullen managed to freeze water with an air pump (52). It wasn't until 1834 that Perkins developed the first machine that was able to sustain constant low temperatures. The first vapor compression cycles were invented in the 1860s and 1870s. At this point in time, refrigeration was primarily used in industry and to create ice, which was then used in ice boxes to provide cooling in residential settings. In the first quarter of the 20<sup>th</sup> century, refrigeration finally bypassed the icebox and was established in homes (52; 53).

Today, refrigeration and air conditioning are vital parts of our daily routine. We expect to use perishable goods in our households. Before those reach their final destination, they have to be transported and stored, both under cooled conditions. We expect our homes, offices, and vehicles to be comfortable in any environment. Less obvious applications are cryogenic cooling, which is of importance in the medical field, and the transport of gaseous fuels, such as natural gas or hydrogen, on trains, airplanes, and other vehicles (which is of increasing interest to manufacturers and policy makers).

This large need for refrigeration on many different temperature levels has created a vast variety of refrigeration and freezing technologies. For the majority of applications, vapor compression cycles and absorption cycles are used. The latter are used for large scale applications, while the former are used widely in applications we encounter on a daily basis. One niche technology that is largely overlooked as a provider of cooling is thermoacoustic refrigeration. Thermoacoustic cooling can be achieved with heat as an input, and the device works without moving parts, thus making it a potentially attractive alternative to the status

quo. This work explores the feasibility of introducing thermoacoustic refrigeration to a broader market. In order to provide a context for this work, we will first elaborate on conventional refrigeration.

## 2.2 SCIENCE OF REFRIGERATION

Vapor compression refrigeration (VCR) utilizes the latent heat of vaporization to withdraw a cooling load from an object and transfer this heat to the environment via a condenser. The peripherals include pumps and secondary heat exchangers that influence the performance of the refrigeration system. The most important requirement for the working fluid is its volumetric cooling capacity (i.e. a measure for the material-specific heat of vaporization) and boiling point (which is pressure dependent). The boiling point, of course, determines the lowest achievable temperature. When large scale refrigeration was introduced in the 19<sup>th</sup> century, natural refrigerants such as carbon dioxide ( $CO_2$ ), ammonia ( $NH_3$ ), and sulphur dioxide ( $SO_2$ ) were used (54).  $CO_2$  provided the safest option then, but it requires a relatively high operating pressure to achieve a useful boiling point. The latter two refrigerants are toxic, which is one reason why replacements were required later, especially when refrigeration moved into residential applications. The breakthrough occurred when chlorofluorocarbons (CFCs) were developed (most notably R-11). They provided safe refrigeration because they were not flammable, toxic, explosive, or corrosive (55).

### 2.2.1 Global Warming and Ozone Depletion Potential

In 1974, it was discovered that the ozone layer was being depleted and also that the use of CFCs was responsible for this phenomenon. Specifically, it is the chlorine component of these refrigerants that is responsible for ozone depletion. One chlorine molecule can degenerate 100,000 ozone molecules ( $O_3$ ) (55). In addition to exhibiting an ozone depletion potential (ODP), CFCs also act as greenhouse gases in the atmosphere. Greenhouse gases are capable of absorbing infrared radiation, which results in a rise in surface temperature. Every gas

exhibits this behavior to a different degree; a measure for this behavior is provided by the global warming potential (GWP). In 1987, the Montreal Protocol on ozone depletion started requiring nations to decrease their production and emission of CFCs and prompted a sharp increase in the development of alternatives. The first step was to develop hydrochlorofluorocarbons (HCFCs) and more recently, hydrofluorocarbons (HFCs). The former still utilizes chlorine molecules and thus has an ODP and a phase-out schedule, while the latter does not contain chlorine and exhibits a zero-ODP. Both types of refrigerants, however, exhibit a relatively large global warming potential.

### 2.2.2 Properties of commonly used Refrigerants

Table 1 lists some relevant properties of several different refrigerants (54; 56). R-12 is used in vehicle applications, but it is being replaced by R-134a (56; 57).  $CO_2$  (or R-744) is being considered again because of its low GWP value. R-22 is used in residential air conditioning systems (56), but will inevitably be phased out as well because of its chlorine content.

Table 1: Material properties of several relevant refrigerants adapted from Kim et al. and DOE Building Energy Data Handbook 2007 for R-134

Refrigerant	R-12	R-22	R-134a	R-744 ( $CO_2$ )
ODP/GWP	1/8500	0.05/1700	0/1300	0/1
Normal boiling point [ $^{\circ}C$ ]	-29.8	-40.8	-26.2	-78.4
Refrigeration capacity [ $kJ/m^3$ ]	2734	4356	2868	22545
Introduction as a refrigerant	1931	1936	1990	1869

The large numbers corresponding to the GWP represent the amount of (reference)  $CO_2$  which would have to be emitted to achieve the same greenhouse effect as one unit amount (commonly measured in tons) of that refrigerant emitted. The ODP is measured using R-11 as the reference value (thus R-22 has an ODP 20 times smaller than R-12). For most refrigerants, the letter  $R$  and a sequence of numbers indicates the number of hydrogen,

fluorine, and carbon atoms in each substance (58). If the description is R-xyz then this corresponds to:

- $x - 1$  Carbon atoms
- $y + 1$  Hydrogen atoms
- $z$  Fluorine atoms

Note that R-744 does not fit this description,  $CO_2$  does not contain 6 carbon atoms, 5 hydrogen atoms, or 4 fluorine atoms. Instead, the description is derived from the classification of the material, where “7” stands for natural substance, and its molecular weight  $M_{CO_2} = 44 \text{ g/mol}$  (59).

### 2.3 REFRIGERANTS USE IN COOLING APPLICATIONS

The 2007 Buildings Energy Data Handbook (DOE) illustrates that R-12 is the single most emitted refrigerant in the U.S. R-134a is also emitted in significant amounts (56). Together, both substances contribute almost half of the total emitted halocarbons (from data ranging until 2001). Both are used primarily in vehicle air conditioning (AC) systems. The other major contributing substance is R-22. Since the implementation of the Montreal Protocol, the use of harmful refrigerants has been decreasing significantly. While already smaller than the GWP of R-12 (10600), the GWP of R-134a (1300) is still very high compared to carbon dioxide (56). As R-134a is a hydrofluorocarbon (HFC) and thus contains no chlorine, its ODP is zero, which is the primary reason for its use. Regardless, the high GWP remains, and, for this reason, R-134a is to be phased out in Europe beginning in 2011 and carbon dioxide (R-744) and R-152 ( $GWP = 140$ ) are considered as possible replacements. In addition, a hydrofluoro-olefin (HFO-1234yf) is also considered as a replacement. The latter substance is flammable, illustrating how, ironically, toxicity and flammability are starting to become accepted again, as long as the GWP of the substance can be decreased. Non-environmental concerns with the change to new air conditioning systems is the added cost and weight because of higher pressure levels and added safety systems (as a result of the flammability

of the refrigerant) (57; 60). Other “natural refrigerants” such as ammonia are also being considered for alternatives as well, although toxicity remains an issue. The performance of several replacements for R-12 have been studied by Baskin et al. (61). Regardless of recent advances in refrigerant research, one can argue that these advances are merely incremental and that the chemical improvement of refrigeration has been exhausted, and that only a new technology can achieve the next major improvement in regard to the environmental impact of refrigeration. The goal has to be equal cooling performance at significantly improved environmental performance. Any new technology will not catch on if the users have to significantly alter their behavior or expectations of performance.

## 2.4 OTHER REFRIGERATION TECHNOLOGIES

There are several other ways to provide cooling and refrigeration than by vapor compression devices. None of these is currently as versatile as vapor compression systems, which is why exposure to the public is limited.

### 2.4.1 Absorption Refrigeration

Absorption refrigeration generally utilizes a binary mixture of a refrigerant and an absorbent. In the so-called two stage process, the refrigerant is evaporated and the vapor is absorbed in a binary solution of absorbent/refrigerant. This mixture is then pumped to a high pressure level where external heat is supplied in order to regenerate the refrigerant out of the mixture. The refrigerant is then cooled in a condenser, brought down to the low pressure level and evaporated once again. The choice of working fluids determines the achievable temperature levels, specifically at the low temperature. Most commonly used are water/ammonia and LiBr/water. Srihirin et al. provide a comprehensive overview of several absorption systems, ranging from the simple single-effect system to the complex triple-effect absorption systems and additional variants. Their overview shows that the COP is generally around 1, with simple systems exhibiting smaller values, while complex systems can exceed the value of

1 (62). Garimella states that while these systems provide many advantages over vapor compression systems, such as fewer moving parts and lack of harmful refrigerants, absorption coolers are limited to large scale applications. Especially highly efficient systems are hindered from entering the small scale market because of system complexity and high cost (63).

#### **2.4.2 Adsorption Refrigeration**

Adsorption systems are also based on withdrawing heat from the surroundings during an evaporation process, much like a vapor compression system. Low grade heat is sufficient as an input for these systems and they run with natural refrigerants such as water, ammonia, or alcohol. Fluorocarbons are also used as refrigerants, subjecting adsorption technology to the known environmental drawbacks. Adsorption cooling is not a continuous process. During the cooling process, the refrigerant is condensed into an adsorbent (such as zeolites, or silica gels) at low temperature. A heat input during the desorption process is used to return the refrigerant to the gas phase. Adsorption cycles can easily be driven by waste heat and also solar heat. Their COP is generally smaller than 1 (64-66), on par with thermoacoustic refrigeration.

#### **2.4.3 Thermoelectric Refrigeration**

A more exotic means to provide cooling is through a thermoelectric system. This technology is based on the Peltier effect, which illustrates how a junction of two materials will change its temperature if an electric current passes through it (the corresponding reversed phenomenon was also explained by Seebeck). Mechanically, it is the simplest design imaginable, as thermoelectric coolers consist of a series of such junctions. The issues with introducing thermoelectric systems on the large scale are their limited achievable cold temperature, low efficiency, and high cost.

#### 2.4.4 Thermoacoustic Refrigeration

In contrast to both conventional and the introduced alternative refrigeration technologies, thermoacoustic refrigerators (TARs) can provide a cost effective alternative for the refrigeration market. TARs do not use refrigerants as absorption and adsorption systems do; neither do they require expensive materials as thermoelectric refrigeration does. At first glance, this introduction shows TARs as the solution to many of the environmental problems that refrigeration causes. However, their inherently lower COP requires a higher heat input to provide the same cooling load as a comparable VC refrigerator. As a consequence of the increased energy input, additional carbon dioxide ( $CO_2$ ) is emitted, which is, of course, also a strong greenhouse gas. Worse, its emission is continuous, as the heat input is necessary during operation (as opposed to the refrigerant in conventional refrigerators and chillers that is only emitted slowly over time through leaks or when the system is discarded). The goal must be then to drive TARs with waste heat, so as to actually significantly decrease the GWP of refrigeration. This requirement has also been mentioned by Garrett et al. (67). To illustrate this issue, the Alternative Fluorocarbons Environmental Acceptability Study (AFEAS) has introduced the “Total Equivalent Warming Impact” (TEWI) which considers the direct warming impact of the utilized working fluid (zero for TARs) and the indirect impact on warming by the operation of the device (higher for TARs than VCRs when driven by electricity) (68). This figure of merit has previously not been considered with respect to thermoacoustic refrigeration.

### 2.5 TOTAL EQUIVALENT WARMING IMPACT (TEWI)

As a reminder, thermoacoustic refrigeration is based on the (externally heated) Stirling cycle, and as a consequence the TAR can be driven by waste heat. Potential locations with large waste heat availability are industrial settings and vehicles. McCulloch has illustrated that residential refrigerators only account for about 10% of refrigerant emissions into the atmosphere. Also, since these systems are hermetically sealed, they generally only pose

a problem when they are improperly disposed of at the end of their life cycle (which is approximately 20 years). Mobile applications, primarily vehicle air conditioning (AC) units, on the other hand, pose a much larger problem because of leakage and accidental spills. The life cycle of the refrigerant in this application is only 6 years (69). When considering the production of the most common refrigerant and R-134, and the two most likely replacements (HFO-1234yf and R-744), it was found that HFO-1234yf has the lowest contribution to  $CO_2$  emission overall (60).

The TEWI considerations, refrigerant consumption of mobile refrigeration, and abundance of waste heat in vehicles renders this application a primary target market of TARs. Mobile refrigeration units for transportation of perishable goods may be the first target because of the large amounts of available space. Ultimately, we can envision TARs to be implemented in passenger cars as well, because this represents a very large market with a large impact on refrigerant use and emission. Zoontjens et al. have conducted an initial feasibility study on this subject and concluded that a mobile application can indeed be a target for TARs (70). To achieve this goal, TARs have to be significantly smaller and more efficient than present technology. The required cooling capacity will drive overall TAR size, and the size of the engine compartment and packaging will drive the research towards alternative resonator shapes. By using waste heat, we can avoid using additional fuel to drive the TAR, but to achieve this, we have to make the driving components of the TAR as efficient as possible, minimizing losses of any kind. In the following section, a qualitative study considering a switch from conventional air conditioning to a system driven by a TAR is presented.

## 2.6 REQUIREMENTS FOR A SUCCESSFUL TRANSITION

Depending on the application, there are several power and temperature requirements that the refrigeration system has to satisfy. For example, the power requirements of current vehicle air conditioning systems is on the order of  $5kW$ , and they typically achieve a cabin temperature of  $18^{\circ}C$ . As shown in the overview, the achievable temperature level is not a limitation for thermoacoustic systems. Rather, their size, which is a function of operating

frequency, and, in turn, a function of the lowest achievable temperature, is a limiting factor of such a system. In a TAR, the highest achievable temperature gradient is smaller than the critical temperature gradient (71). Calculating backwards from a required low end temperature, we can calculate the required regenerator length, and the resulting operating frequency for a TAR. These calculations must be based on an assumed correlation between the actual and critical temperature gradient in the regenerator. For a low end temperature of, say,  $10^{\circ}C$  (which is sufficient to provide a comfortable cabin temperature level of  $23^{\circ}C$  (72), assuming losses in the heat exchange between the inlet air flow and the TAR side) and a high ambient temperature of  $50^{\circ}C$ , which is the assumed ambient temperature for design of thermal equipment (73), the actual required temperature difference is  $40K$ . Assuming a reasonable regenerator length of  $0.1\ m$ , this results in a temperature gradient of  $400K/m$ . Assuming that we have to account for imperfect performance, we will account for a factor of 3 between the actual temperature gradient and the critical temperature gradient (i.e. we can reach 1/3 of the critical temperature gradient). Solving Equation 1.3 for  $\omega$  we see that the operating frequency is

$$f = \frac{\omega}{2\pi} = \frac{\nabla T_{crit} \rho c_p}{p} \cdot F \frac{p}{\rho c} \approx 110Hz \quad (2.1)$$

For this calculation, we assume that the velocity in the stack  $u = 0.2\ u_{max} = p/\rho c$ . The scaling factor  $F = 0.2$  is necessary because the regenerator is not located between the velocity node and the velocity antinode (closer to the former). The placement of the stack is important as the velocity component of the wave is responsible for gas displacement but also for the viscous losses, which is why a placement close to the velocity node is beneficial as the velocity there is lower than close to the velocity antinode.

If we base the design on a half-wave thermoacoustic refrigerator (because this system allows us to contain the thermoacoustic process with its high levels of sound in a closed system, not exposing the surroundings to dangerous levels of sound) this results in a total required length of

$$L = \frac{\lambda}{2} = \frac{1}{2} \frac{c}{f} \approx 1.5m \quad (2.2)$$

This basic calculation shows that the space available in an engine compartment of a vehicle is sufficient to house a TAR. Of course, larger scale applications, such as food transport, are also feasible, with fewer space and weight constraints on the TAR system. The temperature level of the waste heat in vehicles is also sufficiently high to drive a TAR. Note that the cooling water is typically controlled to  $90^{\circ}\text{C}$ , which is not high enough to provide a heat source and is also important for engine management reasons. As a result, the exhaust stream has to be considered for the heat source. In typical operation, the temperatures reached during combustion can reach well beyond  $1000^{\circ}\text{C}$ . However, because of exhaust aftertreatment, the temperature of the exhaust gas has to be maintained to be as high as possible, as the catalytic converters require an operating temperature of at least  $350^{\circ}\text{C}$  for conversion rates of 95% or better of the targeted gases. The so-called “light-off” temperature for CO (which yields, per definition, a 50% conversion into  $\text{CO}_2$ ) is  $220^{\circ}\text{C}$  (74). The requirement for the operation of the catalytic converter still results in a temperature high enough to ensure operation of a thermoacoustically driven cooling system. This assumption is further verified by work done in thermoelectric heat recovery. One example of this work illustrates that the placement for such heat recovery systems is after the catalytic converter, and that temperatures are about  $700^{\circ}\text{C}$ . The exhaust mass flow is given as a range between 0.01 to 0.03  $\text{kg/s}$  for light duty vehicles, which corresponds to an enthalpy flow of approximately 7 – 20  $\text{kW}$  of heat energy (75). Consequently, a switch to alternative cooling techniques is feasible, when we use this available energy as a basis. In the following section, we will illustrate the energetic implications of the switch from a conventional vapor compression air conditioning system to a TAR based air conditioning system.

## 2.7 COMPARISON BETWEEN VC AND TA REFRIGERATION IN VEHICLES

For this comparison, the following assumptions will apply:

- Estimated and constant COPs for both modes of refrigeration;
- The TAR system performance is not influenced by the implementation in a vehicle;

- Both the VC and TA system can provide the same cooling load;
- The considered time span for both systems is determined by the (shorter) life span of the VC system; and
- The entire refrigerant volume from the VC system is allowed to enter the atmosphere, either through leakage or disposal at the end of its life cycle.

As variables, we can calculate the TEWI based on different refrigerants for the VC system and differentiate between two cases for the TAR:

1. utilizing electricity for heat generation, or
2. utilizing waste heat (the obvious ideal case).

Additionally, we could consider a case of electric heating as a supplement to waste heat (which could be important for cold-start considerations). This approach is used for catalytic converters, for example, because they require a certain temperature to fully function, as well. Since current air conditioning systems also require a startup phase, the inherent lag for a TAR driven system would not be of concern, because it does not require different user behavior as the status quo.

### 2.7.1 Fuel Usage for Air Conditioning

Based on the above breakdown of assumptions, the TEWI will be composed of the direct effect of the refrigerant entering the atmosphere and the indirect effect of the additional fuel consumption required to run the pump and compressor of a traditional VC system. The Energy Information Agency publishes information on the number of vehicles used in the U.S., with a very detailed breakdown of total distance driven and fuel consumed (76). Assuming the same percentage of fuel used for air conditioning vs. total average fuel consumption provided by Bhatti (88.8  $l/yr$  and 2672.5  $l/yr$ , respectively, that is 3.3% (77)), this yields a total fuel consumption solely for air conditioning of  $1.4 \cdot 10^{10} l/yr$  (based on  $427.5 \cdot 10^9 l/yr$  total consumption (76)). The U.S. Census Bureau provides some information on the distribution of gasoline and diesel usage. This source shows that for transportation, roughly 80% of total consumption corresponds to gasoline, while the remainder corresponds to diesel (78).

With this information, we can calculate the indirect contribution to the TEWI from burning  $1.4 \cdot 10^{10}$  l of fuel annually. The detailed calculations are provided below.

### 2.7.2 COP Comparison between Technologies

We can extract the total cooling load that AC systems provided, by multiplying the total heating value of the used fuel by a COP. If we divide this number by the COP of the new TAR system, we can determine the amount of heat necessary to create the same cooling load as the fuel-driven AC systems thermoacoustically.

$$Q_{in,TAR} = Q_{in,VCR} \times \frac{COP_{VCR}}{COP_{TAR}} \quad (2.3)$$

As exact values for the COPs of both systems are not readily available, we can illustrate this correlation with COP ranges of both systems, as shown in Figure 7. Obviously, the worst case scenario is the replacement of a VC system with a very high COP by a TAR with very low COP. In most pairings, it is obvious that the TAR will require more heat than the VC system would need. This illustrates that it is important that the TAR be driven by waste heat rather than any other fuel source, such as electricity or even combusting additional fuel. The latter will almost always result in additional fuel consumption and larger GWP, and thus be counterproductive.

## 2.8 CALCULATION OF EMISSIONS

For our calculations, we will consider that 1/6 of the total number of vehicles lose their refrigerant every year (based on the 6-year cycle of AC systems stated above). According to Bhatti, there are approximately 170 million vehicles in use in the U.S. alone (77). Thus, approximately 28 million vehicles must replace their entire refrigerant volume every year. In addition to this direct effect, we have to calculate the amount of  $CO_2$  emitted by powering 170 million AC systems. According to the EPA, gasoline contains  $640.5g C/l$  and diesel

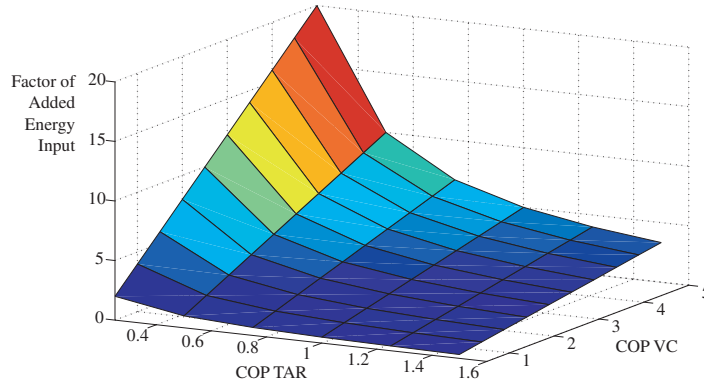


Figure 7: Illustration of the additional energy required to drive a thermoacoustic refrigeration system when it replaces a vapor compression refrigeration system

contains  $735.0g\ C/l$ . According to the guidelines given by the Intergovernmental Panel on Climate Change (IPCC) the  $CO_2$  emissions of gasoline and diesel fuels are as follows:

$$\begin{aligned}
 CO_2 \text{ emissions from gasoline} &= 640.5 \frac{g\ C}{l} \cdot 0.99 \cdot \frac{44\ g\ CO_2}{12\ g\ C} & (2.4) \\
 &= 2,328.0 \frac{g\ CO_2}{l}
 \end{aligned}$$

$$\begin{aligned}
 CO_2 \text{ emissions from diesel} &= 735.0 \frac{g\ C}{l} \cdot 0.99 \cdot \frac{44\ g\ CO_2}{12\ g\ C} & (2.5) \\
 &= 2,672.0 \frac{g\ CO_2}{l}
 \end{aligned}$$

where 0.99 represents an “oxidation factor” that accounts for the fraction of carbon actually present as  $CO_2$  after combustion (1% remains unoxidized) and 44/12 represents the ratio of molecular weights of carbon dioxide and carbon, respectively (79). With the split of 80/20 of gasoline/diesel in all vehicles, the total emission of  $CO_2$  resulting from air conditioning is

$$\begin{aligned}
& [\text{Gasoline carbon content} + \text{Diesel carbon content}] \times \text{AC fuel consumption} & (2.6) \\
& = [0.8 \cdot (2,328.0 \frac{g \text{ CO}_2}{l}) + 0.2 \cdot (2,672.0 \frac{g \text{ CO}_2}{l})] \times 1.4 \cdot 10^{10} \frac{l}{yr} \\
& = 3.35 \cdot 10^{10} \frac{kg \text{ CO}_2}{yr}
\end{aligned}$$

In addition to this number, we must consider the direct GWP of the refrigerant itself. For mobile AC systems, the amount of refrigerant used varies between 0.5 *kg* and 1.5 *kg* and it is estimated that roughly 50% of refrigerants are emitted to the environment over the course of one life cycle on board. During recovery, another 50% of the remaining amount is lost to the environment (80). This emission results in an additional contribution of approximately 50% of those of the indirect GWP resulting from burning additional fuel to power AC systems. This estimate is based on the use of R-134a and does not account for the remaining usage of R-12 (81). As a consequence, the actual number of direct contribution should be estimated to be slightly higher than 50%. The direct carbon-equivalent emission by refrigerant use is thus

$$\begin{aligned}
& \text{Refrigerant loss percentage} \times \text{Refrigerant GWP} = & (2.7) \\
& 0.5 \cdot 3.35 \cdot 10^{10} \frac{kg \text{ CO}_2}{yr} = 1.675 \cdot 10^{10} \frac{kg \text{ CO}_2}{yr}
\end{aligned}$$

and the overall emission of  $CO_2$  resulting from traditional mobile air conditioning is the sum of Equations 2.6 and 2.7 and equals  $5.025 \cdot 10^{10} kg \text{ CO}_2/yr$ . This number corresponds to roughly 1% of the total (energy-related) emission of  $CO_2$  in the U.S. (82). It should be noted that this is a differential contribution; replacing traditional air-conditioning systems with a thermoacoustic system will directly eliminate these emissions. Our approximate calculations illustrate how thermoacoustic refrigeration is a viable alternative to conventional air conditioning systems in vehicles. Its effect is seemingly small, but any decrease in greenhouse gas emissions is desirable. For this shift in technology to become reality, there are several changes current TARs have to undergo.

## 2.9 OTHER POTENTIAL APPLICATION AREAS FOR TARS

Again, it is obvious that a thermoacoustic refrigeration system has to be powered by waste heat in order to fully utilize its advantages. Other potential targets are the transport for perishable goods or medical supply with trains and trucks. There are different requirements depending on the type of food. Ice cream, for example, requires  $-23^{\circ}C$ , frozen vegetables  $-18^{\circ}C$ , meat products  $-1^{\circ}C$ , and fresh vegetables  $1^{\circ}C$  (83). Although these temperature levels are lower than that of a mobile air conditioning system, these applications offer advantages in that the space requirements are relaxed when compared to a passenger vehicle, and also the amount of available waste heat is larger than in light duty vehicles.

### 3.0 LOSS MECHANISMS OF THERMOACOUSTIC DEVICES

Before investigating the effects of thermal properties on the driving components of thermoacoustic devices, it is important to understand the variety of loss mechanisms that occur in the operation of these devices. Most research on loss mechanisms in thermoacoustics has been done on acoustic and streaming losses. One could argue that those are the largest contributors to energetic losses. On the other hand, they might simply be the most obvious losses:

- A wave propagating through a porous medium will experience attenuation,
- A heated gas will experience convection, and
- A gas that undergoes acoustic oscillations will be displaced; the velocity attributed to this oscillation will result in viscous losses and other streaming losses.

These are the loss mechanisms of thermoacoustic devices that are well understood. Sections 3.1-3.3 will elaborate on these in order to provide a general overview of losses in thermoacoustics. Partially, these losses are better understood because they can be determined experimentally, as shown by Thompson et al. (84). The following Section 3.4 will introduce the less known loss mechanisms that are the target of the present investigation. Also, it must be noted that the attenuation of wave amplitude is the driving phenomena in a TAR, but in an engine, it should be considered as negative influence.

## 3.1 STREAMING LOSSES

Gas displacement is an essential part of the existence of the thermoacoustic effect. With a stationary gas, it would be impossible to move heat from the heat source to the heat sink. However, in addition to the necessary gas displacement due to the oscillations, there are two streaming mechanisms encountered in thermoacoustic engines: Gedeon and Rayleigh streaming. Numerous groups have determined that streaming losses contribute significantly to the total losses of Stirling driven thermoacoustic devices (for both engines and refrigerators). In fact, streaming affects the refrigerators and traveling wave engines the most (15) because of their looped resonator section, which forms a continuous path for mass flow. Rayleigh streaming is also encountered in standing wave devices.

### 3.1.1 Gedeon Streaming

Gedeon streaming (or “acoustic streaming around a torus” (15)) is specific to traveling wave engines with looped tubes and in pulse tube refrigerators where a non-zero mass flow can occur (15; 85). It results from the variation in density over the course of a cycle. Essentially, the gas is not displaced the same distance when traveling from the hot to cold side as when it travels from the cold to hot side. The result is a small “direct current” or DC mass flow, as illustrated in Figure 8 for a pulse tube refrigerator (86). Swift points out that one has to differentiate between the “time-averaged velocity at a point” and “time-averaged velocity of a particle,” which are not the same. Only the former should be considered streaming (10).

As a result of this mass flow, supplied heat does not participate actively in the thermodynamic cycle and limits its efficiency. Mostly, Gedeon streaming is mentioned in the context of pulse tube refrigerators. Swift et al. showed that the suppression of streaming would lead to an increased efficiency of a pulse tube refrigerator and that the findings would also apply to looped tube (traveling wave) Stirling engines. Gusev et al. investigated the effect of streaming analytically. They concluded that the enthalpy flux created by this process is significant in magnitude (87). One different note on streaming is provided by Penelet et al. They conclude that there are nontrivial influences of acoustic streaming that actually

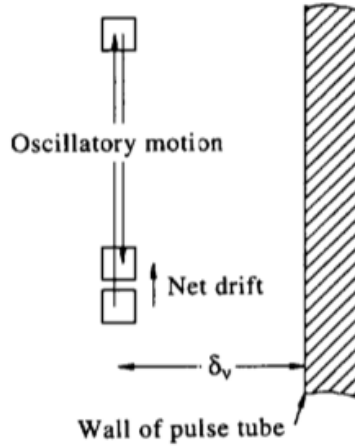


Figure 8: Illustration of drift (Gedeon streaming) resulting from variations in viscosity in the working gas in a pulse tube refrigerator

benefit engine performance. They argue that streaming contributes to the “tuning of the temperature field [in the regenerator] such that additional thermoacoustic amplification occurs” (88). In accordance with the general consensus, however, it must be assumed that streaming is a negative side effect of the oscillations. By transporting enthalpy with a gas flow, it leads to unnecessary loads on the cold side of engine regenerators and unnecessary loads on the stacks of (pulse tube) refrigerators. There are numerous ways of suppressing this streaming in pulse tube refrigerators. As a result, some of these findings may not be directly applicable to this work, as the primary focus lies on the engine. The hydrodynamic suppression method however, may be a useful hint as to how to improve engine performance. Schematically, this idea is illustrated in Figure 9 (71; 89).

When the fluid exits the tube, the streamlines formed are essentially parallel (as long as the flow is laminar). When the fluid enters the tube from open space on the other hand, it is drawn from the semicircle surround the opening, resulting in added resistance. This resistance can be tuned by the shape of the tube’s inlet. A configuration like this can easily be incorporated into traveling wave engines to provide a reduction of Gedeon streaming. Swift et al. also introduced a suppression method specifically for engines. They placed a

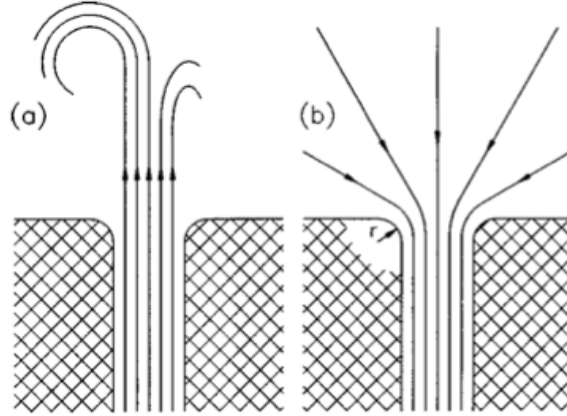


Figure 9: Illustration of flow behavior of a gas flowing leaving a small (a) tube as opposed to entering it (b)

flexible membrane inside the torus of a traveling wave engine and thus increased performance of their device (71).

### 3.1.2 Rayleigh Streaming

Rayleigh streaming occurs in both standing wave and traveling wave engines. It results from the interaction between the oscillating flow and the walls of the resonator, or even the stack or regenerator. It was first mentioned by Rayleigh in his “Theory of Sound” in 1896 (90) and investigated by Lee et al. (91) and Olson et al. (86). Baillet et al. also illustrate acoustic streaming under steady state operation of a standing wave device (92). The first experimental proof of the existence of this loss mechanism was given by Gaitan et al. (93). The first visual evidence of Rayleigh streaming was provided by Yazaki et al. who used smoke tracers to visualize this effect inside a resonance tube (94).

In refrigerators, streaming losses are as detrimental to performance as they are in engines. Rather than removing useful heat from the environment, streaming introduces an unnecessary heat load to the refrigerator by carrying heat from the driving components of the engine. We can see this effect by considering a temperature profile recorded across a

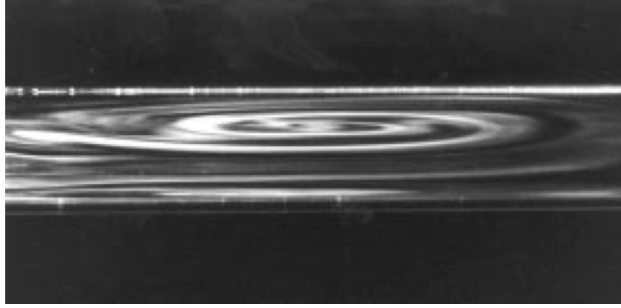


Figure 10: Vortex formed by streaming inside the resonator of a thermoacoustic engine

refrigeration stack driven by a standing wave engine. In Figure 4, this would occur with a secondary ceramic stack placed immediately behind the driving stack, facing the open end. This design is crude, but it illustrates the issue. Upon onset of oscillations, the cold side of the refrigerator is cooled. On the other end, the ambient side is heated because of its close proximity to the driving stack and the convective transport of heated gas into the refrigeration stack. This heat input is eventually propagated to the cold side, which then increases in temperature. Figure 11 shows the thermal behavior of a refrigeration stack after the onset of oscillations driven by a standing wave engine.

The adverse effect of streaming from the engine stack to the refrigeration stack becomes apparent. If it were possible to maintain ambient temperatures at the ambient side (and not allow it to heat to over  $40^{\circ}\text{C}$ ) one can see that this crude refrigerator could achieve temperatures below freezing. With the current experimental setup and unsuppressed streaming, a minimum temperature of about  $20^{\circ}\text{C}$  can be achieved for a short while, before even the cold side experiences the adverse effect of the heating of the ambient side. After 130s, the oscillations were ended, thus the streaming of hot air into the cooling stack ended and the temperatures on both ends began to equalize. At this time, it is not possible to determine whether this effect can entirely be attributed to Rayleigh streaming, but considering that it was seen during operation of a standing wave engine, this is a safe assumption.

One way of alleviating this strain on the cooling stack is to place a membrane between the driving stack and the refrigerator stack (38) (which extends on the idea provided by

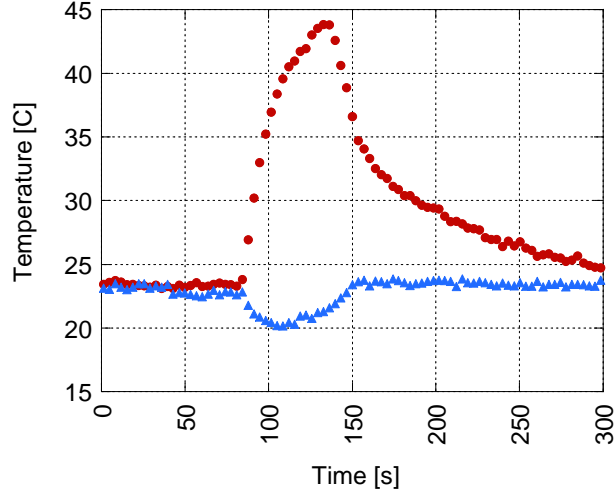


Figure 11: Illustration of heat driven refrigeration: Cooling at onset of oscillation (80 seconds) and subsequent heating of the cold side because of addition of heat from driving stack via unchecked streaming

Swift et al. (71)). This would effectively reduce the transport of heat between the driver and refrigeration stack while allowing the pressure oscillations to propagate from the driver to the refrigerator. Needless to say, though, the addition of a vibrating mass adds yet another loss mechanism to the system. A different way to avoid the heat input from the driving stack is to place the refrigeration stack at a different location. This solution, however, requires that different wave guides be joined together, which leads to a whole new set of problems.

### 3.2 ACOUSTIC LOSSES

Acoustic losses can occur in several ways. For example, an exit of a wave guide can contribute to exit losses, and the shape of the resonator sustaining a standing wave can be such that wave propagation is hindered. Flanges and uneven surfaces inside a wave guide can hinder wave propagation by partial reflection.

There are several examples in the literature on more efficient resonator designs, usually resulting in tapered tubes. Obviously, the proposed work in coiling the resonator is a radical change in the current designs. This will certainly create acoustic losses, but the magnitude of these losses is unknown. The shape of the flow channels and the resonator have been subject to several investigations. Arnott et al. investigated a thermoacoustic stack in regard to the influence of arbitrary cross section compared to a parallel plate and circular cross sections. It was found that the parallel plate configuration results in the best heat and work transfer (95).

In regard to refrigeration, acoustic losses arise when we try to decouple the driving stack and refrigeration stack. Considering the very basic driver/refrigerator configuration again as a starting point, we can illustrate the arising acoustic losses. In order to decouple the driving stack and the refrigeration stack (to avoid the convective losses illustrated above), we could attach a separate resonator to the engine's resonator. By necessity, it needs to be located where the gas undergoes large variations in pressure and small (but non-zero) variations in velocity. This setup removes the refrigeration stack from the driver, but it adds a significant amount of resonance body, again changing the entire system and introducing different losses.

### 3.3 VISCOUS LOSSES

As a result of the velocity component, viscous losses occur. The interactions of the oscillating fluid with the porous stack causes direct viscous dissipation and indirectly causes thermal dissipation. Both mechanisms are known to be the main contributors to losses in thermoacoustic devices (96; 97). As the engine size is decreased, the operating frequency increases (assuming the engine operates at the first harmonic and the engine utilizes the  $\lambda/4$  design). As the operating frequency increases, the thermal penetration depth of the gas decreases (refer back to Equation 1.4) and thus the flow channels have to be smaller to allow proper heat transfer behavior. Obviously, as the hydraulic size of the flow channels decrease, the

surface area per volume increases and thus viscous losses increase. The velocity in a standing wave (*in the free field*) is given by the following correlation (98):

$$u(z) = \frac{p(0)}{\rho c} \sin\left(2\pi \frac{fz}{c}\right) \quad (3.1)$$

where  $p$  is the pressure as a function of the distance  $z$  away from the closed end (velocity node),  $\rho$  is the density, and  $c$  is the speed of sound. It is also dependent on the operating frequency of the device  $f$ . Obviously, the presence of the stack will influence this velocity distribution. The simulation work that will be discussed below will illustrate this behavior in detail. For the purpose of the work in this section, it is safe to disregard the exact pressure behavior as a result of the interaction with the stack. Thus, if a device is scaled down and its working frequency is increased, the gas velocity increases. Consequently, the Reynolds number increases, which corresponds to an apparent increase in viscosity and thus viscous losses.

### 3.4 PARASITIC HEAT FLUX IN A THERMOACOUSTIC REGENERATOR

While streaming, acoustic and viscous losses have frequently been studied, thermal losses are presently not well understood. As mentioned before, thermoacoustic engines (of both operational modes) operate solely based on the temperature gradient present in the stack or regenerator. By nature, this temperature gradient causes a heat flux by Fourier conduction through the stack (or regenerator). Ultimately, the smaller the thermal conductivity of the material, the smaller this heat flux should be. In order to fully understand the influence of this heat flux, and the ability to create sound waves regardless of material used, a simple test setup must be created.

For simplicity's sake, initial tests have been conducted with a standing wave engine. It was built using two sections of Pyrex tubing and a stack made of a piece of Corning Celcor monolith (600cpi, 5/1000in = 0.127 mm wall thickness). This material is noted for its low thermal conductivity and low pressure drop. The ambient side of the stack was cooled with

a copper wire mesh soldered to copper tubing. The tubing carried approximately 3 ml of water per second. The total length of the device was 250mm. During operation, it has been found that the cold side is heated beyond ambient temperature (note that the operating conditions were not set to match a theoretical optimum). Figure 12 shows the measured temperatures at both ends of the stack of the simple standing wave engine.

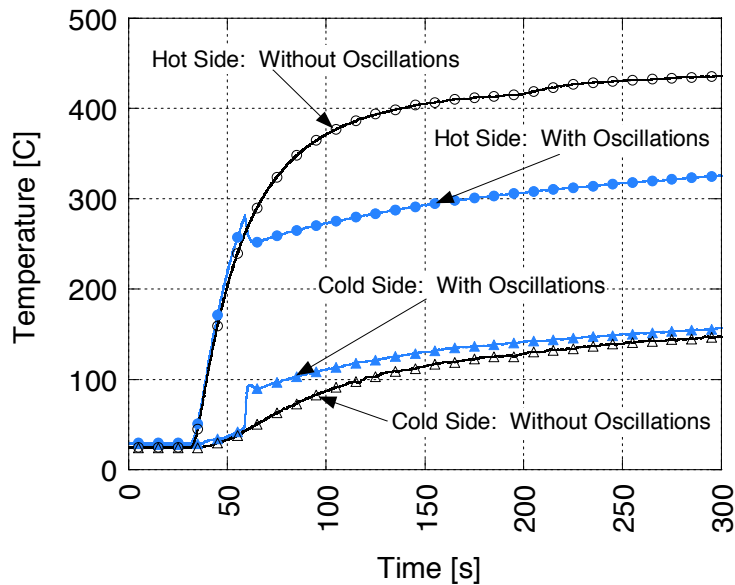


Figure 12: Temperatures on both ends of the stack in a standing wave engine. The heating of the ambient side is apparent

Oscillations were hindered by plugging the open end. The corresponding graphs in Figure 12 have open markers (top and bottom plots). The cold side is heated significantly. When the open end was opened during a second test, oscillations began when the hot side reached approximately  $280^{\circ}C$ . As the oscillations started, the transport of heat away from the hot side became apparent. The corresponding plots have filled markers. The hot side temperature decreases sharply and the cold side temperature rises equally sharply. The temperature difference between the two sides (i.e. the temperature gradient in the stack) remains constant. In either case, it is obvious that the cold side temperature rises too far, resulting in an unnecessary cooling load. There are two possible reasons for this behavior:

1. Not enough cooling capacity, or
2. Too much heating power is supplied.

If we can maintain the same  $\Delta T$  with a different  $Q_{input}$ , the cold side temperature can be reduced, as can the cooling load. Consider the expression for thermal efficiency:

$$\eta_{th} = \frac{\text{Work}_{out}}{\text{Heat}_{in}} \quad (3.2)$$

Assuming that the work output can be written as a heat flux  $Q_{TA}$ , the expression can be rewritten in terms of only heat fluxes:

$$\eta_{th} = \frac{Q_{TA}}{Q_{heat, in}} = \frac{Q_{TA}}{Q_{convection} + Q_{conduction} + Q_{TA}} \quad (3.3)$$

This equation assumes that the heat input is split into three parts, namely into the heat utilized in the thermoacoustic effect, convection losses and conduction losses. This can be rewritten as:

$$\eta_{th} = \frac{Q_{TA}}{\frac{Ak}{L} \Delta T + \left(\frac{h\pi dL}{2}\right) \Delta T + Q_{TA}} \quad (3.4)$$

where  $A$  is the cross-sectional area of the regenerator, dependent on its diameter  $d$ , and  $L$  is the stack length (not the resonator length) and is on the same order of magnitude as  $d$ .  $k$  and  $h$  are the thermal conductivity and the convective heat transfer coefficient, respectively. Equation 3.4 can be rearranged to become

$$\eta_{th} = \left[ \frac{\Delta T \pi d}{Q_{TA} 4L} (kd + 2hL^2) + 1 \right]^{-1} \quad (3.5)$$

An analysis of dimensions of the term inside the parentheses in the above equation shows that  $2hL^2 \ll kd$  when the thermal conductivity of the regenerator material (especially metals) is much larger than the convection of a free surface. Also, the order of magnitude of the lengths  $d$  and  $L$  is tens of  $mm$ . If we assume that the unity term inside the brackets is much smaller than the rest of the expression, we arrive at the final expression of the thermal efficiency

(in terms of diameter, temperature difference, and thermal conductivity of the regenerator material):

$$\eta_{th} = \frac{Q_{TA}4L}{\Delta T k \pi d^2}. \quad (3.6)$$

This final equation illustrates how the thermal efficiency of a regenerator depends on its thermal conductivity. Since it is in the denominator of the expression, the material must be selected so that it has as low a thermal conductivity as possible. It must be noted that this derivation applies mostly to traveling wave engines as they utilize a metal regenerator. If applied to a ceramic stack, the present assumption could create significant error, as the assumption that  $kd \ll 2hL^2$  loses its validity. When considering ceramics, we must utilize Equation 3.5 rather than Equation 3.6.

Another facet of the thermal issues arising in thermoacoustic devices are entrance and joining effects. There is a correlation between the pressure amplitude and the resulting displacement of the gas. In high amplitude pressure waves, the displacement in the direction of wave propagation is significant, and we have to consider the effects of this displacement on the design of heat exchangers. It is not uncommon for the heat exchangers to be of similar size as the magnitude of the gas displacement (10).

The influence of the thermal conductivity of engine components on performance has very rarely been mentioned in the literature. Organ et al. discusses this issue in relation to mechanical Stirling engines. In these devices, the regenerator can be constructed using metal meshes (similar to the ones used in traveling wave engines, except on a much larger scale). In their description, the “connectivity” and “thermal shorting” are discussed. The former describes the way the flow paths are created with stacked wire screens. Similar to this flow path, the path for thermal conduction can be derived. Ultimately, it is concluded that the thermal shorting is a mechanism that is not understood well, and leads to a decrease in engine efficiency (99).

An early mention of the thermal conductivity of components in thermoacoustic engines is given by Rott (100). Chen et al. investigated the coefficient of performance of a thermoacoustic refrigerator as a function of the temperature difference across the stack. They mention that the thermal conductivity influences the COP and that Mylar with  $k = 0.1 \text{ W/m}^2$  results

in the highest COP (101). Herman et al. mentioned the effect of the electrical power supply to the device as an influence on performance. They concluded that if the electrical power needed can be reduced, the COP can be increased (without giving a reason beyond the obvious one that the electrical power is in the denominator of the COP expression). Also, Herman et al. investigated the effect of the Prandtl Number on the COP of a thermoacoustic refrigerator. They found that an increase in Prandtl number (achieved by an addition of various inert gases to helium) results in a decrease of COP (42).

Holmberg et al. investigated the energy balance around a thermoacoustic engine in great detail. They include the conduction heat flow through the stack ( $Q_{cond}$ ), among a multitude of different heat flows. Figure 13 illustrates their energy balance (102). They found that with an increase of the input energy flux  $Q_{in}$ , the losses to the insulation increase, as do the other loss terms to the structure and viscous losses. They conclude that the conductive heat flow through the stack is independent of input energy. Their main point, however, is that the acoustic work flow  $Q_{TAin,1}$  increases more rapidly than any other heat flux loss in the system.

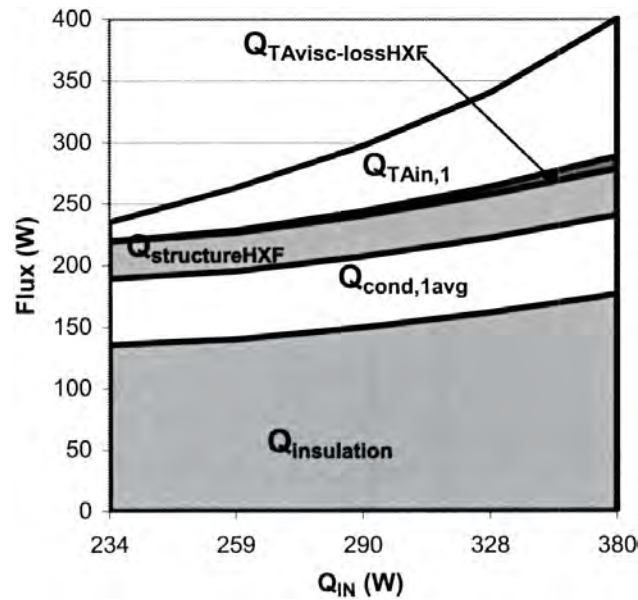


Figure 13: Energy balance of a thermoacoustic engine as a function of heat input

The main point to take from this figure is the existence of the conduction heat flux through the stack, as well as other heat losses. This heat energy does not participate in the thermodynamic process. It is part of the total added heat in the hot side and it is withdrawn on the cold side through the cooling water stream. As the input power is increased, admittedly, the thermoacoustic work output increases, but it is still a relatively small fraction compared to the remaining energy fluxes. Wakeland and Mozurkewich also mention the conductive heat flux through the regenerative unit of thermoacoustic devices, without providing satisfactory details (98; 103). Wakeland uses an engine without a stack, with only heat exchangers. Where the stack usually creates an area where the gas changes temperature gradually, his new design moves the two heat exchangers closer together, separated only by an air gap (the distance is dependent on the hot side temperature and the critical temperature gradient). This eliminates any conductive heat flow between the heat source and sink. The distance between the heat exchangers must be decreased in order for the gas to reach both over the course of one cycle. Thus, heat is given off to the gas at the heat source and transported directly to the heat sink. Resulting from the close distance between the heat exchangers, Wakeland still mentions a (parasitic) heat flow in the gap between the heat exchangers (103). Mozurkewich mentions an “unaccounted loss” that might be attributed to heat conduction through solid parts of the engine (98). In the following section, the influence of the thermal properties of the driving components of a thermoacoustic system on its performance is investigated experimentally and quantified.

## 4.0 EXPERIMENTAL INVESTIGATIONS

It has been explained in detail that there are energy flows in thermoacoustic engines and refrigerators that are unaccounted for. They are not considered design targets, because the focus always lies on maximizing power output and efficiency. It was also shown that operation using waste heat as an input is the only viable option for thermoacoustic refrigeration systems, if we want to benefit from its environmental advantages. In this case, however, it is conceivable that we want to maximize the utilization of said waste heat stream, that is minimize the heat losses that occur within the device. As a first thrust into the investigation of these thermal losses, the choice of materials in the key components of thermoacoustic devices is targeted. In this regard, the stack material of a thermoacoustic standing wave engine as well as the regenerator material of a traveling wave refrigerator will be varied. First, however, and in order to put the thermal losses in context with the other loss mechanisms that are present in thermoacoustic devices, an overview of these is provided as well.

### 4.1 THERMAL LOSS MECHANISMS

As mentioned before, thermal losses caused by the thermal properties of the engine components themselves are not well understood and require more research efforts. With respect to the issue of thermal conductivity, both standing and traveling wave engines are subject to the same issue: a temperature gradient is necessary to drive acoustic oscillations. As the

simplest model for conductive heat transfer, Fourier's Law, shows, the temperature gradient and the required heat flux are related through the thermal conductivity:

$$\dot{\mathbf{q}}'' = \mathbf{k} \frac{dT}{dx} \quad (4.1)$$

This equation illustrates the importance of the thermal conductivity on performance parameters. If  $k$  can be decreased, then  $\dot{\mathbf{q}}''$  can also be decreased, while the temperature gradient remains unchanged. Stacks in standing wave engines are commonly constructed using porous ceramic. Ceramics have very low thermal conductivity, thus making them a good candidate for stack material. Currently, it is coincidence that ceramic monoliths are used as stacks, because they are chosen for their hydraulic properties and they are easy to procure. However, their beneficial thermal properties, such as very low thermal conductivity and thermal expansion coefficient, have been overlooked. On the other hand, traveling wave engines commonly use stacked metal screens as regenerators. Those have a much higher thermal conductivity than ceramics and potentially waste large amounts of energy. Considering that the traveling wave engine is inherently more efficient than its standing wave counterpart, the future of thermoacoustic technology will focus on the former. Resolving the influence of the heat flux through the regenerator on engine performance will lead to a better product. Also, there are benefits in regard to miniaturization of the engine and its components: the smaller the regenerator becomes, the closer the hot and cold side move together. This will lead to more difficulties in separating the two sides, a problem that can also be solved by reconsidering the current material selection for the regenerator. For example, plastics or ceramics might be a viable alternative. Freezecast ceramic regenerators, for example, can easily be produced at very low cost. Ceramic foams may also be considered for a low-cost alternative. In the following sections, the influence of material properties will be investigated, first for engines, and then for refrigerators.

## 4.2 THERMOACOUSTIC ENGINES

### 4.2.1 Design

The components of the TAE testing setup were the stack, the heat exchangers, and the complete assembly. It was an important requirement to be able to test as many materials and combinations of materials while maintaining equal testing conditions between each test. The resonant body of the engine was comprised of three sections of Pyrex tubing, with a 25 mm inner diameter. The hot side heat exchanger was placed in between the compliance tube and the stack chamber. The cold side heat exchanger served as the connector between the stack chamber and the resonator tube.

**4.2.1.1 Hot Side Heat Exchanger** The hot side heat exchanger was realized by cutting a circular hole in a flat piece of ceramic monolith and weaving 22WG NiCr wire through it. This wire allows for a maximum temperature of approximately 1100°C, sufficiently high for this application. The ceramic frame was used to avoiding accidental contact between the wires and also the stack assembly. The frame was covered by two copper screens. The compliance tube was cemented to the stack assembly, as was the glass tube for the stack. The compliance was terminated with a movable plunger to allow for different operating conditions.

**4.2.1.2 Cold Side Heat Exchanger** The cold side heat exchanger was built using the same steel pipe with copper tubing soldered around its circumference (two loops). The copper tubing carried the cooling water around the pipe. At one end, this tubing was covered with a coarse copper screen which removed heat from the stack. This design allowed for a minimally invasive means to remove heat from the stack for the used length scales. Also, the pipe supported the connection of the resonance tube to the stack section.

**4.2.1.3 Fabrication of the Stack** This study is aimed at identifying the effect of thermal conductivity on the thermoacoustic effect in a standing wave engine by varying the

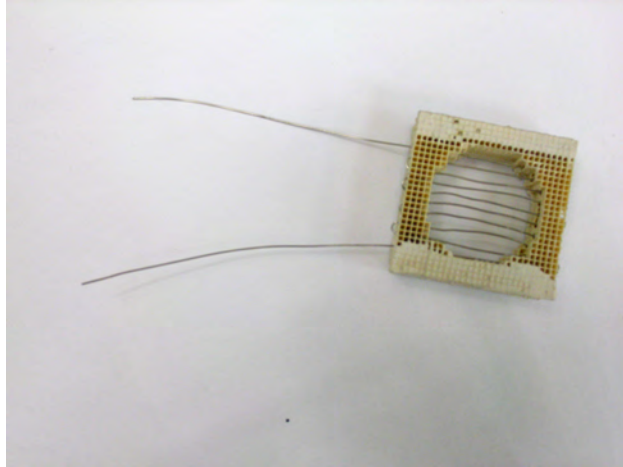


Figure 14: Hot side heat exchanger, ceramic frame with NiCr wire woven through it

material of the stack assembly. Therefore, great care was given to constructing stack assemblies that were hydrodynamically identical to each other. Given the extruded ceramic as a benchmark case, the flow channels and open area relative to total area were chosen to be as close to the benchmark case as possible. An exact replication was not possible because of manufacturing limitations (i.e. metals cannot be extruded as the ceramic is to make the monolith). Ultimately, four different metals were chosen as stack materials that could potentially be used in the fabrication of a thermoacoustic device. Table 2 provides an overview of the used materials.

For aluminum, copper, and brass, identical tubing was available. The stainless steel tubing used had a larger diameter and a thinner wall. For the ceramic stack, the same extruded  $0.127\text{ mm}$  wall thickness monolith was used that was used in the simple demonstrator engine described previously.

- Aluminum, Copper, and Brass
  - outer diameter:  $1.588\text{ mm}$ ,
  - wall thickness  $0.356\text{ mm}$ .
- Stainless steel

Table 2: Material properties of potential stack and regenerator materials

Material	$k$ [W/mK]	$\rho$ [kg/m <sup>3</sup> ]
Steel (AISI 304) (104)	14.6	7900
Aluminum (3003)(105)	192	2730
Copper (C122) (105)	400	8930
Brass (C 260)(105)	121	8500
Cordierite (106)	< 2	$\approx 1.8$

- outer diameter 1.829 *mm*,
- wall thickness 0.289 *mm*.
- Ceramic
  - Extruded 600 cells per square inch (cpi),
  - 0.127 *mm* wall thickness

Each tube was cut into 30 *mm* sections and approximately 180 of these tubes were bundled into a a steel pipe (inner diameter of 23.81 *mm*, outer diameter of 25.4 *mm*) of the same length. The ceramic stack was shaped to fit into the same steel sleeve. Each stack assembly was sandwiched between the mesh screens of the hot side and cold side heat exchanger.

**4.2.1.4 Final Assembly** The final test engine is shown as an exploded view and fully assembled in Figures 15 and 16. In order to investigate the influence of the material properties on the thermoacoustic effect, thermocouples (K-type) were mounted on the hot and cold side of the stack. A microphone (PCB 130D20) was mounted coaxially with the resonator, 100 *mm* from the open end in order to record the sound output of the engine.

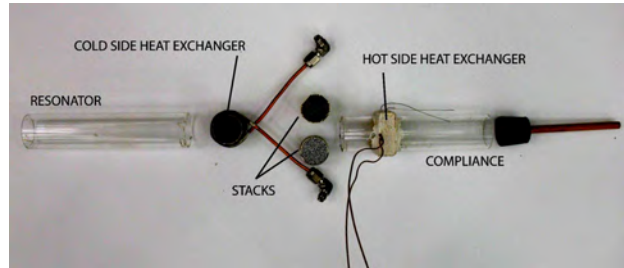


Figure 15: Exploded view of the engine components: resonator, cold side heat exchanger, stacks, hot side heat exchanger, and compliance



Figure 16: Assembled TAE test bed.

### 4.2.2 Data Acquisition

The thermocouples and microphone were connected to a National Instrument Chassis (SCXI 1100) that is equipped with an 8-channel thermocouple module (SCXI 1125 with a SCXI 1325 terminal block, for cold junction compensation) and an 8-channel pressure transducer module (SCXI 1531). The data sampling was handled by the SCXI 1600 module which can read 200  $kS/s$  at 16 bit resolution. Considering the engine setup, with 4 temperature readings and one pressure reading, this allowed for a maximum of 40,000 samples per second to be read for each channel, which is sufficiently high to capture all relevant data (i.e. the hardware does not serve as a bottle neck with regards to data acquisition). Data display and recording was done with Labview running on a Dell Inspiron 1720.

### 4.2.3 Uncertainties in the Data Acquisition

Before discussing the results from the stack material variation, several sources of error should be discussed.

- The hydraulic properties are not equal for all materials. The tubing for stainless steel and the channel size for the ceramic stack are larger than for the remaining three materials. As a result, the ratio of channel size and thermal penetration depth varies. This ratio determines the phase lag between heat transfer and pressure, and thus determines the performance of the engine. However, the thermal penetration depth is a function of temperature. It is conceivable that the effect of the temperature distribution along the channel affects the thermal penetration differently for each material. Ultimately, this effect will be illustrated using temperature data collected from each engine setup.
- The hot side heat exchanger failed several times, prompting a rebuild. Great care was given to ensuring that each assembly was identical to the previous version, however, it must be considered as a potential source of error.
- The location of the hot side thermocouples could not be determined exactly. As a result of the setup, placement of the thermocouple leads was not trivial and visual access to confirm a placement in the assembled state was not possible. Figure 17 shows possible scenarios, and thus a reason for large variation in data collected from the hot side of

the stack (Thermocouples on the cold side were kept in constant locations, which is why data taken there is more consistent).

- The cooling water temperature could not be kept constant. It varied between approximately  $10^{\circ}C$  and  $25^{\circ}C$ . It should be expected that this results in a total shift of temperature readings; the behavior as a function of input power is not affected.

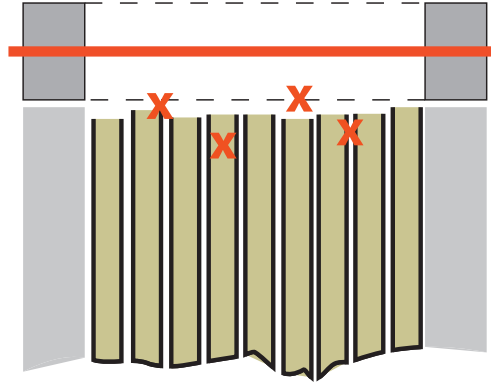


Figure 17: Placement of thermocouples near the hot side heat exchanger as a source of inconsistent measurements

As Figure 17 shows, the thermocouples could be located very close to the screen, in contact with screen and a tube, wedged in between tubes, or inside a tube. Obviously, the data collected from a thermocouple reading the temperature at the screen will be much higher than a reading from inside a tube. It was attempted to always wedge the thermocouples between tubes, in order to collect data of the actual temperature of the stack material, but the data shows that this was not always the case.

## 4.3 RESULTS, THERMOACOUSTIC ENGINE

### 4.3.1 Temperature Behavior of Stacks

During the tests of the different materials in the aforementioned engine setup, temperature data was recorded at each end of the stack, two thermocouples each. In addition, the voltage applied to the heating wire was recorded. In conjunction with the resistance data from the heating wire, the applied electrical power was calculated using the direct correlation derived from Ohm's Law  $P = U^2/R$ . In case of oscillations, the resulting sound pressure level was recorded (all other values are assumed to be 0). The most useful way to disseminate the findings is by analyzing the temperatures on each end of the stack (by taking the average of both measured temperatures). This should indicate the direct influence of the thermal conductivity on the distribution of temperature across the stack assembly. As shown before, it is this temperature difference that is directly responsible for the acoustic output of the engine. Figure 18 shows the hot side and cold side temperatures for the ceramic stack, along with a linear curve fit for each to highlight trends (Also, this data is used below to estimate heat losses and the thermal penetration depth as it varies with temperature). The remaining materials (copper, aluminum, steel, and brass) are treated in the same fashion. The corresponding plots are shown in the Appendix in Figure 114 on page 232.

Comparing the temperature behavior of ceramic with the other materials, it is noticeable that the hot temperatures in the other cases are generally lower than for ceramic, while the cold side temperatures are generally higher. As a first general statement, this shows that ceramic does indeed insulate the cold side from the hot side, resulting in the steepest temperature gradient across the stack. When comparing the other materials, the differences are more subtle. This behavior is easiest to illustrate with the resulting linear curve fits shown in Figure 19 (again, refer to Figure 114 on page 232 for the accompanying temperature data that forms the basis for these curve fits).

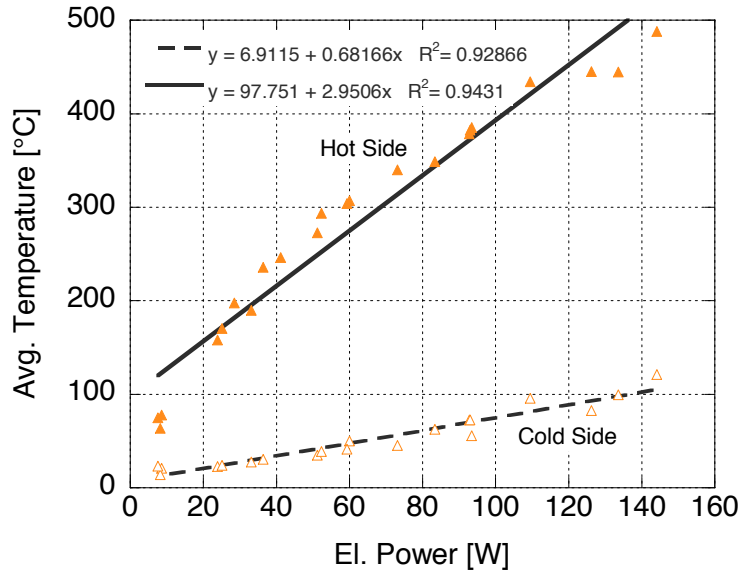


Figure 18: Hot side and cold side temperature across the ceramic stack.

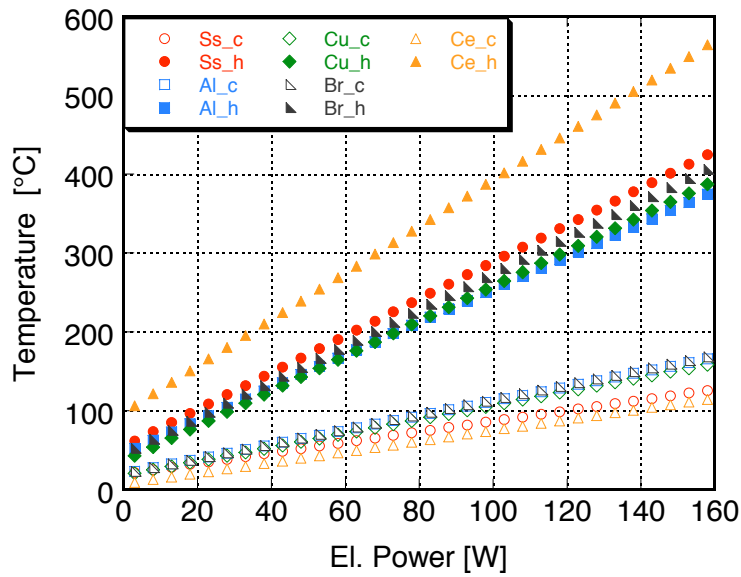


Figure 19: Curve fits of the temperature behaviors depending on stack material

$$\text{Stainless Steel } T_c = 19.68 + 0.67P \quad (4.2)$$

$$T_h = 54.66 + 2.34P$$

$$\text{Aluminum } T_c = 20.28 + 0.92P \quad (4.3)$$

$$T_h = 46.0 + 2.08P$$

$$\text{Copper } T_c = 17.7 + 0.89P \quad (4.4)$$

$$T_h = 36.17 + 2.22P$$

$$\text{Brass } T_c = 19.98 + 0.94P \quad (4.5)$$

$$T_h = 45.53 + 2.28P$$

$$\text{Ceramic } T_c = 6.91 + 0.68P \quad (4.6)$$

$$T_h = 97.75 + 2.95P$$

By investigating the slopes of the cold side temperatures, we see that the materials with low thermal conductivity (i.e. steel and ceramic) exhibit the lowest values. This shows that these materials effectively isolate the hot side from the cold side. Another indication of this fact is the slope of the hot side temperature. For both steel and ceramic, this value is higher than for the other materials. It must be noted here that the data for copper and aluminum show the largest variation of hot side temperature measurements. It could be assumed that the actual temperature of the stack for copper follows the lower values shown in Figure 114, thus further decreasing the temperature difference between hot and cold side. The plots for the temperature difference as a function of input power further confirm the large variation in the collected data, specifically for aluminum and copper. This data is shown in Figure 115 on page 234. Investigating the ceramic case further, we can identify a nonlinear behavior in the temperature difference for high values of input power. Figure 20 shows this behavior. It was shown above that ceramic exhibits the highest temperature levels of all materials studied here. As a consequence, the heat fluxes to the surroundings must be assumed to be the largest. It is conceivable that at high powers, the heat losses are large enough so that a further increase of the temperature difference across the stack is not possible. This range could not be investigated further due to limitations of the heating wire used in this study.

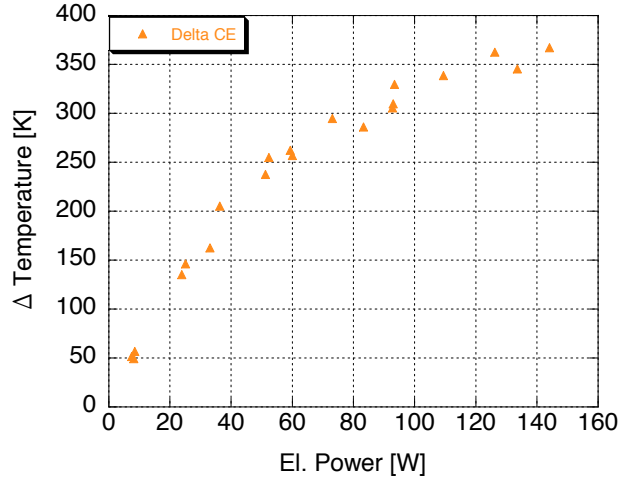


Figure 20: Temperature difference across the ceramic stack.

With the thermal behavior of all different stack assemblies illustrated, the thermoacoustic behavior of each assembly has to be investigated. The results are shown in the following section.

#### 4.3.2 Thermoacoustic Behavior of Different Stacks

As shown above, the temperature behavior across each stack varied for different materials. Ceramic exhibited the highest temperature difference. The temperature gradients for the metallic materials were generally lower. We expect the materials with higher thermal conductivity, and the previously discussed changes in temperature distribution to change the performance with respect to the ability to cause oscillations. Figures 21 (a) and (b) show the results from the material variation.

Part (a) of this figure shows the resulting sound pressure level as a function of input power, part (b) shows the sound pressure level as a function of temperature difference. As mentioned above, if a given power level does not cause a sound output, the SPL value is assumed to be 0, even though this is not physically achievable. It was illustrated above (in the investigation of temperatures) that the temperature difference as a function of input

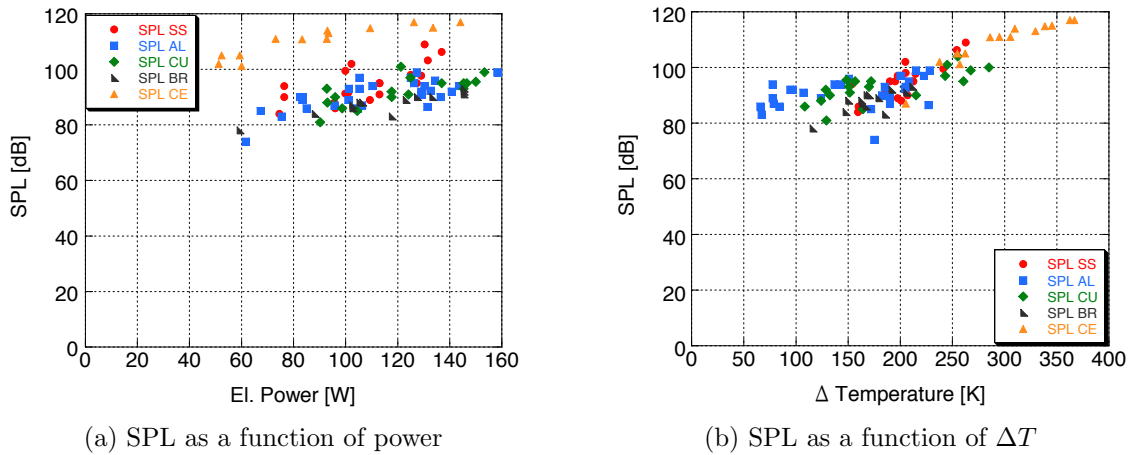


Figure 21: Illustration of the achieved sound pressure level as a function of electrical input power and temperature difference  $\Delta T$

power showed a significant spread of values, especially for aluminum and copper. As a result, the illustration of sound output as a function of temperature difference is also subject to this spread. For this reason, all trends should be explained with Figure 21 (a). The individual data for all materials is provided in the Appendix, in Figure 116 on page 236 for the dependency on input power, and Figure 117 on page 238 for the dependency on temperature difference. It is obvious that the oscillation data as a function of input power results in more definitive trends than the plots of sound pressure level as a function of temperature difference. Again, this is rooted in the uncertainties that are associated with the hot side temperature measurements. In spite of these uncertainties, the following conclusions can be drawn from the variation of the stack materials.

First and foremost, ceramic, having the lowest thermal conductivity and ability to sustain large temperature gradients shows the highest sound pressure level output of all materials. The highest measured SPL for ceramic is about 117 *db*. Further, stainless steel is (generally) located above the other materials, which means at the same electrical input, it achieves the higher sound pressure levels than any other material. Of course, the highest recorded level for stainless steel at 110 *dB* is much lower than for ceramic. Aluminum and copper,

the materials with the highest thermal conductivity, coincide closely. However, the data for aluminum shows that the onset of oscillations occurs at lower values for input power than for copper. Also, both materials fail to show oscillations beyond 100 *dB*, which is an important point to make. This must be considered a result of the limited temperature gradient that can be sustained in these materials with high thermal conductivity. Finally, brass, having a smaller thermal conductivity than both aluminum and copper, does not exhibit a clear trend that follows the findings from the previous materials.

### 4.3.3 Thermoacoustic Similarity of Stacks

It was mentioned above that the hydraulic properties of the different stacks were not identical. It must be assumed that there is an influence of the hydraulic properties on the thermoacoustic properties of each stack. Specifically, the ratio of physical channel size  $D_c$  and thermal penetration depth  $\delta_\kappa$  impacts the heat transfer between solid and gas. In a standing wave engine, the relatively large ratio ( $\delta_\kappa/D_c > 1$ ) causes a delay in the heat transfer as the inherent phase difference between pressure and velocity would otherwise render the amplification of a pressure disturbance impossible.

In addition, it was shown that there are significant differences in the range of temperatures present in the different stacks. As a result, the thermal penetration depth behaves differently for each stack. Thermoacoustic similarity is achieved, if the ratio of channel size and thermal penetration depth is equal for all cases. Recalling the definition of the thermal penetration depth as  $\delta_\kappa = \sqrt{\frac{k}{\pi f \rho c_p}}$  (10), we can see that it has a strong dependency on temperature as the thermal conductivity, density and, specific heat of the gas depend on temperature. Using EES to calculate and plotting the thermal penetration depth over the temperature range present in all stack assemblies, we can show in Figure 22 that this value changes significantly.

Along with the data on the temperature behavior of the different stacks, we must assume that each stack shows a different behavior with respect to thermal penetration depth. Figure 23 shows the range of thermal penetration depth for the ceramic stack (Figure 118 on page 240 shows the remaining data for all materials).

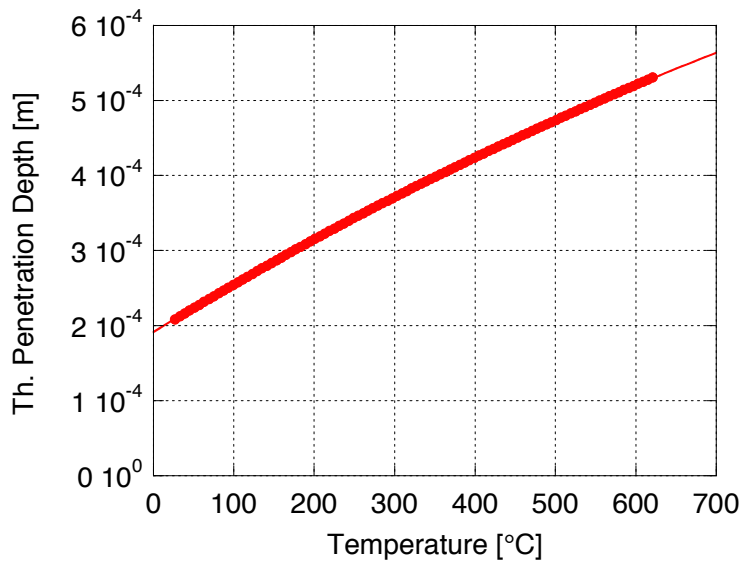


Figure 22: Thermal penetration depth  $\delta_\kappa$  as a function of temperature

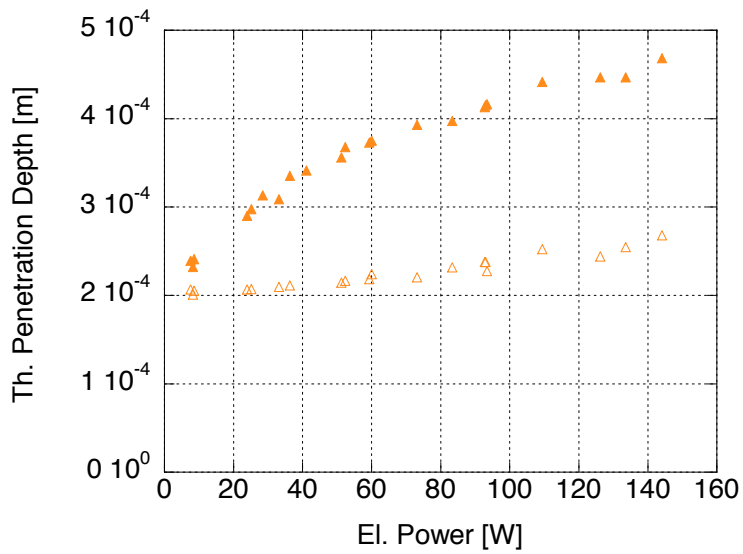


Figure 23: Thermal penetration depth as a function of input power (solid symbols: hot side, outlined symbols: cold side) for the ceramic stack.

For small values of input power, the spread between the cold side and hot side is small. Of course, this is a result of the small temperature difference between both sides for small values of input power. As the stack is heated more, the difference in thermal penetration depth increases. As a result of the highest temperature difference, the ceramic stack exhibits the largest spread of  $\delta\kappa$  of all materials. Brass shows the smallest variation of all materials used. As before, this data is dependent on the uncertainties that are present in the hot side temperature measurements.

In order to show thermoacoustic similarity, we next need to compare the ratios of channel size and thermal penetration depth. Again, for the ceramic case, this information is shown in Figure 24. Figure 119 on page 242 shows the data for the remaining materials. Interestingly, in spite of showing the largest overall range of thermal penetration depth, ceramic shows similar values for the ratio of  $D_c$  and  $\delta\kappa$ . For all materials except stainless steel,  $D_c/\delta\kappa$  starts at 4 for small input powers and decreases to values between 2 and 3 for high input powers. As a result of this behavior, it can be concluded that these cases are thermoacoustically similar. On the other hand, stainless steel shows a very different range of  $D_c/\delta\kappa$ . In this case, its values are 6.5 at small input powers and fall between 3.5 and 5 for high input powers. This is due to the similar temperature levels compared to the other metal cases, but larger channel size for stainless steel. Thus, the oscillation data for the stainless steel stack case cannot be directly compared to the other materials. As a result of the increased values of  $D_c/\delta\kappa$ , the heat transfer between solid and gas is delayed for stainless steel than for all other materials.

In addition to a change in gas properties, it is also conceivable that the choice of stack material influences the thermal heat fluxes throughout the assembly. Most interesting here is an investigation of the convective and radiative heat fluxes. As shown in the data so far, up to 160  $W$  of electrical power is supplied to the test setup. Only a small fraction of this power is ultimately transformed into acoustic power. The remaining energy is lost to the surrounding via convection and radiation. The following section discusses the investigation of these heat fluxes in detail.

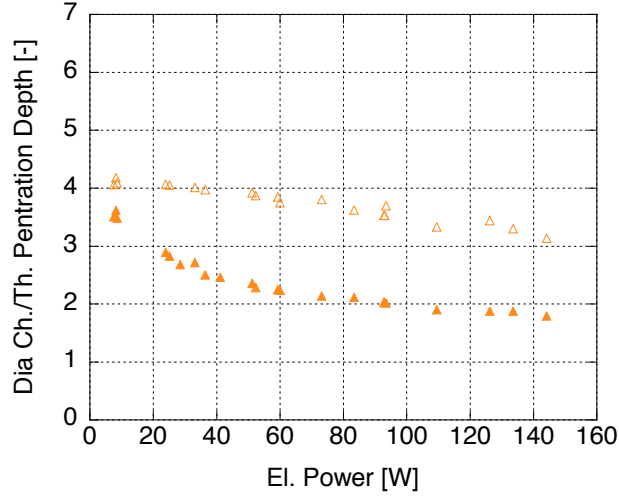


Figure 24: Ratio of channel size and thermal penetration as a function of input power (solid symbols: hot side, outlined symbols: cold side), for the ceramic stack.

#### 4.3.4 Heat Flux Investigation

First, the basic equations in their most general form for each of these heat fluxes should be stated:

$$\text{Convection: } Q_{conv} = h A (T_{surf} - T_{\infty}) \quad (4.7)$$

$$\text{Radiation: } Q_{rad} = k_B \varepsilon A (T_{surf}^4 - T_{\infty}^4) \quad (4.8)$$

$$(4.9)$$

The convective heat flux depends on the convective heat transfer coefficient  $h$ , relevant surface area  $A$ , and the temperature difference between that surface and its surroundings. The radiative heat flux depends on the relevant surface area, the Boltzmann constant  $k_B$ , the surface emissivity  $\varepsilon$  and surface and surrounding temperatures. For an initial estimate, most parameters are easily obtained, as they are independent of temperature. The only

parameter in these equations that requires additional consideration is the convective heat transfer coefficient  $h$ .

The current test setup essentially resembles a horizontal cylinder subject to heating. This results in a coaxial temperature gradient that was quantified for the various materials discussed above. During convection, a heat flux driven by buoyancy leaves the surface of this cylinder. The magnitude of the resulting heat transfer can be described using the Nusselt number for natural convection from a horizontal cylinder. The Nusselt number is a dimensionless heat transfer coefficient. Through empirical experiments, many correlations for the Nusselt number have been determined for a great variety of situations (for various media and flow geometries) where convection occurs. For the present case, the Nusselt number can be expressed by (107):

$$Nu = 0.36 + \frac{0.518Ra_D^{\frac{1}{4}}}{\left[1 + \left(\frac{0.559}{Pr}\right)^{\frac{9}{16}}\right]^{\frac{4}{9}}} = \frac{hD_{char}}{k_{gas}} \quad (4.10)$$

Equation 4.10 depends on the Prandtl number, a characteristic dimension  $D_{char}$ , and the Rayleigh number, which in turn can be expressed by:

$$Ra = Gr Pr = \frac{g\beta(T - T_{\infty})D_{char}^3}{\nu\alpha} \quad (4.11)$$

where  $Gr$  is the Grashof number (describing buoyancy effects),  $Pr$  is the Prandtl number,  $T$  is the surface temperature,  $T_{\infty}$  is the temperature of the surroundings,  $\nu$  is the viscosity of the surrounding gas, and  $\alpha$  is the thermal diffusivity of the surrounding gas. For a useful investigation of the heat fluxes occurring around the stack assembly, the Nusselt number must be considered to be a function of temperature. As seen in Figure 20, the temperature difference across the stack varies significantly with electrical input power. Also, the absolute levels of temperatures present in the stack vary equally drastically. The latter is especially important with respect to radiation, as the temperature is taken to the fourth power. As a result, we have to account for both the temperature level and the temperature difference along the stack for each power level. In order to include this, a program was written that calculated the Nusselt number and the heat transfer coefficient for the range of temperatures of interest. Then, a cubic curve fit was applied to that range of temperatures. Figure 25

shows the resulting plot and curve fit. Note that the fit resembles the actual heat transfer coefficients very well over the range of interest. An extrapolation of this curve fit should not be applied for heat transfer coefficients out of this range because the fit and the trend of the data clearly diverge. This data was taken from the Engineering Equation Solver software package.

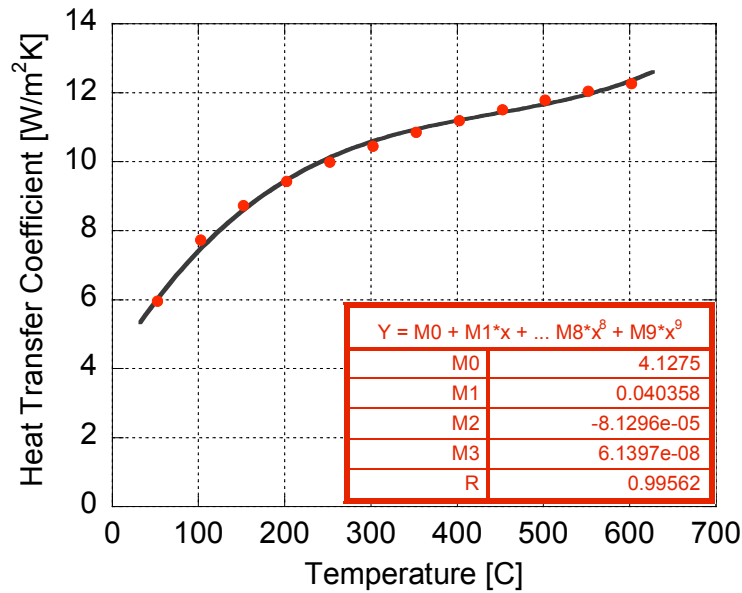


Figure 25: The heat transfer coefficient and its curve fit over the relevant range of temperatures

Next, the range of relevant input power was discretized and the hot and cold side temperatures were estimated using the data taken from Figure 20. This temperature range was then also discretized in order to achieve a temperature-dependent heat transfer coefficient, which was calculated for each discrete temperature. Again, the range of input power lies between 10  $W$  and 160  $W$  and the temperature difference is at a maximum for the ceramic case at high power, where it reaches 400  $K$ . Both ranges were discretized with 100 intervals. Ultimately, the local heat convective and radiative heat flux was calculated for each discrete “slice” of the stack (the worst case scenario for this setup is a temperature difference of 4  $K$  from one section to the next, which is small enough to capture the effects of temperature on

material properties). Finally, each slice was added together to determine the total respective heat flux. This process was repeated for each material used in this investigation.

The heat flux data is presented in Figure 26. The figure contains both convective (a) and radiative (b) heat fluxes. Interestingly, the ceramic case shows the highest amount of heat losses to the surrounding via the stack surface. Mainly, this is due to the fact that convection and radiation is purely driven by temperature difference, and ceramic reaches the highest temperatures across its surface due to its low thermal conductivity. The inherent benefit of lower thermal conductivity is outweighed with regard to thermal losses to the surroundings.

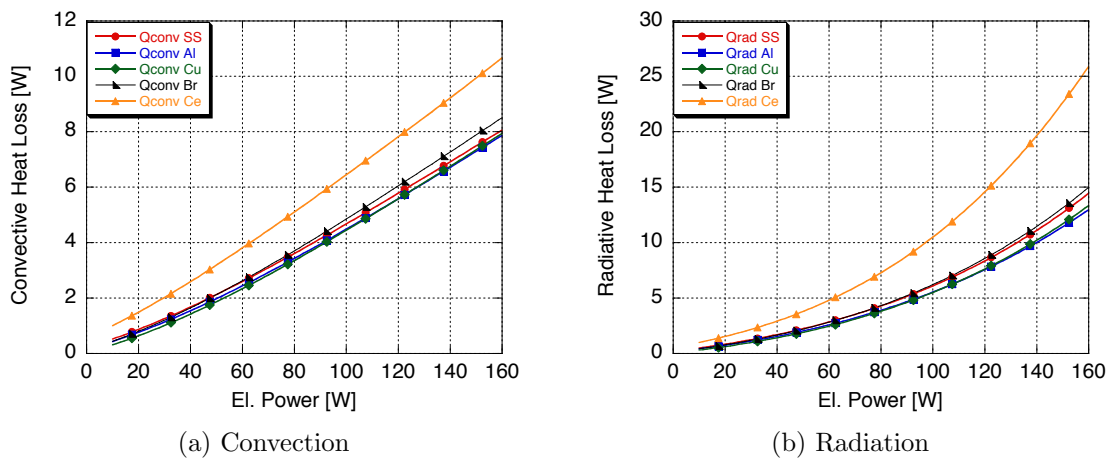


Figure 26: Estimates of the convective and radiative heat flux around the stack assembly

#### 4.4 THERMOACOUSTIC REFRIGERATORS

As this work focuses on thermoacoustic refrigeration, significant testing was conducted on a simple demonstration device. This device served as a testbed for various regenerator structures and materials. First, the basic operating principles of thermoacoustic refrigeration were illustrated. Using only a microphone, the optimal operating frequency of the device was determined. Using this frequency, the behavior of the pressure wave around the key component of a thermoacoustic refrigerator, the regenerator, were shown. In order to fur-

ther show the influence of design parameters, the location of the regenerator with respect to the pressure antinode as well as the cross sectional area of the regenerator were varied. Beyond the general design parameters, the use of mesh screens in thermoacoustic regenerators were investigated. Using a fixed location, and constant operating (both at their previously determined optimal values), the screen density as well as regenerator thickness will be investigated. In addition, stainless steel and Nylon screens were used as the regenerator material in order to show the influence of material properties.

#### 4.4.1 Design

The TAR experimentation was carried out using a half-wave resonator design. In order to ensure equal acoustic environments for each test, a speaker driven system was used instead of a heat driven one. The speaker allowed for easy tuning of the operating frequency when the resonator length was varied. For a half-wavelength system, both ends are closed, allowing us to contain the intense sound pressure levels, and maintain safe levels in the immediate vicinity of the test setup (outside SPL was measured to be approximately 85 *dB*).

A 127 *mm* diameter, 4  $\Omega$  speaker was initially used and connected to a 10 $\times$  signal amplifier. The speaker housing is a wooden box 200 *mm* wide, 250 *mm* long, and 100 *mm* high. In order to ensure a closed system, this enclosure was chosen to be of a sealed type. This speaker was used for part of the data presented below. However, for the majority of data, a different speaker was used, as the previous one failed. The new speaker was a Cadence WB10-4 subwoofer with a design frequency range of 20 – 500 *Hz*. This frequency range ensure as constant a driving power as possible, as the speaker is operated above its rolloff frequency. The efficiency of the driver has been identified as a major source of total efficiency penalty, and it has to be quantified for this investigation (108). Previous work by Nam et al. has shown that the frequency has little effect on the pressure drop characteristics of a regenerator (109). The new woofer was encased in a sealed cubic box with inner dimensions of 320 *mm* for each side. This is the dimension required for efficient operation for this type of enclosure. A separate box with a height of 200 *mm* was used a reducer to channel the sound waves into the resonator tube. The total length of this TAR setup is 2.15 *m*, which

reduces the optimal operating frequency to  $\approx 38 \text{ Hz}$ . Figure 27 shows a schematic of the assembly.

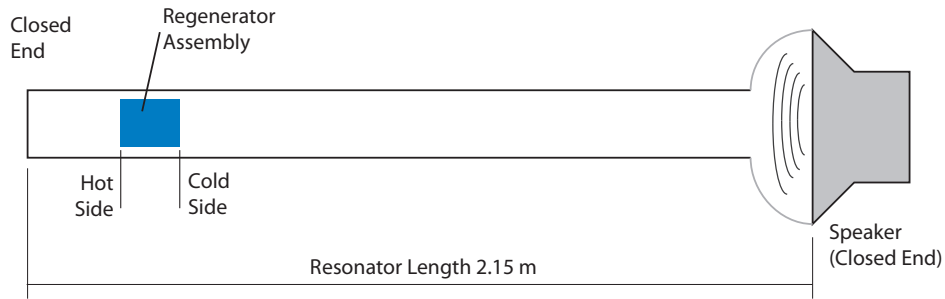


Figure 27: Schematic view of the TAR setup

In both cases, the resonator was built using steel pipe, with an inner diameter of  $38 \text{ mm}$ . At the opposite end of the speaker, a regenerator housing was connected. This was built using plexiglass in order to maintain visual access to the regenerator. The housing was  $305 \text{ mm}$  long with a  $65 \text{ mm} \times 65 \text{ mm}$  cross section. The connection to the resonator was achieved using a threaded hole and rubber cement. At the closed end of the system, a removable face plate was attached with four screws in order to allow access to the regenerator. This face plate was sealed with a silicone gasket. Again, the system was designed to be airtight at all joints, in order to ensure that the maximum acoustic energy was contained on the inside. Leaks were audible, especially at the pressure anti-nodes (i.e. the speaker and the regenerator housing), and thus easy to seal.

Several different regenerator designs were tested. For the basic investigation (regenerator location and inertance dimension), a section of a 900 cpi ceramic monolith was used. For these investigations, water cooling was not implemented. For the stainless steel and Nylon screens, a housing was built. On the heat exhaust side, a water-cooled heat exchanger comprised of two copper screens (open pores of similar size as the ceramic regenerator) soldered to copper tubing (outer diameter  $3.2 \text{ mm}$ ) was used. This heat exchanger was connected to the housing of the regenerator. In order to keep the screens in place, a cover screen was used. This cover was made of another plexiglass frame and a copper screen. It

was wedged inside the regenerator housing. The regenerator housing was designed to ensure constant length of the feedback inductance for all cases of screen stack thickness. In all cases, thermocouples were mounted on the cold and hot sides of the regenerator. The mounting was consistent with the findings by Nam et al. that prescribe that the temperature probes should be mounted close to the regenerator matrix (109). Figure 28 shows the exhaust heat exchanger, the thermocouples on the cold side, and an assembled view of the TAR regenerator.

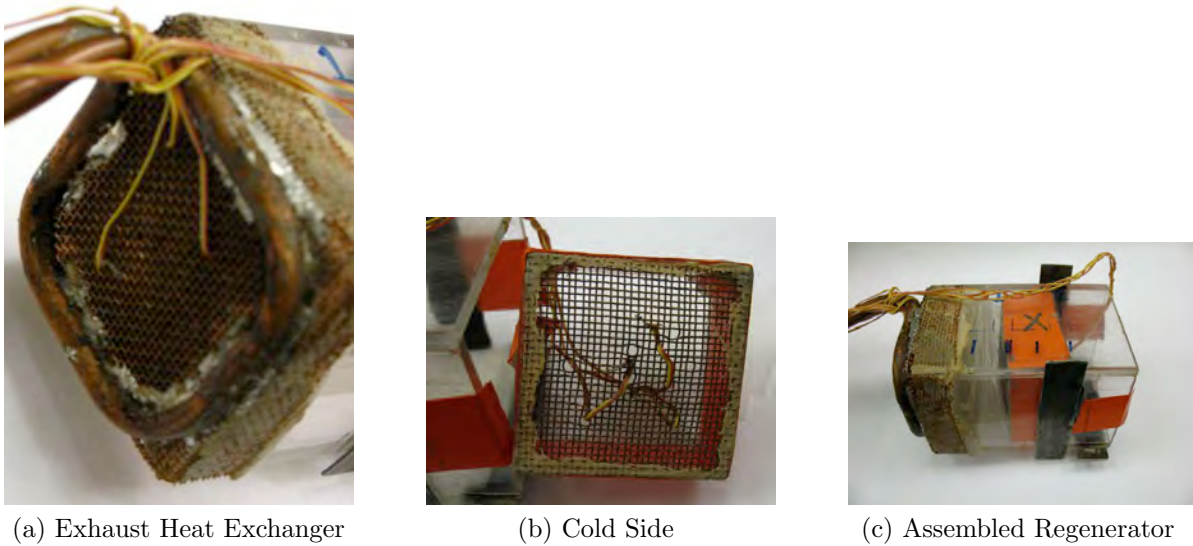


Figure 28: Illustration of the TAR regenerator, individual components, and fully assembled

#### 4.4.2 Data Acquisition

Data acquisition was handled by the same system as for the engine. In addition, this system was used for signal generation. A Labview program generated sine waves; both frequency and volume could be controlled through the program. The built in headphone jack was used to send this signal to the speaker. For the refrigeration setup, all 8 available temperature channels were used. This reduced the maximum available sampling rate per channel to 25,000 samples/s, which is more than sufficient to acquire useful data. As before, K-type thermocouples were used.

## 4.5 INITIAL THERMOACOUSTIC REFRIGERATOR RESULTS

As designed, the regenerator is located close to a pressure antinode on the opposite end of a resonator than the mechanical driver. In order to understand the temperature behavior discussed below completely, the pressure influence on this data has to be eliminated. For this reason, the pressure amplitude is recorded with a microphone in intervals of 25 *mm* starting at the closed end. This covers the range of regenerator locations throughout the experiments. In order to allow for a feasible range of measurements, a PCB 377A12 microphone was utilized. It has a dynamic range of up to 178 *db* and a sensitivity of 0.25 *mV/Pa*. It is connected to a 426B03 preamplifier. As with the engine described above, both the microphone is connected to a PCB 482A22 signal conditioner. For this data, the Cadence WB10-4 subwoofer is used.

### 4.5.1 SPL as a Function of Driving Frequency

Similar to the work done by Jebali et al., this investigation is aimed at identifying the sensitivity of the TAR to driving frequency (110). This section answers questions in regard to the width of the “ideal” driving peak as well as harmonics other than the first, that may also allow for cooling. A rough estimate using the length of the resonator yields an estimated driving frequency of 38 *Hz*. This investigation thus starts at frequencies below this value. The variation of the driving frequency is implemented with a timed loop in the function generator in LabView. First, the behavior of the pressure amplitude inside the regenerator housing was investigated. In order to identify the optimal driving frequency, a variation of the driving frequency was recorded with the aforementioned microphone. It was mounted close to the closed end, which should yield the highest total values (as this location is closest to the pressure antinode in the standing wave). For this investigation, the frequency was varied every 5 seconds. Figure 29 shows the resulting sound pressure levels inside the regenerator housing. Overall, the SPL reaches  $\approx 170$  *dB*. This is well below the dynamic range of the microphone. The highest peak can be identified at roughly 37 *Hz*. The higher order harmonics are also visible, at a lower SPL than the first peak. This

information validates the choice of frequency for the experiments run; assuming, indeed, that the frequency yielding the highest SPL also yields the best cooling performance.

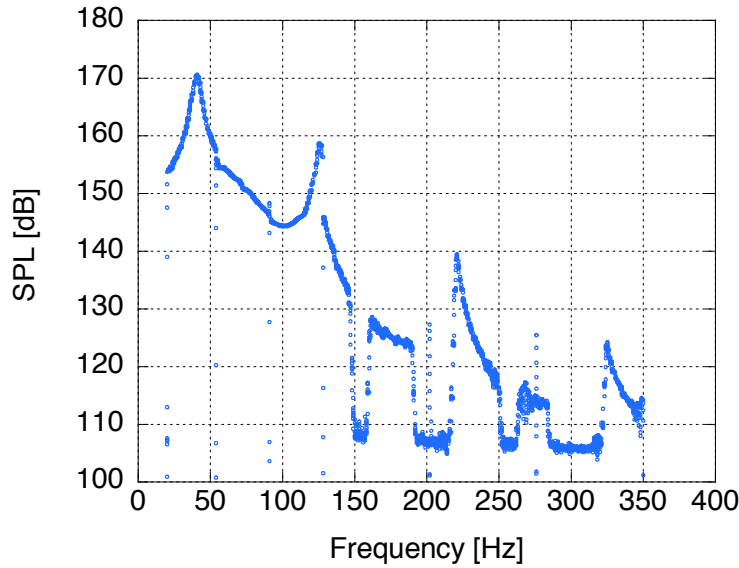


Figure 29: Sound pressure level as a function of driving frequency.

Next, the variation of the SPL throughout the regenerator chamber was investigated. For this information, several access holes were drilled into the chamber in order to provide access for the microphone. From the closed end, these access holes are spaced apart by 25 mm. There are a total of 10 access holes. Each one not occupied by the microphone was closed. Rather than recording instantaneous information, for this measurement the average SPL was recorded over a time of 15 s. Figure 30 shows that the average sound pressure level does indeed increase towards the closed end. In addition, it compares the SPL of the empty regenerator housing (undisturbed standing wave) with the SPL inside the regenerator housing with the regenerator present. As shown in the figure, the presence of the regenerator influences the pressure amplitude that is achieved. The highest achieved SPL in the empty case is 170.7 dB, while the highest value achieved with the regenerator in place is just under 170.2 dB. This corresponds with a change in root mean squared pressure of approximately  $6855 Pa - 6472 Pa = 383 Pa$ .

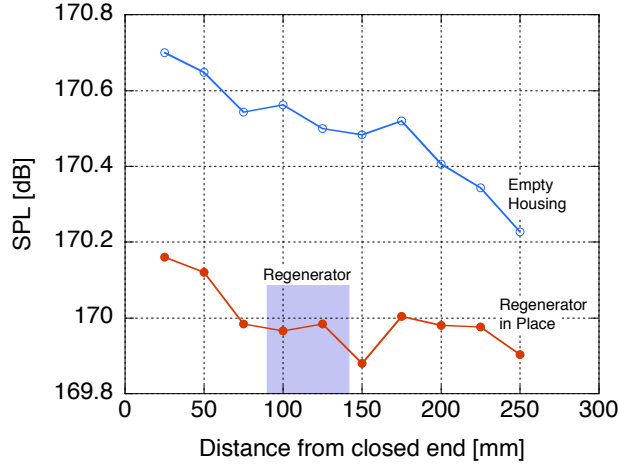
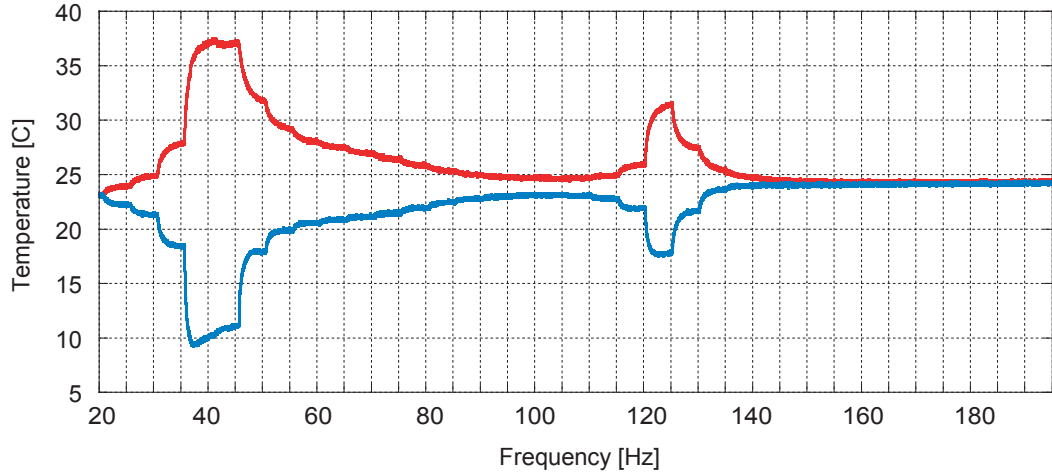


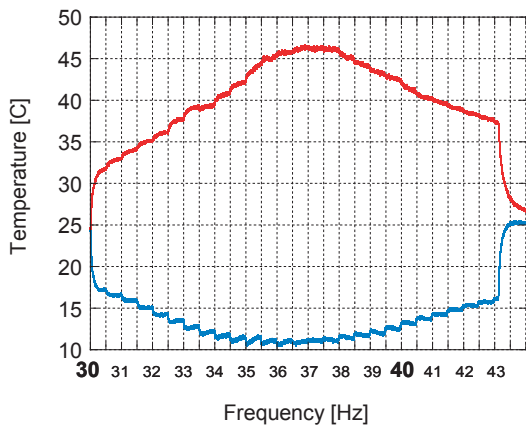
Figure 30: Illustration of the SPL achieved in the regenerator housing empty, and with the regenerator assembly in place.

#### 4.5.2 Temperature Behavior as a Function of Driving Frequency

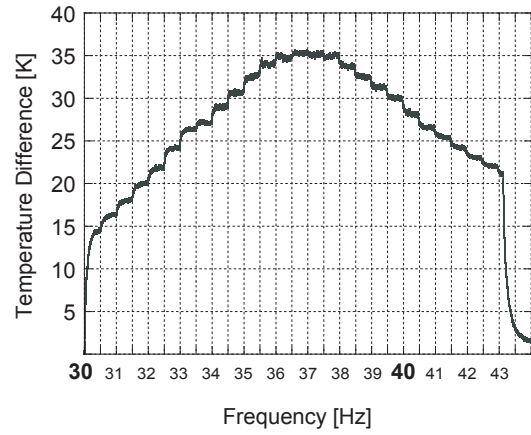
Above, the effect of the driving frequency on the sound pressure level was discussed. This section applies the same concept but introduces a basic regenerator (900cpi ceramic monolith, 50 mm in length, and approximately 44 mm high and wide) in order to understand the influence of the driving frequency on the temperature levels as well as the temperature difference achieved. As before, the data for this test was collected beginning at 20 Hz and ranged up to 200 Hz in increments of 5 Hz. The response time of the temperature is much slower than the pressure amplitude; hence, each frequency was maintained for approximately 5 minutes. In order to illustrate a more exact picture of the temperature behavior in the range of frequencies present in the first peak, a second test was run with a frequency increment of 0.5 Hz, starting at 30 Hz and ranging beyond the first peak. Figure 31 (a) shows both hot side and cold side temperatures for the entire range. Figures 31 (b) and (c) show a close-up of the first (stronger) peak, temperatures and the temperature difference, respectively. Figure 31 (d) shows the temperature difference for the entire range of frequencies.



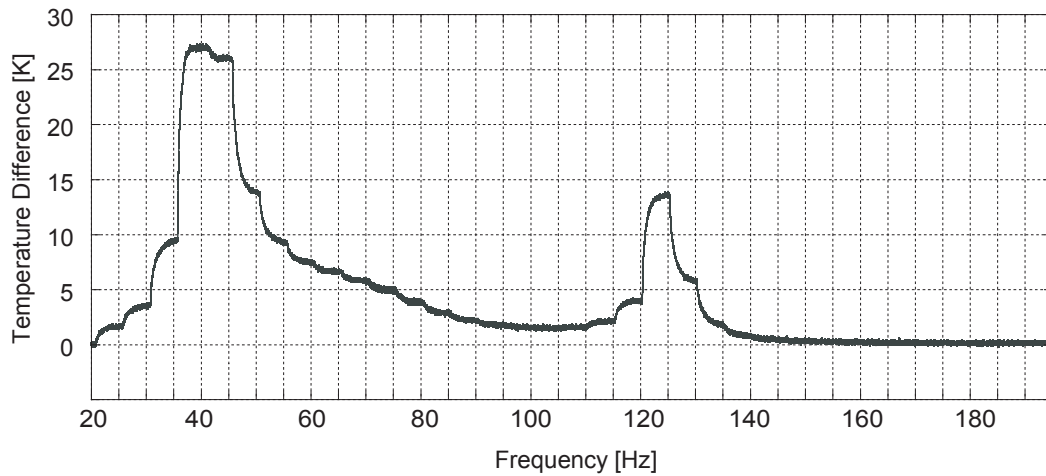
(a) Global range



(b) Detail of first peak



(c) Detail of temperature difference, first peak



(d) Temperature Difference, whole range

Figure 31: Illustration of the temperature difference across the regenerator as a function of driving frequency.

As expected, the optimal driving frequency identified results in both the highest pressure amplitude and temperature difference across the regenerator. All remaining results were taken under the same operating conditions, with the driving frequency now fixed at  $37\text{ Hz}$  when using the Cadence WB10-4 speaker. Under this operating condition, the speaker utilized  $\approx 64\text{ W}$  of electrical power, as determined by measuring the voltage applied to the driving coil and its resistance. Since no thermal load was applied to the regenerators throughout testing, as this was not subject of the investigation, calculations of the COP were not performed. Note that for the measurements using the previous speaker (before its failure), the ideal driving frequency was determined to be  $43\text{ Hz}$ , using the same methodology as discussed above.

### 4.5.3 Varying the Regenerator Location

The influence of the regenerator location and inertance variation was studied using the previous speaker (with a driving frequency of  $43\text{ Hz}$ ). For this investigation, a 900cpi ceramic monolith was used. It was  $50\text{ mm}$  in length, and approximately  $44\text{ mm}$  high and wide. This leaves  $6\text{ mm}$  free space around the regenerator that serves as the feedback inertance, which creates the advantageous traveling wave phasing in the regenerator by shifting the phase of the pressure to coincide with the velocity component of the acoustic wave. The regenerator location is measured relative to the closed end of the resonator. With the described regenerator inside the previously introduced plexiglass box, this allowed a maximum distance of  $225\text{ mm}$  from the closed end. For good resolution, this study was conducted at ten locations, starting at  $225\text{ mm}$  to flush against the closed end, or  $0\text{ mm}$ . The temperature difference between the two ends was used as the metric for optimal placement. For this study, the regenerator is not cooled actively. Figure 32 shows this temperature difference as a function of the regenerator location. Also, a quadratic curve fit is shown. It shows that there is a peak in temperature difference with less optimal placements to either side of it. The more obvious drop occurs farther away the closed end.

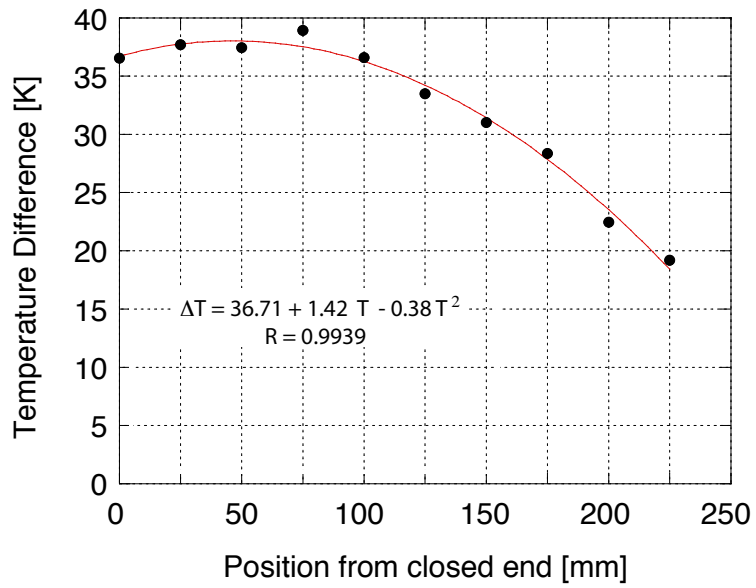


Figure 32: Temperature difference as a function of regenerator location relative to the closed end (measurement locations are spaced 25 mm apart)

#### 4.5.4 Varying the Inertance Dimensions

This investigation showed the influence of the dimension of the feedback inertance. The inertance size was varied by decreasing the dimensions of the regenerator, shifting the ratio of inertance area to total housing cross sectional area (which is  $57\text{ mm} \times 57\text{ mm}$ ). A 900dpi ceramic monolith was used for this study. The first regenerator had an edge length of  $48\text{ mm}$  and a length of  $90\text{ mm}$ . For the ensuing test runs, the regenerator size was decreased by  $\approx 3\text{ mm}$  until the performance dropped (i.e. the achieved temperature difference started to decrease). The temperature was measured at each end (two thermocouples, respectively) and with four thermocouples along the length of the regenerator, protruding into the porous structure. For each case, the regenerator was mounted so it would be in the center of the regenerator housing. It was located approximately  $75\text{ mm}$  from the closed end, which was previously determined to yield the highest temperature difference across the regenerator. It must be noted that varying the size of the regenerator in order to affect the inertance size has side effects. As the regenerator size is decreased,

- the number of channels where the thermoacoustic effect occurs decreases,
- the amount of solid where heat flows from the hot end to the cold end decreases, and
- the thermal losses to the surroundings are decreased due to the smaller surface area of the regenerator.

The first item is clearly an adverse effect that could affect the collected data. The latter items are positive influences, as the thermal losses have been identified as having an adverse effect on device performance. As a result, it is difficult to isolate the effect of the inertance size from this study. By using ceramic as a regenerator, the thermal losses are minimized, and the shown temperature behavior should in fact result largely from the variation of the inertance size, but the exact weight of each influence is unknown. Table 3 shows the different cases of this study, along with the achieved temperatures.

Aside from two measurements that are not consistent with the other data (marked by the asterisk in Table 3, where the shift is likely to have been caused by a movement in thermocouples.), we can see that the temperature distribution is affected by the change in inertance size. The following Figures 33 (a) - (e) show the temperature distributions over

Table 3: Results from the variation of the size of the feedback inertance.

Case	Open Area [%]	$T_{\text{cold } 1,2} [^{\circ}\text{C}]$	$T_{\text{exhaust } 1,2} [^{\circ}\text{C}]$
1	30.5	12.5, 13	48, 44
2	39.5	11, 14	52, 52
3	47.8	11, 12	49, 49
4	55.5	12, 12	46, 65*
5	62.6	13, 14	40*, 52

time for all measurement locations and cases. From this figure, we can see that, in general, the temperature distributions are evenly spaced across the length of the regenerator. Also, generally, the temperatures range from  $10^{\circ}\text{C}$  to  $50^{\circ}\text{C}$ , with subtle differences between the cases. At first glance, Case 2 and Case 3 are the ones that seem to achieve the best heat pumping. The figures also illustrate the problematic temperature readings, namely T 8 for Case 5 and T 7 for Case 4.

Figure 34 shows only the temperature differences between the coldest recorded temperature and the hottest temperature (while not utilizing the value for T 7, Case 4), and gives more insight into the influence of the inertance size. Beginning with Case 1, the temperature difference increases for Cases 2 and 3. For the smaller regenerators, the temperature difference decreases, suggesting that this is a less optimal configuration than the inertance size for Cases 2 and 3. For this claim, it must be noted that the plot for Case 2 should be shifted so that the onset of oscillations occurs at the same time as for the other cases. If this is considered, we can see that this case yields the best temperature difference across the regenerator for all times.

A closer look at only two distinct times (an “established” case after  $\approx 10$  minutes and an “initial” case) shows further effects of the inertance size variation. Figure 35 shows that the difference between each case does not affect the cold side significantly, but rather that

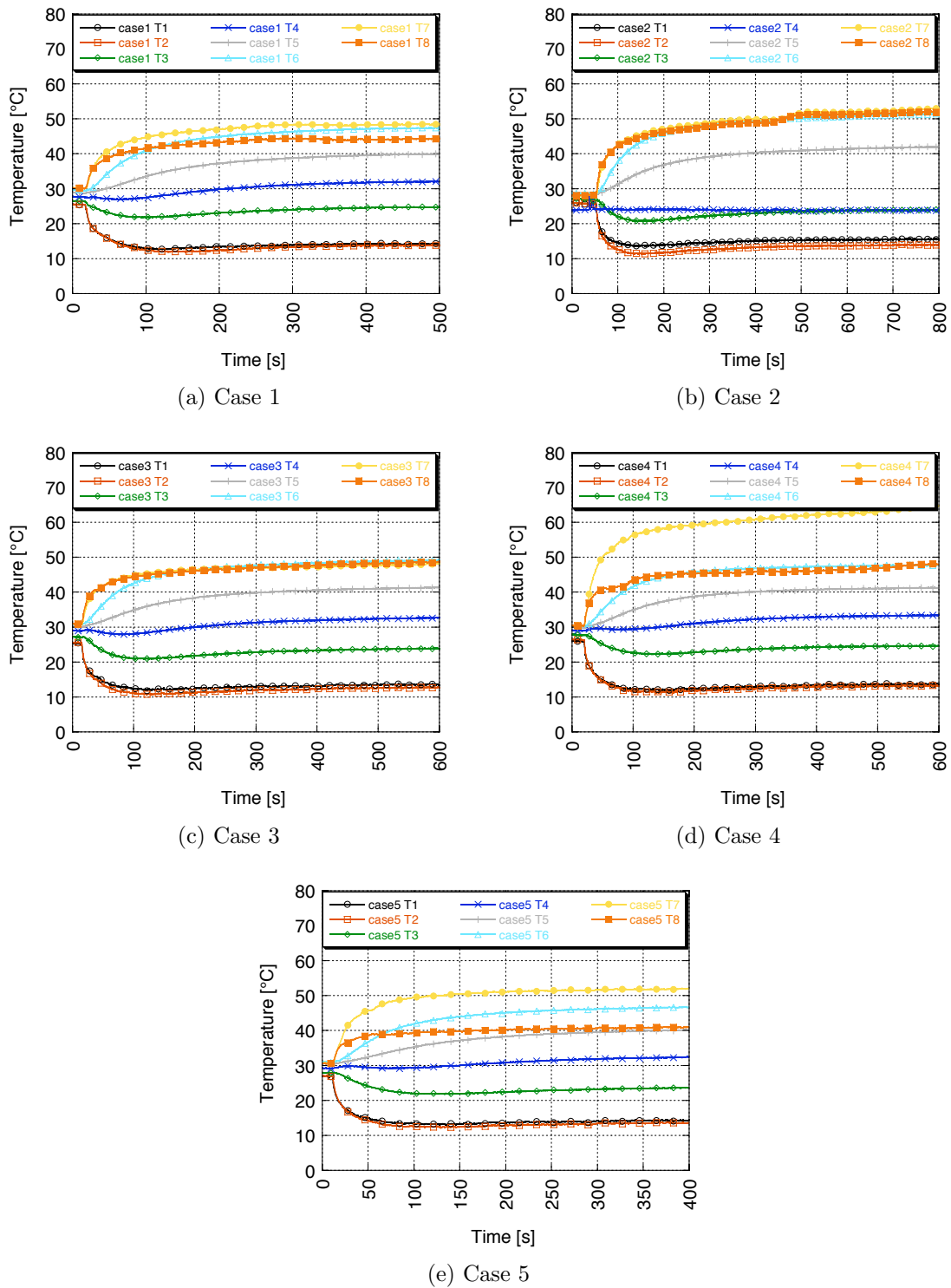


Figure 33: Temperature distribution along the regenerator as a result of the variation of the feedback inertance size (refer to Table 3 for the dimension of each case)

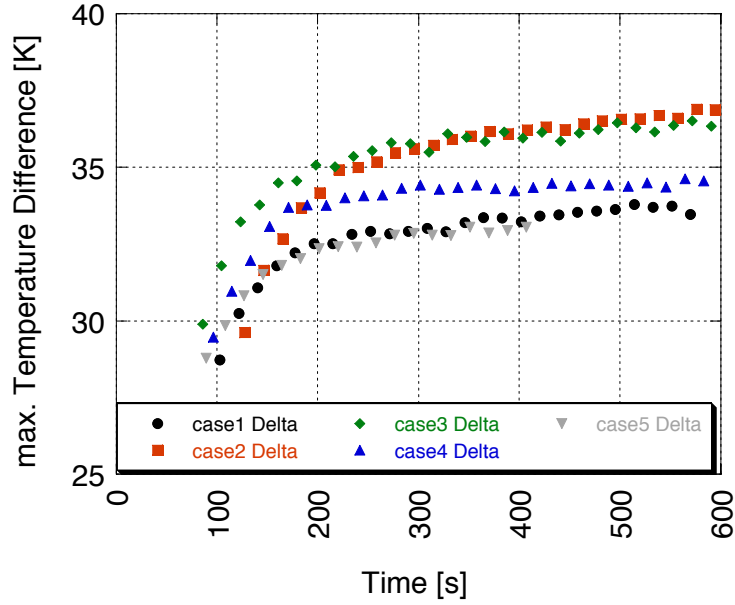


Figure 34: Temperature difference between hot and cold end for all five cases.

the hot side temperatures are much more strongly affected. Also, the difference does not become apparent in the first three quarters of the regenerator length, and only over the length of the final quarter towards the hot end is the difference between cases noticeable. Note that T 1 and T 5 represent the average values of the two cold side and hot side temperatures, respectively. T 7 of Case 4 is ignored, and so for this case, only T 8 was considered. Ultimately, Case 2 is determined to be the optimal case, yielding the highest temperature difference across the regenerator. The regenerator dimension for this case was a cross sectional area of  $45 \times 45 \text{ mm}^2$  yielding an open area of  $\approx 39\%$ .

In summary, these preliminary studies have highlighted several influences that affect thermoacoustic cooling behavior. The findings are summarized in Table 4, and this information was utilized to design the regenerator housing used in the investigations discussed in the following section.

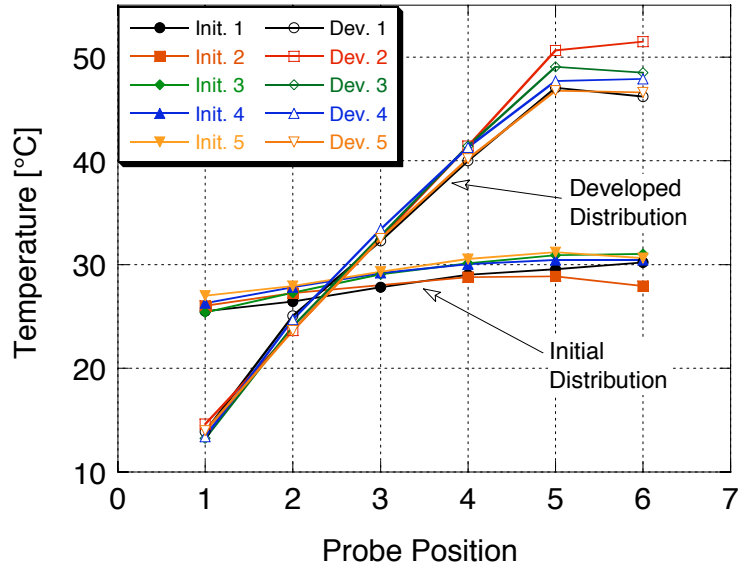


Figure 35: Direct comparison between each case and measurement location, for two different times: initial distribution and an established case (after  $\approx 10$  minutes).

Table 4: Ideal design parameters, to be applied to the screen variation investigation.

Design Parameter	Optimal Value	Notes
Driving Frequency	37 Hz	43 Hz for some preliminary results, before speaker failure
Regenerator Location	75 mm from closed end	Best combination of displacement and pressure amplitude
Regenerator Dimension	45 × 45 mm <sup>2</sup> cross section	Achieving the best temperature difference

## 4.6 SCREEN DENSITY VARIATION

With the optimal driving frequency determined and the general effects of design parameters of thermoacoustic refrigerators having been discussed, this section now focuses on the variation of the screen material and its hydraulic properties, screen packing density, and overall regenerator thickness.

### 4.6.1 Theoretical Considerations for Screen Density

Using screens instead of a continuous solid for the regenerator function is a concern because of the oscillatory behavior of the gas. Depending on operating frequency and location of the regenerator in relation to the velocity node, the gas displacement varies. In any event, the gas reaches peak displacement and compression at the same time (because of the traveling wave phasing), which is the key to the efficient transfer of heat. The transfer of heat has to occur between the gas and the solid, so it is problematic if the solid structure is present at discrete locations rather than continuously. Screens do provide an easy assembly mechanism to achieve very fine pore sizes without using microfabrication techniques. Also, the gaps between the screens result in a net reduction of thermal conductivity of the regenerator. Nonetheless, the issue of the screen spacing in relation to gas displacement must be investigated. First, some theoretical considerations are provided, and secondly, corresponding experiments are described.

This issue can be explained with an illustration shown in Figure 36. The gas is displaced (only one parcel shown) by distance  $d$ , and the screens are spaced apart by length  $\Delta s$ . The screens have a non-negligible thickness  $t_s$ . There are three different but relevant cases of  $d/\Delta s$  that require further investigation:

1. :  $\frac{d}{\Delta s} < 1$
2. :  $\frac{d}{\Delta s} = 1$  (or, more generally, an integer)
3. :  $\frac{d}{\Delta s} > 1$

Keeping in mind that the thermoacoustic effect is based on a heat exchange between a gas and a solid (via the “bucket brigade”), only case 2 should result in a useful device. By

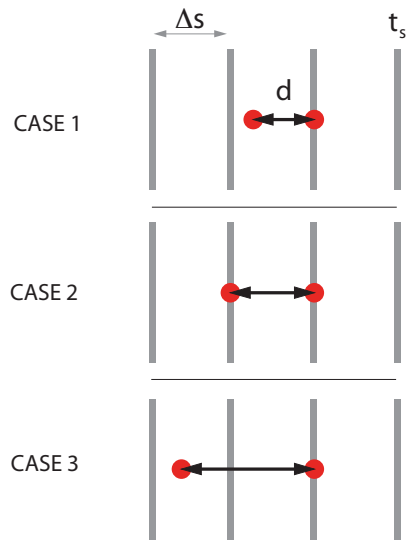


Figure 36: Three ratios of displacement to screen spacing: Case 1 is  $d/\delta s < 1$ , Case 2  $d/\delta s = 1$ , Case 3  $d/\delta s > 1$ .

intuition, neither case 1 nor case 3 should allow for this transfer of heat to occur in an efficient way. As a consequence, we would expect each case to yield a different heat pumping capacity. For efficient operation, it is a requirement that the heat exchange from the gas to the solid (or vice versa) occur at the moment of highest compression or expansion. The design of the traveling wave engine is such that this occurs at the same time as peak displacement (which is the reason for their efficient operation, as explained above). For case 1 then, a gas particle starting out as coinciding with a screen is not displaced to coincide with the next screen. The heat from that particle has to diffuse through an additional length of gas to reach the wall. This, surely, is not an efficient mode of operation. The screen spacing should be reduced (assuming constant operating frequency) to coincide with the gas displacement. In this case, the amount of particles that are participating in the desired heat exchange can be estimated by:

$$\Psi = \frac{t_s}{\Delta s + t_s} \quad (4.12)$$

On the other hand, the remaining particles, of course, do not participate directly in the thermoacoustic effect; they do, however, pass through a screen (possibly depositing heat as well, but as mentioned before, this would happen at non-ideal pressure conditions). By passing through a screen, these gas parcels cause viscous losses, that can be quantified by:

$$\Phi = \frac{\Delta s}{\Delta s + t_s} = 1 - \frac{t_s}{\Delta s + t_s} = 1 - \Psi \quad (4.13)$$

Both parameters  $\Psi$  and  $\Phi$  can be considered factors that the thermoacoustic heat transfer and the viscous losses have to include to account for the effect of the spacing in between screens when considering the stacked screen assembly for a regenerator. Both factors are less than 1, but it is obvious that it should be desirable to increase the screen thickness compared to the screen spacing. Allowing for gas parcels to be displaced through more than one screen, as in case 3, we can differentiate between two different cases:

3 (a) Displacement by any multiple of  $\Delta s$

3 (b) Displacement by an integer of  $\Delta s$

3 (a) is a combination of case 1 and case 2. The viscous losses are at least as large as in case 2, or even higher for multiple screen crossings, while no gas parcels are displaced

between two screens exactly. Ultimately, this case increases the losses ( $\Phi$ ) while decreasing the positive effects ( $\Psi$ ) which is less desirable than case 2. If we apply a further limitation to the displacement and allow it to be only integer multiples of  $\Delta s$ , the correlations for  $\Psi$  and  $\Phi$  take the following form:

$$\begin{aligned} d &= n \cdot \Delta s \\ \Psi &= \frac{t_s}{\Delta s + t_s} \\ \Phi &= n \frac{\Delta s}{\Delta s + t_s} \end{aligned} \tag{4.14}$$

Equation 4.14 illustrates how the positive contribution  $\Psi$  is independent of the number of screens a gas parcel passes, but the negative factor  $\Phi$  is increased as  $n$  increases. Ultimately, these considerations prove that it should be desirable to construct a regenerator so that the ratio of displacement and screen spacing is equal to 1. Finally, we can also consider two extreme cases. First, we can set  $t_s/\Delta s \ll 1$ , and second, we can set  $t_s/\Delta s \gg 1$  (for a continuous regenerator). For the first case, the positive effect  $\Psi$  vanishes, whereas for the second case, the adverse factor  $\Phi$  vanishes. Of course, the second case here can also be considered to be a continuous regenerator, which should be the ideal configuration. Of course, this does not take into account the issues with thermal conductivity, which is adversely affected as the screen spacing decreases. Assuming that the screen assembly is a series of thermal resistances, the net thermal conductivity in terms of  $\Delta s$  and  $t_s$  is given by:

$$k_{net} = \frac{\Delta s k_{gas} + t_s k_{solid}}{\Delta s + t_s} \tag{4.15}$$

For the aforementioned extrema for the ratio of  $t_s/\Delta s$ ,  $k_{solid}$  will become dominant for the continuous regenerator. For any metal, this would certainly result in a negative influence, as heat is now able to be conducted from the hot side to the cold side. Ultimately, the solid's thermal conductivity has to be chosen to be as small as possible for efficient operation. Using a solid with a thermal conductivity equal that of the working gas allows us to use the (ideal) continuous regenerator with no penalty.

### 4.6.2 Experimental Investigation of Screen Spacing

In order to investigate this behavior, the regenerator housing was filled with screens, and the length of the regenerator was then varied for each case. This results in different screen densities for each case. Also, two different materials were used. The resulting cases are shown in Table 5

Table 5: Different regenerators using variable screen counts and regenerator lengths ( $L_R$ ), resulting in a variation of the regenerator density. The ranges used in the experiments are shown.

Material	Screen Count	$L_R$ [mm]
Stainless Steel, $100\mu m$	20-200	10-60
Nylon, $200\mu m$	20-220	10-60
Nylon, $105\mu m$	20-160	5-40

It must be noted that because of the weaving pattern used for the stainless steel mesh, the total thickness of each screen layer is very close to that of the  $200\mu m$  Nylon screen. The open area, on the other hand, is comparable to the  $105\mu m$  screen. Ultimately, a direct comparison between all three types of screens allows a comparison of the influence of the hydraulic properties and secondly a comparison of the thermal properties. The results are presented in the following fashion in Section 4.7

1. Display of hot and cold side temperatures by regenerator length and screen packing density,
2. Display of hot and cold side temperature sorted by screen count, and
3. Comparison of hot and cold side temperature as well as temperature difference for all screen types, by screen count.

## 4.7 RESULTS FROM THE SCREEN DENSITY VARIATION

### 4.7.1 105 $\mu\text{m}$ Nylon Screen

For the thin Nylon screen, the screen count was varied between 20 screens and 160 screens. Because of the thin screens, the regenerator lengths could be chosen to be small compared to the following cases. Also, the screen density is much higher here than in the subsequent regenerator cases.

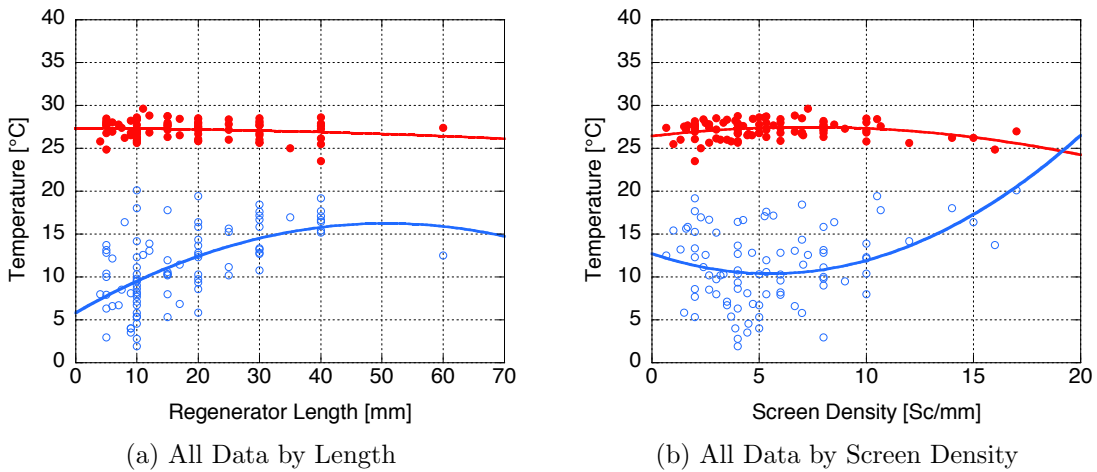


Figure 37: Plots showing all data for 105 $\mu\text{m}$  Nylon, for the whole range of the number of screens and regenerator length

Figure 37 shows the collection of data for the 105 $\mu\text{m}$  Nylon screens. It shows large amounts of variation in the data, especially on the cold side. Each data point resembles the mean value recorded from three thermocouples mounted on either end of the regenerator assembly. The general trend that becomes obvious from Figure 37 (a) is that the performance of the regenerator improves with decreasing thickness. The cold side temperature shows a decreasing trend, in general falling between 2°C and 20°C. The hot side temperature on the other hand is affected less significantly by the variation of the regenerator length. It ranges from 25°C to 30°C. The coldest recorded (average) temperature occurs at a length of 10mm.

When investigating the temperature behavior as a function of screen packing density, the hot side temperature maintains its almost constant behavior over the whole range of densities. The cold side shows a minimum at around 4 screens per millimeter. Ultimately, this leads to the preliminary conclusion that a thin regenerator with a screen density of  $\approx 4 \text{ sc/mm}$  shows the best performance. When comparing this result with the total length of the TAR setup, the regenerator length is almost negligible compared to the resonator length  $L_{res} = 2.15 \text{ m}$ .

In the next step of the data visualization, the effect of the screen count was considered individually by separating the data shown in Figure 37 by screen count. Figures 38 and 39 show a series of data plots with regenerators packed with 20 to 160 screens. This range of plots illustrates the temperature behavior with increasing screen count. Overall, the cold side temperature increases, while the hot side temperature varies less drastically. The curve fits are included to highlight the general trends that the temperature follows as the regenerator length is increased. It must be pointed out that the cold side and hot side do not cross paths as the regenerator length is increased; the extension of the curve fits should merely serve as a guide to where heat pumping would be impossible. As the regenerator length is increased, the packing density is decreased. The limit of heat pumping should occur at the point where gas displacement is smaller than the mean screen spacing. At the same time, of course, the net thermal conductivity of the regenerator is also decreased. This result shows that varying the screen density as a means to achieve a low net thermal conductivity in the regenerator is actually counterproductive.

At small screen counts, the cold side temperature shows a clear minimum. This indicates the importance of the tradeoff between hydraulic resistance (and relatively high thermal conductivity) and the effect of the ratio between screen spacing and displacement. The minimum becomes less pronounced at higher screen counts. Again, on the hot side, the variance in the data as a function of increasing screen count is much smaller than on the cold side. As a conclusion, it can be concluded here that the best performance is achieved at short regenerator lengths with few screens. The lowest temperature was recorded at a screen count of 40 and a regenerator length of 10 mm. This confirms the conclusion drawn above. Another conclusion that can be drawn from the data shown in Figures 38 and 39 is that the

hot side temperature is generally between  $25^{\circ}\text{C}$  and  $30^{\circ}\text{C}$ , while the cold side temperature varies between  $5^{\circ}\text{C}$  and  $20^{\circ}\text{C}$ . At the very low end (20 screens), however, the data shows that the cold side temperature increases compared to regenerators with higher screen count.

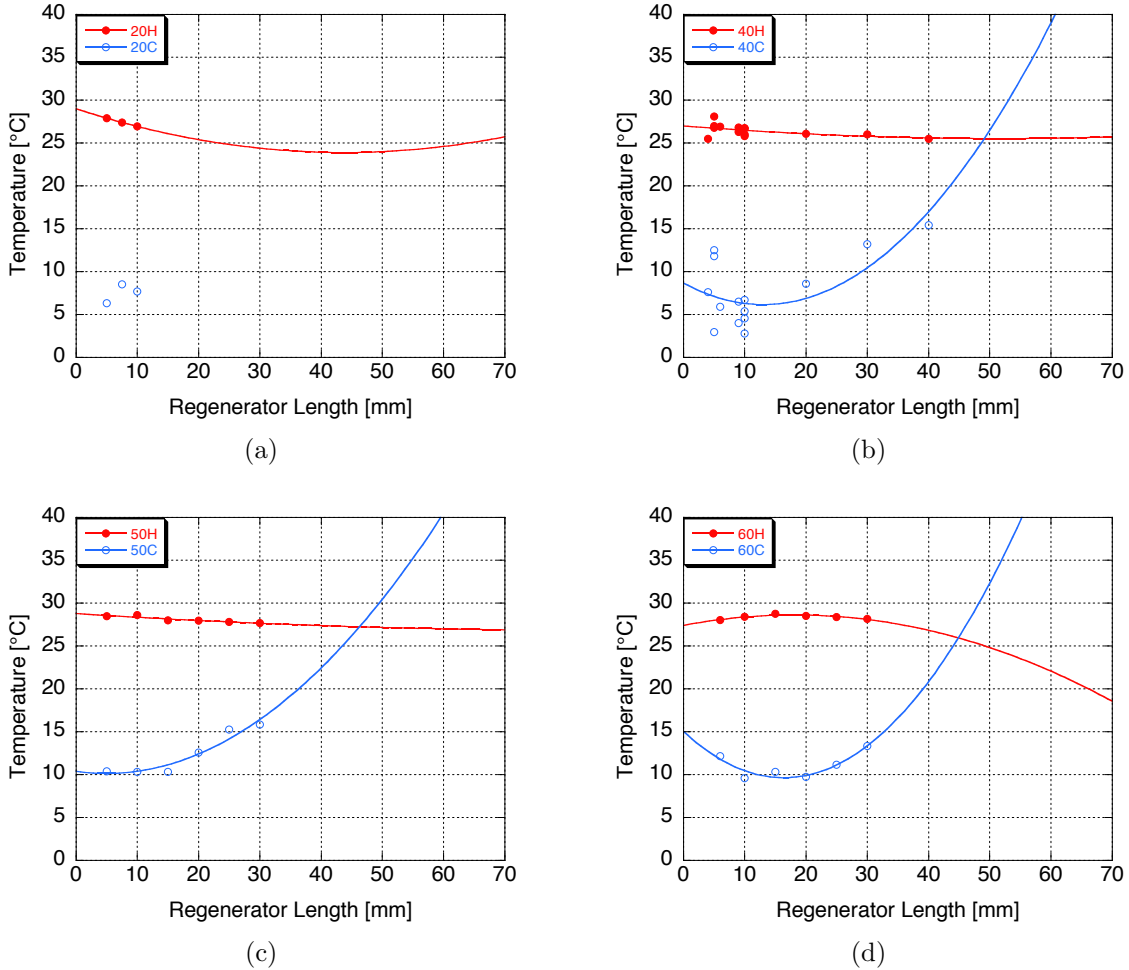
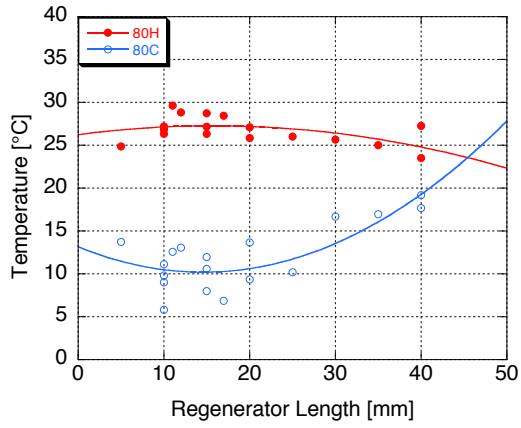


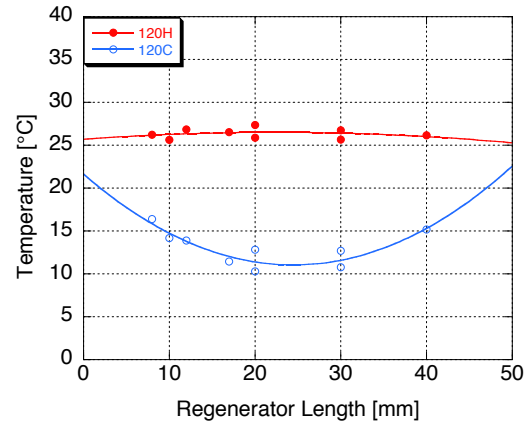
Figure 38:  $105\mu\text{m}$  Nylon, temperature data separated by screen count, as a function of regenerator length, part 1: 20-60 screens

#### 4.7.2 $200\mu\text{m}$ Nylon Screen

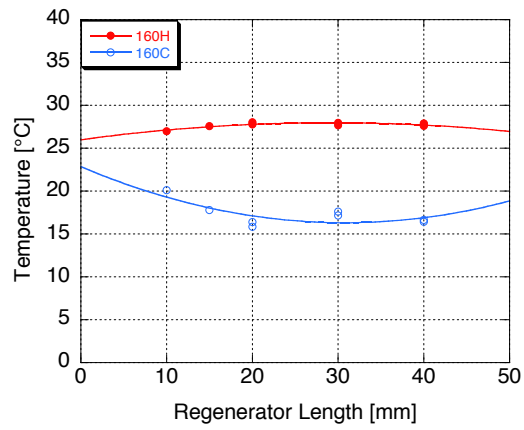
The data for the coarser Nylon screen follows the same format as for the  $105\mu\text{m}$  Nylon. Beginning with a plot of the complete data, the same trend as above can be identified. Figure 40 shows the range of temperatures reached on the hot side and cold side of the



(a)



(b)



(c)

Figure 39: 105 $\mu$ m Nylon, temperature data separated by screen count, as a function of regenerator length, part 2: 80-160 screens

regenerator for the whole range of screen densities and regenerator lengths. The trends that can be identified are similar: the hot side temperature varies only slightly, while the cold side temperature decreases more significantly with small regenerator lengths and low packing densities. The curve fit of this data highlights only trends. It does not show as well-defined a minimum as the corresponding plot from the  $105\mu\text{m}$  screens, as seen in Figure 37 (b). The total range of temperatures recorded on the hot side is similar to the  $105\mu\text{m}$  case, albeit slightly higher, ranging between  $25^\circ\text{C}$  to above  $30^\circ\text{C}$ . On the cold side, the high end achieved is identical to the  $105\mu\text{m}$  Nylon case, but on the low end, a minimum temperature of only  $5^\circ\text{C}$  is recorded. This is slightly higher than the  $2^\circ\text{C}$  achieved in the previous case. From this data, it cannot be concluded which of the Nylon regenerators offers the better performance, as the total range of temperatures achieved is approximately the same. A closer investigation of the temperature data separated by screen count is required.

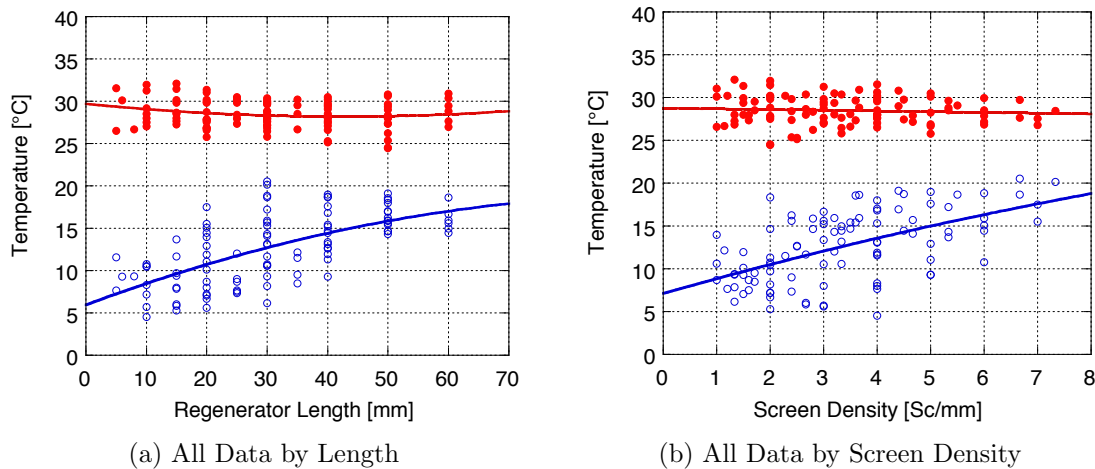


Figure 40: Plots showing all data for  $200\mu\text{m}$  Nylon, for the whole range of number of screens and regenerator length

Again, following the same format as above, the temperature data is separated by screen count. Figures 41 and 42 show that low screen counts also exhibit a clearly defined minimum. This behavior diminishes with increasing screen count. For each figure, the progression shows an increase in the range of screen densities. As concluded before, a higher screen density inhibits the regenerator performance. The influence of the regenerator length decreases as

the screen count increases. This is due to the generally poor performance and high influence of viscous resistance throughout the regenerator. The overall lowest temperature is recorded at a screen count of 40, with a regenerator length of only 10 mm. At the highest screen count, the trend shown by the lower screen counts reverses; the cold side temperature is decreasing as the regenerator length increases.

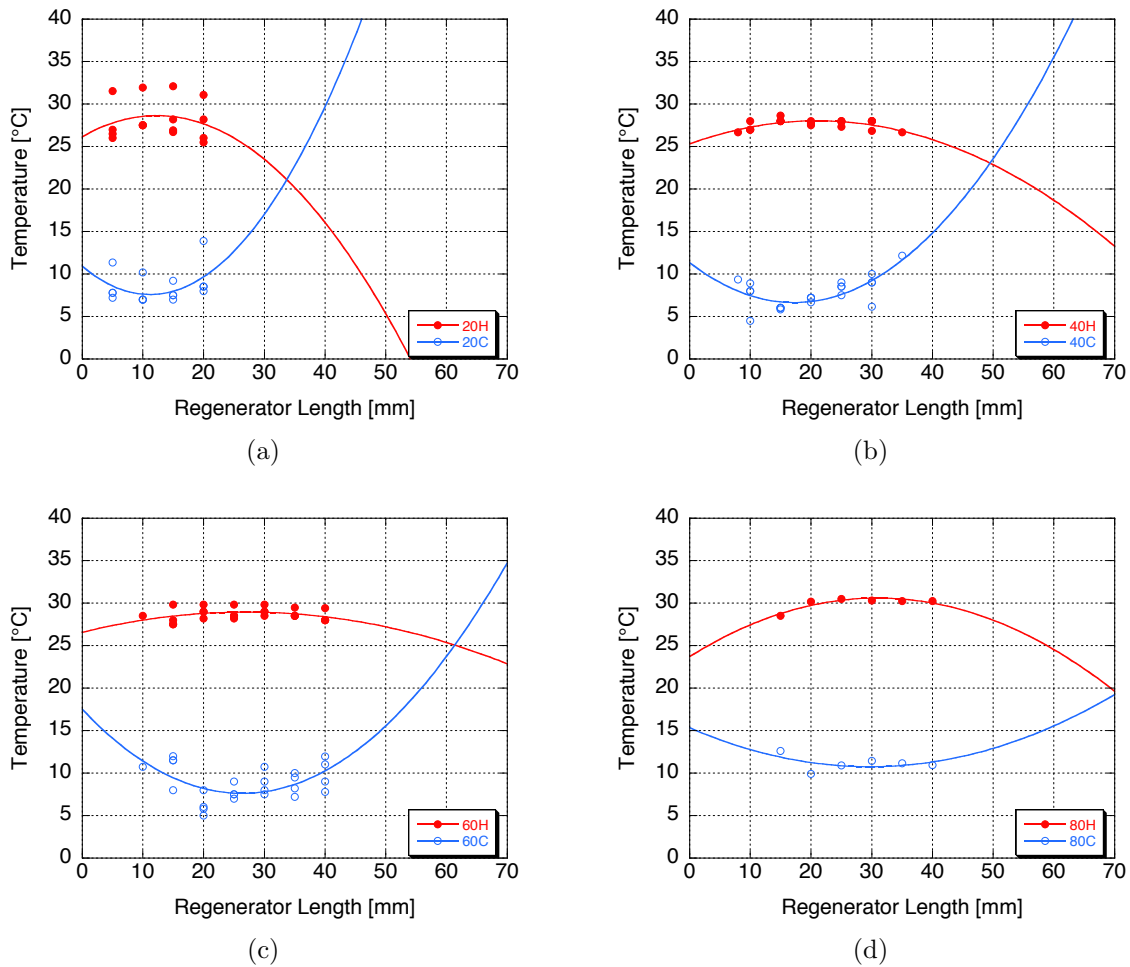
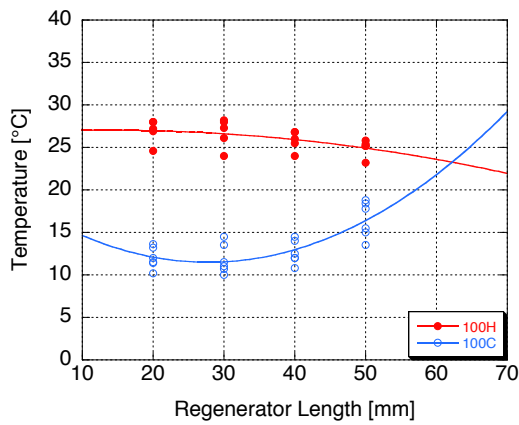
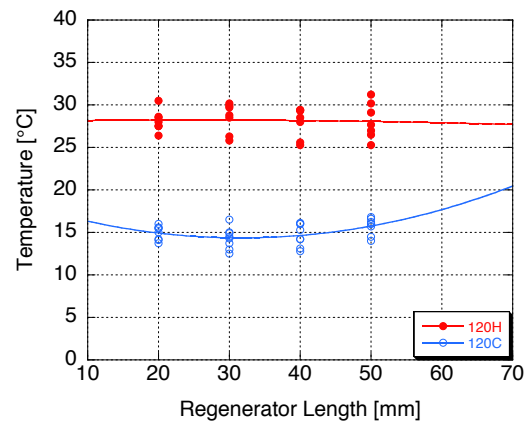


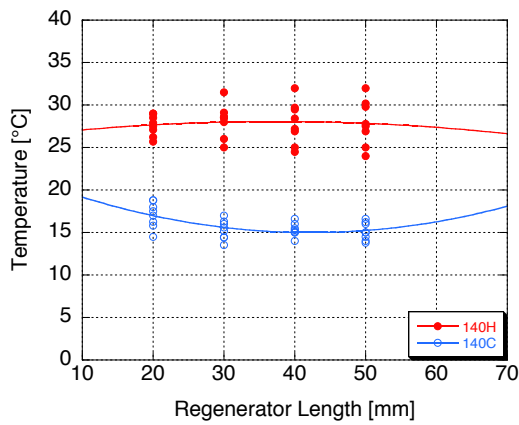
Figure 41: 200 $\mu$ m Nylon, temperature data separated by screen count, as a function of regenerator length, part 1: 20-80 screens.



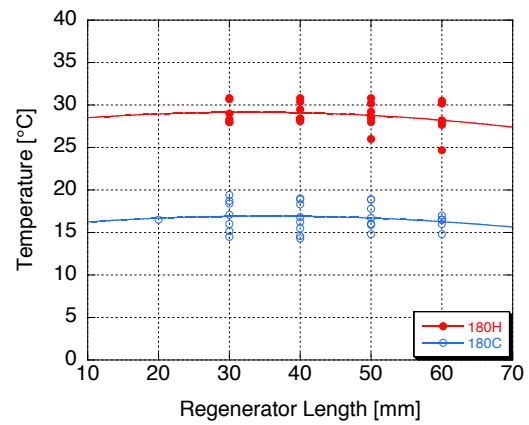
(a)



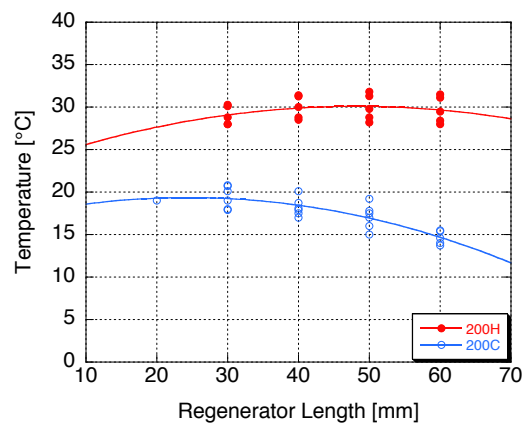
(b)



(c)



(d)



(e)

Figure 42: 200 $\mu$ m Nylon, temperature data separated by screen count, as a function of regenerator length, part 2: 100-200 screens

### 4.7.3 100 $\mu\text{m}$ Stainless Steel Screen

Finally, the stainless steel screen regenerator is discussed. Beginning with the illustration of all data points, the temperature behavior shown by the stainless steel regenerator is very similar to the previous cases, *except at a higher temperature level*, as seen in Figure 43. Immediately, it can be seen that the temperature level on the hot side varies, in general, between 25°C and 30°C. On the cold side, however, the recorded temperatures fall between 10°C and 20°C. The high end on the cold side temperature for stainless steel does not differ from the previously discussed cases. More importantly though, the cold temperature does not achieve the same low levels as it did for the Nylon regenerators. Also, the temperature difference achieved with the stainless steel regenerator does not seem to reach the same levels. Again, the thickness of each screen is comparable to the 200 $\mu\text{m}$  Nylon; the open area (i.e. viscous properties) of the steel screens is comparable to the 105 $\mu\text{m}$  Nylon. Nonetheless, the steel regenerator seems to perform significantly worse than the Nylon cases, owing to the higher thermal conductivity of each regenerator assembly.

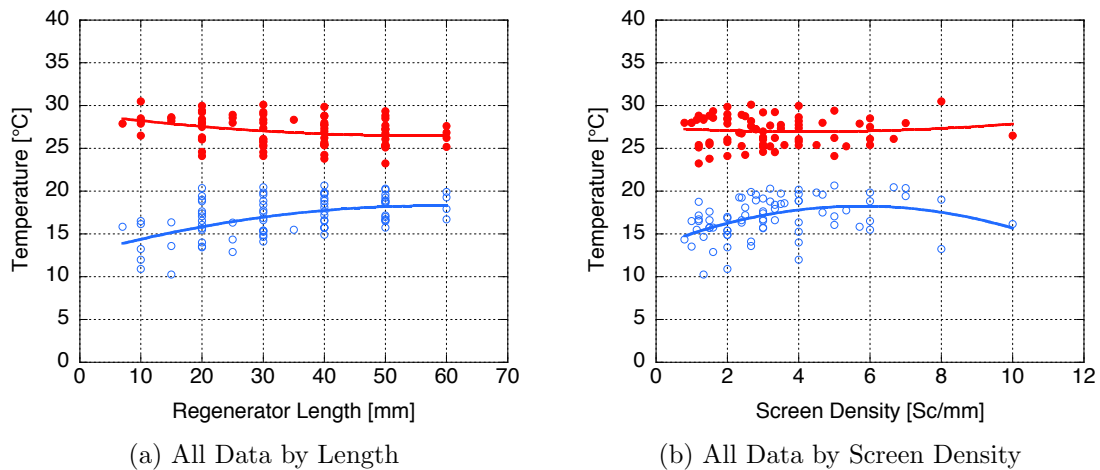


Figure 43: Plots showing all data for 100 $\mu\text{m}$  stainless steel, whole range of number of screens and regenerator length

The breakdown of temperature data sorted by screen count reveals further insights into the performance of the stainless steel regenerator, see Figures 44 and 45. First, the general trends identified before are also found in this case. The cold side temperature reaches a

clear minimum at short distances and low screen counts. The steel case also exhibits a reversal of the cold side temperature trend that was identified at high screen counts and long regenerators: the cold side temperature starts to decrease and does not exhibit a clear minimum as the remaining cases do.

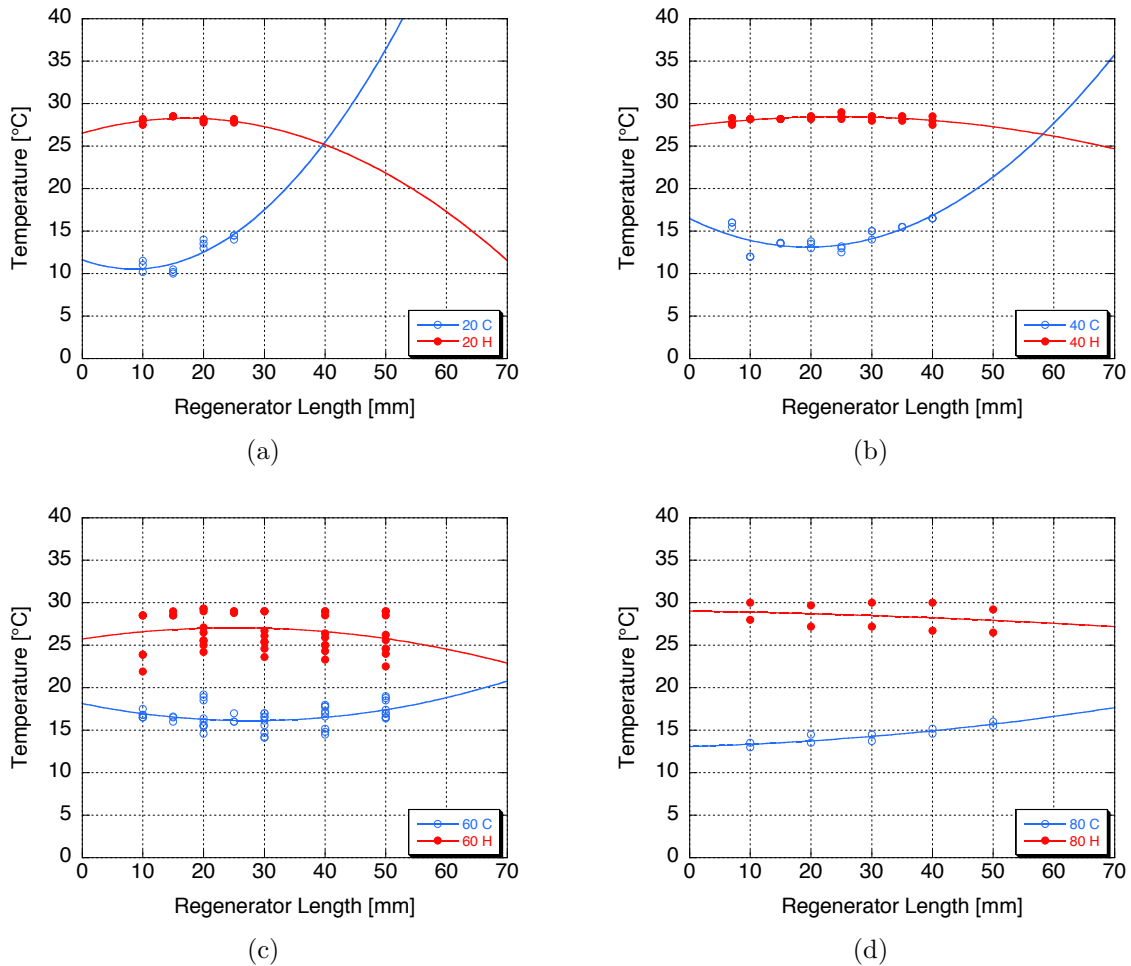
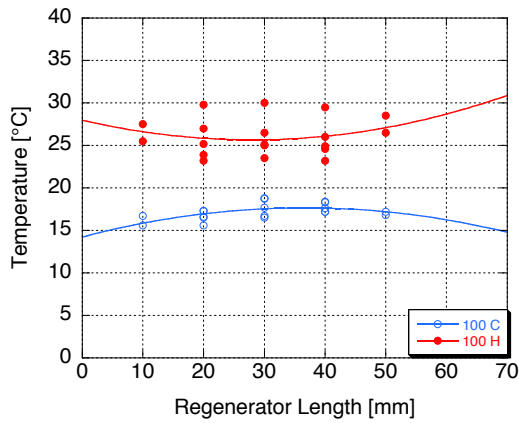
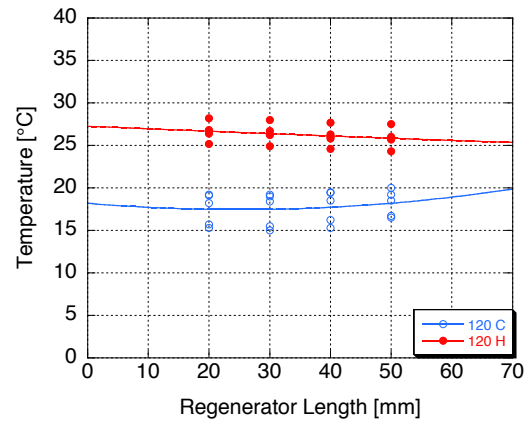


Figure 44:  $100\mu\text{m}$  stainless steel, temperature data separated by screen count, as a function of regenerator length, part 1: 20-80 screens.

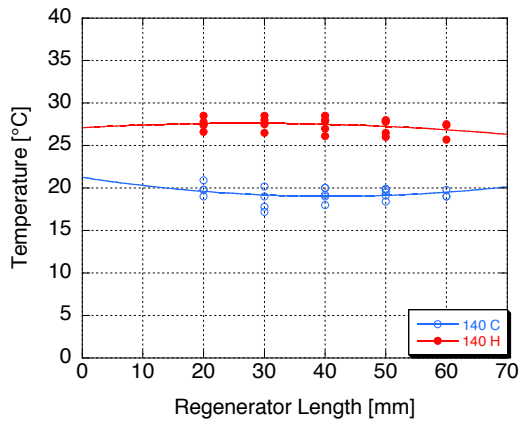
The investigation of the data from each type of regenerator has identified behaviors that are indicative of the influence of the viscous and thermal properties of the regenerator. In order to provide a thorough understanding of these effects, the heat pumping capability of each regenerator is quantified below with an investigation of the temperature levels and temperature differences grouped by screen count.



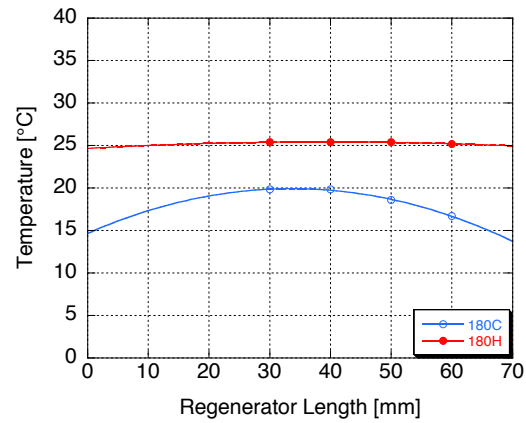
(a)



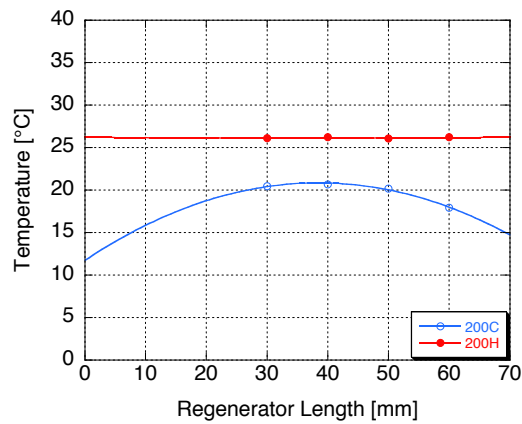
(b)



(c)



(d)



(e)

Figure 45: 100 $\mu$ m stainless steel, temperature data separated by screen count, as a function of regenerator length, part 2: 100-200 screens

#### 4.7.4 Comparing Temperature Levels and Temperature Differences

Figure 46 shows the achievable temperature levels on the hot and cold side, as well as the resulting temperature differences. As a reminder, the figure compares low thermal conductivity Nylon of  $200\mu m$  and  $105\mu m$  thicknesses, with stainless steel of  $100\mu m$  thickness. Figure 46 then illustrates two effects: a change in thermal properties between both cases of the thick screens and the effect of hydraulic properties (i.e. viscous resistance) between the two Nylon cases. It can be seen that the coarse Nylon screens yield the best performance: low cold temperatures paired with a (comparatively) high hot side temperature. It must be noted that the curve fits in Figure 46 (b) only illustrate trends and are not a good approximation of the actual curves.

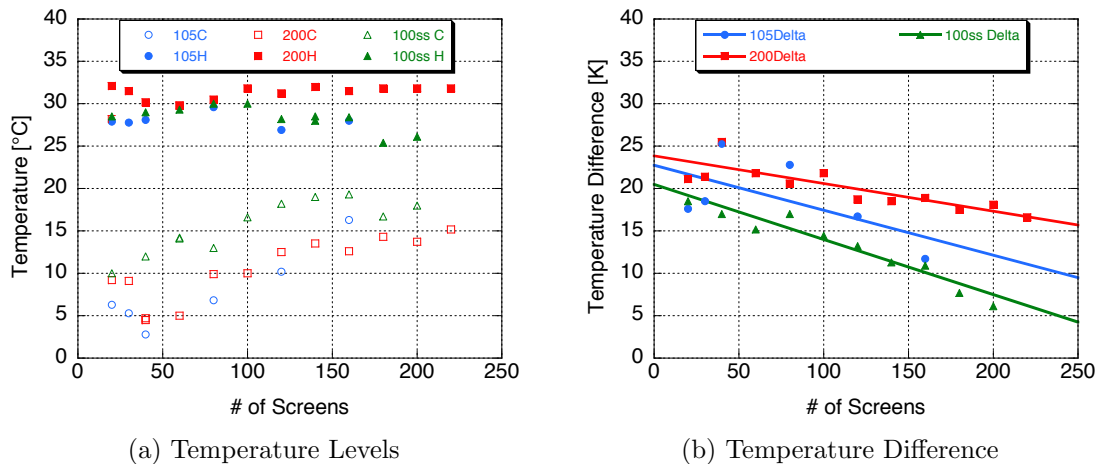


Figure 46: Plots showing the temperature levels (maximum  $T_{hot}$  and minimum  $T_{cold}$ ) for each material and screen count.

The findings from the investigation of the best performance recorded for each screen count can be summarized as follows:

- The coarse Nylon offers the highest temperature difference throughout large sections of the range of regenerator properties used. It is also less susceptible to a variation in screen count, as the slope of the curve fit indicates. The achievable temperature difference clearly decreases towards smaller screen counts than 40. This indicates that there is not

enough regenerator length available to provide for efficient heat pumping. Towards the higher end, the decrease is caused by the increased viscous resistance.

- The fine Nylon regenerator is more susceptible to changes in the screen counts. Towards the high range of screens, the achievable temperature difference decreases rapidly. Again, the mesh is much finer than in the previous case, and thus the viscous resistance plays a more important role in this regenerator. At the peak, also occurring at 40 screens, the same temperature difference can be achieved as with the coarse Nylon. Towards smaller screen counts, the performance deteriorates quickly.
- The stainless steel regenerator, which has the same hydraulic properties as the  $105\mu\text{m}$  Nylon screen, exhibits worse temperature differences throughout the entire range. It does not achieve a clearly defined peak in the achieved temperature difference. The generally worse performance compared to Nylon is caused by the higher net thermal conductivity of the regenerator. This can also be seen in Figure 46 (a), where the cold side and hot side temperatures are generally worse than for the comparable Nylon cases.

These findings lead to the conclusion that heat pumping is aided by low thermal conductivity and low viscous resistance. Obviously, thermoacoustic heat pumping occurs in the gas phase by the oscillating motion of gas parcels and is counteracted by conduction of thermal energy in the opposite direction. The data shown here proves that this is aided by a material with low thermal conductivity and supportive hydraulic properties. It is surprising to find that a regenerator of a length of only  $10\text{ mm}$  is the ideal choice for the present TAR setup. Its total length is  $2.15\text{ m}$ , which is significantly longer than the active region of the device.

#### 4.7.5 Uncertainties in the Temperature Measurements

The ideal operating conditions, specifically the operating frequency, were determined before collecting data. It must be noted however, that the resonant frequency exhibits a temperature dependency that was not quantified. It is assumed that the variation of the surrounding temperature was too small to cause significant error.

The temperature data discussed in this section has proven that a regenerator of low thermal conductivity and (relatively) large flow channels is conducive to efficient operation

of a TAR. It must be pointed out that the temperature measurements discussed in all Figures in this section show some spread. Figures 37, 40, and 43 show some discrepancies between different measurements, especially on the cold side. This is caused by the collection of many influences into one plot. Beyond this, however, the discrepancy is more noticeable on the cold end of the regenerator. The cold side data was taken with thermocouples attached to the movable plunger that was used to maintain a defined regenerator length. Between measurements, this plunger was moved in order to achieve a new regenerator length. Also, between screen counts, the plunger had to be removed completely. This movement is a source of error, which was minimized by recording temperatures with 3 thermocouples. Also, at small packing densities, the screens were able to move; a perfect contact between the screens and the thermocouples is not guaranteed.

To illustrate this, the regenerator housing was used to visualize the oscillating behavior of the gas. Rather than using trace gas, thin strips of paper were mounted inside the regenerator housing at equal spacing, beginning 50 *mm* from the closed end and ending at 250 *mm*. When turned on, the velocity component of the wave caused the paper strips to move. This motion was recorded with a camera (dSLR with a 50mm macro lens and exposure set long enough to record the motion of the paper). In order to show the still position, an additional picture was taken. Both pictures were superimposed, along with a scale that was used to estimate the tip displacement. Figure 47 shows the result for each measurement position (in inches from the closed end) and the estimate of displacement in *mm*. It can be concluded that the displacement decreases closer to the closed end of the resonator. Of course, this investigation reveals the displacement in the undisturbed standing wave. In order to investigate the detailed fluid flow inside the regenerator, more advanced tools, such as particle image velocimetry would have to be used.

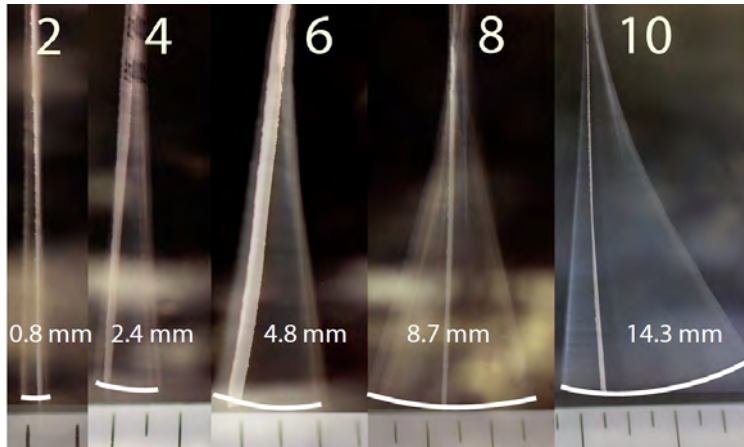


Figure 47: Illustration of the displacement throughout the regenerator housing: measurement position 2 is located at  $50\text{ mm}$ , and each subsequent position an additional  $50\text{ mm}$  further away.

## 4.8 CONCLUSIONS

The goal of these experiments was to investigate the influence of the thermal properties of the driving components of both thermoacoustic engines and refrigerators. Detailed conclusions for both cases are given below.

### 4.8.1 Engines

For the investigation of the engine, a simple standing wave demonstrator device was built. The stack was designed using metal tubes bundled together. Five different materials that could be used in such an application were investigated. The ceramic stack exhibited the lowest thermal conductivity, and copper had the highest thermal conductivity. Aluminum, stainless steel, and brass fell in between these two materials. The sound output as a function of electrical heating power was used as the metric to quantify the performance of each stack. It was found that all materials used were capable of creating the strong sound output typical of a thermoacoustic engine. However, ceramic clearly showed the highest sound pressure

level. Also, ceramic was able to sustain the highest temperature difference of any material investigated. The remaining materials exhibited a decreasing trend in sound level output following their thermal conductivities. The higher the thermal conductivity, the weaker the sound output.

In addition to the direct investigation of the sound output, the thermal losses to the surroundings were also investigated. The temperature data recorded from both sides of the stacks was used to calculate the convective and radiative heat losses to the surroundings. Here, ceramic exhibited the worst performance, mostly because of the high temperature levels that were achieved with the ceramic stack. Ultimately, though, it must be concluded that ceramic, having an extremely low thermal conductivity and beneficial hydraulic properties remains as the ideal choice for thermoacoustic standing wave engines.

#### **4.8.2 Refrigerators**

In order to investigate the influence of the thermal conductivity of the regenerator of a traveling wave system, a thermoacoustic refrigerator was used. This system utilized a subwoofer to create strong sound waves in a half-wavelength resonator. Inside the resonator, close to the opposite end from the speaker, several types of regenerators were mounted. As a preliminary investigation, the influence of driving frequency on the sound and cooling properties of the system were investigated. It was found that the sound pressure level reaches 170 *dB*, and its peaks (as a function of driving frequency) coincided with peak cooling performance. The preliminary data was used to identify the ideal driving conditions for the main focus of this investigation.

For the characterization of the influence of thermal properties, a traveling wave, water-cooled refrigeration regenerator was mounted. The regenerator was built using mesh screens of different materials. Two different types of Nylon were used, as well as stainless steel. In order to show the influence of the regenerator properties, its length and screen density were varied. It was found that between both materials used, Nylon performed better in regard to cooling than steel. Between the two Nylon cases, the mesh having the larger pore size (and thus lower viscous resistance) yielded the higher temperature difference. Also, its

performance was least susceptible to length variation. The finer of the two nylon screens generally yielded smaller temperature differences and high sensitivity to regenerator length. The steel screens, having the same hydraulic properties as the fine Nylon screens, resulted in a worse cooling performance. This result clearly showed that the thermal conductivity of the screen material adversely affects the performance of a TAR. These findings, combined with the results from the TAE section, also lead to the conclusion that a material with a low thermal conductivity should be used as the regenerator in traveling wave engines.

The influence of the thermal conductivity on the performance of thermoacoustic devices has been explained. It is one of two crucial components of the miniaturization of thermoacoustic systems. The influence of the thermal losses increases as devices are shrunk. Next, the introduction of curvature to the resonator tube as a means to decrease device size is investigated. For this investigation thermal/fluid modeling is applied to thermoacoustics.

## 5.0 THERMAL/FLUID SIMULATION

### 5.1 CFD MODELING

The concept of introducing a coiled resonator instead of a straight tube for miniaturization of thermoacoustic devices was explained briefly above. The advantage of coiling the resonator is that the driving engine components would not necessarily be scaled down, thus avoiding the problems in regard to thermal management explained in Section 4.3. However, there are new issues arising from the introduced curvature, upon which the following section will elaborate. First, however, a detailed overview of the computational fluid dynamics approach is given.

#### 5.1.1 Background of CFD Modeling

In general, CFD modeling is very useful in furthering our fundamental understanding of physical phenomena. It allows insights into fluid behaviors that cannot be investigated experimentally or visualized at all or only with extensive financial and time expense. Versteeg illustrates the range of its use: aerodynamics of aircraft, turbomachinery, distribution of pollutants, weather prediction, and many more (111). Any CFD problem is broken up in three separate parts, the preprocessor, the solver, and the postprocessor. During preprocessing, the physical domain of interest is rebuilt as a model and meshed with an array of cells (these cells are the control surfaces or volumes). Also, a set of boundary conditions is imposed so that the physical system is described in as much detail as necessary. The solver is responsible for solving the governing equations of fluid flow and energy transfer for all

control volumes. This occurs by a discretization and iterative solution of these equations and solving this system iteratively. The postprocessor is used for data analysis (111).

Any thermal-fluid system can be described using the conservation of mass, the conservation of momentum, and the conservation of energy. For the 3 –  $D$  case (in cartesian coordinates  $x$ ,  $y$ , and  $z$ , with the velocity components  $u$ ,  $v$ , and  $w$ , respectively), the conservation of mass can be expressed as:

$$\frac{\partial \rho}{\partial t} + \frac{\partial(\rho u)}{\partial x} + \frac{\partial(\rho v)}{\partial y} + \frac{\partial(\rho w)}{\partial z} = 0. \quad (5.1)$$

This notation is used for compressible fluids, where the density is allowed to change. If the fluid can be considered incompressible, the conservation of mass reduces to:

$$\frac{\partial u}{\partial x} + \frac{\partial v}{\partial y} + \frac{\partial w}{\partial z} = 0. \quad (5.2)$$

In even shorter notation, the conservation of mass, for the incompressible case, can be written as:

$$\nabla \cdot \mathbf{u} = 0. \quad (5.3)$$

This latter notation will be used for the ensuing equations. The conservation of momentum (x-, y-, and z- component) can be written as:

$$\frac{\partial \rho}{\partial t} + \nabla \cdot (\rho u \mathbf{u}) = \frac{\partial(-p + \tau_{xx})}{\partial x} + \frac{\partial \tau_{yx}}{\partial y} + \frac{\partial \tau_{zx}}{\partial z} + S_{mx} \quad (5.4a)$$

$$\frac{\partial \rho}{\partial t} + \nabla \cdot (\rho v \mathbf{u}) = \frac{\partial \tau_{xy}}{\partial x} + \frac{\partial(-p + \tau_{yy})}{\partial y} + \frac{\partial \tau_{zy}}{\partial z} + S_{my} \quad (5.4b)$$

$$\frac{\partial \rho}{\partial t} + \nabla \cdot (\rho w \mathbf{u}) = \frac{\partial \tau_{xz}}{\partial x} + \frac{\partial \tau_{yz}}{\partial y} + \frac{\partial(-p + \tau_{zz})}{\partial z} + S_{mz} \quad (5.4c)$$

The terms  $S_{mi}$  account for the momentum sources in each direction. For Newtonian fluids, the viscous stresses  $\tau_{ij}$  can be expressed by strain rates, that is the rate of change of

the velocity components ( $\nabla \mathbf{u}$ ) and the fluid's viscosity  $\mu$ . The general momentum equations then reduce to the Navier Stokes equations:

$$\frac{\partial \rho u}{\partial t} + \nabla \cdot (\rho u \mathbf{u}) = -\frac{\partial p}{\partial x} + \nabla \cdot (\mu \nabla u) + S_{mx} \quad (5.5a)$$

$$\frac{\partial \rho v}{\partial t} + \nabla \cdot (\rho v \mathbf{u}) = -\frac{\partial p}{\partial y} + \nabla \cdot (\mu \nabla v) + S_{my} \quad (5.5b)$$

$$\frac{\partial \rho w}{\partial t} + \nabla \cdot (\rho w \mathbf{u}) = -\frac{\partial p}{\partial z} + \nabla \cdot (\mu \nabla w) + S_{mz} \quad (5.5c)$$

Finally, since the fluid in the present simulation can be considered incompressible (because of the low range of Mach numbers encountered, as the fluid velocity is much less than the speed of sound of the gas. This assumption is confirmed below in the Section 6.2.1), the density terms are independent of time and location and the Navier Stokes equations can be generalized further:

$$\rho \left[ \frac{\partial u}{\partial t} + \nabla \cdot (u \mathbf{u}) \right] = -\frac{\partial p}{\partial x} + \nabla \cdot (\mu \nabla u) + S_{mx} \quad (5.6a)$$

$$\rho \left[ \frac{\partial v}{\partial t} + \nabla \cdot (v \mathbf{u}) \right] = -\frac{\partial p}{\partial y} + \nabla \cdot (\mu \nabla v) + S_{my} \quad (5.6b)$$

$$\rho \left[ \frac{\partial w}{\partial t} + \nabla \cdot (w \mathbf{u}) \right] = -\frac{\partial p}{\partial z} + \nabla \cdot (\mu \nabla w) + S_{mz} \quad (5.6c)$$

In similar fashion, the conservation of energy can be written as:

$$\rho \left[ \frac{c_v T}{\partial t} + \nabla \cdot (c_v T \mathbf{u}) \right] = -p \nabla \cdot \mathbf{u} + \nabla \cdot (k \nabla T) + \Phi + S_E \quad (5.7)$$

where  $c_v$  is the constant volume heat capacity,  $\Phi$  is the dissipation term, and  $S_E$  the energy source terms. In CFD problems, it is this set of equations that is discretized and solved for iteratively throughout the computational domain (111).

By its nature, a thermoacoustic system is based on the interaction of a fluid and a solid subject to heat transfer. As a result, a CFD analysis can provide useful insights into the phenomena occurring in thermoacoustic devices. The most interesting feature of a thermoacoustic engine is the stack area, because it is the location of highest velocities and the area where the thermodynamic process occurs. As such, it is also the area where the

highest amount of losses occur, requiring the most investigation. With a CFD analysis, we can investigate the fluid flow close to the solid walls of the regenerator or stack. We can also visualize streaming phenomena. Another important insight is the effect of the stack on the spatial velocity and pressure distribution compared to the free field. CFD analysis in Fluent is advantageous as we can model the entire engine at once, visualizing every aspect of it. One way of simulating the thermoacoustic engine is to build a mesh that resembles reality closely: use a compliance and a regenerator, and a “stack” represented by heated walls in between the compliance and resonator. Despite the advantages of applying CFD analysis to thermoacoustics, examples of successful CFD models of thermoacoustic devices are very rare in the literature.

### 5.1.2 Previous CFD Modeling in Thermoacoustics

As of today, few examples of CFD simulation of thermoacoustic devices exist. Chronologically, the previous efforts were published by Hanschk et al. (112; 113), Nijholt et al. (114), and Zoontjens et al. (115; 116).

Hanschk et al. used Fluent 4.4.4 to simulate a Rijke tube (which is similar to a classic thermoacoustic engine, except that the oscillations are created with one heated wire screen rather than a stack). The boundary conditions are a steady velocity inlet and an open end, with a heated screen in the center. The setup is illustrated in Figure 48 (113). The fluid properties used are adjusted so that the heat transfer would be large enough to cause oscillations. As a consequence, however, the thermal conductivity for the gas that is 10 times higher than the realistic value for room temperature (112; 113). This corresponds to a Prandtl Number that is 10 times lower than the real value for their gas at room temperature (which equals approximately 0.7).

Nijholt used the commercial solver CFX to simulate a traveling wave engine inside a Helmholtz resonator, mimicking the design built by Bastyr et al. (20). This model is illustrated in Figure 49 (114). Rather than modeling the regenerator geometrically, the group modeled this region with body forces to account for the viscous forces acting on the gas. This includes a volume porosity to account for the solid fraction in the regenerator

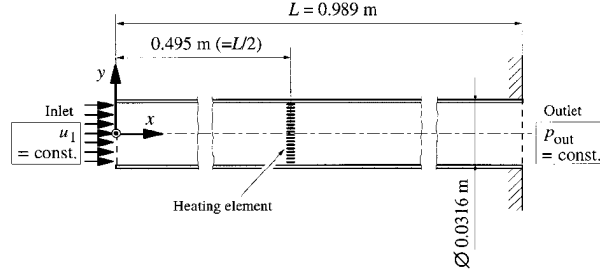


Figure 48: Rijke tube as modeled by Hanschk et al.

region. The pressure drop across the heat exchangers and regenerator are modeled following the work done by Thomas et al. on the friction and heat transfer behavior of gases in Stirling regenerators (117):

$$\Delta p = \left( C_{fd} + \frac{C_{sf}}{Re} \right) \frac{\rho u^2}{4d_w} \quad (5.8)$$

This is dependent on the Reynolds number, density  $\rho$ , velocity  $u$ , and wire diameter  $d_w$ , as well as “correlation constants” which are determined empirically. The group used a very coarse grid, and a time step that used approximately 100 samples per period of the oscillations (at  $53Hz$ ). Their simulation covered a total time of 1.5 seconds and did not reach a steady state of constant amplitude.

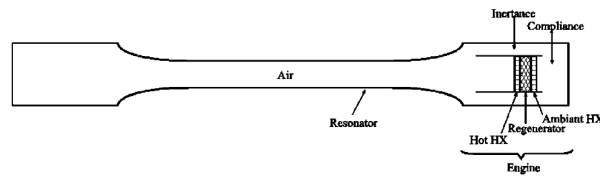


Figure 49: Traveling wave engine, basis for CFD model by Nijholt et al.

The most recent efforts in the CFD analysis of the thermoacoustic effect were done by Zoontjens et al. His dissertation extensively described his chosen model. Primarily, it was

based on a section of a stack plate and half of a channel as well as a section of a (half wave) resonance tube. It is based on related numerical studies that do not utilize commercial code in the solution of the governing equations. Below, the relevant previous efforts that form the basis of the CFD simulation performed by Zoontjens are summarized.

- Atchley et al. (118): Theoretical evaluation of temperature in stack,  $DR \approx 1\%$ ,  $200 Hz < f < 700 Hz$ ,  $100 kPa < p_m < 368 kPa$ . *Findings*: Non-linearities in temperature, deviation from linear theory for  $DR > 0.4\%$ .
- Cao et al. (119): Thin plate,  $0.01 < Ma < 0.05$ , variation of channel height,  $\lambda/4$  resonator. *Findings*: Energy flux along stack plate.
- Worlikar et al. (120; 121): Illustration of time evolution,  $0.28\% < DR < 2\%$ ,  $f \approx 700 Hz$ , focus on stack, no account of the resonator. *Findings*: Vortices at stack ends, agreement of simulation and Atchley measurements, temperature difference under variation of stack position, agreement with Cao for energy flux distribution.
- Besnoin et al. (122; 123): Thin plate, includes heat exchangers,  $2\% < DR < 8\%$ ,  $f = 700 Hz$ ,  $p_m = 100 kPa$ . *Findings*: Energy transfer between gas and heat exchangers.
- Ishikawa et al. (124): Based on Cao, no heat exchangers,  $1.7\% < DR < 8.5\%$ , compressible NS equation,  $f = 100 Hz$ ,  $p_m = 10 kPa$ . *Findings*: Comparison (and agreement) with Cao’s results.
- Marx et al. (125–128): Cao model, with heat exchangers,  $0.7\% < DR < 11.2\%$ ,  $f = 20 kHz$ ,  $p_m = 100 kPa$ . *Findings*: Velocity profile, temperature non-linearities, enthalpy flux, effect of stack location relative to velocity node and  $DR$  on temperature and velocity behavior, “critical stack length” where non-linearities exist.
- Blanc-Benon (129): Summary of work by Marx, same model conditions. *Findings*: effect of  $DR$  on temperature and velocity inside stack.
- Piccolo et al. (130): As Cao,  $0.5\% < DR < 6\%$ ,  $f = 100 Hz$ ,  $p_m = 10 kPa$ , Helium. *Findings*: Investigation of the influence of the convective heat transfer coefficient.
- Zoontjens et al. (115; 116): CFD Simulations of “Cao domain” and extension to multiple stack plates, variation of stack geometry, account for solid material, time dependence,  $f = 100 Hz$ ,  $p_m = 10 kPa$ , Helium. *Findings*: Findings are in agreement with measurements and previous work (non-linearities, vortices, energy flux).

Results from Atchley’s investigation of the temperature behavior along a single plate inside a resonator (118) form the basis of Cao’s model (119). The other models discussed are elaborations on Cao’s model. All simulations share the 2-D nature of the computational domain of thermoacoustic stack assemblies of solid walls under the influence of oscillating gas. In all cases, the oscillations are caused by an oscillating boundary condition caused by the superposition of two (counter propagating) traveling waves. This is to simulate a mechanical driver (or also a thermoacoustic driver). The models all refer to a thermoacoustic refrigerator instead of an engine. Figure 50 (115) illustrates the model that was used (with slight variations) by all studies ranging from Cao to Zoontjens. The shaded area represents the solid region of the stack, the unshaded area represents the gaseous region of the computational domain.

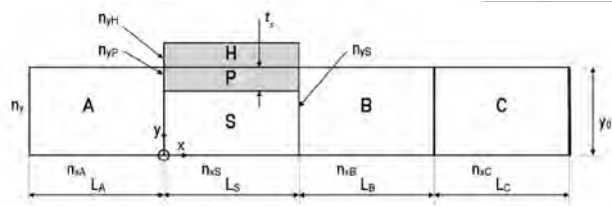


Figure 50: Illustration of computational model used extensively in numerical investigations as well as CFD study by Zoontjens

To the best of our knowledge and after an extensive review of the thermoacoustic literature, these examples are the only CFD studies of the thermoacoustic effect. They were published about eight years apart, which further emphasizes the lack of efforts in this direction, especially in regard to thermally driven thermoacoustic engines, where Hanschk and Nijeholt are the only previous examples. These models form the basis of the presented model. Relevant results from Zoontjens’ investigations of the half-wave device will be discussed below, as the nature of the thermoacoustic effect is identical in TARs and TAEs.

### 5.1.3 Motivation for CFD Modeling

In order to miniaturize TAEs and TARs, and thereby increase their potential applications, coiling the resonator is another idea to decrease the device's footprint (rather than scaling the entire engine). Whether in a standing wave or traveling wave engine, a resonator is necessary to sustain the driving acoustic waves. A straight resonance tube is the easiest design, and will minimize losses. However, there is no study quantifying the effect of resonator coiling. Generally, thermoacoustic devices are large in size: Tang et al. illustrate that the typical resonator lengths used in thermoacoustic engines range between 4 *m* and 9 *m* (131). If we can effectively coil a 9 *m* resonator into a space of, say,  $1 \times 1 \text{ m}^2$ , the savings in engine footprint are significant. Even for a transition to traveling wave-mimicking engines with a feedback inertance rather than a looped feedback path, this problem is not fully addressed as this design still requires a resonator. In general, it should be advantageous to maintain a regenerator with dimensions on the order of *cm* (and flow channels on the order of  $10\mu\text{m}$ ) because those sizes can be achieved with conventional manufacturing techniques and do not require micro fabrication. The size of the regenerator then determines the length of the resonator. Consequently, in order to pursue thermoacoustic devices with small footprints, investigating a coiled resonator is equally as important as investigating the scaling of the entire device. Figure 51 illustrates the suggested design.

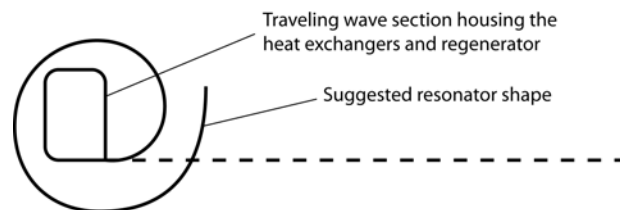


Figure 51: Suggested resonator tube design (solid line), curled around the traveling wave loop rather than the traditional straight design (dashed line)

The suggested design clearly improves the engine footprint while maintaining energy efficient engine parameters. However, the curvature may introduce losses not encountered with the straight resonator. There is only one example in the literature, by Olsen et al., that

investigates curvature. However, their work primarily investigates waves in liquids. They also investigate Helium gas (132), but their results do not duplicate the goals of this work, as they do not discuss the effects of curvature on the heat transfer during the thermoacoustic cycle. The developed simulation model for Fluent is instrumental in the investigation of the curvature effect on engine performance. Here, CFD provides a cost effective way to gather necessary information quickly, once the boundary conditions of the simulation are tuned to represent reality correctly. Its visualization features will also support the solution of the issues at hand, and, as detailed in Section 5.1.2, provide unprecedented insights into the localized behavior of TAEs and TARs.

#### 5.1.4 Losses due to Resonator Geometry-Curvature

In Section 3.1, acoustic losses were described. Primarily, these were attributed to flanges and attachments, as well as engine components that hinder lossless wave propagation. When we introduce curvature to the waveguide, we must expect further losses, but again, there is no parametric study on this topic that quantifies these. Figure 52 illustrates the idea of different curvatures.

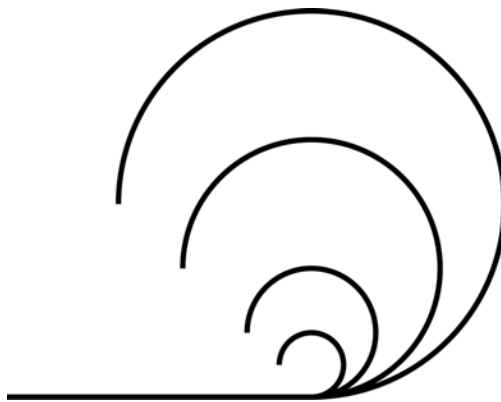


Figure 52: Suggested resonator curvatures

It is expected that resonators with a small curving radius will exhibit higher losses than resonators with less curvature. One goal of this study is to find the smallest feasible radius for a given channel size. Investigations on this topic includes the effects of:

- Using gradual corners,
- Overall length of curved resonator,
- Using sharp corners with straight section in between them, and
- Operating conditions, such as static pressure and frequency.

As a result of this investigation, the tradeoff between efficiency and degree of the coiling will be determined. This investigation will be done using computational techniques, as this can ensure constant boundary conditions for all computational systems.

## 5.2 DEVELOPMENT OF THE CFD MODEL

Given the underrepresentation of CFD modeling in thermoacoustics, specifically the whole engine, a thorough CFD model of an engine was developed using realistic fluid properties and boundary conditions. Although Fluent allows for modeling of porous media by means of body forces and virtual porosity, much like the model developed by Nijholt, discussed in Section 5.1.2, the present model was developed with a physical description of the stack geometry. This approach allowed for a replication of the thermoacoustic effect, and also an investigation of physical phenomena relative to the location in the stack. This approach is more closely related to the work presented by Hanschk et al. (113).

### 5.2.1 Mesh

For the initial models, a very simple standing wave engine was replicated in Gambit. In order to construct a simple model and maintain low computing times, a 2 –  $D$  model of the engine was constructed. This model resembled a slice of our demonstrator engine. Here, the resonator length is 150  $mm$ , and the stack is 10  $mm$  long and placed 30  $mm$  away from the closed end. The stack in this case had square channels of approximately 0.5  $mm$  height, which is sufficiently large to be modeled in Gambit. The grid is built using triangular cells, with a baseline total cell count of approximately 20,000 cells. Using triangular cells allowed for a smooth increase in cell density, or rather decrease in cell size towards the stack area.

This is important as this is where the velocity is expected to be high. The Courant  $C$  number is defined as:

$$C = \frac{v\delta t}{\delta x} \quad (5.9)$$

For transient simulations, the timestep  $\delta t$  and the cell size  $\delta x$  have to be chosen so that the Courant number is less than 1 in order to ensure numerical stability. As a consequence, the cell size has to be chosen to be small to accommodate for the large velocities inside the stack. An overview of the computational domain is provided in Figure 53, and a detailed view of the meshed stack area of the model is shown in Figure 54.

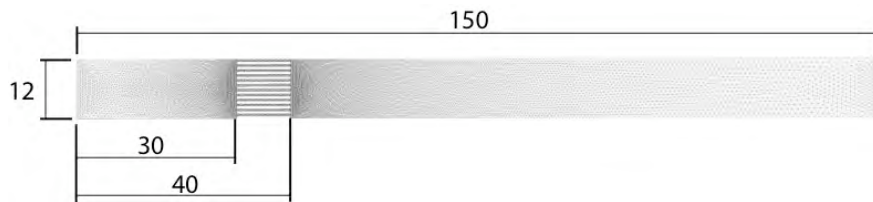


Figure 53: Dimensions of the computational domain for the TAE

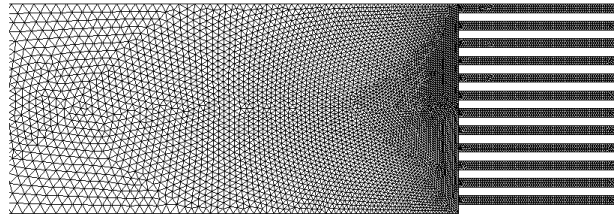


Figure 54: Section of the CFD grid, developed in Gambit

In addition, an investigation of the Womersley number can provide an insight into the requirements for modeling detail in the flow channels of the stack. As originally defined, this

dimensionless number was used to describe arterial flow, but it has also been applied to the analysis of Stirling machines (133). The Womersley number is defined in (134) as:

$$W_o = \sqrt{2} \frac{R}{\delta_\nu} = R \sqrt{\frac{\omega \rho}{\eta}} \quad (5.10)$$

where  $R$  is half of the characteristic channel dimension (here  $R = 0.25 \text{ mm}$ ). For small values of  $W_o$  (also referred to as  $\alpha$ ), the oscillatory flow behaves like a Poiseuille flow, while for larger values, there is a  $90^\circ$  phase lag between velocity and pressure (135). For the current case, the Womersley number can be estimated to be:

$$W_o = \sqrt{2} \frac{0.25 \cdot 10^{-3} \text{ m}}{9.03 \cdot 10^{-5} \text{ m}} \approx 4 \quad (5.11)$$

where  $\delta_\nu$  taken from DeltaE for  $f = 614 \text{ Hz}$ ,  $T = 300 \text{ K}$ ,  $p = 101325 \text{ Pa}$ . As a result, the flow cannot be modeled as a straightforward Poiseuille flow, and the phase lag between pressure and velocity must be taken into account.

### 5.2.2 Boundary Conditions

Of all boundary conditions, the horizontal stack surfaces are the most critical. The horizontal walls in the stack are given a temperature with a gradient from  $700\text{K}$  down to  $300\text{K}$  over the length of the stack. The temperature follows the following function:

$$T(x) = 1000 - (500 + 200 \cos(\pi \frac{x}{L_{stack}})) \quad (5.12)$$

The  $x$ -coordinate is of course referenced to the closed end of the compliance, which is why the constant term of the temperature distribution is not  $700 \text{ K}$ . As a reminder, the stack begins at  $x = 0.03 \text{ m}$  and  $L_{stack} = 0.01 \text{ m}$ . This temperature gradient is independent of time. The temperature distribution is implemented in Fluent with a “user defined function” (UDF), which is given below:

```
#include "udf.h"
#define PI 3.141592654

DEFINE_PROFILE(temp_profile, thread, position)
{
```

```

real r[ND_ND];          /* this will hold the position vector */
real x;
face_t f;              //Face. not cell

begin_f_loop(f, thread)
{
F_CENTROID(r,f,thread);
x = r[0]; // zero is the index for x-direction.
//function for temperature distribution
F_PROFILE(f, thread, position) = 1000-(500+200*cos(PI*x/0.01));

}
end_f_loop(f, thread)
}

```

The function given inside the loop is the temperature distribution. It shows that a sinusoidal distribution was used. The heat transfer coefficient between the stack walls and the fluid was set to be  $50 \text{ W/m}^2\text{K}$ . This value is consistent with calculations carried out by Liu et al. The group calculated the complex Nusselt number for a channel subject to a temperature gradient as a function of the Lautrec number (which describes the ratio of hydraulic radius and thermal penetration depth). The real part of the Nusselt number was found to be constant (at small Lautrec numbers, which is typical for standing wave devices with large channels) at a value of  $Nu \approx 1$  (136). Using material properties for air, we then can derive the heat transfer coefficient to be:

$$h = \frac{Nu \ k}{D} \approx \frac{1 \cdot 0.0242}{0.0005} = 48.4 \frac{W}{m^2K} \quad (5.13)$$

For this work, the heat transfer coefficient is assumed to be constant and independent of operating conditions. Of course, this approach does not follow the traditional path of using a Nusselt law to determine the heat transfer coefficient. It is conceivable that a channel subject to a sound wave could be assumed to behave like a channel subject to laminar or turbulent flow, even subjected to entrance effects (as a result of the repeated flow reversal). For these cases, Nusselt correlations exist (107). Mackley et al. have investigated the heat transfer behavior of oscillatory flows and compared the results to the traditional values for the Nusselt number for laminar, transitional, and turbulent tube flows. They found that the heat transfer coefficient was significantly increased over the laminar case when the flow was

subject to oscillations. The reason for this behavior is small scale mixing as a result of the continuous reversal of flow direction. Figure 55 illustrates their findings (137).

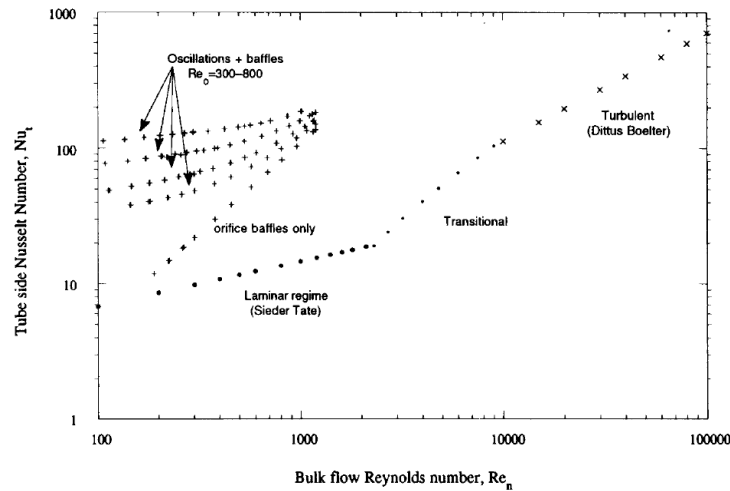


Figure 55: Heat transfer behavior of tube flow subject to oscillations, compared to laminar, transitional, and turbulent heat transfer correlations.

Although the range of Reynolds numbers that are present in the oscillatory flow are very small, the heat transfer coefficient was found to be of a similar order of magnitude as for the transitional to turbulent pipe flow (Dittus-Boelter correlations). These results are reason enough to consider the value of  $h = 50W/m^2$  a good estimate for the present model, especially since it was sufficient to replicate the thermoacoustic effect. This value also falls in a similar range as values determined by Piccolo et al. These results also show that the heat transfer coefficient is constant for a significant portion of the stack length (130). The influence of an increase of the heat transfer coefficient on the magnitude of oscillations will be estimated as part of the sensitivity analysis.

The horizontal stack surfaces are modeled as walls with a non-zero thickness. All other surfaces are trivial and are modeled as adiabatic walls, save for the open end of the resonance tube, which is modeled as a pressure inlet with ambient pressure ( $101325 Pa$ ). The equation of state used for the working gas is the ideal gas equation. With the boundary conditions established, this model is a good representation of the physical engine shown in Figure 4.

### 5.2.3 Simulation Settings

There are a variety of settings that must be established correctly in order for the simulation to be successful. The simulation is divided into two parts: first, a steady state simulation to find the initial condition of a pressure disturbance, and, secondly, an extensive transient simulation of the transition from this initially disturbed state to sustained pressure oscillations. For either case, the gas is modeled as an ideal gas. This equation of state is sufficient to capture the temperature dependence of the density. The governing equations for fluids as introduced in Equations 5.2, 5.6a, and 5.7 are only valid for laminar flows. The stack area in the present model has a very high surface to occupied volume ratio, with sharp inlet and outlet conditions, depending on flow direction. As a result, a non-linear flow field will develop. Various vortex structures develop throughout one cycle, as shown in experiments conducted by Berson et al. (138) and Mao et al. (139). These vortex structures have also been investigated numerically by Worlikar et al. (120; 121) and Zoontjens (115). It must be kept in mind, however, that these examples were taken from simulations of a single thermoacoustic couple that was excited using an oscillatory boundary condition (rather than thermally induced as in the present model of a TAE).

### 5.2.4 Modeling Turbulence

In order to incorporate turbulent flow, the governing equations have to account for chaotic velocity fluctuations in addition to a steady mean velocity, which is known as the Reynolds decomposition (111). The velocity is then described as  $u_{turb} = \mathbf{U} + \mathbf{u}'$ . Using the time averaged velocity and entering it in the x-component of the momentum equation yields:

$$\frac{\partial U}{\partial t} + \nabla \cdot (U\mathbf{U}) + \nabla \cdot (\overline{u'\mathbf{u}'}) = -\frac{1}{\rho} \frac{\partial P}{\partial x} + \nu \nabla \cdot (\nabla(U)) \quad (5.14)$$

The third term on the left hand side of Equation 5.14 represents a product of the fluctuating components of the velocity and thus a convective transfer of momentum (111). Expanded, these so-called Reynolds stresses result in:

$$\nabla \cdot (\overline{u'\mathbf{u}'}) = \frac{1}{\rho} \left[ \frac{\partial(\overline{\rho u'u'})}{\partial x} + \frac{\partial(\overline{\rho u'v'})}{\partial y} + \frac{\partial(\overline{\rho u'w'})}{\partial z} \right] \quad (5.15)$$

where  $\overline{\rho u'u'}$  represents a normal stress due to turbulence, and  $\overline{\rho u'v'}$  and  $\overline{\rho u'w'}$  represent shear stresses due to turbulence (111). In a similar fashion, the time averaged transport equation for a scalar variable (for example, temperature) written as  $\Phi = \overline{\Phi} + \varphi'$  contains new terms arising from turbulence:

$$\frac{\partial \Phi}{\partial t} + \nabla \cdot (\Phi \mathbf{U}) = \frac{1}{\rho} \nabla \cdot (\Gamma \nabla \Phi) + \left[ -\frac{\partial \overline{u'\varphi'}}{\partial x} - \frac{\partial \overline{v'\varphi'}}{\partial y} - \frac{\partial \overline{w'\varphi'}}{\partial z} \right] + S_\Phi \quad (5.16)$$

It is these additional terms in the momentum and energy equations that require special attention. Because they appear in these equations as a result of time averaging, these equations are known as the Reynolds-averaged Navier Stokes Equations (RANS). These additional terms are modeled with turbulence models, such as the  $k - \varepsilon$  model. Other common models are known as the:

- Mixing length model (0),
- Spalart-Allmaras model (1),
- $k - \omega$  model (2),
- Algebraic stress model (2), and
- Reynolds Stress model (7).

The number in parentheses refers to the number of additional transport equations that are solved during each iteration (the  $k - \varepsilon$  model also requires two additional equations to be solved) (111). In the present case of the thermoacoustic engine, the  $k - \varepsilon$  model is chosen to account for the turbulence. This model is chosen because it is the one used most widely and

is valid for a wide range of flows (140). The description of the model refers to the creation ( $k$ ) and dissipation ( $\varepsilon$ ) of turbulent kinetic energy. The two transport equations are (111):

$$\frac{\partial(\rho k)}{\partial t} + \nabla \cdot (\rho k(U)) = \nabla \cdot \left[ \frac{\mu_t}{\sigma_k} \nabla k \right] + 2\mu_t S_{ij} \cdot S_{ij} - \rho \varepsilon \quad (5.17a)$$

$$\frac{\partial(\rho \varepsilon)}{\partial t} + \nabla \cdot (\rho \varepsilon(U)) = \nabla \cdot \left[ \frac{\mu_t}{\sigma_\varepsilon} \nabla \varepsilon \right] + C_{1\varepsilon} \frac{\varepsilon}{k} 2\mu_t S_{ij} \cdot S_{ij} - C_{2\varepsilon} \rho \frac{\varepsilon^2}{k} \quad (5.17b)$$

These equations contain five adjustable constants. Their values are determined from experimental data. For the standard model, the values are (111):

$$C_\mu = 0.09 \quad \sigma_k = 1.00 \quad \sigma_\varepsilon = 1.3 \quad C_{1\varepsilon} = 1.44 \quad C_{2\varepsilon} = 1.92$$

The standard  $k - \varepsilon$  model also contains values for two additional constants, the energy and wall Prandtl numbers, respectively. These allow for an advanced description of the effect of buoyancy on the turbulence generation and are not considered important for the current model. In the current model, an extension of the standard  $k - \varepsilon$  model is used. The *realizable*  $k - \varepsilon$  model is a more recent development that improves the description of flows subject to large pressure gradients and recirculation. The associated constants are (141):

$$\sigma_k = 1.00 \quad \sigma_\varepsilon = 1.2 \quad C_{2\varepsilon} = 1.9 \quad (TDR Pr = 0.85 \quad TKE Pr = 0.85)$$

In the present model, the standard values are used for all model constants, including for both *TDR Pr* (Prandtl number corresponding to the turbulent dissipation rate) and *TKE Pr* (Prandtl number corresponding to the turbulent kinetic energy) (141).

### 5.2.5 Summary of Simulation Settings

In addition to the selection of a turbulence model and the appropriate model constants, there are several additional simulation controls that must be set. First, an appropriate solver should be selected. The expected range of Mach numbers does not require the model to account for compressible behavior, thus the pressure based solver (as opposed to the density based solver) can be chosen. This choice requires the use of the implicit scheme. As the flows in the thermoacoustic system are expected to be non-rotating, the absolute velocity formulation is used. The method for description of gradients is chosen to be the Green-Gauss node based, as it is the suggested method for use with meshes using triangular cells. In order to increase the accuracy of the velocity description in small fluid passages, the physical velocity is enabled in the porous formulation.

These simulation settings have proven to be very stable, with no convergence problems. The under-relaxation factors for all variables are thus kept at their default values. The discretization for all flow variables is chosen to be of second order for increased accuracy. Pressure is discretized with the PRESTO! scheme, as it yields the highest accuracy for flows in porous media. The PISO scheme is chosen for the pressure-velocity, because it allows for the highest accuracy in transient flows. In order to maintain similar settings between the steady and transient parts of the simulation, it is also chosen for the steady calculations (although it may not be necessary in this case, since the time savings that would result from using a lower order coupling are negligible when compared to the transient simulation). Tables 6 through 9 summarize all of the simulation settings. Each table includes a chosen value and its justification. The specific settings for the transient simulation are given further below in Table 10.

As mentioned above, the steady simulation was stable and was used to introduce a pressure disturbance and an initial flow field interacting with the heated walls. Below, the results of this steady simulation are discussed.

**5.2.5.1 Steady Simulation: Initializing the Pressure Disturbance** Numerical instabilities are not sufficient to prompt the thermoacoustic effect, so small pressure distur-

Table 6: Choices of simulation controls for the steady simulation: Solver

<b>Group</b>	<b>Choice</b>	<b>Justification (141)</b>
Solver	Pressure based	Non-compressible flow
Formulation	Implicit	Only choice
Velocity Formulation	Absolute	Used for non-rotating flows
Gradient Option	Green-Gauss Node Based	Increased accuracy for unstructured/triangular meshes
Porous Formulation	Physical Velocity	Improved description of velocity within small fluid passages

Table 7: Choices of simulation controls for the steady simulation: Solution Controls

<b>Group</b>	<b>Choice</b>	<b>Justification (141)</b>
Under-Relaxation Factors		
Pressure	0.3	Value for Pressure and Momentum must sum to 1
Density	1	Chosen to be as large as possible
Body Forces	1	Chosen to be as large as possible
Momentum	0.7	
Turbulent Kinetic Energy	0.8	Default
Turbulent Dissipation Rate	0.8	Default
Turbulent Viscosity	1	Chosen to be as large as possible
Energy	1	Chosen to be as large as possible

Table 8: Choices of simulation controls for the steady simulation: Discretization

<b>Group</b>	<b>Choice</b>	<b>Justification (141)</b>
Pressure-Velocity Coupling	PISO	Used for transient simulation and for consistency, also for the steady simulation
Pressure	PRESTO!	High Re flows, porous flows
Density	2 <sup>nd</sup> order upwind	Most accurate
Momentum	2 <sup>nd</sup> order upwind	Most accurate
Turbulent Kinetic Energy	2 <sup>nd</sup> order upwind	Most accurate
Turbulent Dissipation Rate	2 <sup>nd</sup> order upwind	Most accurate
Energy	2 <sup>nd</sup> order upwind	Most accurate

Table 9: Choices of simulation controls for the steady simulation: Initialization (all areas)

<b>Group</b>	<b>Choice</b>
Temperature	300 <i>K</i>
Velocities	0 m/s
(Gauge) Pressure	0 <i>Pa</i>
Turbulent Kinetic Energy	1 $m^2/s^2$
Turbulence Dissipation Rate	1 $m^2/s^3$

bance has to be introduced to the system. Thus, a positive 10  $Pa$  pressure inlet condition is applied at the “closed end” of the resonator. The simulation is then run to determine a steady state for this case. It results in non-zero values for the pressure and velocity distributions throughout the system, as well as initializes the temperature distribution in the stack area. Figures 56, 57, and 58 show the overall distribution of pressure, temperature, and velocity as well as a closeup of the stack area.

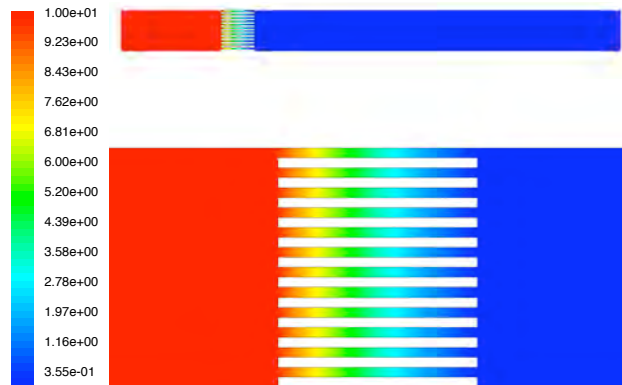


Figure 56: Initial Condition, Pressure [ $Pa$ ],  $0^\circ$  bending case

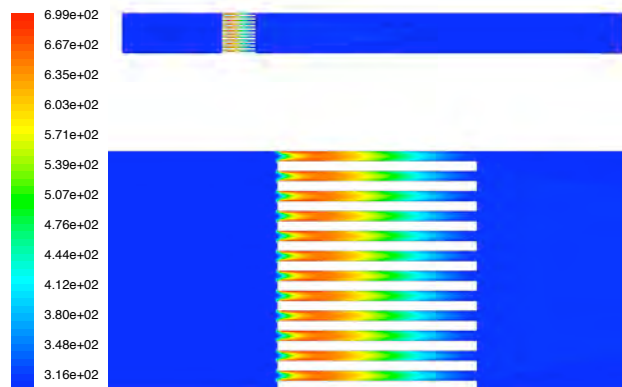


Figure 57: Initial Condition, Temperature [ $K$ ],  $0^\circ$  bending case

This initial condition shows a high pressure in the compliance and a sharp pressure drop across the stack. Also, a non-zero gas displacement is present inside the stack. With this

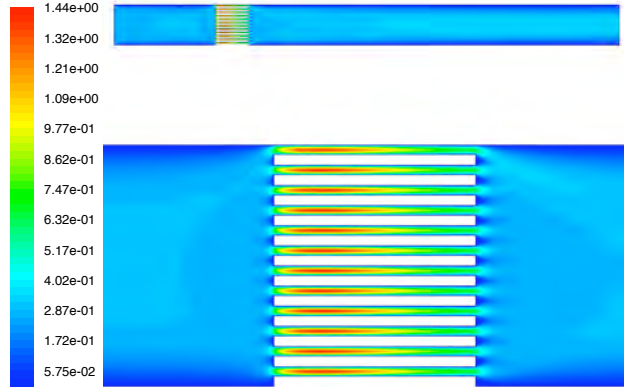


Figure 58: Initial Condition, Velocity [ $m/s$ ],  $0^\circ$  bending case

initial condition in place, it was possible to replicate the thermoacoustic effect indicated by strong pressure oscillations in the resonator.

**5.2.5.2 Transient Simulation: Transition to Sustained Oscillations** Most factors from the steady state simulation carry over to the transient case. In addition, of course, values for the time dependent simulation settings have to be chosen. Most settings were kept constant from the steady simulations. For the transient part, settings relevant to the time advancement are discussed. The transient solver was chosen to be first order implicit, since using a higher order was determined to be unnecessary. The time steps were chosen to be constant. In theory, Fluent determines whether the time step used can be increased in order to simulate processes more quickly. However, in light of post-processing many different cases, the time steps were chosen to be the same for all cases; specifically, the time step is chosen to be  $10\mu s$ . As discussed below, this resulted in approximately 160 time steps per period of oscillation. The default value of 20 iterations was used per time step. This value was sufficiently large to allow convergence for each time step, and small enough to allow for quick advancement of time steps. As with the steady simulation setting, Table 10 provides a summary of the settings specific to the transient simulation.

Table 10: Extension of solution controls for steady solution to include controls for the transient simulation.

<b>Group</b>	<b>Choice</b>	<b>Justification (141)</b>
<i>Solver</i>		
Unsteady formulation	1 <sup>st</sup> order implicit	Higher order not necessary for accuracy
<i>Iteration</i>		
Time stepping method	Fixed	Post processing $\neq$ function of time step
Time step	$1 \cdot 10^{-5} s$	Much less than the oscillation period
Max. iteration/time step	20	Default, <i>sufficient to achieve convergence each time step</i>

The simulation successfully replicates the amplification of pressure waves sustained in the resonator. If the length of the resonator is used to calculate the expected frequency of these oscillations, we reach a value of  $580Hz$ :

$$L = 0.15m = \frac{\lambda}{4} \rightarrow \lambda = 0.6m$$

$$\rightarrow f = \frac{c}{\lambda} = \frac{350m/s}{0.6m} = 580s^{-1} = 580Hz$$

where  $c$  is the speed of sound. Of course, we can also analyze the data from the simulation. Measuring the distance between peaks of the pressure plot, this results in a period of  $\tau^* = 163$  timesteps, or  $\tau = 1.63\mu s$ . The inverse of this period length is the frequency, thus

$$\frac{1}{\tau} = f = 614 Hz \quad (5.18)$$

This frequency is not exactly equal to the previously estimated value, but this is due to the assumption of constant speeds of sound of  $350 m/s$ . Figure 59 illustrates a section of the oscillations attained by the simulation in Fluent (112). It shows the transition from amplification to a steady state over the course of 60,000 timesteps or 0.6 seconds. The final amplitude is approximately  $5125Pa$ , which corresponds to an sound intensity of  $168dB$ . These values are very high considering the simple design of the engine. However, this simulation did not consider any loss mechanisms (such as heat fluxes through the walls). Therefore, it is not surprising to achieve high sound levels. During the steady state, energy is dissipated by turbulence generation and also through the open end.

Another interesting insight is gained by the temperature contours in the compliance and stack section of the engine. The time step corresponds to a flowfield where the x-velocity is negative (i.e. into the compliance) which explains the convective transport of hot gas away from the stack into the compliance, as shown in Figure 60. We can see that the temperature distribution in the stack area remained constant after initialization with the UDF. This corresponds to a constant heating behavior.

With the initial simulation successfully completed, a discussion of the influence of all boundary conditions, especially the dependence of the solution on the grid properties follows in the next section.

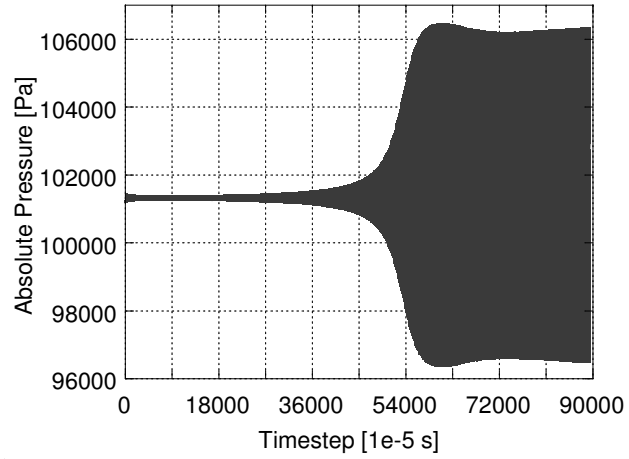


Figure 59: First replication of thermoacoustic oscillations, transitioning from amplification to approaching a steady state (called the limit cycle by Hanschke et al.)

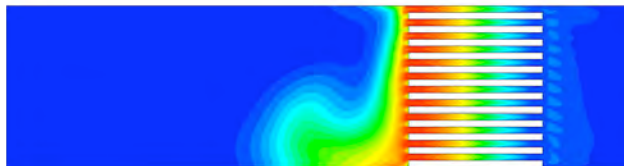


Figure 60: Temperature contours in the compliance and stack (ranging from  $700K$  to  $300K$ ). The hot gas is streaming through the stack into the compliance.

## 5.3 SENSITIVITY ANALYSIS

As mentioned before, the simulation data was collected with a certain set of boundary conditions. The transition from a given pressure disturbance to a state of strong sustained pressure oscillations inside the engine compliance was shown successfully. Of course, this solution may depend on the simulation conditions as given below:

- Grid design,
- Temperature boundary condition,
- The heat transfer coefficient between the stack walls and the fluid, and
- Initial pressure disturbance.

### 5.3.1 Solution Dependence on the Grid Properties

The immediate tradeoff between cell size and computation time is obvious. The more times the constitutive equations have to be solved per iteration, the longer the entire simulation process will take. Utilizing a coarse grid will introduce numerical inaccuracies. On the other hand, it must be ruled out that it is these numerical errors that cause the oscillations and illustrate the effect of cell density on the magnitude. Four different meshes were developed for the straight resonator. As the CFD analysis is designed to investigate the effect of curvature, the difference between differently curved resonators is shown as well. Section 6.3 below will illustrate the details on the new grids and the complete set of results. Table 11 shows the achieved pressure amplitude and frequency from various meshes (and a straight resonator). Also, the CPU time to achieve the sustained oscillations is noted. The coarsest mesh with only 15,000 cells does not achieve oscillations. The next refinement achieves oscillations at a frequency of 614  $Hz$  and a pressure amplitude of 5,219  $Pa$ . Further refinement leads to a decrease in pressure amplitude but the frequency is constant throughout. The difference between the 120,000 cell grid and the 190,000 cell grid is much smaller than between the 36,000 cell grid and the 120,000 cell grid. Mesh independence (with an error of  $\approx 3\%$ ) is thus achieved at 120,000 cells.

Table 11: Frequency  $f$  and final pressure amplitude  $\Delta p$  depending on grid properties, for a straight resonator

Cell Count	$f$ [Hz]	$\Delta p$ [Pa]	CPU Time [days]
15,000	0	0	1
36,000	614	5219	2
120,000	614	4068	8
190,000	614	3962	15

Obviously, the grid coarseness at 36,000 cells influences the replication of the thermoacoustic effect. However, the penalty of CPU time with increased cell densities is significant. For this reason, it is feasible to use the coarse grid for data collection and qualitative conclusions. In order to verify the validity of this assumption, it must be shown that the effect of resonator curvature is captured equally by the coarse mesh and the fine mesh. Figure 61 shows the normalized pressure amplitudes achieved by a TAE with differently curved resonators. As shown in the table above, the absolute amplitudes vary significantly. When normalized with respect to the maximum pressure amplitude for each case, the behavior pressure behavior is shown to be similar for both types of grid. The maximum error is less than 1%. Thus, the following results from the simulations are taken from the coarse grid in order to minimize calculation time.

### 5.3.2 Solution Dependence on the Temperature Boundary Conditions

Experimentation on the TAE has shown that an increase in hot side temperature yields an increase in the sound output. Of course, the more heat energy is supplied to the system, the more of it can be converted into sound energy (of course, the thermal losses also increase). The following simulations are based on boundary conditions that yielded oscillations during experimentation. For this reason, the temperature profile that was applied to the stack

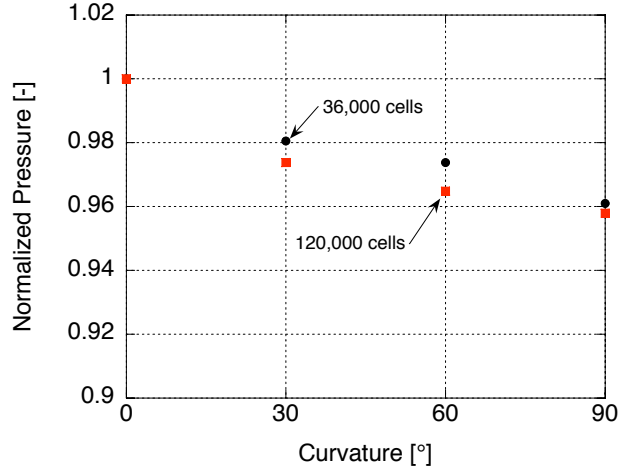


Figure 61: Illustration of the difference in pressure amplitude between the various curved resonator geometries.

in the simulation model ranged from 700  $K$  to ambient temperature at 300  $K$ . In order to show the influence of this choice, additional simulations were set up that used different temperature ranges. This was implemented by varying the UDF and, consequently, the function shown in Equation 5.12. Figure 62 shows how the oscillations are affected by a change in hot side temperature. When a temperature difference of only 600  $K$  is applied, the energy supply is not sufficient to cause the thermoacoustic effect. This threshold is also known from experiments (although not necessarily at 600  $K$ ). As expected, when applying 800  $K$  as the hot side temperature, the oscillations increase. For all remaining simulations, the hot side temperature was chosen to be 700  $K$ .

### 5.3.3 Solution Dependence on the Heat Transfer Coefficient

The heat transfer coefficient defined on the wall is what drives the energy transfer between the walls and the fluid, thus it is responsible for creating the strong oscillations. The value used for the simulation described above was derived in Section 5.2.2. As this property determines the heat exchange between the gas and wall, it must be expected that a variation of the

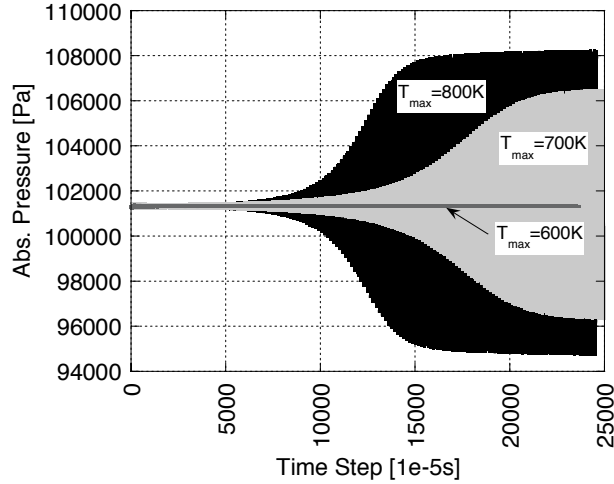


Figure 62: Sensitivity of the solution to the prescribed temperature profile, hot side temperatures of 800 K, 700 K, and 600 K. The cold side is constant at 300 K

heat transfer coefficient affects the magnitude of oscillations. As was shown in Figure 55, the chosen value is actually on the lower end of heat transfer coefficients we could expect to see in oscillatory flows. A simulation based on the straight resonator and coarse grid ( $\approx 30,000$  cells) was used as a basis for the comparison of different heat transfer coefficients. It was found that the influence of this parameter is minimal. Table 12 shows the change in pressure amplitude in the established case of oscillation for both checked heat transfer coefficient values. The change is very small, and the influence on the other flow parameters is assumed to be negligible.

#### 5.3.4 Solution Dependence on the Initial Pressure Disturbance

In order to cause thermoacoustic oscillations, an initial pressure disturbance is applied to a steady simulation. In order to show the influence of this initial pressure disturbance on the representation of the thermoacoustic effect, a variation of this disturbance was performed for a TAE with a straight resonator.

Table 12: Maximum pressure amplitude achieved and deviation from the standard case ( $h = 50 \text{ W/m}^2\text{K}$ ) as a function of the heat transfer coefficient between the gas and wall in the stack

$h$ [ $\text{W/m}^2\text{K}$ ]	$\Delta p_{\max}$ [Pa]	$\Delta p_{\text{HTC}}$ [Pa]
25	5103	-6
50	5109	<i>base case</i>
100	5127	18

The first difference that can be noted as a result of various initial disturbances is the behavior during the steady simulations. The higher the initial pressure disturbance, the longer the simulations require to achieve a steady state. Also, the transition between the initial condition and thermoacoustic oscillations is also affected by the difference in pressure disturbance. Each case exhibits an initial decrease in pressure amplitude at the start of the transient simulation. When showing the same total time period for each initial pressure disturbance, it can be seen that the lowest value used ( $1 \text{ Pa}$ ) results in a very small final amplitude. This initial disturbance is not sufficient to result in a good representation of the thermoacoustic effect. Figure 63 shows the behavior of the compliance pressure resulting from five different initial pressure disturbances. The shapes of all curves are similar, but (as expected) the amplitude of these early oscillations are different between each case.

When the initial disturbance is increased to  $5 \text{ Pa}$  and beyond, on the other hand, thermoacoustic oscillations are achieved. After the initial decrease, the pressure amplitude increases significantly after approximately 10,000 timesteps. This sharp increase occurs later for initial pressure disturbances larger than  $10 \text{ Pa}$ . For the time period investigated (0.3 seconds) the resulting pressure amplitudes and frequencies are shown in Table 13.

The final amplitudes for  $5 \text{ Pa}$  and  $10 \text{ Pa}$  are very similar. A further increase shows a decrease in the final amplitude, and, more importantly, a significant delay of the establishment of thermoacoustic oscillations. Since the initial disturbance of  $10 \text{ Pa}$  yields the quickest

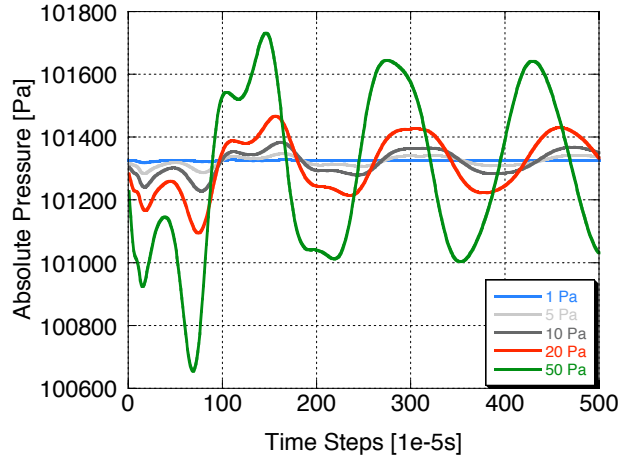


Figure 63: Transition behavior as a result of different initial pressure disturbances

Table 13: Final state of oscillations, frequency  $f$ , final pressure amplitude  $\Delta p$ , as a result of various initial pressure disturbances  $\Delta p_0$

$\Delta p_0$ [Pa]	$f$ [Hz]	$\Delta p$ [Pa]
1	614	< 5
5	614	5290
10	614	5131
20	614	4649

transition to thermoacoustic oscillations and is thus chosen as the initial disturbance for the following cases. Again, since the solution does depend on the initial condition, the qualitative nature of the results presented below must be emphasized again.

## 6.0 RESULTS OF THE CFD ANALYSIS

The results presented above prove that Fluent is capable of simulating the operation of a thermoacoustic device. Below, detailed findings for several TAE designs are outlined. First, results from the conventional straight resonator will be shown. This will allow for a baseline for this type of analysis. Following these basic results, a comparison of several different cases of curved resonators will be discussed.

### 6.1 VISUALIZATION METHODOLOGY

The model for this case has been extensively introduced above. Also, the transition from the small pressure disturbance to the strong sustained oscillations has been discussed. Now, all pertaining variables will be investigated in detail. First, the methodology for the visualization of all relevant data will be discussed. Of course, the main purpose of this work is to compare the behavior of a thermoacoustic engine under the effect of different resonator shapes. The flow variables of primary concern are the pressure, velocity, temperature, and Reynolds number. It must be expected that the behavior of each variable changes throughout the stack as well as across a flow channel (i.e. close to the wall or mid channel). For this reason, data was collected at numerous locations throughout the stack, in the center of a channel as well as close to a wall. Figure 64 illustrates the location and distribution of said data probe points in the model.

The transition from the initial disturbance to sustained oscillations required a large range of time steps. In order to illustrate the thermoacoustic effect in detail as well as for a comparison between different resonator geometries, data from a single period for each case is

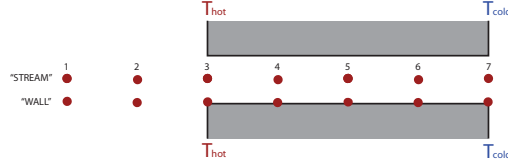


Figure 64: Illustration of the probe points along the stack. 10 points are located along the interior of the stack, 4 points outside the stack towards the compliance and 4 points outside of the stack towards the open end. Half of the points are located along the center of a channel, the other half are located near the wall.

sufficient. For this reason, all data shown below are extracted after strong oscillations were established. This time was chosen to be 0.3 seconds or 30,000 timesteps. From this time forward, a transient simulation was performed for the duration of one period, using the same timestep ( $\Delta t = 1 \cdot 10^{-5} s$ ) as before. From these separate simulations, data was extracted at the probe locations discussed above. As a first step, the information gained is interpreted for each variable individually. This way, the influence of the stack on the various parameters can be easily illustrated.

In addition, when discussing the thermoacoustic effect in general, it is more useful to perform a direct comparison between all three flow variables, as magnitudes are of less importance than phase and other oscillatory behavior. This is achieved by a normalization of each variable and plotting this information in the same graph. This normalization is not necessary when comparing differently curved resonators. Here, a direct comparison of all variables is once again more useful. Finally, as a benefit of a CFD analysis, a visualization of the entire flow field is also possible (and useful, to gain insights into fluid behavior that may otherwise not be possible). In accordance with these analysis approaches, this chapter is divided into the following sections:

- Individual variables in order to highlight in influence of the stack on the fluid behavior,

- Normalized variables in order to illustrate the thermoacoustic effect and compare behavior differences between mid-channel and close to the wall,
- Individual variables illustrating the effect of curvature, and
- Visualizing the entire flow field.

As an additional analysis, we can also

- Compare the pressure distribution as it occurs in a thermoacoustic engine to the theoretical free field distribution.

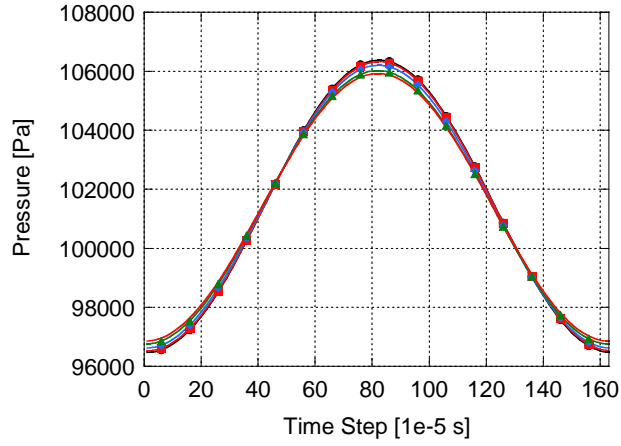
## 6.2 INVESTIGATING THE THERMOACOUSTIC EFFECT

First, the individual data taken from the simulation of the straight resonator is characterized and interpreted.

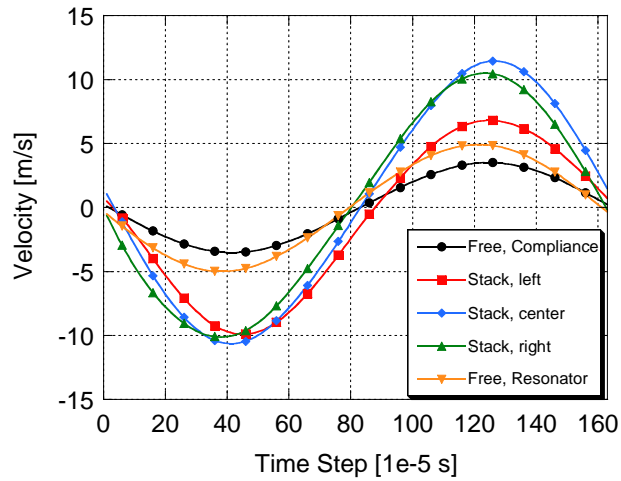
### 6.2.1 Individual Data Plots

This information is used to illustrate the thermoacoustic effect in more detail than it has been described before. Figure 65 shows the basic flow variables of pressure, temperature, and velocity taken from the channel center location, outside of the stack (compliance side), hot side, center, cold side, outside of the stack (resonator) (Probes 1,3,5,7, and 9 in Figure 64).

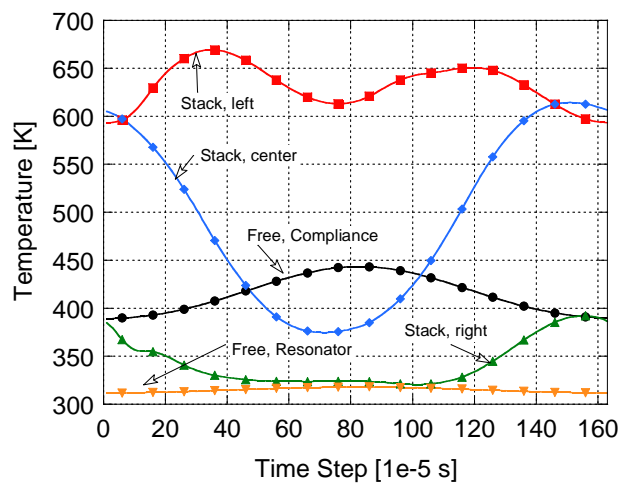
The pressure amplitude changes very little along the stack, as shown in Figure 65 (a). This is consistent with the variation of the pressure amplitude relative to the pressure antinode (again, the closed end of the engine is the pressure antinode, the open end is the pressure node). There is very little variation between measurement locations. As expected with a quarter-wave design, the maximum pressure amplitude is located at the hot end of the stack, with the amplitude decreasing steadily throughout the stack. Obviously, the amplitude would reach zero at the open end. The first impression of this pressure behavior is that the stack does not influence the pressure distribution that we would expect from a standing wave in the free field. A comparison between the theoretical free-field distribution and the data taken from the simulation is given below in Section 6.6 on page 177.



(a) Pressure



(b) Velocity



(c) Temperature

Figure 65: Pressure, velocity, and temperature measured in the center/stream location, straight resonator.

The velocity component of the wave is influenced by the stack more significantly than the pressure component. The magnitude of the oscillation over the course of one period changes more drastically between probe locations. The velocity in the open areas outside of the stack should be the lowest, and the data shown in Figure 65 (b) confirms this expectation. Also, the velocity is strictly sinusoidal, which is consistent with the expectations of the velocity in a free standing wave and also the numerical findings by Marx et al. (126). The first observation is that the maximum in velocity is achieved at different times throughout the stack. The highest overall velocity amplitude is achieved in the center position of the stack. The magnitude of the velocity is very high, but when comparing it with measurements by Mao et al. (139) (maximum velocity of  $\approx 3.5$  m/s at a drive ratio of 1%), the results are not unreasonable (at the present drive ratio of approximately 6%). In addition, we see that the displacement peaks (zero velocity) are not reached simultaneously at all locations, which is consistent with the phase difference in the velocity maxima and minima. Also, the magnitude of the velocity shown here confirms the assumption on incompressibility of the gas made above in Section 5.1.1. The velocity is always much lower than the speed of sound of the gas (which is on the order of 350 m/s), thus the Mach number in the domain is much less than 1, which allows us to model the gas as incompressible.

Figure 65 (c), finally, shows the temperature distribution at the same probe location. The individual plots show that the temperature is heavily influenced by the stack. The temperature behavior changes drastically in the center location between probe locations. In accordance with the highest velocity at probe 5, the temperature oscillation is also strongest there. The convective influence introduces large volumes of cold gas and hot gas in each half of the cycle. The wall temperature at this location is 500 K, and it appears that the oscillation is symmetric about this value. The amplitude of the temperature oscillation at either end of the stack is much lower than at the center location.

It is noteworthy that the hot side temperature has two peaks over the course of one period. This behavior is due to the superposition of convective heat transport and a temperature change as a result of gas compression. The second peak, coinciding with the positive displacement, is due to convective transport of heated gas towards this probe location. The first peak, however, occurs during negative displacement. At this time, colder gas is trans-

ported to the probe location, which should result in a temperature decrease. It must be noted that at this time, the pressure increases and thus the gas is compressed.

Finally, the temperature in the resonator, away from the stack's cold side (position 9), is nearly constant. This shows that the convective influence there is minimal. On the opposite side, the temperature changes slightly, with an amplitude of approximately 30  $K$ . This probe location is clearly at the far end of the region where the convective transport of heat occurs.

### 6.2.2 Direct Comparison of Velocity, Temperature, Pressure, and Wall Heat Transfer

In order to incorporate the relevant variables into one plot, in order to usefully analyze their interrelated effects, pressure, velocity and temperature must be normalized, as the magnitudes for each variable differ significantly. This data is taken from a simulation of the straight resonator after 30,000 timesteps. The most meaningful approach to normalizing each variable is given below:

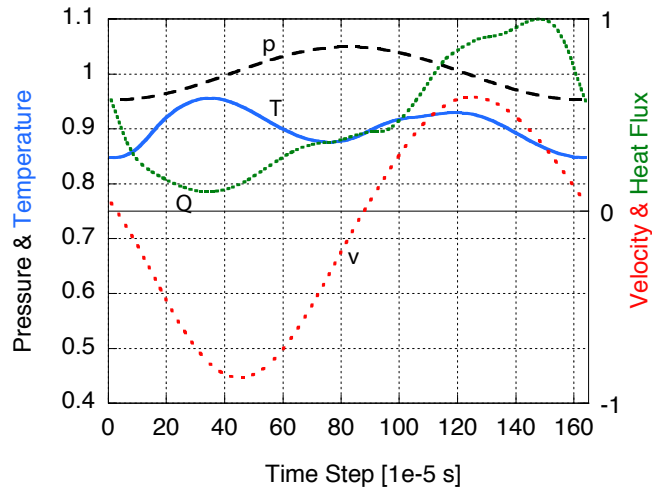
$$\begin{aligned}\bar{p} &= \frac{p}{p_{atm}} \frac{p}{101325 \text{ Pa}} \\ \bar{v} &= \frac{v}{\max\{v_{max}(pos. 1, pos. 2, \dots, pos. 9)\}} = \frac{v}{v_{max}(pos. 5)} \\ \bar{T} &= \frac{T}{T_{hot}} = \frac{T}{700 \text{ K}} \\ \bar{Q} &= \frac{Q}{|Q_{max}|}\end{aligned}$$

Figure 66 shows the normalized pressure, velocity, and temperature for the center channel location for three axial positions (hot side, center and cold side). The heat flux data is taken from the wall opposite each previously mentioned probe point. Since the pressure is normalized with respect to its ambient value, the plot oscillates around 1. There is no obvious variation between the different probe locations throughout the stream. The velocity is normalized with respect to the highest value *overall*, which is why the velocity reaches a value of 1 in the center plot, but not in the other two plots, showing data for the hot side and cold side, respectively. The temperature is shown relative to the highest occurring

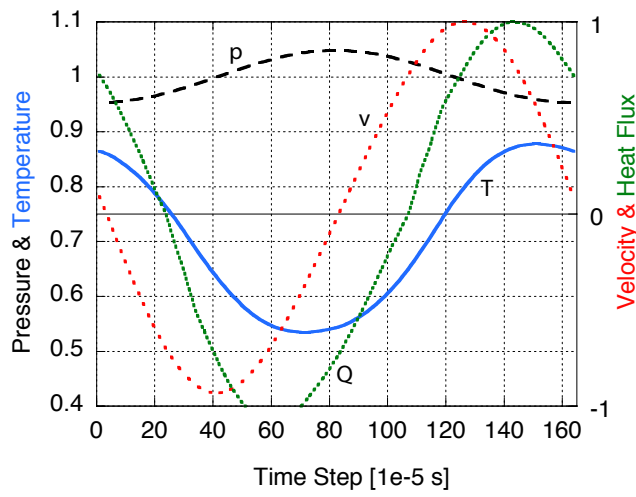
temperature in the domain, which is  $700\text{ K}$ , and so always falls between 0 and 1. Finally, the heat flux is normalized with respect to the absolute highest value occurring at each location. For this reason, each plot reaches a (absolute) value of 1. It must be kept in mind that the plots show the heat transfer from the wall to the gas. The wall temperature at the hot end is always higher than the gas, so  $Q > 0$ , but at the cold end, the wall is always colder than the gas, which is why  $Q < 0$ . At the center location,  $-1 < Q < 1$  because the gas temperature varies strongly enough that it is both higher and lower than the wall temperature throughout the cycle. Piccolo et al. have conducted a numerical investigation in the of the time averaged heat flux along a stack surface (130). They compared their findings with other numerical investigations literature (119; 124). The main findings are in alignment with the findings presented here; the time averaged heat flux (from wall to gas) is greater than 0 at the hot end, less than 0 at the cold end, and equal to zero in between.

In general the following conclusions about the behavior of the individual flow variables can be drawn:

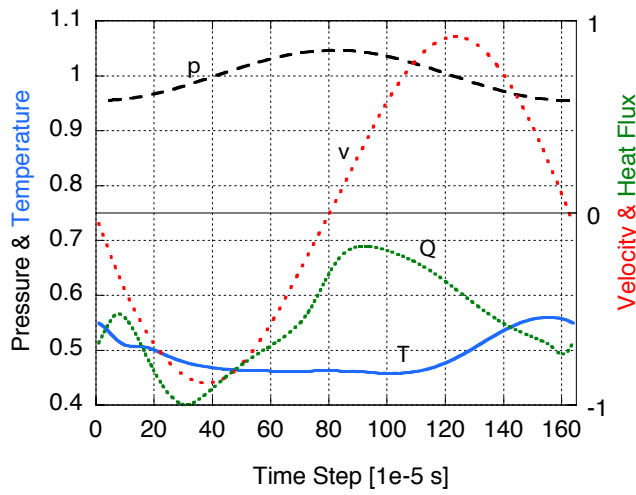
- The heat flux follows the velocity component closely. This shows that the heat transfer is driven by convection. The center location exhibits the largest delay between heat flux and velocity.
- There is very little influence of the pressure on the temperature behavior in the stream. Again, the temperature is dominated by convection.
- The plots of the variables in the center location exhibit linear behavior. As with the other locations shown, the pressure is sinusoidal. But in the center location, pressure, velocity, and heat flux also show sinusoidal behavior. Hydrodynamic entry effects are not present.
- Both the hot and cold side location exhibit hydrodynamic entry effects that are shown in the heat flux and temperature. The behavior deviates from a strictly sinusoidal behavior. This effect has been explained with numerical studies by Zoontjens (115), Marx et al. (126), Besnoin et al (123). These temperature non-linearities are caused by the heat transfer between the solid and gas at the stack edges. The mean heat transfer in the center of the stack is zero, which corresponds to Marx et al. and illustrates the “critical stack length” where non-linearities occur, which is determined to be roughly



(a) Hot Side



(b) Center



(c) Cold Side

Figure 66: Normalized Pressure, Velocity, Temperature, and Heat Flux (stream probes 3, 5, and 7)

four times the particle displacement (128). Gusev also concluded that the additional temperature harmonics are caused by a non-linear convection term only present at the stack edges (142).

- Hot side: During positive displacement ( $t >$  time step 90), gas enters the stack from the free field. As the gas enters, the temperature increases. As the velocity approaches its maximum, the rate of change for both the heat flux and the temperature decreases, which is shown in the flatter curves.
- Hot side: The lowest value of heat transfer occurs a few time steps after the reversal in the flow direction, changing from positive to negative. At this point, entry effects have caused the difference between the wall and free stream temperature to be at its smallest value.
- Cold side: During negative displacement ( $t <$  time step 80), gas from the resonator side of the stack is displaced into the stack. This gas is near the wall temperature, so the heat transfer is decreasing. At the highest *negative* velocity, the decrease of heat transfer occurs more rapidly than a sinusoidal behavior. As the velocity decreases, the heat transfer decreases as well.
- Cold side: The heat transfer assumes its worst value after a flow reversal from negative to positive. This is a similar effect that occurs at the hot side, since entry effects have forced the temperature difference between the wall and channel center to be at its lowest value.
- During positive displacement,  $t >$  timestep 80, the heat transfer from the fluid to the gas is enhanced, as the effect of convection is enhanced by increasing velocity. Gas from the hotter regions of the stack is introduced into the cold end.
- At the end of the cycle, a superposition of the pressure effect is noticeable. As the pressure reaches a minimum, the gas is cooled by expansion, as well as due to the diminished influence of convection. This is noticeable here because the absolute temperature level is much lower than anywhere else in the domain.
- In the center location, the highest temperature occurs before the positive displacement is complete. At the same time, the pressure is decreased below ambient, so this early decrease in temperature may be attributed to a cooling through expansion.

- The temperature levels reached in the center location ( $\bar{T}_{max} \approx 0.88$  and  $\bar{T}_{min} \approx 0.54$ ) do not correspond to the highest temperature at the hot end and the coldest temperature that occurs at the cold end, respectively. This implies that the displacement of the gas is less than the distance between these probe locations.

Again, the heat flux data discussed above was taken from the wall opposite each probe point that was used for pressure, velocity and temperature. This implied that there was a temperature difference between the wall and the channel center, which is the driving force behind convective heat transfer (which, as was identified, is the dominant mechanism). Below, the difference in the behavior of the pressure, velocity, and temperature will be discussed.

### 6.2.3 Comparing Flow Variables between Channel Center and Wall

Figure 67 illustrates the comparison between the behaviors of flow variables in the free stream and close to the wall. This data is taken at the hot end. Part (a) contains the same information as Figure 66 (a), but it is scaled differently as to allow a meaningful comparison with the data taken from the wall. Also note that the right-hand axes are scaled differently in part (a) and (b). Both velocity components are scaled with respect to the maximum velocity in the free stream. As expected, the velocity near the wall is significantly smaller than in the free stream.

The following can be observed when comparing wall and channel center behavior.

- The temperature level is higher at the wall than in the center of the channel. This is expected as the gas at the wall reaches the wall temperature, which is 700 *K*.
- The influence of the velocity is diminished at the wall. Obviously, close to the wall, the velocity is much less than in the center of the channel. As a result, the influence of gas displacement is diminished.
- The temperature variation is smaller at the wall than in the channel.
- After approximately 60 time steps, the wall temperature is constant for about 40 time steps. At this time, the gas displacement is negative, introducing colder gas to the

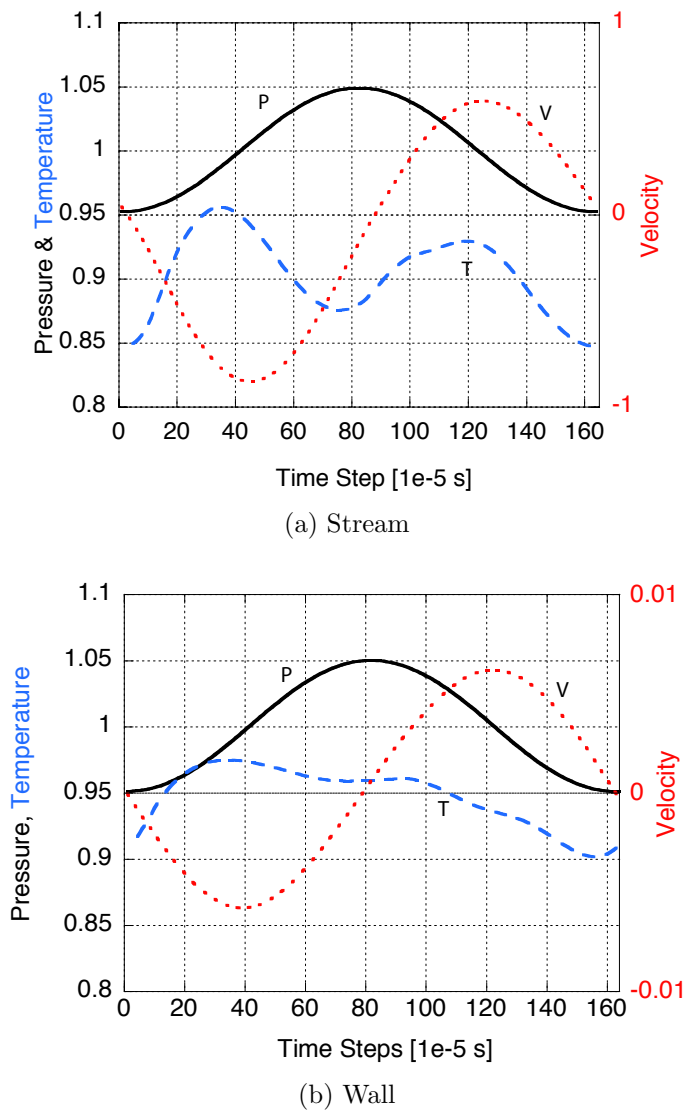


Figure 67: Comparison between free stream and wall temperature, pressure, and velocity behavior at the hot end of the stack revealing the influence of pressure on the temperature change.

hot side probe point. However, as the effect of convection is very small, the increasing pressure causes the temperature to be nearly constant.

- During positive displacement and decreasing pressure, the temperature decreases. Again, this is dominated by the gas expansion.
- As the pressure starts increasing again and the flow direction reverses from positive to negative (at the end of the period shown) the temperature starts to rise.
- Finally, it is noteworthy that the maximum and minimum temperature values are reached earlier at the wall than in the center of the channel.

### 6.3 THE EFFECT OF RESONATOR CURVATURE

The previous section was concerned with the behavior of a gas inside a stack of a simple thermoacoustic engine. As a means to decrease the footprint of such devices, it was proposed to introduce curvature to the resonator instead of solely utilizing straight designs. The usefulness of this modification was discussed in Section 1.3.1. Continuing in the same approach as introduced for the straight resonator, the pressure, velocity, and temperature behavior are now shown for the curved resonator cases. In addition, the Reynolds number, as well as a comparison of the instantaneous heat transfer and total energy transfer between the different curvature cases is shown. This will allow us to draw a quantitative conclusion about the influence of curvature.

#### 6.3.1 Development of new Grids

In addition to the initial “straight” case, three differently curved geometries were modeled. The resonator was curved to three different degrees over a length of 80 *mm*, measured from the open end. This implies that the stack geometry is not influenced, as are the boundary conditions that are imposed there. The mesh was built in such way that the number of cells was as close to identical as possible. Table 14 shows the actual numbers of nodes and cells for each of the four cases. In conjunction with identical boundary conditions, the different

behaviors in the flow variables can be considered a result of the curvature, and not because of discrepancies in simulation settings. Figure 68 shows the four grids superimposed on each other. The differently bent geometries are illustrated.

Table 14: Number of cells and nodes for each of the simulated cases of curvature.

Curvature	Number of Cells	Number of Nodes
0°	36,220	55,603
30°	36,348	55,795
60°	36,356	55,810
90°	36,330	55,768



Figure 68: Illustration of the differently bent resonators (0°, 30°, 60°, 90°)

As introduced in Section 6, each sample is taken over the course of one period starting from an established case (after approximately 30,000 time steps). In order to provide a useful comparison, the data is plotted so that the peaks of each variable coincide. Because of the long calculation time, each case does not result in perfectly coinciding plots of pressure, velocity, and temperature. Using the compliance pressure for each case as a reference, the simulation was run for the duration of two periods. All data was sampled at the aforementioned probe points. In addition, the compliance pressure as well as the integral value of the heat flux on the horizontal surfaces in the stack was extracted. In order to present the data

so that the peaks coincide, only one period of data was plotted, beginning with the time step where each case exhibited a minimum in the compliance pressure. A script was written to identify this minimum for each case and then to note the index (i.e. timestep) where this minimum occurs. This value was then used as a starting point to extract data from all other variables. Figure 69 details this process for clarification.

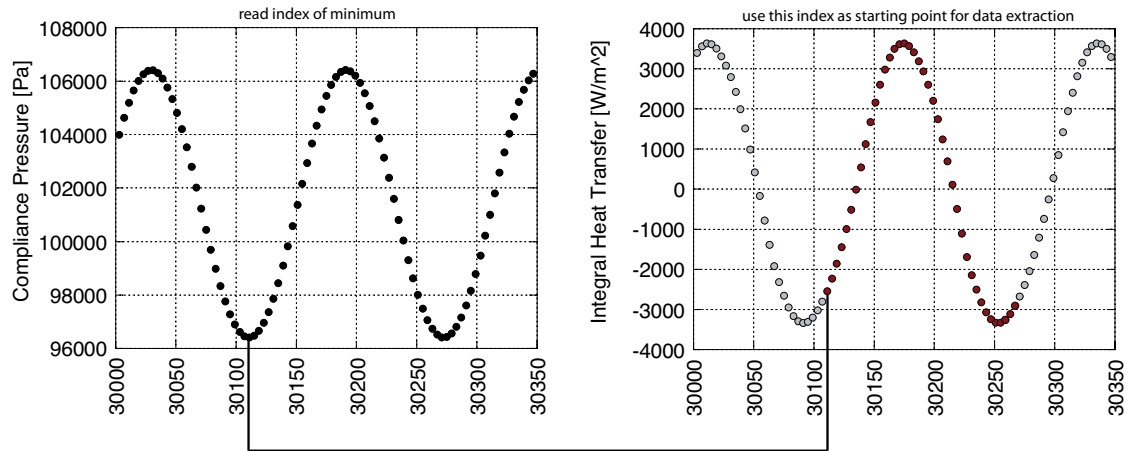


Figure 69: Illustration of the collection of data relative to the minimum of the compliance pressure (after 30000 timesteps)

### 6.3.2 Pressure

First, comparing the pressure distribution of each case, the influence of curvature is obvious. As the curvature increases, the amplitude of the oscillations decreases. Table 15 provides an overview of the effect of curvature on the pressure. The data is shown for the average nodal values of the vertical wall in the compliance (which is the pressure antinode). Consequently, the pressure values shown represent the highest pressures in the system. Figure 70 contains the same information in graphical form.

The total decrease in pressure amplitude is 200 Pa or 3.83%. It is noteworthy that the sharpest decrease in amplitude is due to the initial introduction of curvature, and that the change in amplitude between 30° and 60° is significantly less than a further increase to 90°.

Table 15: Pressure evaluation for four different cases of resonator curvature (data corresponds with plots shown in Figure 70)

Case	$p_{\max}$ [Pa]	$\Delta p$ [Pa]	SPL [dB]
0°	106544	5219	165.33
30°	106442	5117	165.14
60°	106407	5082	165.11
90°	106341	5016	164.99

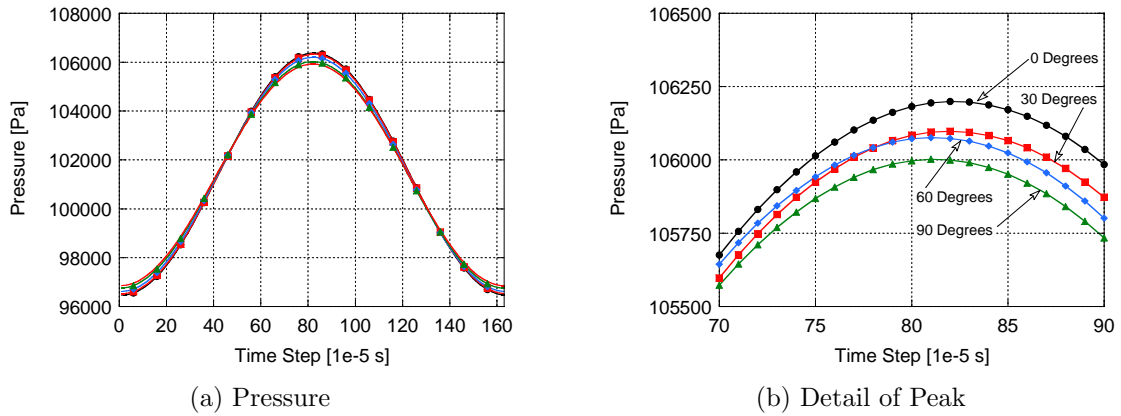


Figure 70: Comparison of pressure behavior under the influence of different degrees of resonator curvature.

### 6.3.3 Velocity

In addition to the pressure, the velocity component of the wave must be investigated. It was shown above that the velocity (in axial direction) is largest at the center position of the stack. Of course, for a standing wave in the free field, it is largest at the pressure node (in this case the open end). Figure 71 illustrates the behavior of the velocity. First, it can be noted that the velocity magnitude is rather large, and that it is different between the positive direction and the negative direction. In addition, and as expected from the previous investigation into the pressure behavior, the magnitude decreases as the bending degree increases. Table 16 contains the (absolute) values for both velocity peaks. This data will ultimately be plotted as a function of bending radius and its behavior compared to the behavior of the other variables under the influence of curvature.

Table 16: Values of the velocity at negative and positive peaks (basis for functional correlation between velocity amplitude and curvature)

Case	neg. Peak [m/s]	pos. Peak [m/s]	% Change[neg/pos]
0°	10.65	11.95	0/0
30°	10.5	11.26	-1.41/ - 5.77
60°	10.45	11.22	-1.88/6.11
90°	10.3	11.05	-4.67/ - 7.53

In addition to the comparison of the individual cases of curvature, it is also important to compare the engine behavior with a standing wave in the free field. It has been implied before that we must expect the stack to interfere with the free field behavior of the wave; this next investigation highlights this difference. Following the similar format as used for the pressure in Equation 6.10, and assuming a zero net velocity, the free field velocity can be described by:

$$u(x) = u_{max} \sin\left(\frac{x}{\lambda}2\pi\right) \quad (6.1)$$

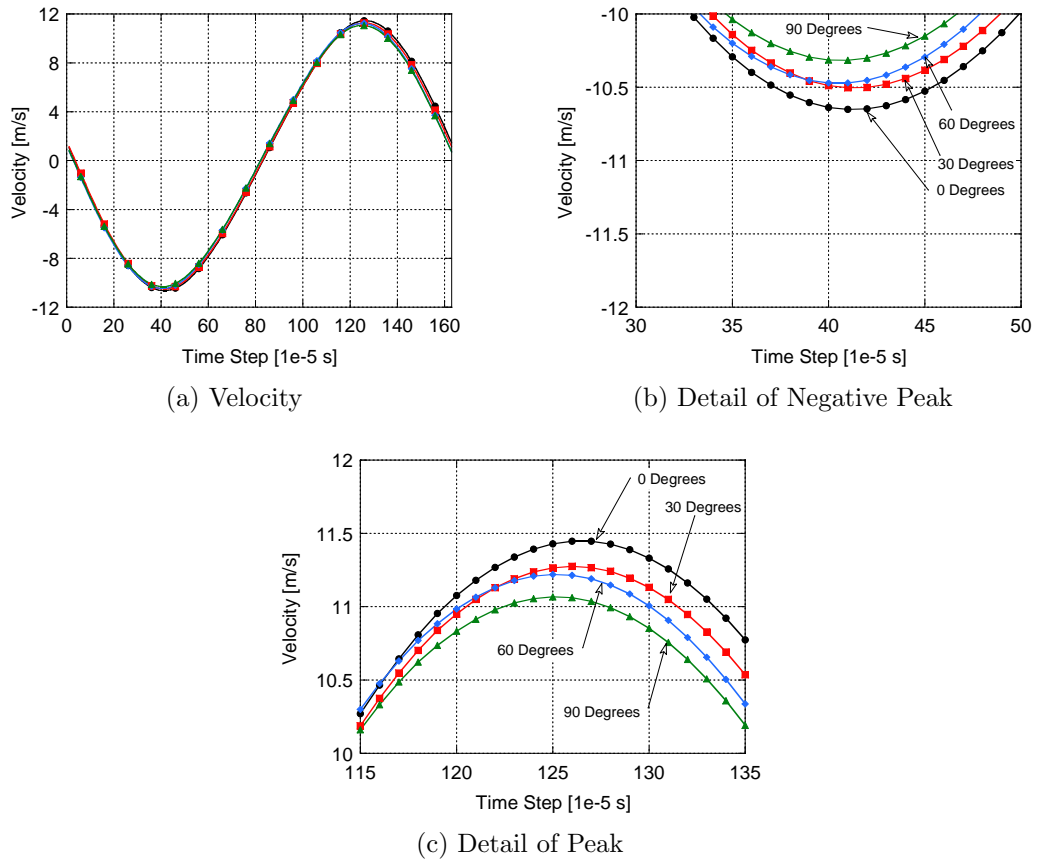


Figure 71: Comparison of velocity behavior under the influence of different degrees of resonator curvature.

Evaluating this equation at the center of the stack (which is approximately  $\frac{1}{17}^{th}$  of the wavelength in the present simulation setup) the expected maximum velocity can be calculated to be:

$$u(\lambda/17) = u_{max} \sin\left(\frac{\lambda/17}{\lambda}\pi\right) \approx 0.36 \cdot u_{max}. \quad (6.2)$$

A comparison of the velocity in the center of the stack with the velocity at the open end ( $= u_{max}$  in Equation 6.2) shows that the two values are almost identical. This behavior is shown in Figure 72 (a). It can be concluded that the stack influences the velocity distribution significantly and causes a much higher velocity in the stack than is suggested by the free-field estimate in a standing wave. Figure 72 (b) shows the integral value of the velocity (which is not the same as the displacement as this data corresponds to a single location (Eulerian view) and does not follow one fluid particle (Lagrangian view); see below for additional considerations on this issue). This illustrates that the outlet velocity is symmetrical whereas the velocity in the stack is in fact asymmetrical about 0. This is proof of the presence of a streaming mechanism, as discussed in Section 3.1. This information provides further insight into the fluid behavior inside the stack and can be useful in future modeling efforts, as an elaboration of the efforts discussed below in Section 8.

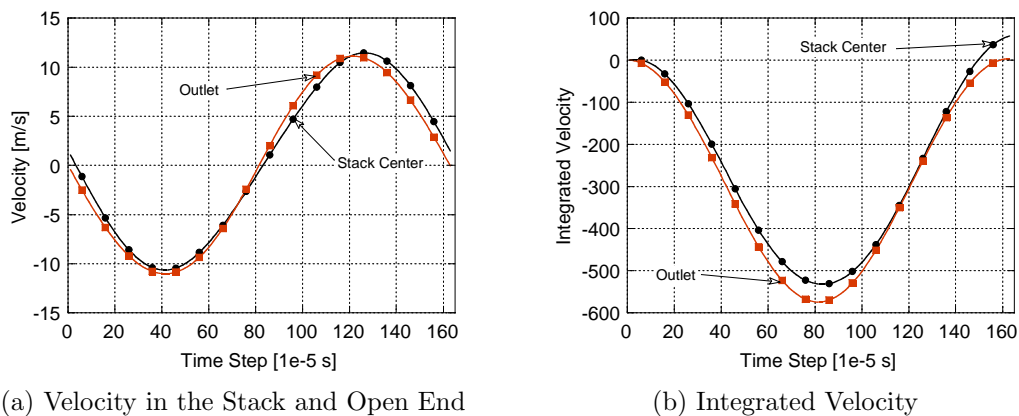


Figure 72: Comparison of velocity behavior in the stack and the outlet for the straight resonator (velocity antinode).

### 6.3.4 Eulerian and Lagrangian Point of View

Before elaborating on the velocity in its non-dimensional form, one additional aspect of the velocity component, specifically the resulting gas displacement, must be developed. It was mentioned above that the velocity here has been described from the Eulerian point of view, that is, the observer is fixed. In order to track an individual particle, Fluent uses injections of particles into the computational domain. These particles range from inert gases to solid particles. Ultimately, these particle tracking methods have not proven to be useful in the current case. As a means to avoid particle tracking with injections, a translation of the Eulerian coordinate system to the Lagrangian point of view could be used. However, this requires that the velocity of the tracked particle has to be known at all times. Assume, for example, that for a time,  $t$ , the velocity of the fluid is known at all node points. Focusing on node  $x_i$ , a particle there has velocity  $v_i$ . In order to calculate the location of this particle after a time  $\Delta t$  has passed, we write:

$$x_{i+1} = x_i + v_i \cdot \Delta t \quad (6.3)$$

The following location can be calculated advancing by another time step:

$$x_{i+2} = x_{i+1} + v_{i+1} \cdot \Delta t \quad (6.4)$$

The problem is now becoming apparent. While the velocity  $v_i$  is known because we chose a particle that was located at  $x_1$  which is a node, the new location  $x_{i+1}$  is *not necessarily* a node. This in turn means that we do not know the velocity at the new location, which would force an interpolation, and could result in errors. Ultimately, the translation from the Eulerian view to the Lagrangian view is possible. All that is required is a mesh that ensures that the Courant number is always less than 1, so as to ensure that the “new” locations  $x_{i+1\dots n}$  coincide with nodes. Alternatively, the mesh should be designed fine enough to ensure small errors during the interpolation of velocity values. In either case, this translation is beyond the scope of this work. Maintaining the Eulerian point of view, the velocity will now be discussed in its non-dimensional form. The following subsection will provide a discussion of the behavior of the Reynolds number inside the stack.

### 6.3.5 Reynolds Number

Again, the Reynolds number can be expressed by  $Re = \frac{\rho u D_{char.}}{\mu}$ . It describes the ratio of inertial forces to viscous forces in a fluid. Figure 73 shows the values for the Reynolds number for probe locations 1, 3, 5, 7, and 9 for the case of a straight resonator. The Reynolds number is always positive, as it considers the velocity magnitude and not its direction. Therefore, the plot contains two positive peaks.

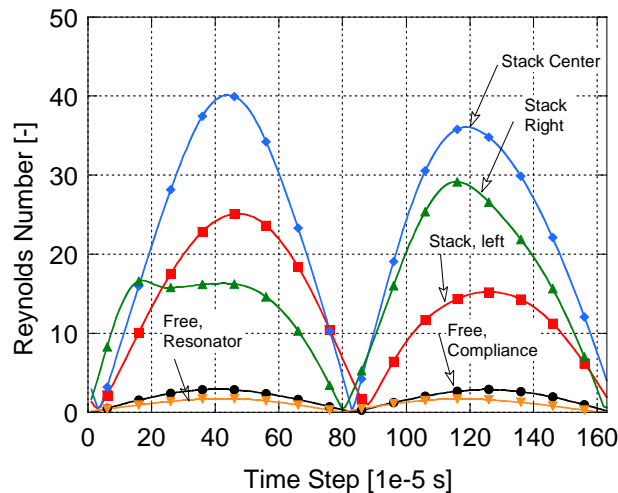


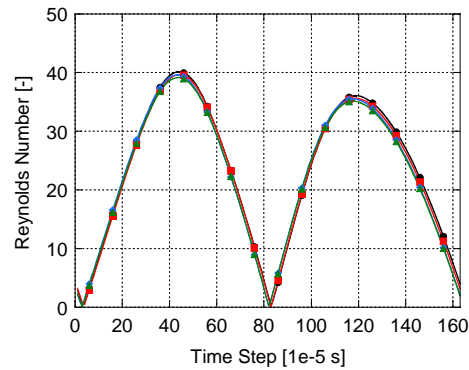
Figure 73: Reynolds number for probes 1, 3, 5, 7, and 9, center of the channel.

It can be noted that the first peak is generally higher than the second peak, except for the “stack right” position (i.e. the cold end of the stack). The velocity here is negative, which means that gas is entering the small channel from the open resonator. The flow is thus subject to entry effects, which obviously results in a decrease in velocity locally, which is manifested in the small value for the Reynolds number.

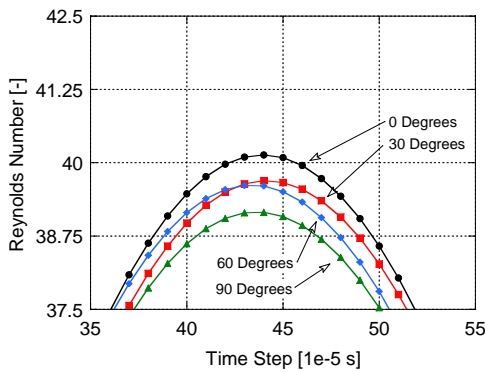
Figure 74 shows a plot of the Reynolds number at probe location 5 (the stream/center location) for all four cases of resonator curvature. Recalling the velocity plots shown above, we found that the magnitude was larger for the second peak than the first peak. However, the first peak of the Reynolds number (which corresponds to the first velocity peak) is larger than the second one (which corresponds to the positive velocity peak). Obviously, the fluid

properties that are combined in the Reynolds number behave in such way to outweigh the influence of the velocity on the magnitude of the Reynolds number.

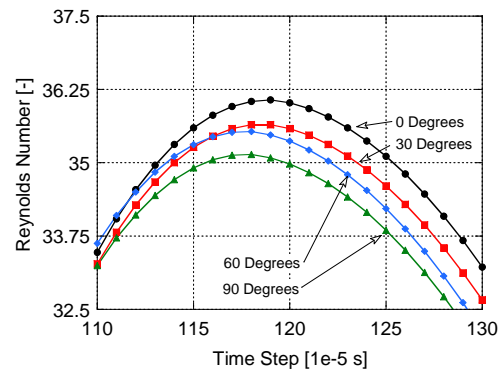
When introducing curvature, the tendencies of the previously discussed cases are consistent with intuition; the Reynolds number decreases as the curvature of the resonator increases from  $0^\circ$  to  $90^\circ$ .



(a) Reynolds Number



(b) Detail of first Peak



(c) Detail of second Peak

Figure 74: Comparison of the Reynolds number behavior under the influence of different degrees of resonator curvature.

The range of Reynolds numbers computed by Fluent at this point must be subject of further discussion. The highest peak appears to be at a value of  $Re = 40$ . By traditional standards, this is clearly within the laminar region, but if we calculate the Reynolds number

from its normal definition, accounting for channel height, density, and viscosity (at room temperature), and the peak velocity during one cycle (see above), a higher value of

$$Re = \frac{u\rho D}{\mu} \approx 480 \quad (6.5)$$

can be calculated. Of course, this is still within the laminar region. However, the traditional calculation for steady flows does not account for the effect of oscillations that are present in the present case. Mackley et al. explain the effect of flow oscillation on heat transfer. They use a definition for the Reynolds number that includes the oscillation frequency (137):

$$Re_{osc} = \frac{f}{2\pi} \frac{|u_{max}|\rho D}{\mu} \approx 46,700 \quad (6.6)$$

This definition includes the frequency  $f$  as well as maximum velocity amplitude  $|u_{max}|$ . In the present case, an estimate for  $Re_{osc}$  is a value of 47,600 which clearly reaches into the turbulent regime, justifying the use of a turbulence model. The very low values extracted from Fluent apparently do not account for the channel geometry or the operating frequency.

### 6.3.6 Temperature

So far, all of the data have been shown for the free stream location (i.e. the center of the stack), neglecting any boundary layer effects. Continuing with the analysis of the temperature, the difference in its behavior when probing in the free stream and near the wall for all four cases of curvature can be shown. Figure 75 shows this comparison for several probe points along the stack. Part (a) shows the free stream case, and part (b) shows the wall case (shown for the hot side, center and cold side of the stack). This analysis shows a clear difference between the temperature variations between the center location and the probes close to the wall. Furthermore, we have found that there is no drastic difference in the temperature behavior between the different cases of resonator curvature.

It was shown above in Figure 67 how the pressure and the stack entrance influence the temperature of the working gas. These influences were found to dominate at locations close to the wall, where the effect of convective transport of heat is limited. Due to the interaction

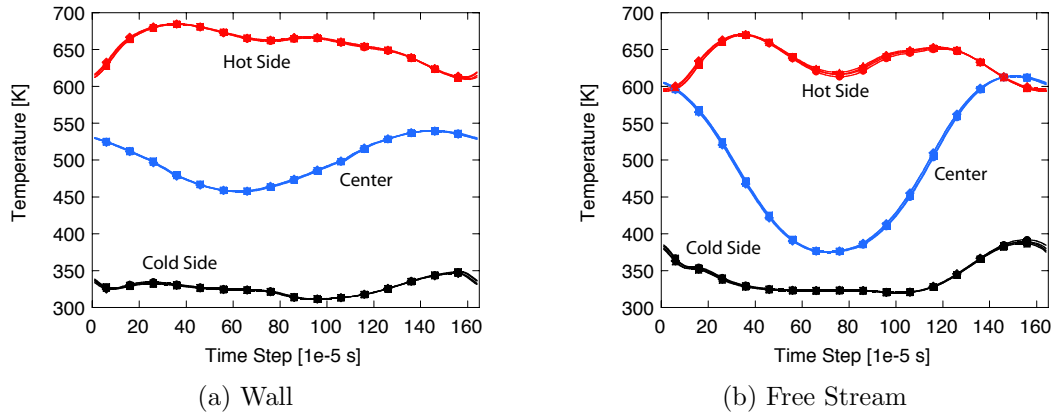


Figure 75: Comparison between wall and free stream temperature behavior.

with the wall, the temperature then changes further. Figure 76 illustrates the superposition of all effects in the temperature plots for four different cases of curvature.

The data in Figure 76 is provided for one location (stream/center) for all cases. The maximum temperature reached by the gas is lower as the curvature degree increases. Again, this is consistent with intuition. As the stack temperature is constant for all four cases, this difference must be a result of the difference in pressure amplitude (as shown in Figure 70) and the velocity magnitude (Figure 71). As curvature increases, the new losses increase, resulting in a smaller pressure amplitude, which in turn results in a smaller isentropic temperature change. Coupled with a smaller displacement, the result is the temperature behavior shown in the present figures. In addition to the investigation of the individual variables of interest, the energy transfer between solid and gas can also offer valuable insights into the effects of curvature.

### 6.3.7 Heat Transfer between Solid and Gas

In summary, the relevant flow variables, pressure, velocity, temperature, and Reynolds number, exhibit peculiar behavior during each period of oscillation. It was shown that the behavior is not generally strictly sinusoidal; wall effects, entry and exit effects, as well as

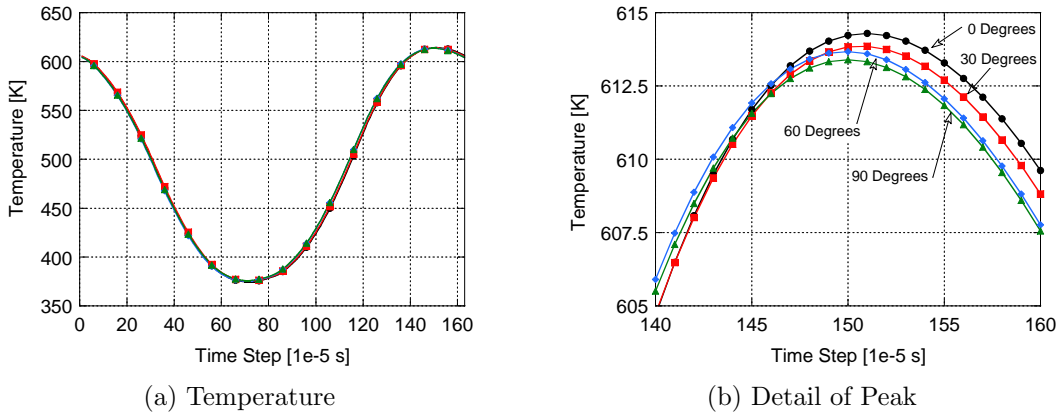


Figure 76: Comparison of temperature behavior under the influence of different degrees of resonator curvature.

superposition of convection and gas pressure changes cause unique behavior. Cumulatively, the heat transfer between the walls of the stack and the fluid merges all of these influences. The local heat transfer was discussed above during the investigation of the thermoacoustic effect. In this section, the focus shifts to the total heat transfer on the entire horizontal surface area of the stack. The velocity and temperature distribution changed significantly as a function of axial coordinate. As the heat transfer depends on all of the other variables discussed previously, the local behavior would also change along the axial direction. However, as a metric for quantification of the effect of curvature, the integrated value of the heat transfer over the entire (horizontal) stack surface is much more useful. This value is derived by:

$$Q_{int}(t) = \int_{A_{Stack}} q''(t) dA \quad (6.7)$$

The value  $q''(t)$  is derived in Fluent with Equation 6.8:

$$q''(t) = h_{Wall} (T_{Wall}(t) - T_{Fluid}(t)) \quad (6.8)$$

The value for the heat transfer coefficient was developed above in Section 5.2.2. It is derived for the present case of fluid flow subject to oscillations. Nonetheless, the values for energy transfer cannot be considered absolute, especially in light of the parameters that are known to influence the solution, as discussed in the sensitivity analysis above. Still, the influence of the thermoacoustic effect on the heat transfer inside the stack can be illustrated qualitatively. Figure 77 shows the instantaneous transfer of heat from the stack surface to the fluid. The negative values correspond to a transfer from the fluid to the wall. This figure illustrates that the general shape of the heat flux curve is not influenced by the introduction of curvature.

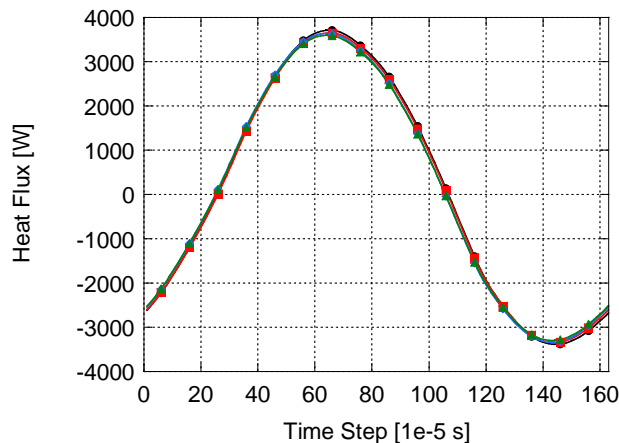
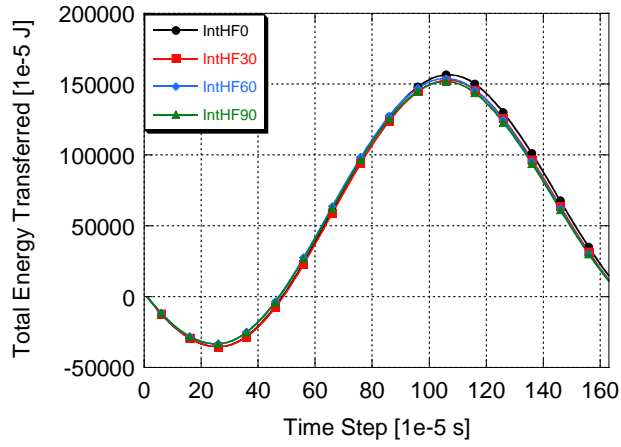


Figure 77: The integrated heat flux ( $Q_{int}$ , as derived in Equation 6.7) over the horizontal stack surfaces, comparing four different resonator shapes ( $0^\circ$ ,  $30^\circ$ ,  $60^\circ$ ,  $90^\circ$ ).

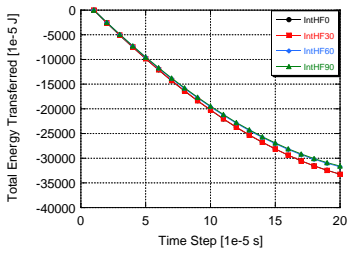
At first look, this plot seems to be symmetrical about 0. However, if we integrate this data with respect to time (i.e. time steps), we can deduce the total *energy transferred* during one cycle:

$$\Delta E = \int_{Period} Q_{int}(t) dt \quad (6.9)$$

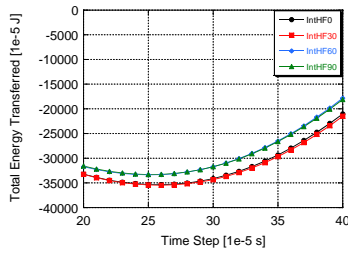
The value derived from Equation 6.9 has units of  $W \cdot s / \Delta s$ , where  $\Delta s = 1 \cdot 10^{-5} s$  is the size of the time step used. The integration is done with respect to time steps, and not seconds. Thus, and similar to the values shown in Figure 77, the values shown in Figure 78 have to be multiplied by the time step size to be representative of a physical energy transfer in Joules.



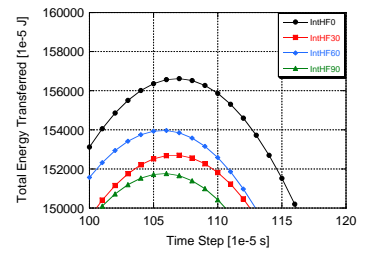
(a) Energy Transfer



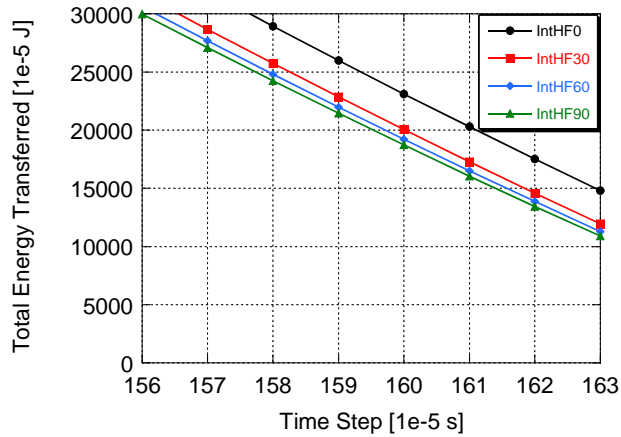
(b) Detail 1



(c) Detail 2



(d) Detail 3



(e) Detail 4

Figure 78: Energy transferred ( $\Delta E$ ) for the horizontal stack surface. Comparing four different resonator shapes ( $0^\circ$ ,  $30^\circ$ ,  $60^\circ$ ,  $90^\circ$ ).

Figure 78 is broken up into three parts. Part (a) shows the evolution of  $\Delta E$  over time for each resonator case. The plots start at 0, and go into the negative region first. This is because while early in this specific cycle, the net heat transfer occurs from the fluid to the wall. As this behavior reverses, the total energy transferred becomes positive. Towards the end of the cycle, when the instantaneous heat transfer is once again negative, the integrated value decreases. Figures 78 (b), (c), and (d) show details of the evolution of the energy transfer approaching the end. The final values represent the *total energy transferred per cycle*. This is the only relevant value for this investigation, as it illustrates the effect of curvature. First, we notice that this value is non-zero for all cases shown. This shows that the plot shown in Figure 77 is in fact not symmetrical about 0. Also, this behavior is expected as this energy transferred closes the energy balance of the thermoacoustic engine; the energy transferred from the stack to the fluid is used to sustain the pressure oscillations shown in Figure 70. In addition, as we decrease the curvature towards the 90° case, this value decreases. Figure 79 shows these final values along with the decrease in sound pressure level.

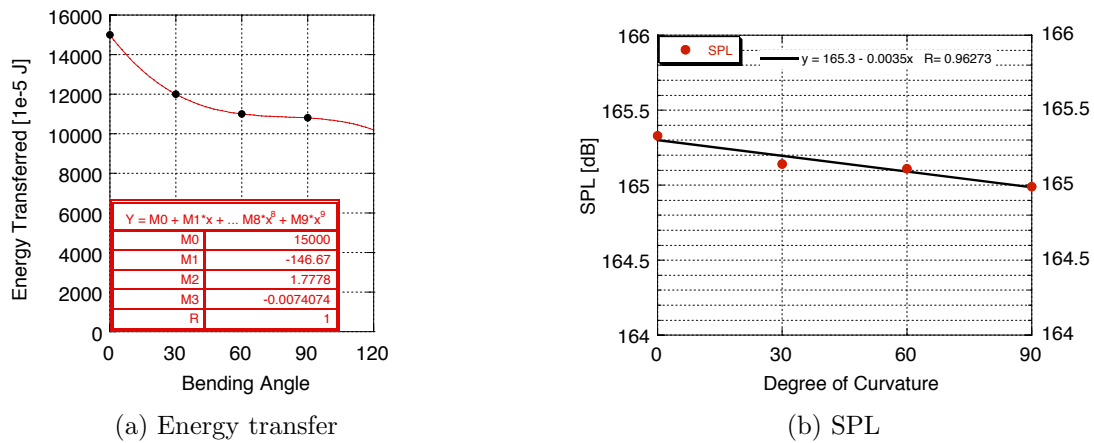


Figure 79: Effect of the curvature on energy transfer and sound pressure level

This behavior could be expected by intuition. One deduction from this behavior is, that the increased curvature influences the heat transfer in not yet understood ways, and, *as a result*, decreases the pressure amplitude of the oscillations. On the other hand, we could also deduce that the decreased pressure oscillations *cause* the decrease in heat transfer. To date,

it is not clear which argument is valid; the exact distribution of cause and effect among the discussed variables remains under investigation.

## 6.4 VISUALIZATION OF THE FLOW VARIABLES

As a second benefit of a CFD analysis, the visualization of flows can contribute significantly to the understanding of flow phenomena. This section will introduce these flow visualizations. Of all previously introduced variables, the pressure is the least important to consider, as the simulation assumes an incompressible flow field, and thus the pressure is not affected, and therefore does not affect any of the other flow variables. Illustration of the velocity will show sources of loss. Visualizing the temperature will highlight convective effects, that is a superposition of the velocity field under the influence of pressure oscillations and subject to heating from the stack's walls. Finally, we can also illustrate the generation of turbulence, as part of the  $k - \varepsilon$  model.

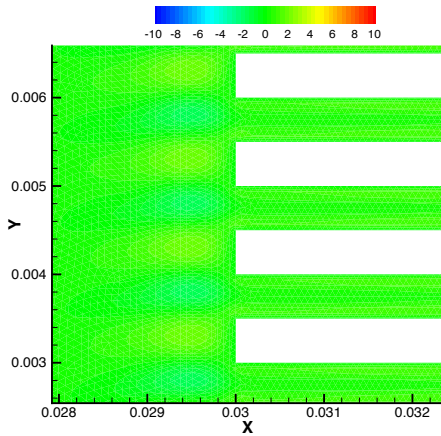
### 6.4.1 Visualizing Entry and Exit Effects

During the discussion of the temperature behavior above (see Section 6.2) the influence of entry and exit effects were briefly noted. In order to investigate these effects further, the visualization capabilities of Fluent and Tecplot were utilized. The following data was extracted from a straight resonator, again, after oscillations were fully established. The effects are visualized using the velocity and temperature at four distinct time steps:

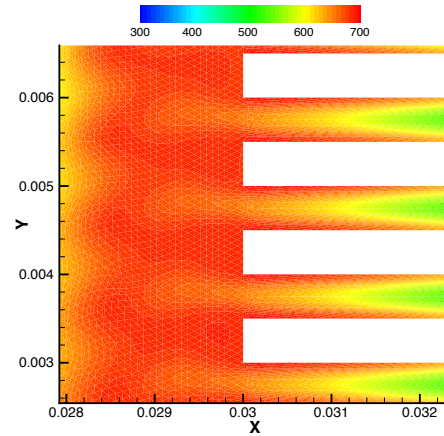
1. Zero velocity (minimum displacement),
2. Maximum velocity,
3. Zero velocity (maximum displacement), and
4. Minimum velocity.

Consistent with the period of oscillation, each characteristic time is 41 time steps apart. The following figures illustrate the velocity and corresponding temperature side by side. It must be noted that “minimum velocity” corresponds to the highest *negative* velocity. The

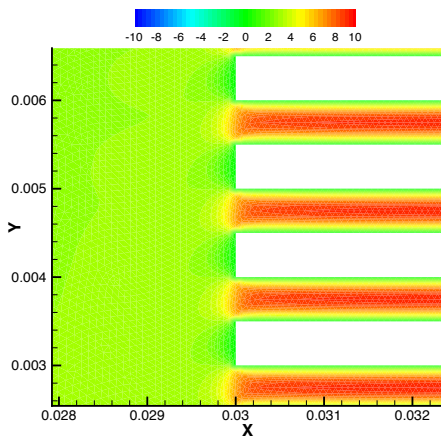
velocity *at the respective probe point* is 0 at each peak displacement. The investigation of the following velocity plots shows that the velocity is not zero for the entire domain shown at each point of maximum displacement. Figure 81 shows the velocity and temperature distribution for each distinct point in time.



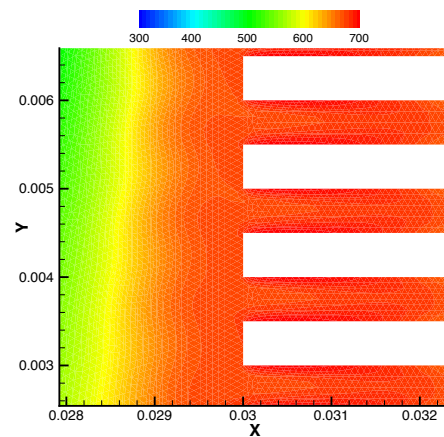
(a) Velocity (hot, min displacement/zero velocity)



(b) Temperature (hot, min displacement/zero velocity)



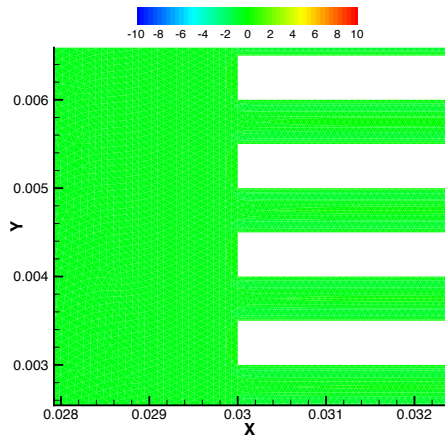
(c) Velocity (hot, max velocity)



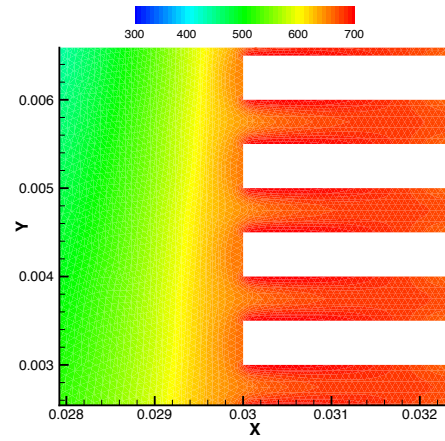
(d) Temperature (hot, max velocity)

Figure 80: Entry/exit effects on the hot side of the stack, part 1

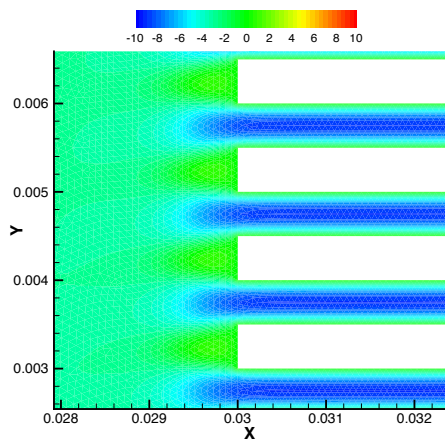
- Beginning with peak negative displacement (Figure 81 (a)), the velocity is generally small. There are distinct areas of non-zero velocity present inside the compliance just opposite the open channel as well as opposite the solid portions of the stack. These areas



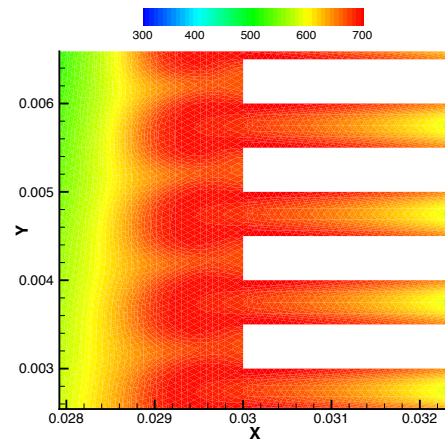
(a) Velocity (hot, max displacement/zero velocity)



(b) Temperature (hot, max displacement/zero velocity)



(c) Velocity (hot, min v)



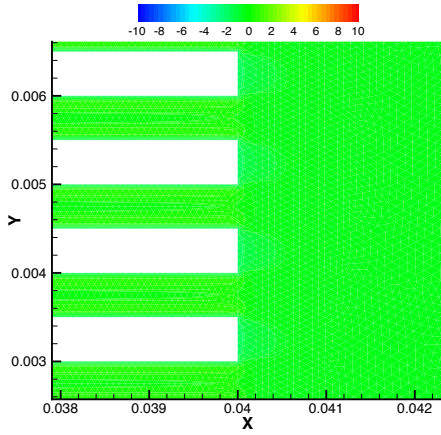
(d) Temperature (hot, min v)

Figure 81: Entry/exit effects on the hot side of the stack, part 2

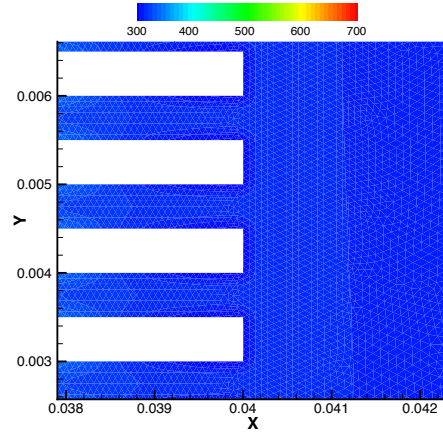
are indicative of vortices that will be further visualized by velocity vectors below. These vortices are also explained in the previous numerical investigation of thermoacoustic couples by Zoontjens (115), Marx et al. (125), and Besnoin (123). In addition, these vortices have been visualized using particle image velocimetry (PIV) by Berson (138). Again, the direct comparison with previous models and experimental data (taken from mechanically driven TARs, but nonetheless relevant) follows below.

- The temperature shows the largest displacement of hot gas into the compliance (Figure 81 (b)). Clearly, there are bubbles of cooler gas that are displaced into the compliance. The size of these bubbles is approximately 1 *mm*, which is an indication of the displacement magnitude during the oscillation. Inside the channel, a jet of cold gas is also present.
- Next, during maximum (positive) velocity (Figure 81 (c)), the influence of the stack channels becomes apparent. Outside of the stack, the velocity is clearly higher than in the previous case, but inside the channel, the velocity reaches its highest values. The area of hot gas inside the compliance is also smaller than in the previous case, and the temperature inside the channel is homogenous (Figure 81 (d)). This indicates mixing effects that occur as gas enters the channels.
- At the maximum displacement (Figure 81 (e)), the velocity in the domain shown is uniformly zero. The flow at this time is fully developed, and there is no indication of vortices. The displacement of hot gas through the channels has reached a maximum, and the temperature at the channel center probe position is at its lowest point due to the introduction of “cold” gas from the compliance into the channels (Figure 81 (f))
- Finally, during maximum negative velocity (Figure 81 (g)), the velocity magnitude is clearly very high inside the channel, and decreases quickly inside the compliance. There is an indication of zero (or slightly positive) velocity opposite the vertical stack sections. Also, the effect of the wall on velocity is apparent inside the channel. Close to the wall, the velocity is much smaller than in the center of the channel. The temperature plot (Figure 81 (h)) now exhibits bubbles of hot gas extending into the compliance. These areas extend over approximately 1 *mm*.

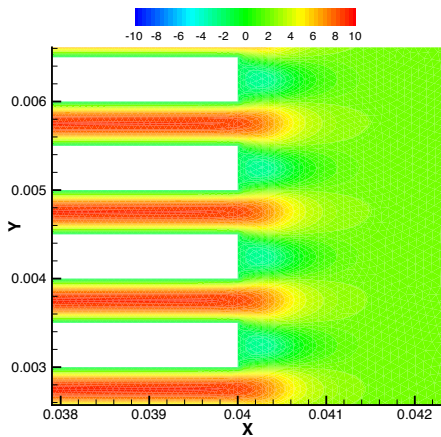
Figure 83 shows the same set of contour plots for the cold side.



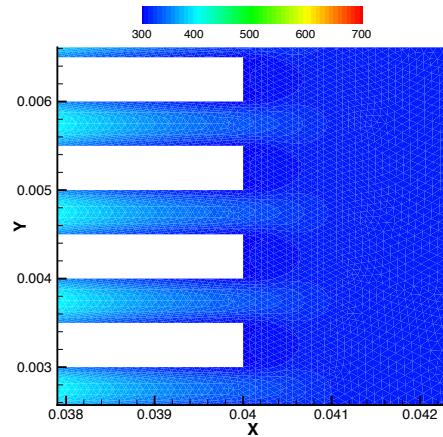
(a) Velocity (cold, min displacement/zero velocity)



(b) Temperature (cold, min displacement/zero velocity)

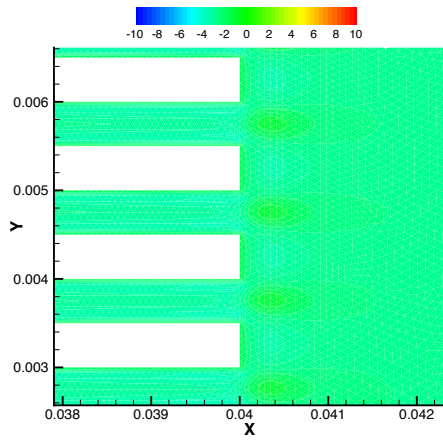


(c) Velocity (cold, max v)

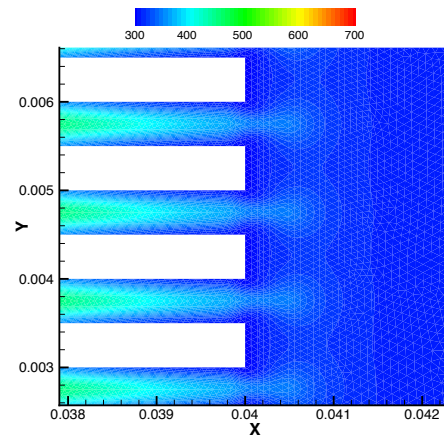


(d) Temperature (cold, max v)

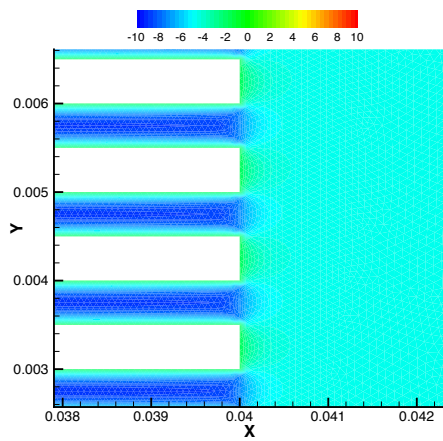
Figure 82: Entry/exit effects on the cold side of the stack, part 1



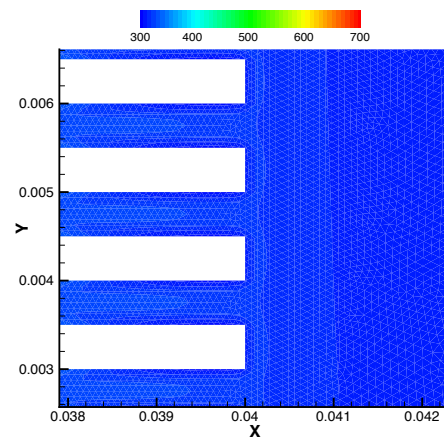
(a) Velocity (cold, max displacement/zero velocity)



(b) Temperature (cold, max displacement/zero velocity)



(c) Velocity (cold, min v)



(d) Temperature (cold, min v)

Figure 83: Entry/exit effects on the cold side of the stack, part 2

- Again, beginning at the time of minimum displacement (Figure 83 (a)), a very homogeneous distribution of both velocity and temperature is apparent (Figure 83 (b)). This case corresponds to a time where entry effects at the transition from the resonator into the stack have subsided completely.
- During maximum velocity (Figures 83 (c)) and (d), bubbles of warm gas are displaced into the open resonator area. As on the hot side of the stack, this influence is apparent over a distance of approximately 1 *mm*. It is coincidental with jets of high velocity that extend into the resonator. Also, there are distinct areas of negative velocity present close to the stack and in between the channel openings. Again, these areas are indicators of vortices that will be illustrated by plots of the velocity vectors.
- These vortices continue to form stronger as the flow reaches maximum displacement (Figure 83 (e)). Largely, flow reversal is already occurring, with zero velocity at the probe point that was used to identify the time of maximum displacement. At this time, the bubbles of warm gas clearly extend into the resonator area with jets of additional hot gas showing inside the channel (Figure 83 (f)).
- When the velocity reaches its negative peak, its highest values occur inside the stack channels (Figure 83 (g)). There are areas of stagnation just along the face of the solid sections of the stack. The temperature distribution, again, is very homogeneous. In general, the temperature variation in the area of the cold side is much weaker than on the hot side. For this reason, the temperature distribution is generally more homogeneous on the cold side than on the hot side of the stack (Figure 83 (h)).

#### 6.4.2 Visualizing the Velocity by Vectors

Again, the vectors correspond to the same timesteps as before (established oscillations, minimum displacement, maximum velocity, maximum displacement, and minimum velocity *in the center of the flow channel*). Each case is displayed for the hot side (Figure 84) and the cold side (Figure 85).

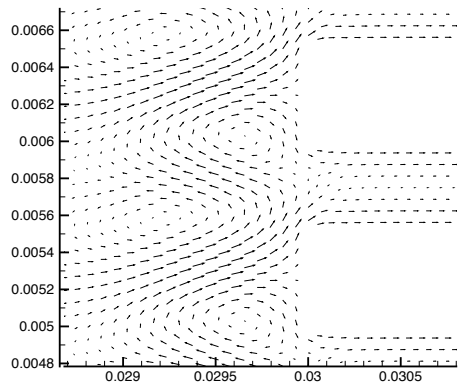
On the hot side, at minimum displacement (84 (a)), areas of strong recirculations can be identified. At the lower corners of the solid sections of the stack, the recirculation flow is

rotating clockwise, while a second area of recirculation located further away from the stack in the compliance is rotating counterclockwise. Just outside of the stack, the velocity is clearly non-zero. In fact, the velocity in the center of the channel is zero, but closer to the wall, flow is actually occurring in the positive direction. This shows that the reversal of flow direction does not occur simultaneously over the entire cross section of the channel.

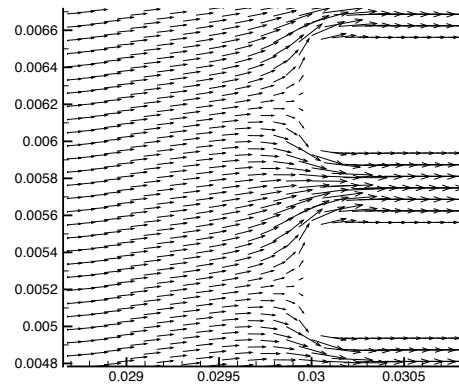
As the velocity reaches its maximum (84 (b)), the flow is much more aligned, and recirculations do not appear. The increase in velocity as the gas enters the stack becomes apparent. Also, there are stagnation points between the flow channels. The well developed velocity distribution during positive displacement is shown at maximum displacement (84 (c)), where the velocity is approximately zero throughout the shown area. Again, the areas close to the wall show an early sign of flow reversal by non-zero velocity close to the walls. At peak velocity in the negative direction (84 (d)), recirculation develops as a result of the gas leaving the confined flow channels and entering the compliance. It is noteworthy that there are three stagnation points, two of which are located near the face of the stack channel. The rotation about each stagnation point is clockwise for the lower point, and counterclockwise for the upper point.

On the cold side, some effects shown on the hot side also appear. At minimum displacement, the velocity is now distributed evenly. On this side, flow reversal is not occurring. As the velocity reaches its maximum, similar areas of recirculation (as shown in the minimum velocity case on the hot side) appear. Again, rotating flow can be identified about two stagnation points close to the face of the stack wall, with one additional stagnation point located further into the resonator area. At minimum velocity, the vectors indicate the same behavior as on the hot side while entering the stack; its velocity increases significantly. Also, as before, there are stagnation points located between each channel. Rotating flow cannot be identified.

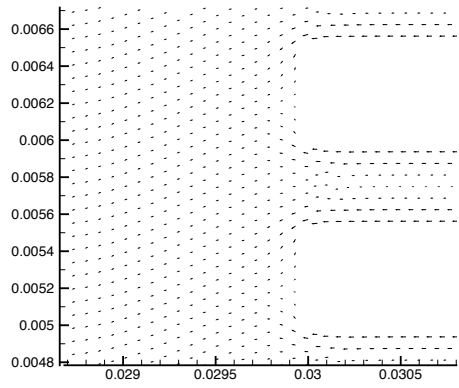
The vectors illustrated here are in good agreement with experimental measurements performed by Berson (138). Samples from the extensive collection of the state of the velocity field with respect to time show the same counter rotating vortices at the stack face during times of maximum (exit) velocity as well as the rotation during times of peak displacement that occurs opposite the stack exits. These vortices have also been described in the previous



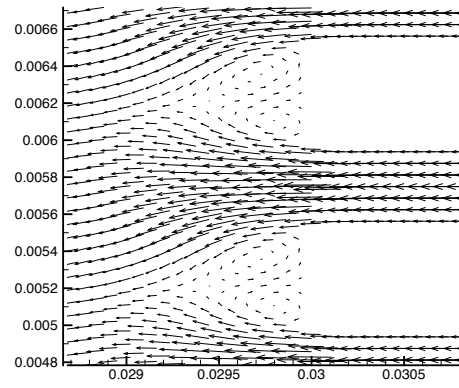
(a) Min displacement



(b) Max Velocity

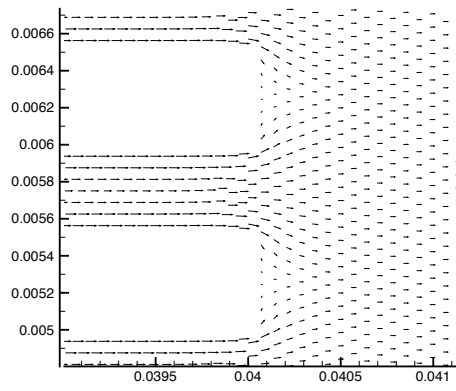


(c) Max Displacement

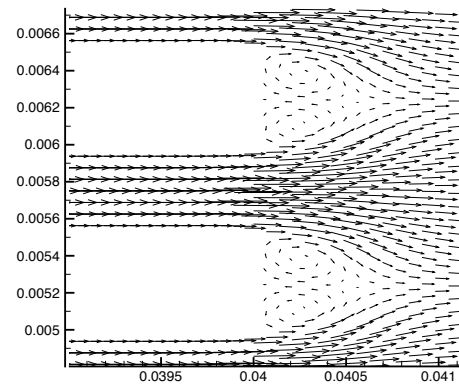


(d) Min Velocity

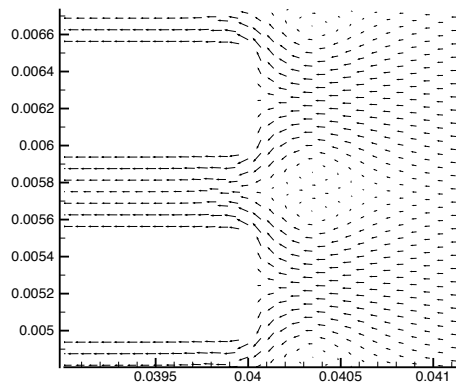
Figure 84: Velocity vectors at the hot side



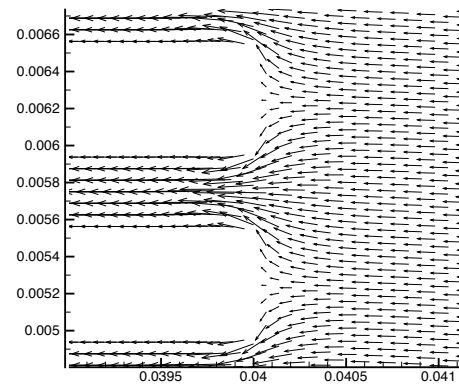
(a) Min displacement



(b) Max Velocity



(c) Max Displacement



(d) Min Velocity

Figure 85: Velocity vectors at the cold side

numerical models (as introduced above in Section 5.1.2), which further validates the present model. Figure 86 shows these results (138). Mao et al. (139) have also performed PIV measurements of the velocity field in thermoacoustic stacks. As mentioned above, their measurements have confirmed the order of magnitude of the velocities encountered during the present numerical study. In addition, the group investigated the vortices formed at the end of the stacks (similar to the work done by Berson). Mao et al. described the development of vortices during different phases of the velocity component (accelerating and decelerating). Figure 87 shows one of the plots shown in (139) that highlights the presence of vortices at the stack edge.

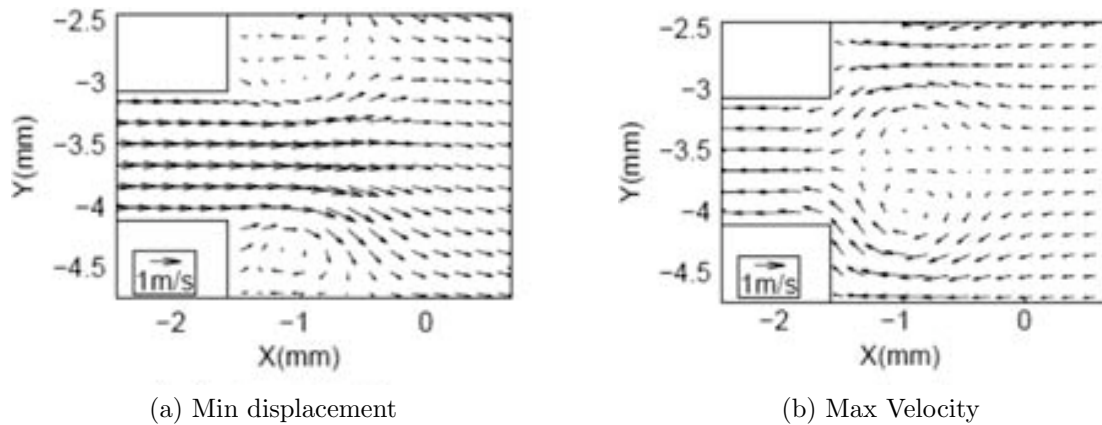


Figure 86: Velocity vectors as a result from PIV investigation of the thermoacoustic effect as published by Berson et al.

### 6.4.3 Visualizing Vortices with Stream Traces

The vortices that were discussed above can be visualized better with stream traces rather than vector plots. TecPlot offers the capability to calculate stream traces that correspond to the *instantaneous flow field*. This visualization does not illustrate the actual stream trace, since the flow is highly unsteady, but it does illustrate the rotating nature of the flow just outside of the stack area at times of maximum and minimum displacement as well as minimum velocity (this corresponds to the times that exhibited the strongest vortices).

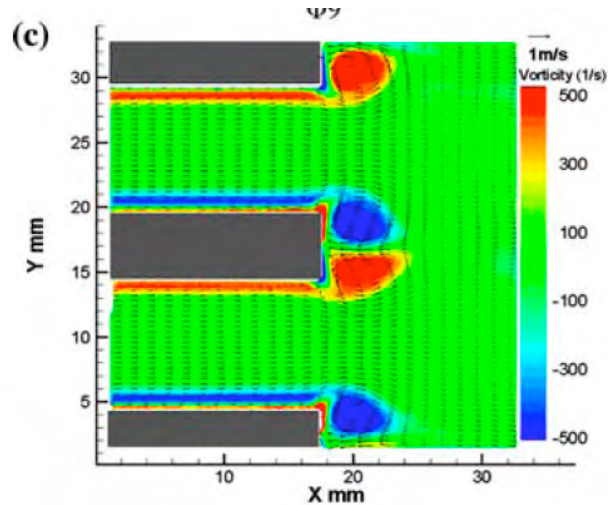
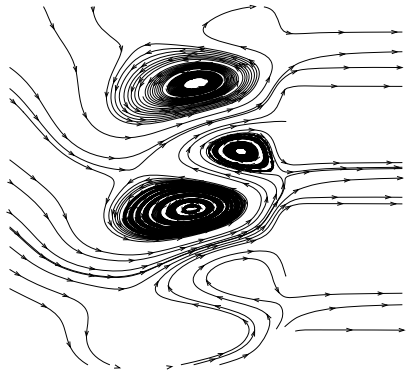


Figure 87: Vortex structure at the stack outlet, as measured through PIV by Mao et al.

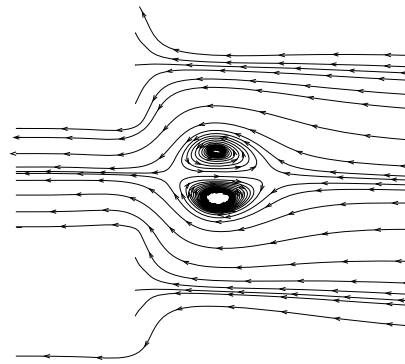
Figure 88 shows the stream traces for each case. The vortices generated at the exit of the cold end of the stack during maximum velocity are symmetrical to the ones generated at the hot end during minimum displacement, and thus are not shown separately.

The strongest vortices are present during minimum displacement (88 (a)). While the magnitude of the velocity is relatively small, strong rotational flow is present inside the compliance area. The stream traces of this flow regime indicates the nature of these flows and shows that the direction of rotation is different for the vortex closer to the stack than the ones deeper in the compliance. It was shown above that the flow field at the respective entry area of the stack at time of peak displacement exhibited a well developed flow. Thus, for the time of maximum displacement (88 (b)), vortices form at the cold side of the stack. This time corresponds roughly with the minimum displacement on the cold side, but as shown in the vector plot, the velocity in the flow is not equal to zero; flow reversal has occurred already. This flow from right to left causes two distinct vortices to form just outside of the stack channel. The lower one is rotating clockwise, the upper one rotates counterclockwise. Stagnation areas are also present, as indicated by the termination of stream traces in between open channels, caused, of course, by the vertical stack faces.

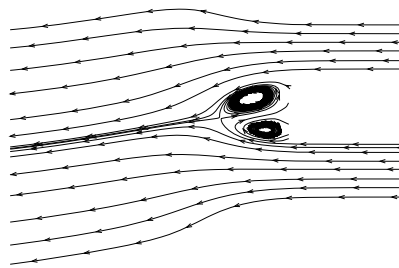
Finally, at times of minimum and maximum velocity magnitude (88 (c)), vortices form between the channels. Again, this case is symmetrical for both maximum and minimum velocity and is only displayed once. Similar to the case of maximum displacement, two distinct vortices form, only this time, this occurs between channels rather than opposite the channel opening. As before, these vortices exhibit opposite directions of rotation. The presence of vortices at both ends of the stack explain the mixing effects.



(a) Min displacement



(b) Max displacement



(c) Min velocity

Figure 88: Instantaneous stream traces for times with strong vortex generation (high velocity magnitude and flow reversal).

## 6.5 VISUALIZING THE INFLUENCE OF CURVATURE

In addition to illustrating general fluid behavior under the thermoacoustic effect, the influence of resonator curvature can also be investigated by a visualization of the flow field. The relevant flow variables here are the velocity, pressure and turbulence. In order to ensure relevance in conjunction with the previously shown data, the flow visualization here also occurs at times of minimum and maximum pressure as well as peak velocities. Table 17 shows the timesteps where the data was extracted for the TecPlot visualization (it should be noted that this data is extracted for the same fully developed case of oscillations, after 30,000 iterations).

Table 17: Derivation of the timestep for TecPlot data

Case	$\Delta ts_{p_{\min}}$	$\Delta ts_{v_{\min}}$	Timestep ( $v_{\min}$ )
0°	66	41	30,107
30°	25	41	30,066
60°	111	41	30,152
90°	128	41	30,169*

As noted by \*, the timestep for the 90° case is more than one period past 30,000, thus in order to minimize iteration efforts, the data was extracted at timestep 30,006. Below, the pressure field is shown at the time of minimum compliance pressure.

### 6.5.1 Visualizing the Pressure Field

The comparison of the pressure fields is done at the time of lowest compliance pressure. As indicated by the legends, the pressure ranges from roughly 95,000 Pa to ambient pressure at the open end. The comparison of the four different resonator cases shows that the straight case reaches the lowest pressure in the compliance. The minimum pressure increases continuously with increasing curvature. This result was shown before in Figure 70. It is noteworthy

that the isobars are perpendicular to the resonator (and compliance) walls in all cases. The pressure distribution across the resonance tube is thus not affected by the introduction of curvature.

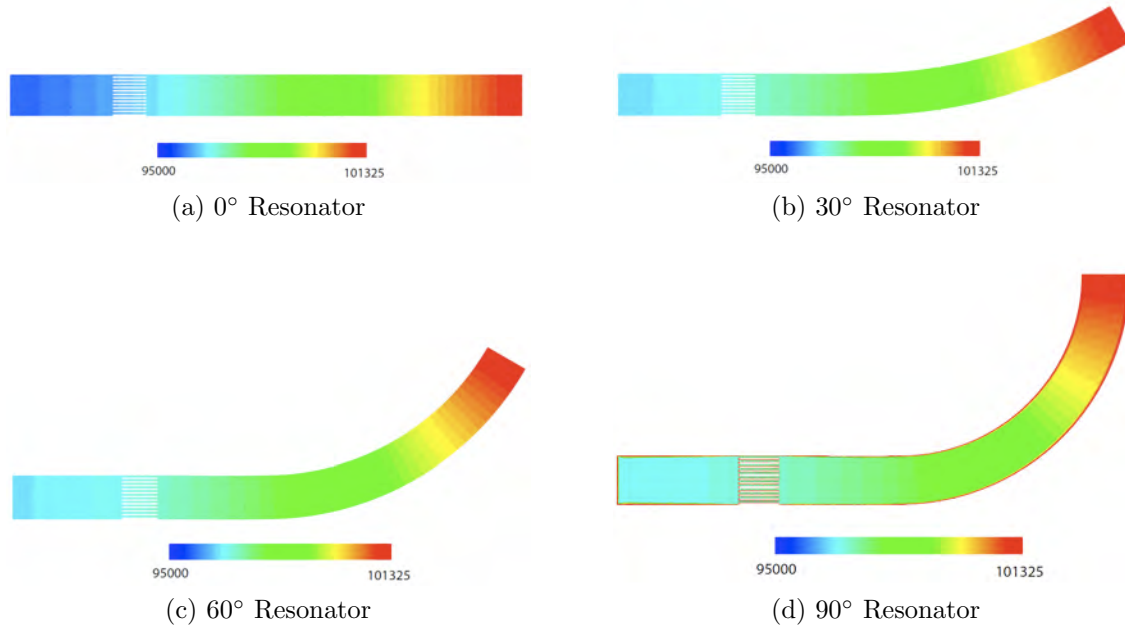


Figure 89: Pressure distribution for the whole domain for four cases of resonator curvature.

### 6.5.2 Visualizing the Velocity Field

The velocity component is the variable that is responsible for convective transport of heat in the stack and viscous losses in the stack area. Also, it was found that there are significant interactions with the wall in the resonance tube. In this capacity, the velocity is the source of significant loss and a major influence. In light of this investigation, the illustration of the velocity for the entire domain offers the most insight into the effect of curvature. The four plots shown are on the same scale, ranging from 0  $m/s$  to 14  $m/s$ . As mentioned above, this timestep corresponds to the largest *negative* velocity, thus gas is streaming from right to left. Figure 90 illustrates this data. It can be noted that the velocity within the stack is indeed of similar amplitude as at the open end. This was also previously discussed with Figure 72. Furthermore, it can be noted that the total magnitude of velocity at the open end is lower for

the curved cases. Locally, the case of  $90^\circ$  curvature actually exhibits a higher velocity than the other curvature cases, however, the *average* value is lower, as the distribution of velocity over the open end is not uniform (i.e. the lines of equal velocity are not perpendicular to the resonator walls as were the isobars shown above). In general, this means that the spatial velocity gradients in the  $90^\circ$  case are higher than in the other cases, which hints at higher shear within the fluid, and leads to the conclusion that this case exhibits the most viscous losses, even inside the resonator.

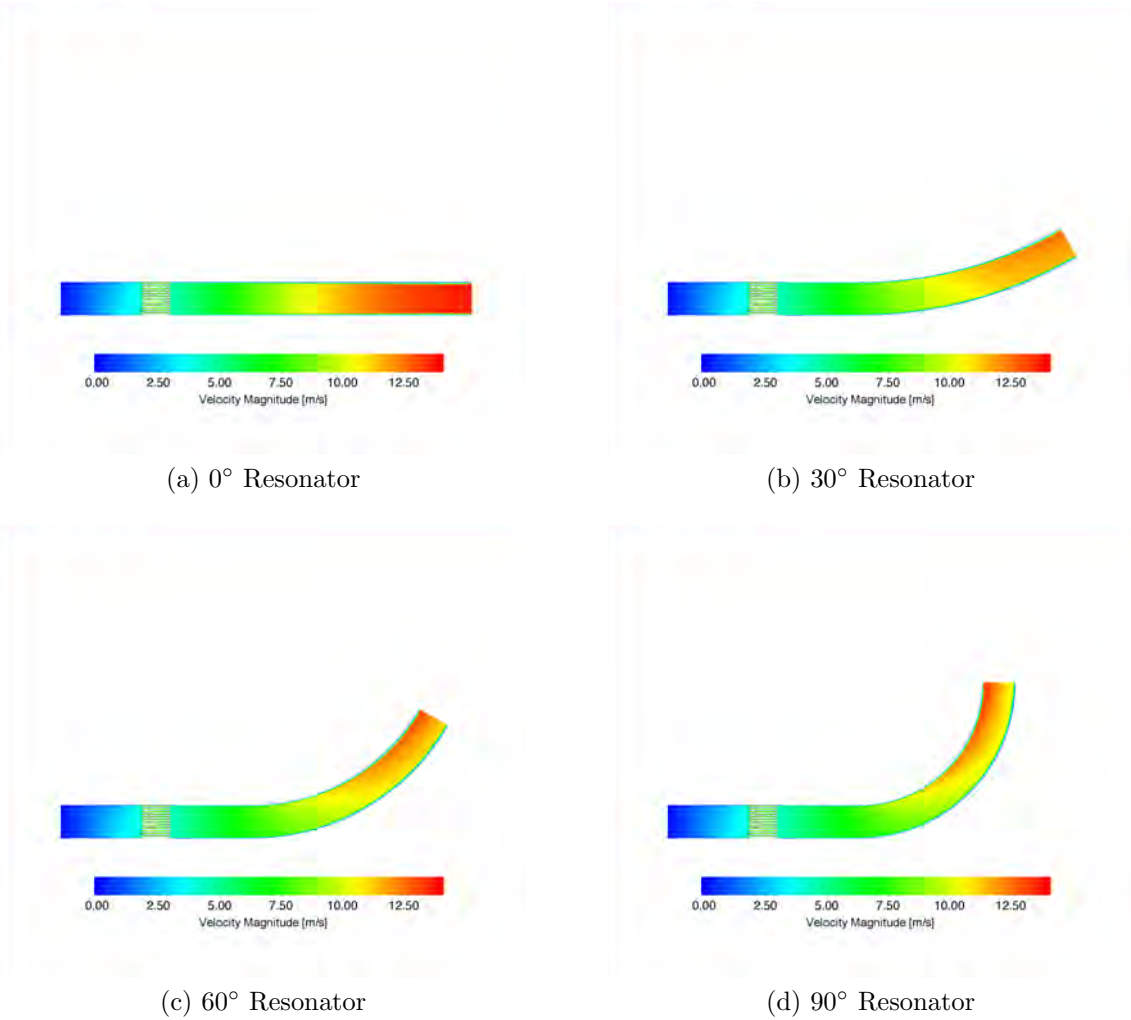


Figure 90: Velocity field for the entire domain for four cases of resonator curvature.

### 6.5.3 Visualizing the Turbulence Intensity

Finally, the visualization of the turbulence generation also indicates the effects of curvature. Figures 91 (b), (c), and (d) show that the magnitude of the turbulence intensity increases as the curvature of the resonator is increased. It should be noted that the inside curve of the 90° case (the same location that exhibits the high velocity magnitude) has the highest intensity of turbulence. In addition, the turbulence intensity inside the compliance is also higher for the more severely curved resonators than for the straight one.

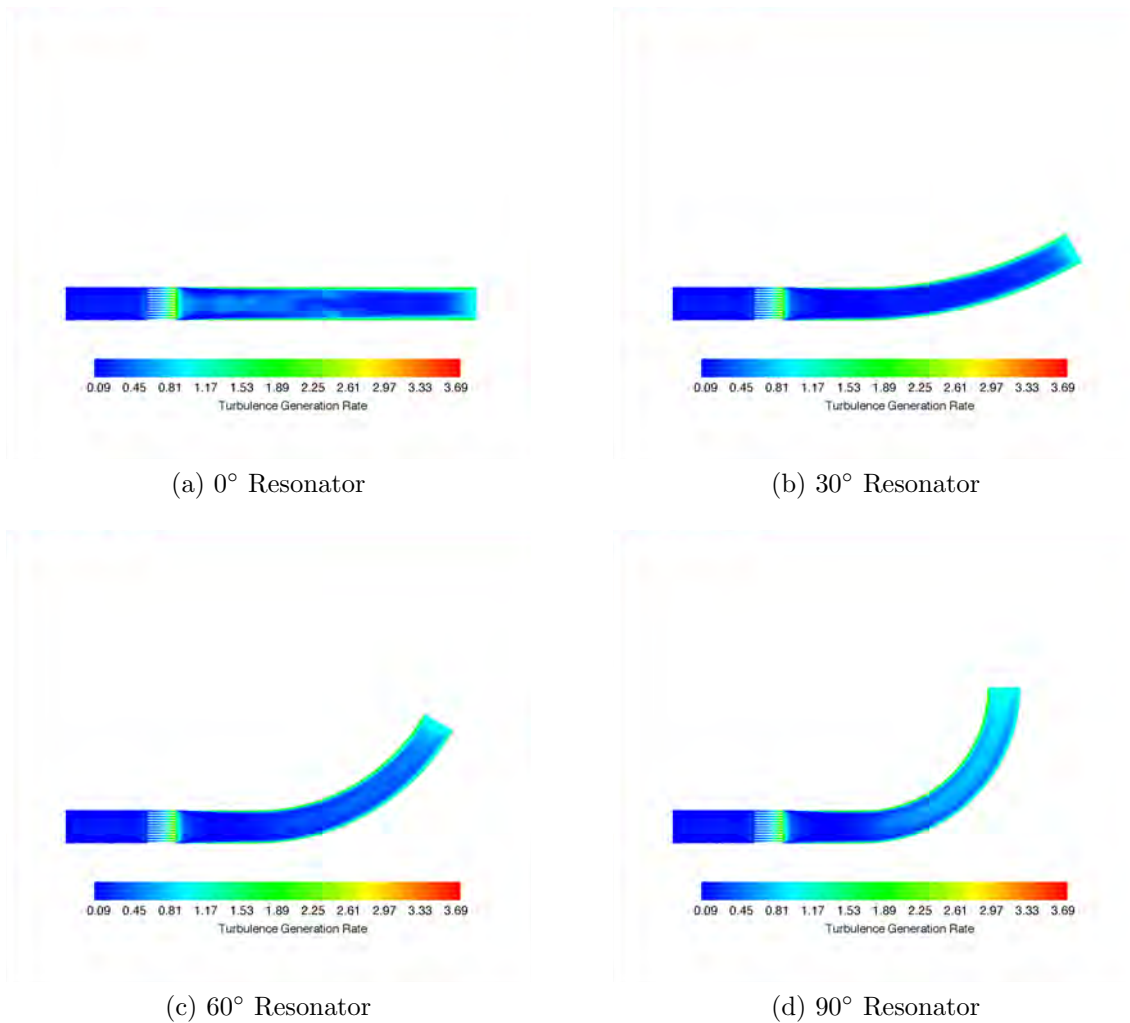


Figure 91: Turbulence generation for the whole domain for four cases of resonator curvature.

#### 6.5.4 Discussion of the Flow Field Visualization

It was shown before that the introduction of curvature to the resonator influences the gas behavior inside the stack. In addition to this effect, it was also found that the gas behavior in the resonator is also affected. As a result of the curved resonator section, the velocity, the pressure and turbulence generation is influenced. Through the higher degree of turbulence generation, energy is dissipated which yields a decrease in the pressure amplitude through the thermoacoustic effect. It must be noted that this investigation is based on a 2-D simulation. It cannot account for secondary flows behavior that may be present in a physical engine. A computationally more expensive 3-D simulation would be able to investigate the effect of curvature more accurately. However, the present results are an important contribution to the initial understanding of the influence of resonator curvature.

### 6.6 COMPARISON OF SIMULATION DATA WITH THE FREE FIELD PRESSURE DISTRIBUTION

As a final component of the simulation, the effect of the stack on the pressure distribution is investigated. It was mentioned before that the presence of the stack should influence the free field pressure distribution. Again, the simulation based on the straight resonator was used for this investigation. During established oscillations, specifically at peak pressure, the pressure was extracted from the various probes introduced in Figure 64. Figure 92 shows a closeup of the pressure peaks as well as a comparison with these peaks and the free field pressure distribution. Focusing only on the black markers, it can be seen that the peak pressure does decrease through the stack. When compared to the free field pressure distribution following Equation 6.10:

$$p(x) = p_0 + \Delta p_{max} \cos\left(\frac{x}{\lambda} 2\pi\right) \quad (6.10)$$

where the maximum compliance pressure amplitude from the same simulation is used for  $\Delta p_{max}$ , it can be seen that the pressure in the compliance is slightly higher than in the free

field distribution, whereas the pressure drop through the stack results in a slightly lower pressure than the free field values towards the cold end of the stack.

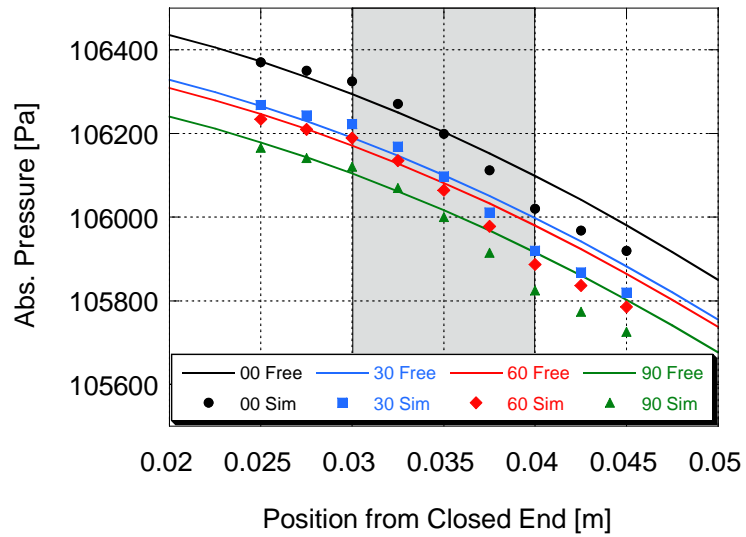
This result can prove useful in future modeling efforts, where knowledge of the distribution of pressure throughout the stack is necessary. This results also shows that using a free field distribution model is more accurate than assuming constant pressure amplitude throughout the stack.

## 6.7 DISCUSSION OF RESULTS

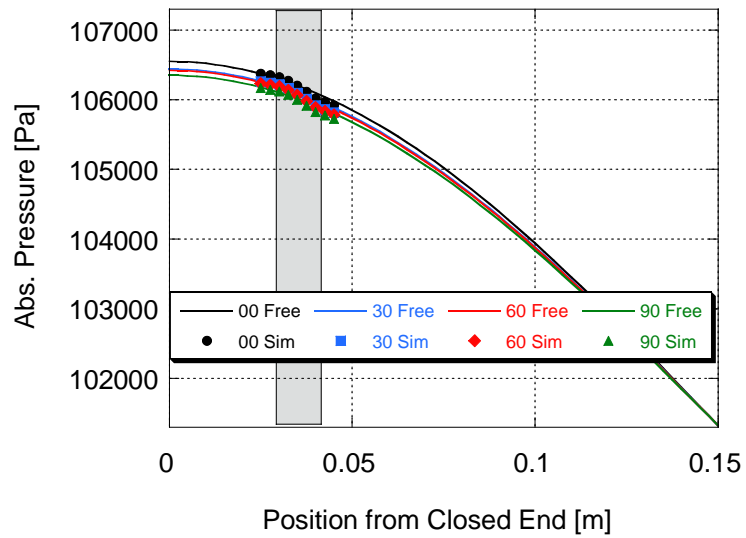
The results to this point have illustrated how the resonator curvature affects the thermoacoustic effect. A large amount of data has been presented, and the influence of curvature has been explained. However, a direct comparison of the individual properties (pressure, velocity, temperature, and heat transfer) has not been done. A discussion of the similarities and differences in the behavior of each variable is presented below. This is the culmination of all of the data previously discussed, and the most clear illustration of the curvature effect. Table 18 contains the maximum and minimum values for all of the relevant variables.

In order to display this data in a useful manner (i.e. on the same plot for direct comparison) we must normalize each value. Table 19 contains the normalized values for each peak. The maximum peak values for each variable are normalized with respect to the highest value (which is the value for the straight resonator). For the minimum peak values, the smallest recorded value was used for normalization. Figure 93 shows the same data that is given in Table 19. It is important to note that, for the case of “heat flux” ( $Q$ ) and total energy transferred ( $\Delta E$ ), the data corresponds to data extracted from the entire horizontal stack surface. As such, this data lumps together several individual effects that occur throughout the stack. The individual variables shown in Figure 93 are taken from the center stream location. This point showed the largest variation in temperature and velocity.

As a result of curvature, the value for the energy transferred  $\Delta E$  decreases significantly, dropping by approximately 25%. It is important to point out that the most significant decrease in energy transfer occurs with the introduction of 30° of curvature. The comparison



(a) Detail



(b) Free Field

Figure 92: Pressure peaks throughout the stack, and comparison with the free field pressure distribution of a standing wave.

Table 18: Maximum and minimum values for all variables discussed above, with dependence on curvature.

<b>Case</b>	<b>0°</b>	<b>30°</b>	<b>60°</b>	<b>90°</b>
$\Delta E$ [J]	14805	11951	11282	10892
$V_{max}$ [m/s]	11.339	11.191	11.178	11.067
$V_{min}$ [m/s]	-10.651	-10.504	-10.471	-10.317
$P_{max}$ [Pa]	$1.062 \cdot 10^5$	$1.061 \cdot 10^5$	$1.061 \cdot 10^5$	$1.06 \cdot 10^5$
$P_{min}$ [Pa]	96620	96713	96735	96805
$T_{max}$ [K]	614.29	613.85	613.67	613.39
$T_{min}$ [K]	374.61	375.28	375.22	375.99
$Q_{max}$ [W]	3708.4	3653.1	3636.8	3594.8
$Q_{min}$ [W]	-3387.7	-3344.4	-3337.1	-3297.4

between 0° and 30° shows a drop of 20% in energy transfer, while the change to 90° only results in an additional loss of 7% points compared to the initial value. On the other hand, the individual variables decrease, except the minima of pressure and temperature. This means that the temperature amplitude decreases, which is consistent with the results that were discussed above as well as intuition. The respective maximum values of the pressure and temperature oscillations decrease. Both effects illustrate a net decrease in oscillation amplitude. The minima for velocity and heat flux are negative values. For this reason, the behavior of the respective plots is not the same as the minima for pressure and temperature. Both plots show similar tendencies, as both decrease as curvature increases. This is synonymous with a decrease in amplitude, which is in turn consistent with the minima for pressure and temperature. The maxima for velocity and heat transfer decrease as well with increased curvature. This is consistent with the data shown for pressure and temperature. However, the decrease of velocity and heat flux is much more severe than for the

Table 19: Same data as in Table 18, but normalized with respect to maximum value (if normalizing maxima) and minimum value (if normalizing minima).

<b>Case</b>	<b>0°</b>	<b>30°</b>	<b>60°</b>	<b>90°</b>
$\Delta E$	1	0.80728	0.76210	0.73572
$V_{max}$	1	0.98695	0.98580	0.97601
$V_{min}$	1	0.98620	0.98310	0.96864
$P_{max}$	1	0.99906	0.99887	0.99812
$P_{min}$	1	1.0010	1.0012	1.0019
$T_{max}$	1	0.99928	0.99899	0.99853
$T_{min}$	1	1.0018	1.0016	1.0037
$Q_{max}$	1	0.98509	0.98071	0.96937
$Q_{min}$	1	0.98723	0.98508	0.97336

other two variables. Ultimately, we can conclude that resonator curvature affects all aspects of the fluid flow in a thermoacoustic engine. The velocity inside the stack is influenced the most, which in turn results in a significant influence on convective heat exchange between the stack's walls and the fluid.

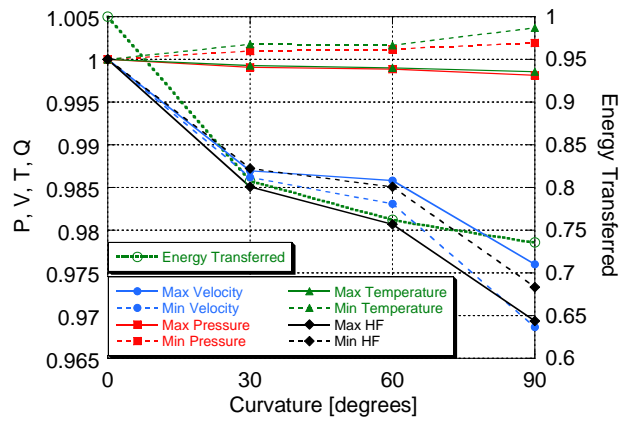


Figure 93: Illustration of the dependence of pressure, velocity, temperature, heat transfer and energy transfer on resonator curvature (normalized).

## 7.0 EFFECT OF THE THERMAL PENETRATION DEPTH

It is well understood that the thermal penetration depth of the working gas in the stack is an important variable in the design of thermoacoustic engines. It can be calculated from material properties and device design parameters. For stacks in standing wave devices, the channels must be larger than the thermal penetration depth in order to delay heat transfer, while the channels of traveling wave regenerators have to be smaller than the thermal penetration depth in order to ensure (close to) ideal thermal contact between the solid and gas. As an extension of the work shown above, a variation of the ratio between channel size (fixed) and the thermal penetration depth of the gas can be performed. Rather than changing the mesh of the model, this can be achieved by varying the appropriate material properties. As a reminder, the thermal penetration depth (10) and the Prandtl number are shown below:

$$\delta_{\kappa} = \sqrt{\frac{2 k}{\omega \rho c_p}} = \sqrt{\frac{2 k \mu}{\omega \rho Pr}} \quad \text{and} \quad Pr = \frac{\mu c_p}{k}$$

The thermal penetration depth can be influenced by changing the thermal conductivity or specific of the gas. Of course, the density should not be varied, because it would have a direct effect on the propagation of the sound waves. The flow channels are designed to be 0.5 mm, as introduced above. In the case of air as a realistic medium (at standard pressure), the thermal penetration depth is  $1.074 \cdot 10^{-4} m$  at 300 K and  $2.316 \cdot 10^{-4} m$  at 700 K (which is the range encountered during the simulation). Ultimately, the Prandtl number of the gas can be varied to create different values for  $\delta_{\kappa}$ . As discussed in more detail in the following sections, Tables 20 and 21 show the values that were implemented in Fluent. Understanding this influence, and being able to formulate a direct correlation between the ratio of channel size

to thermal penetration depth and the heat transfer behavior between the stack and the gas is important in modeling efforts as illustrated in Section 8. All simulations for this section are carried out for the straight resonator case with identical boundary conditions as previously described (10 Pa initial pressure disturbance, 10μs timestep, 300K to 700K temperature distribution, etc.). Of course, both thermal conductivity and specific heat appear in the expression for the Prandtl number and thermal penetration depth. Doubling the specific heat results in the same value for the Prandtl number as halving the thermal conductivity. For this reason, this section is broken into two subsections that discuss first the variation of the thermal conductivity, and also the variation of the specific heat.

## 7.1 VARIATION OF THE THERMAL CONDUCTIVITY

Again, a decrease of the thermal penetration depth should result in a lower amplification behavior of a thermoacoustic engine. The analysis in the following data is presented in terms of  $\alpha$ , which is the ratio of the hypothetical thermal conductivity and the physical value (denoted by \*):

$$\alpha = \frac{k}{k^*} \quad (7.1)$$

where:

$$\frac{Pr}{Pr^*} = \frac{1}{\alpha} \quad (7.2)$$

From these equations, we can derive the ratio of the thermal penetration depths as:

$$\frac{\delta_{\kappa}}{\delta_{\kappa}^*} = \sqrt{\alpha} \left( \frac{f^*}{f} \right) \quad (7.3)$$

It must be noted here that the ratio of the frequencies is not assumed to be independent of  $\alpha$ . Table 20 illustrates which values of  $\alpha$  were used in this study, and contains information about the resulting pressure amplitude as well as the frequency shifts that occurred as a result of the change in thermal conductivity. As a reminder here, the channel height is

$5 \cdot 10^{-4} m$ , which is larger than the thermal penetration depth encountered in the physical gas under the occurring temperatures.

As expected, a decrease in thermal conductivity enhances the thermal contact and consequently increases the pressure amplitude. However, the achieved pressure amplitude ultimately decreases after a peak in the range of  $\alpha = 3-4$ . Also, the frequency increases steadily as the thermal conductivity is increased. Figure 94 shows the results the lower range of  $\alpha$ . It is obvious that the decrease in Prandtl number increases the thermal penetration depth, and thus increases the thermal contact between the wall and the fluid. Consequently, the thermoacoustic effect has an earlier onset for both cases, and results in stronger oscillations. Also, the onset of oscillations occur much sooner for the decreased Prandtl number.

As shown in Table 20, the oscillations begin to decrease after  $\alpha$  reaches approximately 4. Figure 95 shows the corresponding pressure plots. The pressure behavior for  $\alpha = 8$  looks very similar to the physical case and requires a more detailed section of the plot Figure 96 shows a close-up of the pressure plots during the well-established phase Both cases require a long time (compared to the previously discussed cases) to develop the sustained oscillations. In addition to showing the smaller amplitude for  $\alpha = 8$  the increased frequency also becomes obvious in this plot.

On the other hand, an increased Prandtl number results in adverse heat transfer conditions between the wall and fluid. As expected, the transition from the  $10 Pa$  boundary condition to sustained oscillations is affected adversely. Figure 97 shows how the oscillations of the high-Pr gas decrease. Ultimately, both cases do not show the thermoacoustic effect; the pressure throughout the computational domain reaches  $101.3 kPa$ . In addition to the pressure behavior, it is also noticeable how the operating frequency changes between cases. As the Prandtl number increases, the operating frequency increases as well. This behavior is unexpected and requires additional investigation.

As a result of the variation of the thermal conductivity, a functional dependency of thermal penetration depth, pressure, and frequency on  $\alpha$  can be deduced. First, the unexpected behavior of the frequency is demonstrated. Figure 98 shows how the frequency increases as  $\alpha$  increases.

Table 20: Variation of  $\alpha = k/k^*$  and results from the simulation

<b>Standard Values</b>			
$Pr^* = 0.7$	$k^* = 0.0242 \frac{W}{m \cdot K}$	$c_p^* = 1006.4 \frac{J}{kg \cdot K}$	
$\delta_\kappa^* =$	$\begin{cases} 1.074 \cdot 10^{-4} m \text{ (at 300K)} \\ 2.316 \cdot 10^{-4} m \text{ (at 700K)} \end{cases}$		
<b>Variation of Thermal Conductivity</b>			
$\alpha$	Oscillations	$p_{rms}$ [Pa]	$f$ [Hz]
0.25	N	-	-
0.5	N	-	-
0.75	Y	-	610
1	Y	4105.0	614
1.5	Y	5200.0	621
2	Y	6155.0	625
3	Y	6650.0	641
4	Y	6792.0	649
6	Y	5660.0	657
8	Y	3814.8	665

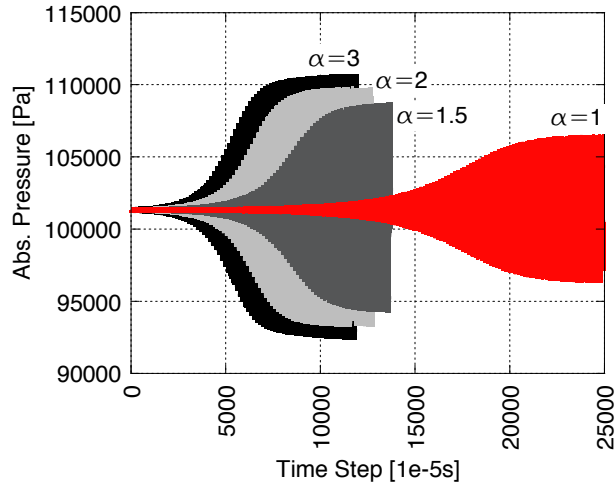


Figure 94: Pressure behavior for four values of  $\alpha$  (1, 1.5, 2, and 3), compared to the physical case.

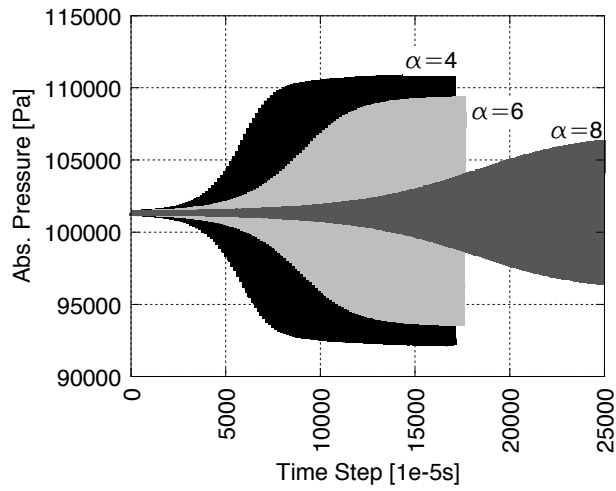


Figure 95: Pressure behavior for three values of  $\alpha$  (4, 6, and 8), compared to the physical case.

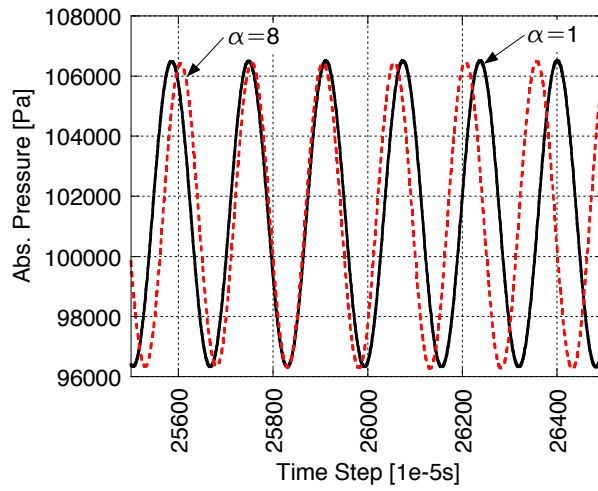


Figure 96: Pressure behavior for three values of  $\alpha$  (4,6, and 8), compared to the physical case.

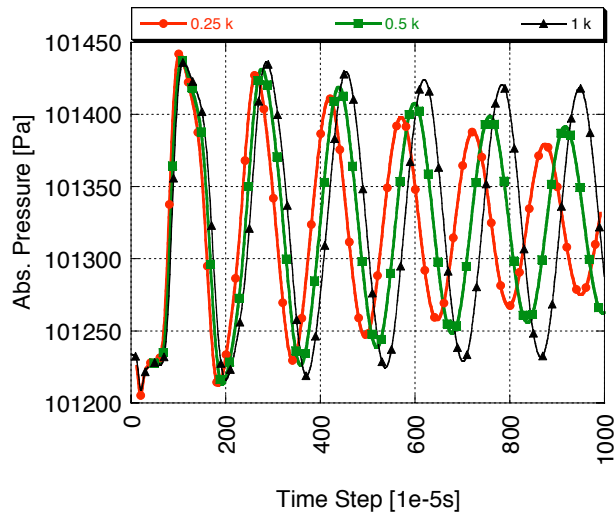


Figure 97: Pressure behavior for three different Prandtl numbers (physical,  $\times 2$ , and  $\times 4$ ) by variation of the thermal conductivity.

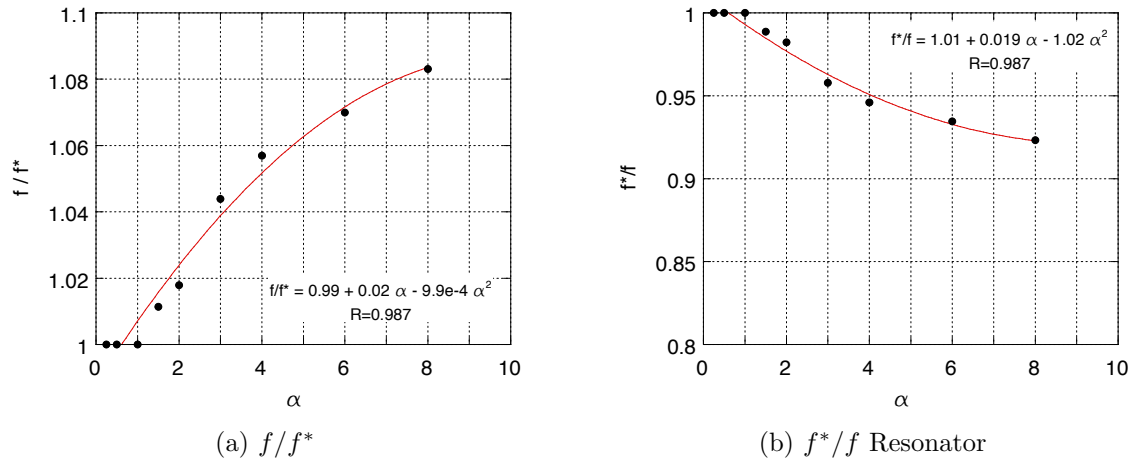


Figure 98: Change in operating frequency (normalized with respect to physical case) and its inverse (as used in Equation 7.3) as the thermal conductivity is increased.

As shown above, the thermal penetration depth depends on the ratio of the frequencies, which is why it does not follow a trivial path. The behavior of  $\delta_\kappa/\delta_\kappa^*$  is shown in Figure 99.

Finally, the behavior of the pressure as  $\alpha$  is increased is shown in Figure 100. The previously discussed behavior becomes apparent. As the thermal conductivity is increased, the resulting pressure amplitude increases as well, reaching a maximum between a value of 3 and 4. Then, it decreases steadily to reach the highest investigated value of  $\alpha = 8$ . This study shows that the ideal thermal conductivity should be approximately four times that of the physical value. This also means that the ideal thermal penetration depth is approximately two times higher than the one used presently. Ultimately, though, it is impossible to physically vary only the thermal conductivity; rather, one can change the working gas. Needless to say, this results in a change in all other material properties. As an alternative, we can change the channel size of the flow channels to affect the ratio of this dimension and the gas' thermal penetration depth. This in turn also influences the behavior of the engine, as previously discussed in Section 8.

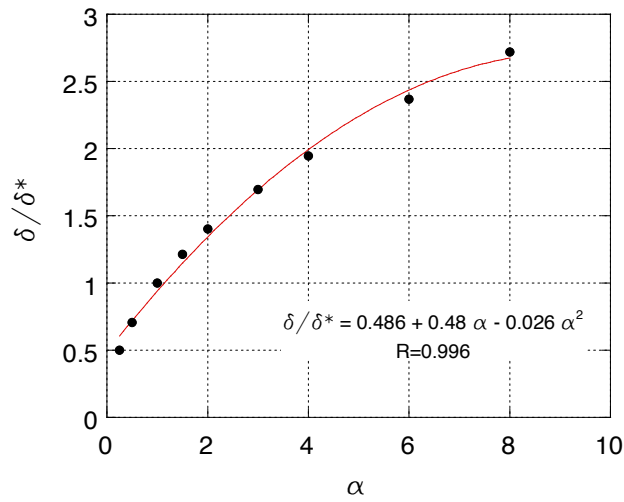
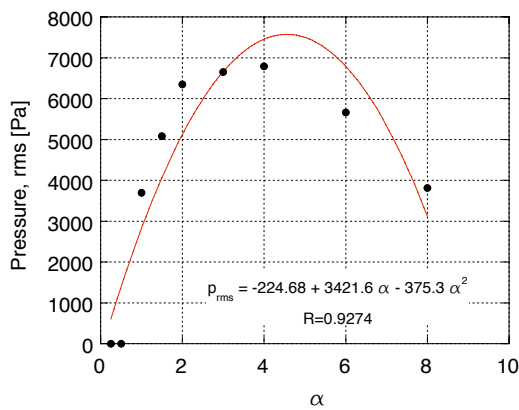
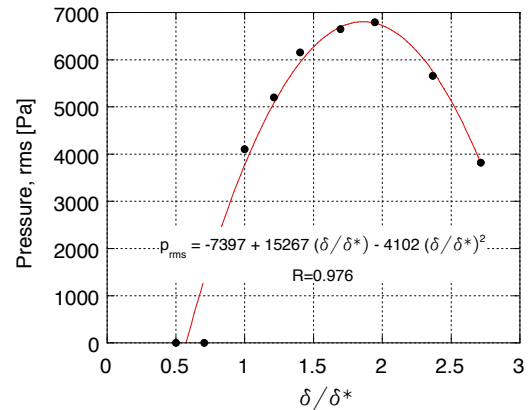


Figure 99: Change in thermal penetration depth as the thermal conductivity is increased.



(a) Pressure as function of  $\alpha$



(b) Pressure as function of lumped influence,  $\alpha$  and change in frequency

Figure 100: Change in pressure amplitude as the thermal conductivity is increased, shown as a function of  $\alpha$  directly and as a function of (normalized) thermal penetration depth.

## 7.2 PHASESHIFTS AS A RESULT OF THE VARIATION OF THE PRANDTL NUMBER

In order to provide additional insights into the influences of the variation of the thermal penetration depth, an investigation into the phase shift between pressure, velocity, and heat transfer is shown. As previously discussed, the standing wave engine naturally is subject to a roughly  $90^\circ$  shift between the pressure and velocity. The variation of the thermal conductivity has a significant influence on all aspects of the thermoacoustic engine operation. This is also true for the phasing of velocity and pressure. Figure 101 shows the collected data for the various values of phase shift  $\varphi$  and  $\alpha$ . Note that the phase shift is taken between the respective pressure minimum and the velocity minimum. However, in regard to the operation of a thermoacoustic engine, the location of the pressure extrema relative to the displacement extrema is much more relevant. Naturally, the maximum displacement occurs halfway between the two velocity peaks, or  $90^\circ$  before the velocity minimum. The right y-axis of Figure 101 refers to the displacement, rather than the negative velocity peak.

The respective shifts in phase are calculated by the number of time steps in between the peaks divided by the total number of time steps per period multiplied by  $360^\circ$ . The minimum phase shift suggested by the quadratic curve fit lies around the same value that also corresponded with a the maximum of the pressure amplitude.

Having discussed the Prandtl number's influence on the pressure and on the phase between velocity and pressure, its effect on the transfer of heat is discussed. It was shown that the pressure amplitude peaks around  $\alpha = 4$ . At the same value, the phase difference between velocity and displacement was shown to be the smallest value there. Figure 102 shows the phase relationship between the heat transfer  $Q$  and the pressure. A curve fit of the data is also shown. The general trend is that the largest phase shift between pressure and heat transfer also lies at around  $\alpha = 4$ .

Interestingly, the values for  $\alpha = 6$  and  $\alpha = 8$  do not fit the curve fit as expected. In order to show this information more clearly, the curve fit is recalculated for a data set omitting either one of these values in Figure 103. In the case where the final value for this phase shift is not accounted for the trends discussed above hold. The phase shift between pressure and

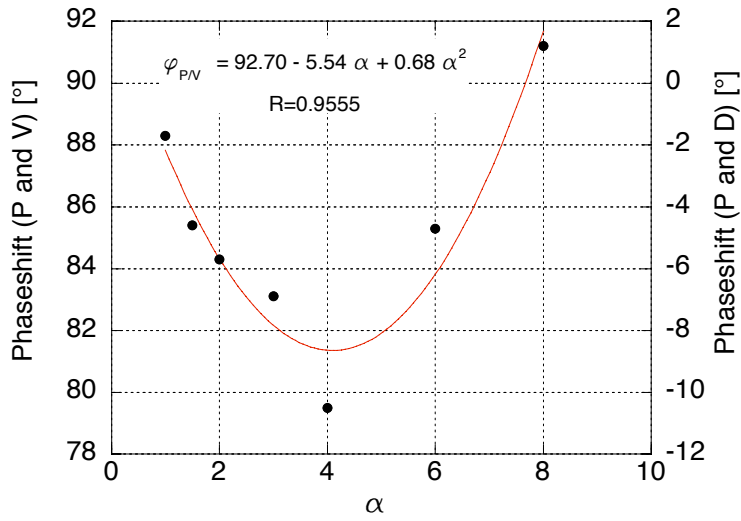


Figure 101: Change in phase shift between pressure and velocity as the thermal conductivity of the gas is increased.

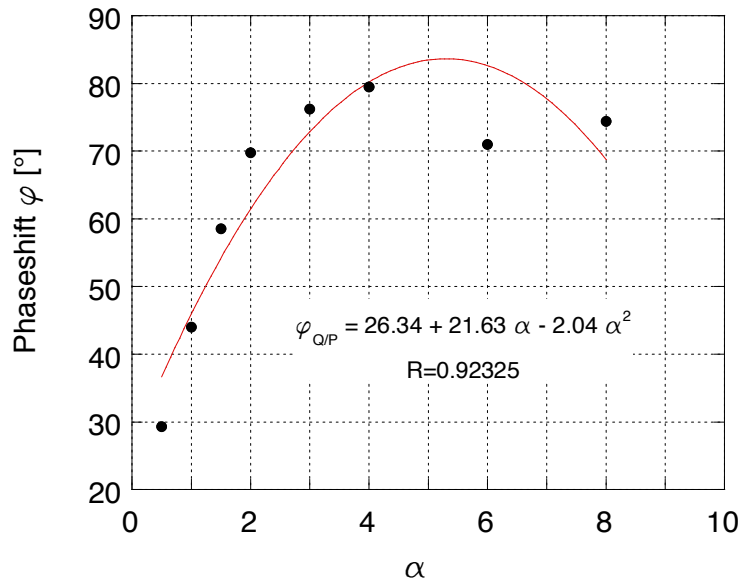


Figure 102: Phase difference between pressure and heat transfer as the thermal conductivity of the gas is increased.

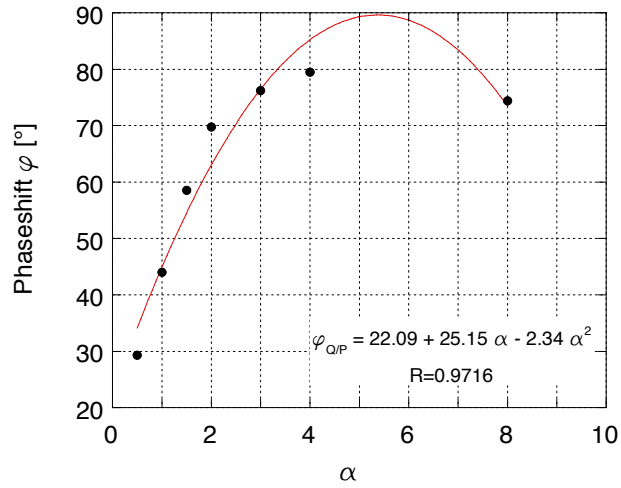
heat transfer peaks for a value of  $\alpha = 4$  and the quadratic fit accounts for this behavior. It must be assumed that the strong deviation from physical properties for high values of  $\alpha$  is the reason for this behavior.

### 7.3 THE STABILITY LIMIT

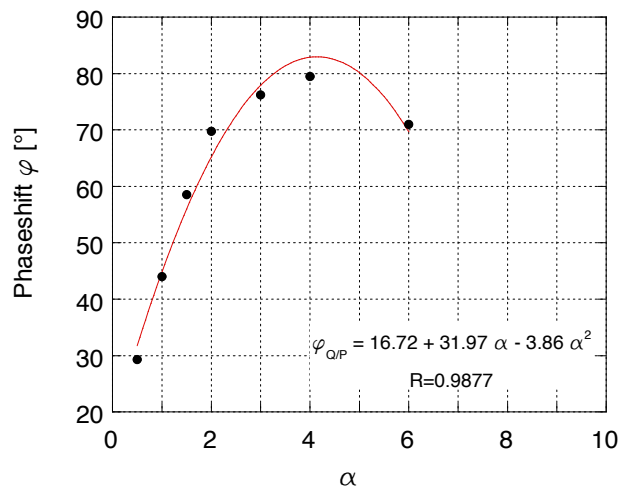
The final issue that should be investigated as part of the variation of the thermal conductivity is the area between the physical value, which we know results in oscillations under the current set of boundary conditions, and the case of decreased thermal conductivity, where oscillations do not occur. Somewhere in between, we expect a stability limit, where the system is able to maintain oscillations, but not amplify them to the same degree as illustrated in all cases where  $\alpha > 1$ . This should be considered to be the point where the ratio of thermal penetration depth and channel size is too small for the thermoacoustic effect to occur, and is not a useful point of operation. Figure 104 shows the results from a simulation case where  $\alpha = 0.75$ . It shows that the transition from the initial disturbance to oscillation takes significantly longer than in any other case discussed previously. It is not precisely the stability limit, as an amplification does occur, but we can conclude that the stability limit lies between  $\alpha = 0.5$  and  $\alpha = 0.75$ . As expected (and continuing the trend shown in Table 20, the frequency for  $\alpha = 0.75$  is lower than for the physical case. As a result, the ratio of  $\delta_\kappa/\delta_\kappa^*$  is slightly lower than  $\sqrt{3/4}$ .

### 7.4 VARIATION OF THE SPECIFIC HEAT

Of course, the thermal penetration depth and the Prandtl number can also be changed by varying the specific heat of the working gas, resulting in a very similar investigation. Intuitively, one would expect identical behavior of the oscillations for both cases of *new* Prandtl numbers. In this part of this investigation, the ratio  $c_p^*/c_p$  is expressed by  $\beta$ . Table 21 shows the results from the corresponding simulations.



(a)  $\alpha = 6$  omitted



(b)  $\alpha = 8$  omitted

Figure 103: Phase difference between pressure and heat transfer and quadratic curve fits, omitting either  $\alpha = 6$  or  $\alpha = 8$ .

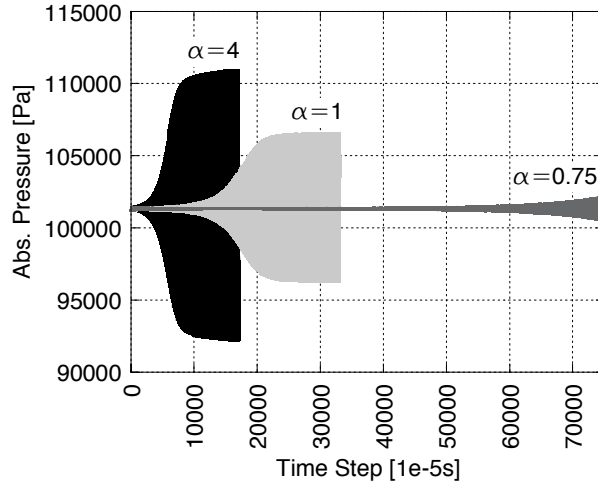


Figure 104: Illustration of the approaching stability limit, where an amplification of the pressure amplitude does not occur,  $\alpha = 4$ ,  $\alpha = 1$  and  $\alpha = 0.75$  shown.

Table 21: Variation of  $\beta = c_p^*/c_p$  and results from the simulation

Standard Values			
$Pr^*$	=	$k^* = 0.0242 \frac{W}{m \cdot K}$	$c_p^* = 1006.4 \frac{J}{kg \cdot K}$
$\delta_\kappa^*$	=	$\begin{cases} 1.074 \cdot 10^{-4} m \text{ (at 300K)} \\ 2.316 \cdot 10^{-4} m \text{ (at 700K)} \end{cases}$	
Variation of Specific Heat			
$\beta$	Oscillations	$p_{rms}$ [Pa]	f [Hz]
1	Y	4105.0	614
2	Y	4974.5	800
4	Numerical Error		

However, a comparison between two cases of equal Prandtl numbers, specifically  $Pr = 2 Pr^*$  shows that the two variations result in drastically different pressure behavior. Figure 105 shows the comparison for both cases. Specifically, the oscillations take longer to develop for the variation of the specific heat. Secondly, the final amplitude for the variation of the thermal conductivity is much higher than for the case of varied specific heat. In addition, and not obvious from the figures discussed here, the frequency of the oscillations in the variation of the specific heat significantly deviates from the physical case. Recall from Table 20 that the frequency for  $k = 2k^*$  was 625  $Hz$ . This value was only slightly higher than that of the physical case. However, for the case of  $c_p = 0.5c_p^*$ , the resulting operating frequency is 800  $Hz$ . With this result, the influence of the change in oscillation behavior cannot be clearly attributed to the change in apparent thermal penetration depth, but is influenced strongly by the change in operating frequency. One reason for this is the behavior could be, that the thermal conductivity appears in the isentropic coefficient  $\gamma = \frac{c_p}{c_v}$  which in turn appears in the expression for the Mach number  $M = \sqrt{\gamma R T}$ . If the Mach number is affected by a change in the specific heat, it is reasonable to deduce that this also affects the wave propagating properties of the gas. In addition, and on the other end of the range of variation of the specific heat, it was found that Fluent was not capable of simulating a fluid with a specific heat of less than a quarter of its physical value (i.e.  $c_p = 1/4c_p^*$  or  $Pr = 1/4Pr^*$ ), whereas this change in Prandtl number was easily achieved by varying the thermal conductivity. This further indicates that the specific heat has deeper effects on the fluid behavior than the thermal conductivity, which complicates its variation as a means to investigate different thermal thermal penetration depths.

## 7.5 CONCLUSIONS FROM THE PRANDTL NUMBER VARIATION

The data discussed here illustrate the influence of the ratio of physical channel size and thermal penetration depth of the gas. It is a quantification of the influence of this ratio on the phase shift between heat transfer and pressure, as well as achievable pressure amplitude. As the Prandtl number of the gas is decreased, that is the, the thermal contact between the

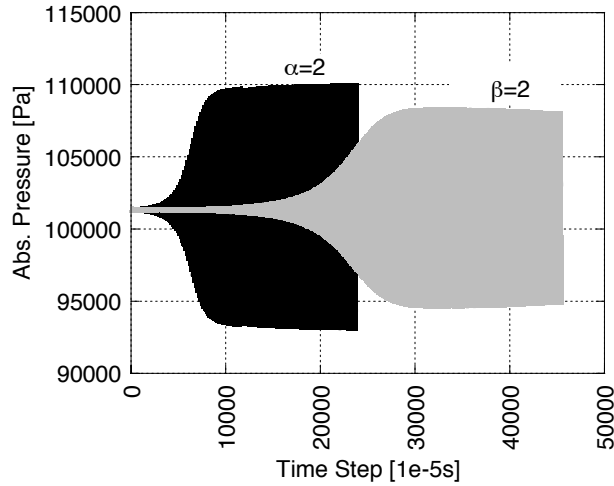


Figure 105: Illustration of the difference in oscillation behavior for a Prandtl number variation as a result of changing  $c_p$  and  $k$ .

gas and solid improves, and the oscillations occur sooner and reach higher amplitudes. On the other hand, if the Prandtl number is increased, the thermoacoustic effect is not replicated, and oscillations are not achieved. It must be pointed out that the change in Prandtl number only produced useful results for a variation of the thermal conductivity of the gas. When changing the specific heat of the gas, the gas behavior under oscillations is changed so drastically that the thermoacoustic effect cannot be replicated with the simulation. This phenomenon can be explained by the influence of the specific heat on the Mach number, and thus the ability of the gas to propagate waves.

## 8.0 OPTIMIZATION APPLIED TO THERMOACOUSTICS

The final section of this work combines results from both previous thrusts. Specifically, the results from the temperature investigations recorded from the thermoacoustic engine are combined with information gained from the CFD analysis, and applying optimization techniques to thermoacoustics is explored.

### 8.1 MOTIVATION FOR OPTIMIZATION

The results from Section 4.2 have shown that the thermal losses encountered in a simple engine setup are not negligible when compared to the input power supplied. The temperature levels encountered in the stack region top  $400^{\circ}C$ , and a significant thermal gradient is also present. While this is obviously required for operation, these temperature levels are the source of significant thermal losses. We only investigated a single stack geometry. It is intuitive to expand on this design and consider the influence of the stack geometry on the performance of the stack assembly with regard to thermal losses. Of course, as a constraint, the thermoacoustic performance has to be considered.

## 8.2 INTRODUCTION TO OPTIMIZATION AND PREVIOUS EFFORTS

### 8.2.1 Previous Optimization Efforts

Optimization techniques as a design supplement are severely under-utilized, and previous efforts in the optimization of thermoacoustic devices are rare. Minner et al. (143) consider the optimization of a thermoacoustic refrigeration system. This work uses extensive model development and seeks to optimize the coefficient of performance. The group considers geometric parameters and fluid properties of the system and a simplex algorithm to search for the optimal solution. In order to account for the thermoacoustic operating conditions, DeltaE is used extensively. Both Wetzel and Besnoin discuss optimization of thermoacoustic devices in their work. Wetzel targets the optimal performance of a thermoacoustic refrigerator (144), Besnoin targets the heat exchangers (123).

In addition to these optimization efforts, parametric studies have been utilized to estimate the effect of single design parameters on device performance. Zoontjens et al. illustrated the optimization of inertance sections of a thermoacoustic devices. Upon closer inspection, they used DeltaE to vary individual parameters to determine optimal designs (145). Ueda et al. also determined the effect of a variation of certain engine parameters on pressure amplitudes (18). Tijani et al. attempted to optimize the stack spacing; however, they also utilized DeltaE for this work (146). This is by no means a complete list of the “optimization” of engine components, but it is a good overview of optimization targets. Each work is undoubtedly a valuable addition to the thermoacoustic community, but they should not be considered optimizations in the classical sense, but rather parametric studies. In all likelihood, each “optimal” design is a local optimum, as the optimization performed by each group considers one variable and all else equal.

One common trait of all previous optimization efforts is that thermal losses to the surroundings that occur in the operation of the devices are not considered. In reality, however, we can optimize a thermoacoustic device with regard to one of the following objectives:

1. Power output,
2. Heat input,

3. Viscous losses in the individual channels, and
4. Heat loss through the device boundaries and cooling medium.

### 8.2.2 Motivation

In considering the simple thermoacoustic engine discussed in Section 4.2, the thermal energy flows were investigated. An increase in heat input to the thermoacoustic engine increased the work output (i.e. sound level). Estimates of the convective and radiative losses to the surroundings were performed, and it was shown that they account for a sizable portion of the total input power. Thus, thermoacoustic engines (and refrigerators) should be designed while accounting for the thermal behavior of the system components in mind. This section of the work introduces a method for designing thermoacoustic devices with the thermal behavior of the components. As a starting point, this work targets a standing wave thermoacoustic engine. These systems provide a simple geometry to demonstrate the feasibility of our methodology.

## 8.3 MODEL DEVELOPMENT

The challenge in this work was to account for the temperature distribution throughout the stack in an accurate way. The solution to a three-dimensional heat conduction problem subject to convective and constant temperature boundary conditions requires significant efforts (147). For our initial model, only the stack geometry is considered; the model does not consider any variation in operating condition or the interdependency of stack location and performance.

### 8.3.1 Computational Domain

Because of the symmetry present in the stack, the problem could be reduced to a two dimensional domain, accounting for two constant temperature boundary conditions, one convective boundary, and finally one adiabatic boundary, as shown in Figure 106. In order

to maintain relevance to its actual purpose, thermoacoustic energy flows are also considered, albeit in basic form.

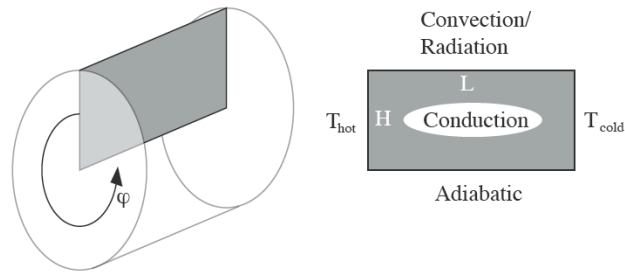


Figure 106: Illustration of computational domain and implemented boundary conditions

The temperature distribution throughout the rectangular domain was calculated using COMSOL Multiphysics, a finite element solver. The simple geometry allowed for little computational efforts when building and meshing the domain, as well as solving for the temperature distribution. In order to consider all relevant energy fluxes correctly, the resulting outer surface area as well as the face areas must be calculated by integrating over the angular component (defined as  $\varphi$ ) of the cylindrical coordinates. In addition to calculating the temperature distribution in the stack efficiently, COMSOL also allows for very good integration into Matlab, which is important for the ensuing optimization, where the domain size was varied repeatedly.

The rectangular representation of the stack was meshed using triangular cells. As the domain size will be varied over the course of the optimization, we have to maintain equal cell density for all domain sizes. Thus, the cell size was chosen to be constant for all domains used (i.e. fixed cell count per unit area). The cell type was chosen to be “Lagrange quintic” in order to minimize numerical errors.

The error from using lower order elements manifested itself in the temperature profile on the surface of the domain. The temperature profiles in the horizontal direction are expected to be linear from the hot side to the cold side at the adiabatic boundary, and convex at the top surface as a heat flux leaving that surface is imposed. The simulation yielded a temperature profile that decreased faster than the expected one. As the iterations progressed, the error

was amplified, resulting in the temperature dropping below the ambient (and cold side) temperature before continuing along the expected path. Figure 107 shows this temperature behavior in the early stages of a simulation. Figure 120 in the Appendix illustrates this behavior for all other possible element types allowed in COMSOL, linear through quintic. The reason for this behavior could be an instability resulting from the large discrepancy between initialized domain temperature and the imposed boundary temperature which is greater than the initial temperature. For the simulation, the quintic element was chosen, as it exhibited the smallest error.

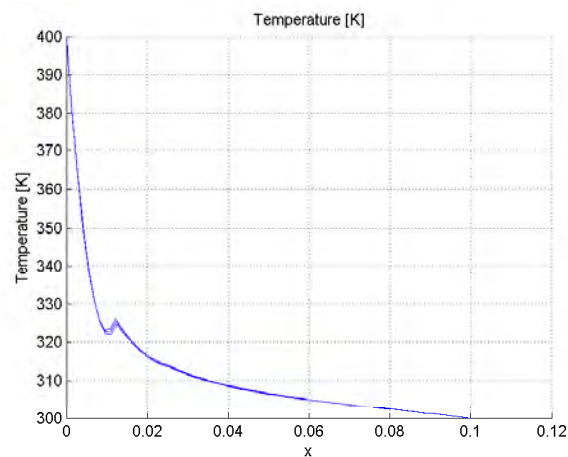


Figure 107: Error in the temperature distribution resulting from use of quadratic mesh elements

### 8.3.2 Boundary Conditions

The boundary conditions on the modeled rectangle are prescribed as follows (left vertical wall as number 1, going counter-clockwise):

1. Constant temperature ( $T_{hot}$ ),
2. Adiabatic boundary, modeling the axis of the cylindrical stack,
3. Constant wall temperature ( $T_{cold}$ ), and

4. Free convection and radiation to surroundings (at  $T_\infty$ ) with a temperature-dependent heat transfer coefficient.

The material properties of the solid are assumed to be constant. The temperature of the domain is initialized to  $300K$ . The channels of the stack are not modeled explicitly, but they are accounted for by assuming an anisotropic thermal conductivity.

### 8.3.3 Anisotropic Thermal Conductivity

In order to account for the anisotropic nature of the stack as a result of the channels, the model was given two different thermal conductivities, one for the axial direction (open channels and solid in parallel), and one for the radial direction (open channels and solid in alternating series). COMSOL allows for anisotropic material properties in the form of

$$\mathbf{k} = \begin{pmatrix} k_{xx} & k_{xy} \\ k_{yx} & k_{yy} \end{pmatrix} \quad (8.1)$$

With this option, we can derive an advanced description of the stack without actually modeling the channels individually. As a basis, we consider the bulk thermal conductivity of the solid material being used, in addition to the channel size with the gas' thermal conductivity for the net cross-channel thermal conductivity. Only the values for axial and transverse thermal conductivity  $k_{xx}$  and  $k_{yy}$  are of interest. They can be calculated as shown in Equations 8.2 and 8.3:

$$k_{xx} = \frac{t_w k_{solid} + d_c k_{gas}}{t_w + d_c} \quad (8.2)$$

$$k_{yy} = \frac{k_{solid} \cdot k_{gas} (t_w + d_c)}{k_{solid} d_c + k_{gas} t_w} \quad (8.3)$$

In order to show the influence of the anisotropic material properties, we evaluated the temperature field in the rectangular domain for two different materials (copper and polymethyl methacrylate (PMMA)), in order to show two different extremes of bulk thermal conductivity). Figure 108 shows the results. We see that the thermal conductivity of the bulk material

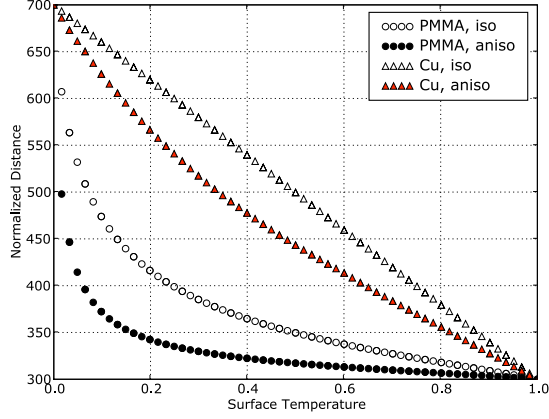


Figure 108: Temperature differences between isotropic and anisotropic thermal conductivity for Copper and PMMA,  $L \times H = 0.4 \times 0.2$ .

influences the surface temperature significantly. Also, the influence of the anisotropic thermal conductivity is important. One conclusion we can draw from this figure, is that thermal losses to the surroundings are much larger for materials with higher thermal conductivity, as the temperature difference to the environment is much higher along the stack surface. This result agrees with the results discussed previously in Section 4.3.

## 8.4 OBJECTIVE FUNCTIONS

With the computational domain defined, the objective functions can now be developed. In the present work, these are the conductive heat flux from the stack's outer surface, the conduction through the stack, the acoustic work, and the viscous resistance.

### 8.4.1 Convective and Radiative Heat Flux

In the introduction, we have illustrated the magnitude of the convective heat flux from the outer surface of the stack to the surroundings in order to provide a motivation for this

work. There, a linear temperature profile was used to estimate the heat transfer coefficient and the heat flux to the surroundings. In this model, however, the actual temperature distribution throughout the stack is taken into account by utilizing COMSOL, which captures the temperature dependence of the heat transfer coefficient. For the solid portion of the stack, these considerations assume bulk material properties that are independent of temperature. The convective heat transfer coefficient and the radiative heat flux to the surroundings are assumed to be dependent on the temperature. The total convective heat transfer across the cylindrical shell in its integral form can be described by:

$$Q_{conv} = H \int_0^{2\pi} \int_0^L h(T(x)) (T(x) - T_\infty) dx d\varphi. \quad (8.4)$$

The heat transfer coefficient  $h$  is derived from a Nusselt law. It is shown for the case of a horizontal tube subject to free convection (107):

$$Nu = 0.36 + \frac{0.518 Ra_D^{\frac{1}{4}}}{\left[1 + \left(\frac{0.559}{Pr}\right)^{\frac{9}{16}}\right]^{\frac{4}{9}}} = \frac{h D_{char}}{k_{gas}} \quad (8.5)$$

This expression depends on the Prandtl number, a characteristic dimension  $D_{char}$ , which is the lateral domain dimension  $H$  in this case, and the Rayleigh number, which in turn can be expressed by:

$$Ra = Gr Pr = \frac{g\beta(T - T_\infty)H^3}{\nu\alpha_{th}} \quad (8.6)$$

where  $Gr$  is the Grasshoff number,  $Pr$  is the Prandtl number,  $T$  is the surface temperature,  $T_\infty = 300K$  is the (constant) temperature of the surroundings,  $\nu$  is the viscosity of the surrounding gas, and  $\alpha_{th}$  is the thermal diffusivity of the surrounding gas (air). Like all Nusselt number correlations, it is an empirical expression for this specific case of heat transfer. In order to derive the actual convective heat transfer coefficient, the Nusselt number is multiplied by the thermal conductivity of the surrounding gas, and divided by the characteristic dimension of the surface under consideration (again, stack radius  $H$  in this case).

The radiation heat flux becomes increasingly important as  $T_{hot}$  increases, and is derived in Equation 8.7:

$$Q_{rad} = H k_B \int_0^{2\pi} \int_0^L \varepsilon (T(x)^4 - T_\infty^4) dx d\varphi \quad (8.7)$$

The final heat flux objective for the top surface of the domain is the sum of both the convective and radiative heat fluxes:

$$Q_{obj,1} = Q_{conv} + Q_{rad} \quad (8.8)$$

where  $k_B$  is the Stefan Boltzmann constant, and  $\varepsilon$  is the surface emissivity, which depends on the emitted wavelength, and in turn is a function of temperature (an effect that may not be negligible if the temperature difference across the domain is sufficiently large).

#### 8.4.2 Conductive Heat Flux

This heat flux is representative of the heat loss across the cold end of the domain. As the temperature gradient there is non-zero, a heat flux must be present. It is assumed that thermal energy is removed via the cooling water flow. Similar to the cylindrical shell, this heat flux has to be integrated over the whole surface representing the cold side:

$$Q_{cond} = Q_{obj,2} = \int_0^{2\pi} \int_0^H \left( k_{xx} \frac{dT}{dx} \right) dx d\varphi \quad (8.9)$$

In addition to the thermal energy fluxes inside the stack, we also must account for energy fluxes that are inherent to thermoacoustic engines. The acoustic power and the viscous resistance expressions are developed below.

#### 8.4.3 Acoustic Power

According to Swift, the acoustic power per channel is given by:

$$W = 1/4\Pi L\omega \left[ \delta_\kappa \frac{(\gamma - 1)p^2}{\rho c^2(1 + \varepsilon_{hc})} (\Gamma - 1) - \delta_\nu \rho u^2 \right] \quad (8.10)$$

which is composed of the thermal contribution minus the viscous effects (10).  $\Pi$  is the channel circumference,  $\omega$  is the operating frequency,  $\gamma$  is the ratio of the specific heats (isochoric and isobaric),  $\rho$  is the gas' density, and  $\Gamma$  is the ratio of critical temperature gradient and local temperature gradient, which has previously been introduced with Equation 1.3 (71).  $p$  and  $u$  are the pressure and velocity amplitude achieved in the stack. With data taken from the engine assembly shown above, the pressure amplitude in the stack is assumed so that  $p_{max} = 500 \text{ Pa}$ . With this information, the velocity amplitude can be derived from Equation 8.11, which describes the velocity distribution in a standing wave:

$$u(x) = i \left( \frac{p}{\rho c} \right) \cos \frac{x}{\lambda} \quad (8.11)$$

to be  $u_{max} = p_{max}/(\rho c) = 1.3 \text{ m/s}$ . For this study, both amplitudes are assumed to be constant for all stack geometries and materials. Finally,  $\varepsilon_{hc}$  is the so-called ‘‘plate heat capacity ratio’’ (41) and can be expressed by:

$$\varepsilon_{hc} = \frac{(\rho c_p \delta_\kappa)_{gas} \tanh((i+1)y_0/\delta_\kappa)}{(\rho c_p \delta_s)_{solid} \tanh((i+1)l/\delta_s)} \quad (8.12)$$

This expression can be simplified to values of  $\varepsilon_{hc} = y_0/\delta_\kappa$  if  $y_0/\delta_\kappa < 1$  and  $\varepsilon_{hc} = 1$  if  $y_0/\delta_\kappa > 1$  where  $y_0$  is half of the channel height,  $l$  is half of the wall thickness,  $\delta_s$  is the solid's thermal penetration depth. As mentioned above, the expression for the work output is provided for a single channel. In order to provide a physical representation and to be consistent with the remaining assumptions, we estimate the total number of round channels  $N_c$  as a function of cross section size for the cylindrical stack. For a circular domain, this estimate equals the ratio of overall domain size and cross sectional size of each channel, decreased to 70% of this value to account for the solid percentage of each channel:

$$N_c = \frac{4\pi H_t^2}{\pi d_c^2} \cdot 70\% \quad (8.13)$$

An added degree of accuracy would be achieved by determining the actual number of channels by utilizing a packing correlation for square surfaces in a circular domain. For the sake of simplicity, this is omitted.

#### 8.4.4 Viscous Resistance

The viscous resistance for each channel is given by:

$$R_\nu = \frac{\mu\Pi L}{A_c^2\delta_\nu} \quad (8.14)$$

where  $\Pi$  is the circumference and  $A_c$  is the area of the channel. This expression has the units  $[kg/m^4s]$ . In order to express this in terms similar to the other variables used, we multiply Equation 8.14 by the volumetric velocity  $[m^3/s]$  and the oscillating frequency  $[1/s]$ , yielding  $[W/m]$  as a final unit for the viscous resistance per channel. Just as the total acoustic power of the stack was dependent on the total number of channels, the viscous resistance also depends on this value. As the full stack represents a network of parallel resistances, we divide the value for the individual resistance by the same factor  $N_c$  derived above for the acoustic power. Below, we describe how the objective functions are conditioned and implemented in the optimization routine.

### 8.5 SOLUTION STRATEGY

Since we are attempting to find a geometric optimum of the stack geometry, the radius and length of the stack have to be varied as part of an optimization loop. Each time, the temperature distribution must be calculated. The overall process can be summarized as follows:

1. Initial guess for domain dimensions,
2. COMSOL solution for temperature distribution and heat fluxes,
3. Matlab evaluation of the objective and penalty functions, and
4. Repeat, if not optimal; else, terminate.

### 8.5.1 Normalizing Objective Functions

The objective functions as introduced above in Section 8.3 are given in a general form, all with different units and also different orders of magnitude. This would result in skewed results from the optimization as the optimizer considers all objectives as a sum. For this reason, all objectives must be scaled so as to provide dimensionless values that are on a similar scale.

The maximum work output is always achieved when the domain size is maximized. This is obvious, because the larger the cross section of the stack, the more channels we can fit in it, and there is a linear relationship between power and stack length. Thus, the maximum work output is achieved at the maximum allowable length and cross section, as shown in Equation 8.15 (multiplied by the open area coefficient, as defined in Equation 8.13):

$$W_{max} = N_c|_{H_{max}} \cdot \frac{\delta_\nu \delta_\kappa (\Gamma - 1) \omega p_{max}}{\rho c^2 (1 + \varepsilon_{hc})} \left( \frac{\nabla T}{\nabla T_{crit}} - 1 \right) \quad (8.15)$$

All parameters used here are the same as introduced above in Equation 8.10. For the viscous resistance, the maximum value is achieved with the longest channel, as this provides the most surface area and thus the highest viscous loss (Equation 8.16). The maximum total resistance is achieved at the smallest tube cross section, because it can fit the least number of channels (which is accounted for by the factor  $N_c|_{H_{min}}$ , Equation 8.17):

$$R_{\nu,max,c} = \frac{\mu \Pi_{min} L_{max}}{A_{c,min}^2 \delta_\nu} = \frac{4\mu \delta_\nu L_{max}}{\delta_\nu^2 \delta_\nu} = \frac{4\mu L_{max}}{\delta_\nu^2} \quad (8.16)$$

$$R_{\nu,max} = 1/N_c|_{H_{min}} \cdot R_{\nu,max,c} \quad (8.17)$$

The work output and resistance expression depend only on terms that are constant, and simple terms that depend solely on domain dimensions. For this reason, the normalization of both objectives is straightforward:

$$Obj = \frac{\text{value}}{\text{max. value}} \quad (8.18)$$

For both of the heat fluxes, the normalization is less straightforward, as it is not immediately clear where their maximum and minimum values are achieved. For this reason, a

separate COMSOL calculation is performed, evaluating all heat fluxes for all possible combinations of domain dimension that are allowed within the imposed boundaries on the domain ( $L_{min}$ ,  $L_{max}$ ,  $H_{min}$ ,  $H_{max}$ ). This domain is discretized with a separate grid, and all heat flux values are calculated and stored in a matrix. The respective maximum and minimum values of this matrix are then used to normalize the heat fluxes according to Equation 8.19:

$$Obj = \frac{\text{value} - (\text{min. value})}{(\text{max. value}) - (\text{min. value})} \quad (8.19)$$

With these normalization schemes in place, all objectives vary between 0 and 1, and both values are achievable within the domain. This allows us to optimize with respect to their sum, as the system is dimensionless and all four objectives are now on the same order of magnitude. In order to provide bounds on the variables used in this study, we implemented the following penalty functions.

### 8.5.2 Penalty Functions

Two penalty functions are used for each decision variable (for the upper and lower bounds). This is done to avoid solutions such as the long and thin stack (“pencil” shape) or the short and large-radius stack (“disc” shape). The penalty functions are only evaluated if the variable is actually violating the boundary, otherwise they assume a value of 0.

In our current case, the variables that need to be constrained are the axial and radial dimensions of the rectangular domain, L and H, respectively. They take the same format for both variables:

```
if H_min - H > 1e-12
penalty = 10 + (H_min - H) * 1e8
end
```

and

```
if H - H_max > 1e-12
penalty = 10 + (H - H_max) * 1e8
end
```

As soon as the constraint is violated, the constant term of the penalty ensures an immediate effect on the border of the feasible region, while the linearly increasing term ensures that the algorithm will avoid solutions further away from the feasible region.  $H_{min} - H > 1e^{-12}$  instead of  $H_{min} - H > 0$  is used as a check for violation, as 0 is not well defined in numerical terms. The latter check could lead to numerical instabilities. In order to still provide a reasonable gradient as the domain violation becomes more severe, the difference  $H_{min} - H$  (and similarly  $H - H_{max}$ ) is multiplied by a large constant. The summation of the normalized objectives and the penalty functions form the total objective function  $F_{obj}$ :

$$\text{minimize } F_{obj} = \sum_i w_i \cdot f_{obj,i} + \sum_i p_i \quad (8.20)$$

where  $p_i$  represent all penalty functions, and  $w_i$  represent weights used to weight the individual objectives. The weighting factors can be used to shift the design emphasis on, say, the convective heat flux, or on work output, for example. Clearly, the reduction of a multicriteria optimization problem to a single objective function introduces significant subjectiveness to the problem. By choosing weights before optimizing, the quality of this decision is not known and introduces uncertainty (148). Ultimately, this approach is no ideal, but only a starting point to better designs in thermoacoustics.

It can be shown that unconstrained optimization using penalty functions can yield the optimal solution of the original objective if the penalty imposed on the new “auxiliary function” (which is the combination of the “primal function” and the penalty) is sufficiently large. On the other hand, a penalty that is too large can lead to problems when trying to solve the optimization problem; the problem can become “ill-conditioned” (149). Consequently, the penalty function has to assume a value of 0 when the design constraints are not violated, and “large” if a bound is violated. The following sections will elaborate on the derivation of the objective functions and the penalty functions specific to this problem.

### 8.5.3 The Optimization Method: Nelder-Mead Simplex

The Nelder-Mead search algorithm (150) in a  $d$ -dimensional space uses  $d + 1$  points to determine a downhill direction of an objective function. It does not rely on gradients, and

thus the function does not have to be differentiable for the algorithm to be successful. As such, it is classified as a “direct search method” (151). For any given surface, the algorithm uses three points (corners of a triangle), evaluates the function values, and then applies one of four moves to the worst point: reflection, expansion, contraction, and shrinkage. The simplex changes its shape, and the one new function value is evaluated and compared to the one it has replaced. Based on the behavior of the function value from one iteration to the next, the algorithm chooses which modification to apply (152). The algorithm uses an initial guess as input, and then varies the variables according the simplex function values. In the current case, it will vary both axial and lateral dimensions of the used rectangular domain. The hot side temperature is estimated before the first iteration based on the axial domain dimension and a given bulk temperature gradient. Locally, this temperature gradient varies significantly as the heat flux across the top surface is accounted for (as calculated by COMSOL).

## 8.6 IMPLEMENTED OPTIMIZATION ROUTINE

As introduced above, the optimization requires knowledge of the maximum possible value of each of the four objectives. A preprocessor using COMSOL calculates the heat fluxes across the top and cold surfaces for all possible domain permutations. The feasible region is subdivided into a grid of L,H points and at each node, the objective functions are evaluated. The result is a matrix of objective function values as a function of both L and H:

```

given Lmax, Hmax
i,j=1
for i=1:stepsize
  for j=1:stepsize
    L = i * Lmax / stepsize
    H= j * Hmax / stepsize
    objective(i,j) = COMSOL calculations (L,H)
  end
  j=1
end
return objective

```

This solution routine is shown graphically in Figure 109. First, we calculate the extrema of the objectives that can be reached given a set of allowable domain dimensions. Function 1 (F1) passes this information into COMSOL, where the temperature distribution for each case is calculated. As a result, we determine the work output, viscous resistance and the heat fluxes that correspond to each of the extreme domain sizes. This information is stored in a file.

Next, we define a vector  $\mathbf{v}_0$  that contains the initial guess for variables  $L$  and  $H$ . `fminsearch` passes this information into Function 2 (F2), which in turn calls COMSOL to perform temperature calculations for the specific domain. As a result, the “local” work output, resistance and heat fluxes are calculated. The values for the extrema calculated before are read from a file and used to normalize the objectives. If the algorithm determines that the current solution is optimal, it terminates the process; otherwise, it derives a new guess for domain dimensions which is passed back into the algorithm.

### 8.6.1 Mesh Dependence of the Solution

We conducted a sensitivity analysis in regard to the heat flux through the top surface of the domain (subject to convective heat flux). The mesh was refined in 5 steps, increasing the cell count by a factor of approximately 4 each time. The initial mesh contained 516 cells. The largest mesh that COMSOL was able to solve contained over 132,000 cells. We found that relative to the total value of the heat flux, the error resulting from the coarse mesh is approximately 2%. Figure 110 shows a plot of the heat flux post-processing data versus used mesh size. It shows that the step improvement is leveling off after a value of  $10^5$ , and thus a further increase of error can be assumed to be negligible.

### 8.6.2 Pre-Processing Accuracy

Preprocessing for the optimization calculates all possible values for work output, resistance, and heat fluxes in the feasible domain. Their values are dependent on the domain dimensions, where all other previously mentioned parameters (such as channel size and temperature gradient) are assumed to be constant. This allows for visualization of the results using

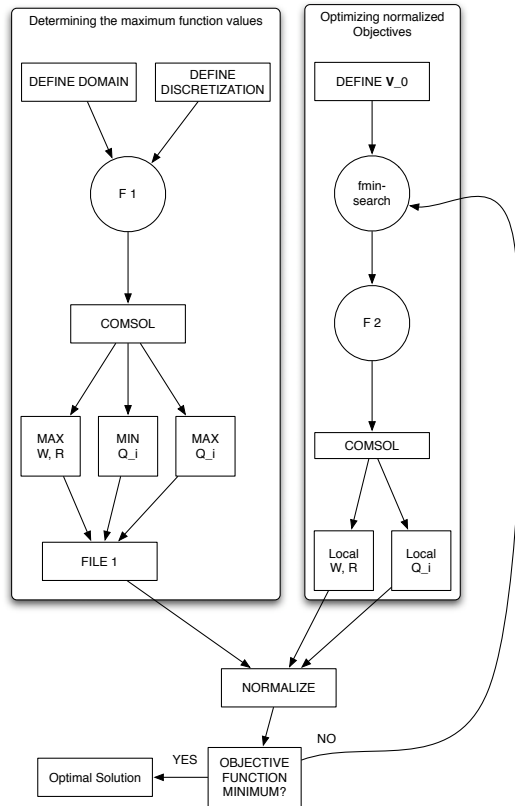


Figure 109: Flow diagram of the optimization routine, including the preprocessor

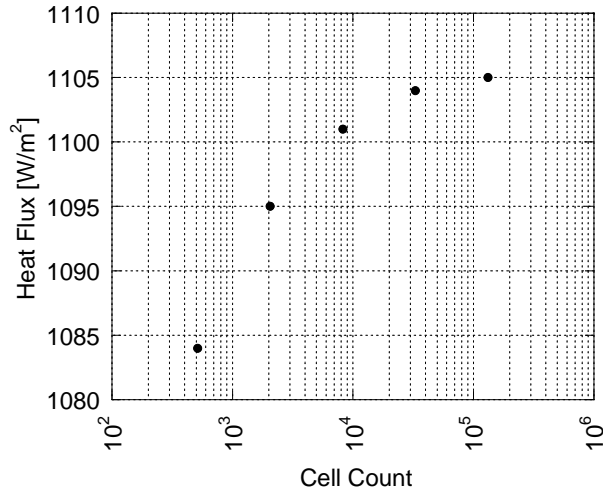


Figure 110: Illustration of the error resulting from using a coarse mesh rather than a refined mesh in COMSOL. The error is less than 2% and not expected to rise further with increasing cell count.

surface and contour plots. The calculation of the normalized heat fluxes requires COMSOL to be executed twice for each combination of domain width and height. This is very resource intensive\*, and can severely slow down the entire process, especially when considering that this optimization is for only two decision variables. The optimization (the right hand side of Figure 109) only requires one COMSOL evaluation. The hardware used is a computer with a 3.2 GHz Pentium 4 processor, using 2GB of RAM. This sensitivity analysis was done with grids of  $5 \times 5$ ,  $10 \times 10$ ,  $20 \times 20$ , and  $40 \times 40$  cells. The domain sizes were kept constant. The results are shown in Table 22.

The sensitivity analysis in regard to the pre-processing and determination of the respective extreme values of the heat fluxes calculated by COMSOL shows that there is very little variation when the discretization of the grid is changed. This is because the functions for the heat fluxes are monotonous, and their maxima and minima occur on the boundary where

---

\*A discretization of  $40 \times 40$  cells requires 1600 COMSOL evaluations

Table 22: Sensitivity analysis for the grid size during the calculations of maximum values of heat fluxes

Discretization	$Q_{\text{top,max}}$	$Q_{\text{top,min}}$	$Q_{\text{out,max}}$	$Q_{\text{out,min}}$	Sol'n time
$5 \times 5$	174.6	6.88	65	0.003	approx. 5 min
$10 \times 10$	174.6	6.83	65	0.003	approx. 10 min
$20 \times 20$	174.6	6.62	65	0.003	30 min
$40 \times 40$	174.6	6.4	65	0.003	90 min

L and H are at extrema as well. This is an important discovery, and could not have been assumed before doing this evaluation.

## 8.7 RESULTS

The feasible domain for the length and height (or radius) a thermoacoustic stack is defined to be  $0.1m$  to  $0.5m$ . This range is large, but it is chosen in order to illustrate the behavior of the objective functions outside of the “practical” range. The results are presented in the form of contour plots of the objective function and a variation of the stack material, a variation of the initial guess (for constant material and weights), and finally a variation of the weights for each of the four objectives.

### 8.7.1 Shape of the Objective Function

As a result of the preprocessor, we can determine the overall shape of the objective function. Since it is only dependent on two parameters, it can be illustrated using a surface plot, as shown in Figure 111. This figure represents the objectives weighted equally at 25% each. By visual inspection, we can immediately see that this function is not convex. However, it

shows a clear maximum at high values of  $L$  and a rising objective value for small  $L$  and increasing  $H$ . For the range of variables provided, there is a weak local minimum at  $H_{max}$  and  $L \approx 5$ . The global minimum is located at  $L_{min}$  and a value of  $H \approx 0.1 H_{max}$ . We must ensure that the solution disregards the local minimum and considers only the global minimum as the true solution.

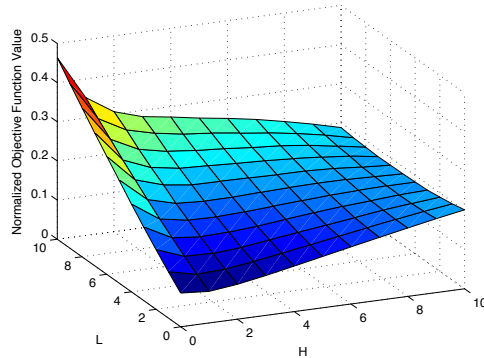


Figure 111: Objective function as a function of domain dimensions for PMMA

In order to provide more insight in the behavior of this function depending on the material used for the stack, we ran this optimization for five additional (feasible) materials. The physical properties of the materials used are given in Table 23. These results are given in the Appendix in Figure 121. The overall trend is the same regardless of material, but we can notice slight variation in the shape of the objective function. The highly thermally conductive materials (aluminum and copper) are shown to be more sensitive to a variation in stack dimension than the alternative materials.

### 8.7.2 Optimization Behavior

The behavior of the optimization routine can be shown when we consider a contour plot of the objective function and plot the domain size for each function call. This result is shown in Figure 112. It shows how the optimizer changes the domain variables for each iteration step for different initial guesses (constant  $L$ ,  $H$  varying). Because of the shape of the objective

Table 23: Properties (density, specific heat, and thermal conductivity) of the materials used in the material variation.

<b>Material</b>	$\rho$ [kg/m <sup>3</sup> ]	$c_p$ [J/kgK]	$k$ [W/mK]
<i>Aluminium</i>	2700	900	160
<i>Copper</i>	8700	385	400
<i>Titanium</i>	4940	710	7.5
<i>Steel</i>	7850	475	44.5
<i>PMMA</i>	1190	1420	0.19
<i>SiO<sub>2</sub></i>	220	730	1.4

function in the area of the initial guesses, the solution converges to the same combination of  $L$  and  $H$  for each case, and the local minimum is ignored. Figure 122 in the Appendix illustrates additional cases of this analysis, including some where the solution converges to the local minimum. This is a result of the stepsize that is prescribed by the Nelder-Mead Simplex method.

### 8.7.3 Varying the Weights

For the PMMA case\*, we varied the weights, with all cases highlighting emphasis on one objective or group of objectives (i.e. power and resistance is one group, the heat fluxes another group). Table 24 shows the weight distribution for all cases.

Figure 113 shows the case for an emphasis on just the heat loss via convection and conduction (Case 5). We can see that in order to minimize the heat losses, we must design the stack to be as small as possible. This is a change from the previously discussed case of equal weights for all four objectives. The remaining contour plots are shown in Figure 123 in the Appendix.

---

\*The tendencies that are shown in this variation are very similar for all other materials considered.

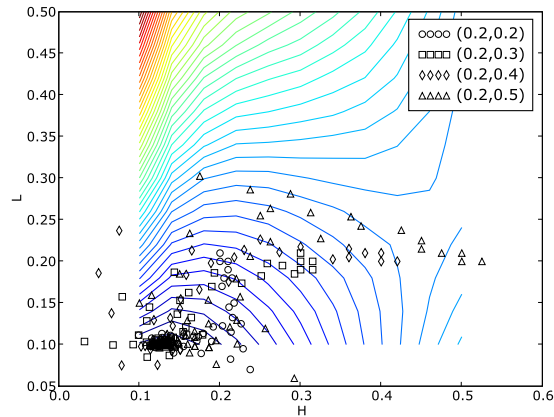


Figure 112: Behavior of the optimization as a function of initial guess

#### 8.7.4 Interpretation of the Results

The surface plots for all materials show that the objective function is not convex. For this reason, there are several local optima, but from a visual inspection, only one global optimum. It is obvious that the total length is always decreased to its imposed minimum value. The penalty functions keep this boundary from being violated. This location corresponds to a mechanically feasible design, as it shows that the radius of the stack should be roughly 20% larger than the length of the stack (again, provided the designer weighs all objectives equally). As a result of the material variation, we can identify slight changes in the absolute values of the objective function, but not a drastic change in the general tendencies and shape. The ideal design remains at the smallest value for  $L$  and a slightly larger value for the radius.

The illustration of the optimization behavior showed all combinations of  $L$  and  $H$  that `fminsearch` considered. It demonstrated that for most starting points, the area of the minimum objective value was reached. For starting points that were in the plateau regions of the objective function, `fminsearch` was not able to reach this global optimum, which could be a result of limited step size. For large initial values of  $L$  and  $D$ , the optimization

Table 24: Weight distribution (in %) for all objectives (acoustic work  $W$ , viscous resistance  $R_\nu$ , convective and conductive heat fluxes  $Q$ )

Case	W	$R_\nu$	$Q_{\text{conv}}$	$Q_{\text{cond}}$
1	70	10	10	10
2	10	70	10	10
3	10	10	70	10
4	10	10	10	70
5	0	0	50	50
6	50	50	0	0

found the other “optimum” which would result in as large a design as possible. This is again rooted in the limited initial step size.

The variation of the weights for each objective shows how the design would change if emphasis is given to one objective in particular; for example, maximum power while essentially ignoring all losses. In this case, the result showed that as large a design as possible is the solution (which we could have derived from investigating the function for power in Equation 8.10), refer to Figure 123 for the corresponding plot. A more interesting derivation is the design with an emphasis on avoiding the convective/conductive heat loss or the conductive heat loss (and the combination of both), which can be interpreted as “as small as possible.” The following design criteria can then be deduced:

- Design as small as possible to minimize thermal losses;
- Increase tube diameter to increase power output, at cost of higher thermal losses, with an optimum at about  $H \approx 1.2L$ ;
- Design as large as possible to maximize power output.

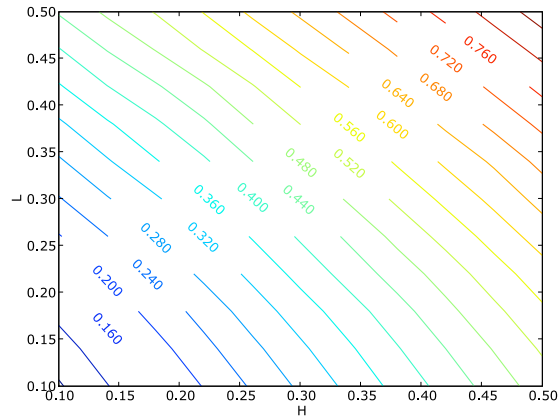


Figure 113: Contours for Case 5: emphasis on the heat flux objectives (convection and conduction)

### 8.7.5 Discussion of the Solution Strategy

In this section, one method of optimization applied to the design of thermoacoustic stacks was introduced. The approach utilized several subjective inputs that render the minima found here as “global” only within the framework of each selection of weights as well as the penalty function. The performed optimization is commonly referred to as “blackbox optimization” (BBO) because the optimization routine has no knowledge of the exact behavior of the objective function. As a result, we cannot determine the mathematical description of the objective function, which forces the utilization of a search-based optimization routine. Kolda et al. (153) state that search methods were used widely in early optimization techniques but then abandoned because they lack exact mathematical description, which is apparent in the present model. Thus, exact calculus based optimization cannot be applied. Nonetheless, the general methodology is still applied today (154). Wang et al. (155) state that BBO is not guaranteed to find a global optimum (also apparent in the presented results in Figure 122) because it can only make decisions based on limited search history. In the present model, the

search direction is determined by the three-sided simplex and does not consider any previous information.

Furthermore, Kargupta et al. (156) state that using penalty functions causes a separate set of optimization as there is an optimal penalty function for each objective where the solution is neither infeasible (weak penalty function) or dominated by it (strong penalty function). A problem arises because the optimal penalty functions are initially not known. In the present case, the penalty functions are only set once and not investigated further. Consequently, it must be stated that the used methodology is generally suboptimal. The results must not be considered global optima. In spite of its introductory nature, the presented work is an important contribution to thermoacoustics as it merges the theoretical optimization approach with thermal investigation and thermoacoustics.

## 9.0 CONCLUSIONS

### 9.1 SUMMARY

Thermoacoustic devices are currently used in niche applications, especially in cryogenic refrigeration. In general, refrigeration has been and will be the primary application of thermoacoustic systems. Their operation does not rely on conventional refrigeration cycles or conventional refrigerants. Instead, TARs' operation is solely based on the interaction of a benign working gas with a porous solid. It was shown that thermoacoustic is refrigeration environmentally sound, and the potential to advance into broader marketability was demonstrated. In addition, the systems are mechanically simple, exhibiting good cradle-to-grave performance. Traditionally, thermoacoustic refrigerators are large in size and a decrease of their footprint is required in order to achieve a more mainstream application. In smaller systems, however, the influence of the thermal properties of the driving components increases in importance. To date, the thermal properties of these components are largely ignored during the design phase, partially because the traditional design “works,” and partially because of a lack of understanding of the thermal energy fluxes that occur during operation. This work approached the issues arising due to miniaturization in three separate ways.

### 9.2 SUMMARY OF THE EXPERIMENTATION

First, a direct quantification of the influence of the thermal conductivity of the driving components on the performance of a thermoacoustic engine and refrigerator was performed. For the engine, stacks of several materials were used and the effect of the thermal conductivity

on the temperature distribution and sound generation was evaluated. It was found that the ceramic stack exhibited the best performance in regard to sound generation. It achieved the highest sound levels (upward of 110 *dB*) and required the lowest energy input of any material used to do so. As a result of the very low thermal conductivity of ceramic, however, the thermal losses to the surroundings were estimated to be the highest among all materials used because of the high temperature levels achieved.

The stack made of stainless steel tubes also exhibited good performance. Compared to the remaining materials (aluminum, brass, and copper) it has a low thermal conductivity. Thus, the sound levels achieved with stainless steel were also relatively high, but less than ceramic. The materials with a high thermal conductivity showed the worst performance as a thermoacoustic driver, although a clear distinction between each case was not possible. This was largely due to measurement uncertainties. Ultimately, however, it was found that the thermal properties of the driving stack influence the performance of a thermoacoustic engine, and should be considered in the design of these devices.

In order to investigate the influence of the thermal properties of the driving components of a thermoacoustic refrigerator, a speaker driven, half-wavelength TAR was designed. Inside the resonator, located close to the pressure antinode and velocity node, several thermoacoustic regenerator assemblies were tested. Beginning with a general investigation of the effects of regenerator placement, the ideal placement and driving frequency were determined. This information was gathered by temperature measurements through thermocouples and sound pressure measurements with a microphone and a ceramic regenerator. Once the ideal operating conditions were determined, a regenerator housing was inserted into the resonator. This assembly allowed for various regenerators designed with wire mesh screens to be tested under similar conditions. The regenerator assembly was water cooled. In order to show the influence of the thermal properties of the regenerator, two wire materials were chosen. Low thermal conductivity was achieved with Nylon screens, and high thermal conductivity was achieved with steel screens. In addition, two types of Nylon screen were used. One grade was hydraulically similar to the steel screen, while the second was finer. Obviously, the finer mesh resulted in a higher viscous resistance than the coarse mesh. The investigation was performed for several regenerator thicknesses and screen densities. The performance of

each assembly was quantified by the temperature difference and temperature levels achieved during operation.

Similar to the results from the engine, it was found that the thermal properties of the regenerator influence its heat pumping capabilities. As a result, it can be concluded that Nylon screens with a coarse mesh result in the best performance. That material yielded the highest temperature difference. The fine Nylon screen showed the next best performance overall. This illustrated that the thermal conductivity of the regenerator is an important design aspect, similar to the hydraulic properties. The fine mesh regenerator exhibited a high sensitivity to regenerator length, much more so than the coarse screen regenerators. The steel regenerator (having the same hydraulic properties as the coarse Nylon screen) exhibited the overall worst performance. The maximum achieved temperature difference was lower than for both Nylon regenerators. It was also found that the ideal regenerator length is very short compared to the total resonator length. In all cases, the best performance was found with regenerators of only 10 *mm* in length (compared to a length of greater than 2 *m* for the entire assembly). This shows that viscous losses start influencing the performance drastically as the regenerator length is increased.

As a conclusion, it must be stated that the thermal properties of the materials used in the driving components of thermoacoustic devices have to be considered in the design phase. Lower thermal conductivity has to lead to better performance in both engines and refrigerators. Ultimately a design utilizing a continuous regenerator rather than screens should be used. In accordance with the other findings, this regenerator should be made of a material with a very small thermal conductivity.

### 9.3 SUMMARY OF THE CFD ANALYSIS

Next, as a second means to achieve a decreased footprint of a thermoacoustic system, the introduction of curvature to the resonator tube was investigated. To this end, a CFD analysis was performed. The reason for this was two-fold. First, using CFD as an analysis tool in

thermoacoustics is heavily underused. Secondly, this tool allows for a detailed investigation of the thermoacoustic effect that is difficult, if not impossible, to achieve with experimentation.

There are few examples of working CFD simulations of thermoacoustic devices. The present simulations combined the ideas presented in two previous studies and successfully recreated the thermoacoustic effect in a standing wave engine. A constant temperature gradient across the stack of the model was sufficient to sustain strong oscillations. In order to cause these oscillations, the flow field was initialized with a small pressure disturbance.

First, the simulation was used to investigate the thermoacoustic effect in detail. The phase difference between the pressure and velocity components of the wave was investigated. Both components exhibited strictly sinusoidal behavior. The behavior of the gas temperature inside the stack, on the other hand, showed proof of the interaction of the stack assembly and the fluid. With respect to time, the temperature did not show strictly sinusoidal behavior as it is subject to entry and exit effects at both ends of the stack. These effects were further investigated using Fluent's visualization capabilities. Using contour plots, vector plots, and instantaneous stream traces, vortices in the vicinity of the channel openings were identified. It is these vortices that contribute to mixing effects that influence the gas temperature.

Furthermore, the simulation was used to investigate the influence of resonator curvature on the thermoacoustic effect. In addition to the straight tube base case, the thermoacoustic resonator was modeled with a 30°, 60°, and 90° bend that was applied over approximately half of the total device length. It was found that with increased curvature, the pressure amplitude in the compliance of the TAE (i.e. the pressure antinode) decreased. Also, it was shown using an energetic analysis inside the stack, that the heat transfer between the solid walls and the gas is adversely affected by resonator curvature. It is not conclusive, though, whether the change in heat transfer is cause or effect of the decreased pressure amplitude.

Visualization of the flow field was also applied to the investigation of curvature. As a metric for comparison, the pressure, velocity, and turbulence generation were investigated. It was verified that the minimum pressure achieved in the compliance (which is synonymous with a decrease in amplitude) was higher when the resonator was curved more severely. In addition, it was found that the curvature of the resonator caused a non-uniform velocity distribution in the resonator, specifically during time of negative velocity (i.e. gas streaming

from the open end towards the stack). This caused severe velocity gradients, which in turn caused high viscous stresses within the gas. This behavior is responsible for energy losses that contribute to the adverse effects of resonator curvature. Finally, it was also found that the generation of turbulence was also highest for the case of the highest degree of bending. This is consistent with the previous findings that an increased bending of the resonator decreases the performance of the thermoacoustic device.

As an additional study using the CFD simulation, the influence of the ratio of channel size and thermal penetration depth of the working gas was investigated. Rather than changing the model, the material properties of the working gas were changed to achieve this variation. Specifically, the thermal conductivity was increased to improve the thermal contact between the solid stack and the gas. It was found that there is a clear optimum of thermal contact. When thermal contact is weaker, the maximum pressure achieved is lower. The pressure amplitude also decreases if the thermal contact is better than the ideal value. This behavior is caused by the effect of the thermal contact on the phasing between pressure, velocity, and heat transfer. For the given simulation configuration, it was found that a gas having a thermal conductivity of roughly 4 times that of air resulted in the best performance of the TAE.

#### 9.4 SUMMARY OF THE OPTIMIZATION

Finally, combining the numerical modeling aspect of this work with the investigation of the thermal properties of the driving components, an optimization scheme is applied to thermoacoustics. This investigation focused on the stack of a simple standing wave engine, with the optimal geometry as the target of the optimization. In order to account for the temperature distribution inside the stack, a FEA model was utilized. The temperature information was used to calculate the heat flux across the outer shell of the stack, as well as the conductive heat flux leaving the cold end of the stack. This model was joined with simple representations of the thermoacoustic work and viscous resistance that are characteristic for each stack geometry. Assuming a cylindrical design, the stack radius and length were varied.

A simplex solver was used to find the optimal combination of the design parameters subject to four objectives. This investigation was performed for a variety of weights between each objective, as well as a variety of stack materials. It was found that the optimal design (using equal weights for acoustic power, viscous resistance, and both heat fluxes) is not trivial. The length should be chosen to be as small as possible, but the radius then showed a trend to be approximately 1.2 times the length. When focusing solely on acoustic power, the device should be designed to be as large as possible, meaning maximizing the length and radius of the stack.

## 9.5 OUTLOOK

This work has presented important advances in our understanding of thermoacoustic engines and refrigerators. These insights have been gained through novel experimental investigations and sophisticated CFD models. Of course, there are also potential extensions to this work, as described below, that could provide further insights into the fundamental science of thermoacoustics.

### 9.5.1 Advanced Experimentation

An improved engine setup will yield a better distinction between various stack materials. Specifically, a larger setup will allow for more robust data collection, also due to improved use of thermocouples. The temperature levels achieved in the TAR were much higher than for other thermoacoustic refrigeration systems. As the temperature differences increase, the effect of the thermal conductivity becomes easier to investigate. An improved TAR setup could yield lower total temperatures, closer to the cryogenic region.

### 9.5.2 Advanced Modeling

The presented CFD model disregards fluid behavior that may result from transport through a porous medium. Nijeholt et al. (114) had introduced a fluid model based on body forces

as a description for the regenerator in a thermoacoustic device. Combining their work with the present model will allow future work to explore traveling wave engines as opposed to standing wave engines. The importance lies in the applicability of the traveling wave engine compared to the standing wave counterpart. De Lemos (157) provides a detailed insight into the modeling of porous media, and the turbulence associated with them. Beginning with the Darcy velocity, the continuity equation can be re-written (from the standard form introduced above in Equation 5.2) as

$$\frac{\partial(\varphi\rho)}{\partial t} + \nabla \cdot (\rho\mathbf{u}_D) = 0 \quad (9.1)$$

where  $\varphi$  is the volume porosity defined as the ratio of open volume to the open and fluid volume. The Darcy law of motion is given by Equation 9.2 (157):

$$\mathbf{u}_D = -\frac{K}{\mu} (\nabla p \rho \mathbf{g}) \quad (9.2)$$

where  $p$  is the pressure, and  $K$  is the medium permeability. An elaboration on this model is given by Brinkmann (157). This elaboration shown in Equation 9.3 accounts for the behavior of the velocity profiles near the walls.

$$\mathbf{u}_D = -\frac{K}{\mu} (\nabla p \rho \mathbf{g}) + K \nabla \cdot (\nabla \cdot \mathbf{u}_D) \quad (9.3)$$

Yet another elaboration on this model is given by Forchheimer, as shown in Equation 9.4 (157):

$$\mathbf{u}_D = -\frac{K}{\mu} (\nabla p \rho \mathbf{g}) + K \nabla \cdot (\nabla \cdot \mathbf{u}_D) - \frac{F|\mathbf{u}_D|\mathbf{u}_D}{\nu} \quad (9.4)$$

In the Forchheimer equation, the inertia coefficient  $F$  accounts for inertia effects. Using this approach in modeling thermoacoustic devices will enable future models to account for the effects of fluid behavior inside the regenerator. Accounting for these effects mathematically rather than physically will reduce the meshing requirements significantly as the size of the flow channels decrease to traveling wave levels, especially relative to resonator dimensions. Also, additional heat transfer considerations, as shown in by Piccolo, Paek and Mozurkevich (98; 130; 158) may be included in the simulation to account for a more realistic interaction

between the solid and gas. Also, the stack of the model could be meshed and accounted for as solid instead of accounted for as walls with non-zero wall thickness.

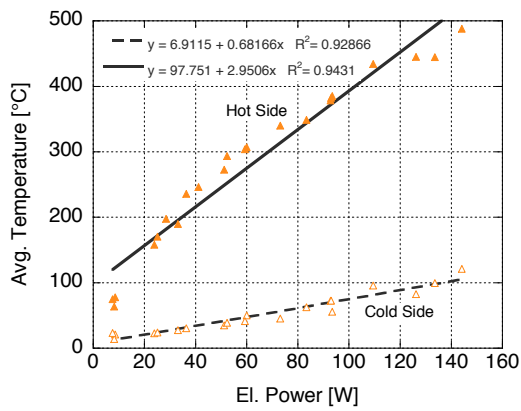
Additional accuracy in the investigation of the effect of curvature can be gained by applying a 3-D model instead of the presented 2-D model. This type of simulation may include secondary flows that the present simulation may not capture. However, this evolution of the simulation results in a significant increase in the computational cost but could provide a more accurate representation of a physical engine.

## APPENDIX A

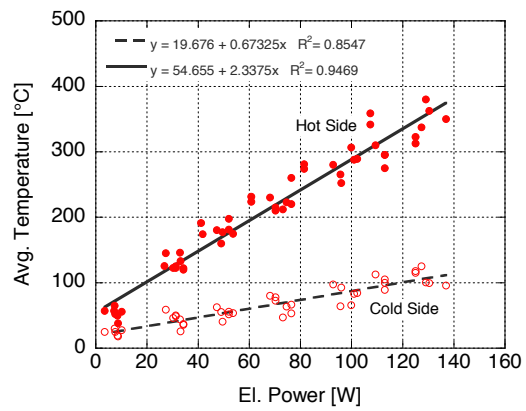
### ADDITIONAL PLOTS: STACK MATERIAL VARIATION

#### A.1 TEMPERATURE DATA (COLD AND HOT) STACK MATERIAL VARIATION

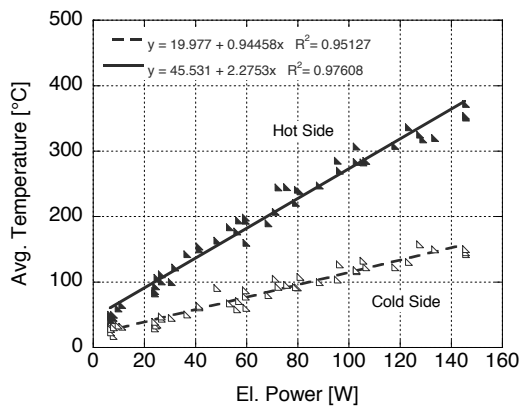
Complete temperature data from the experimental investigation of the stack material variation of the thermoacoustic engine. The decrease of the hot side and increase of the cold side temperature as the thermal conductivity of the stack increases.



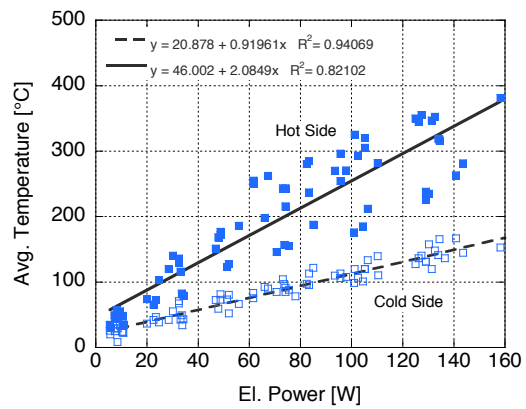
(a) Ceramic



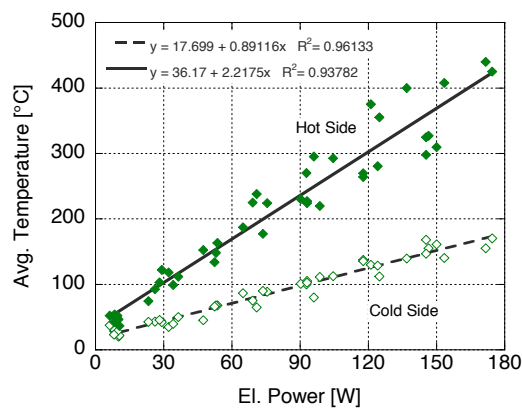
(b) Stainless



(c) Brass



(d) Aluminum

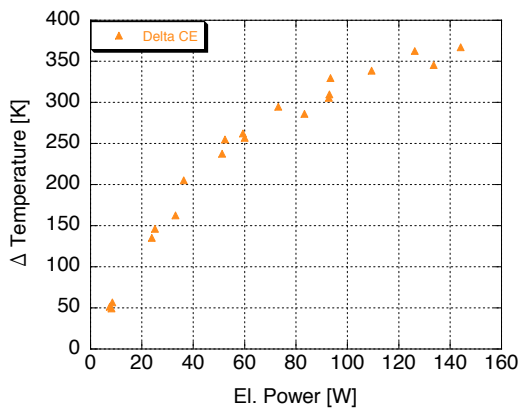


(e) Copper

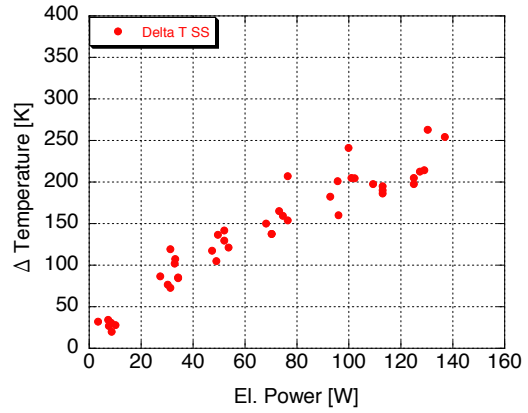
Figure 114: Hot side and cold side temperature, including linear curve fits, for various stack materials ranging from low thermal conductivity (a) to high thermal conductivity (e)

## **A.2 TEMPERATURE DIFFERENCE OF DIFFERENT STACK MATERIALS**

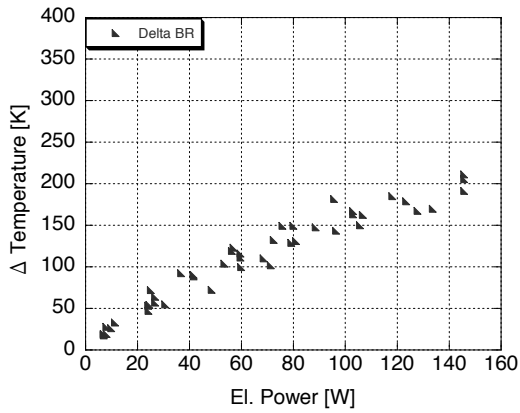
Complete data, temperature difference from the experimental investigation of the thermoacoustic engine. The ability to sustain a driving temperature gradient across the stack decreases as the thermal conductivity of the stack increases.



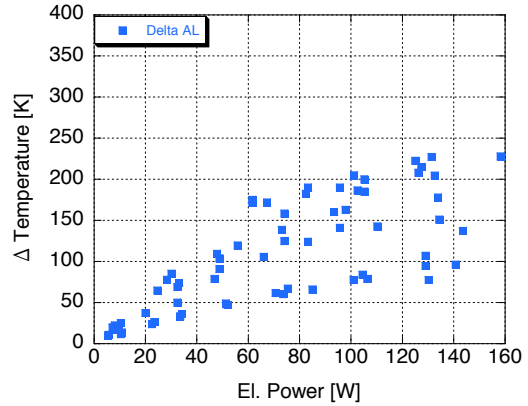
(a) Ceramic



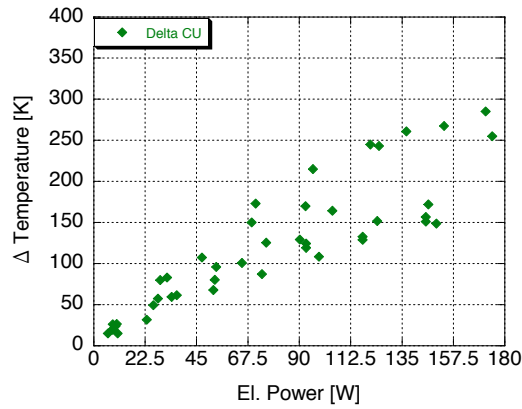
(b) Stainless



(c) Brass



(d) Aluminum

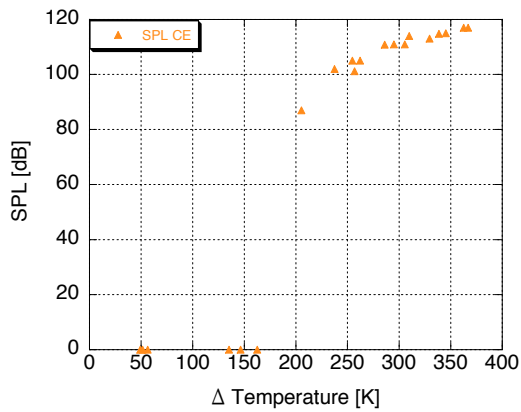


(e) Copper

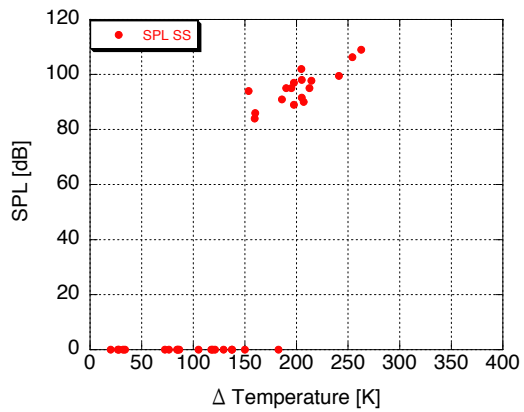
Figure 115: Temperature difference across the stack ranging from materials with low thermal conductivity (a) to high thermal conductivity (e)

### **A.3 SOUND PRESSURE LEVEL AS A FUNCTION OF TEMPERATURE DIFFERENCE**

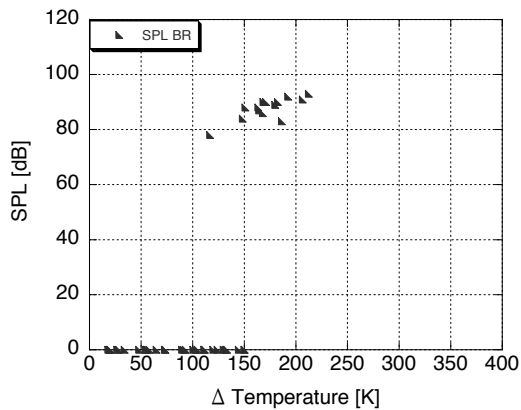
Individual data plots of the sound pressure level from the material variation of the thermoacoustic engine. As the thermal conductivity of the stack increases, the SPL of the engine decreases. The data is presented as a function of temperature difference.



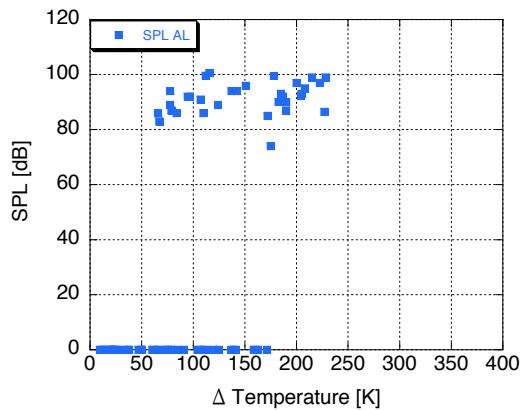
(a) Ceramic



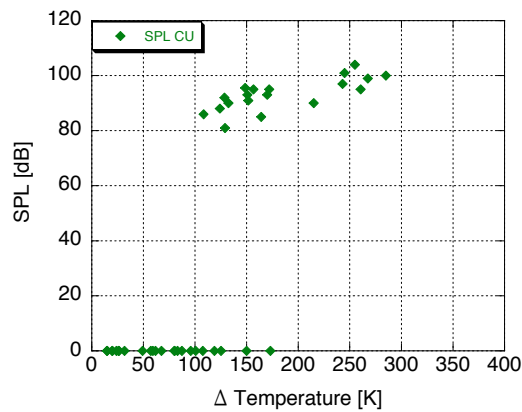
(b) Stainless



(c) Brass



(d) Aluminum

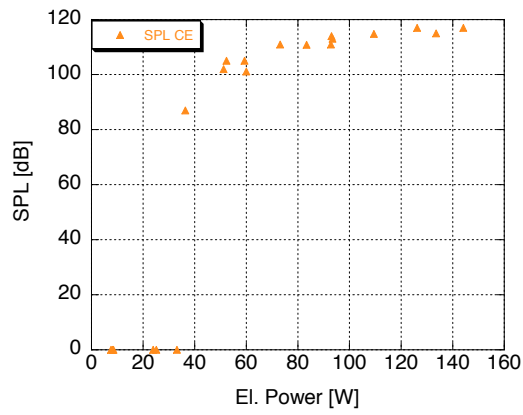


(e) Copper

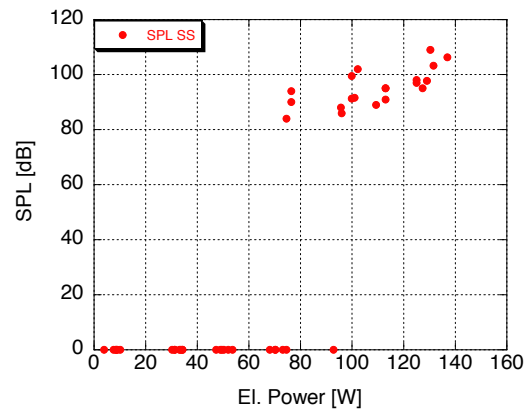
Figure 116: Sound pressure level achieved by each stack as a function of temperature difference, ranging from materials with low thermal conductivity (a) to high thermal conductivity (e)

#### A.4 SOUND PRESSURE LEVEL AS A FUNCTION OF INPUT POWER

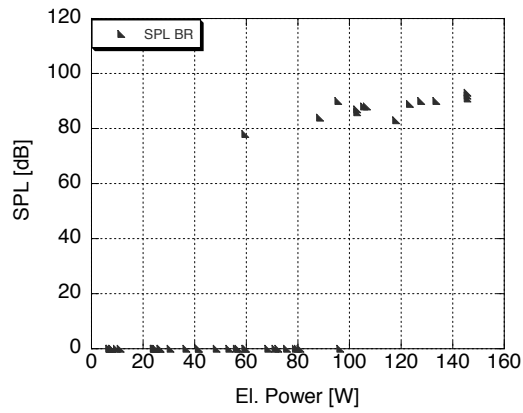
Individual data plots of the sound pressure level from the material variation of the thermoacoustic engine. As the thermal conductivity of the stack increases, the SPL of the engine decreases. The data is presented as a function of electrical input power.



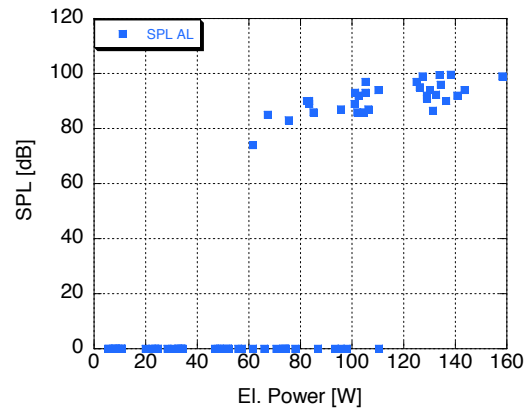
(a) Ceramic



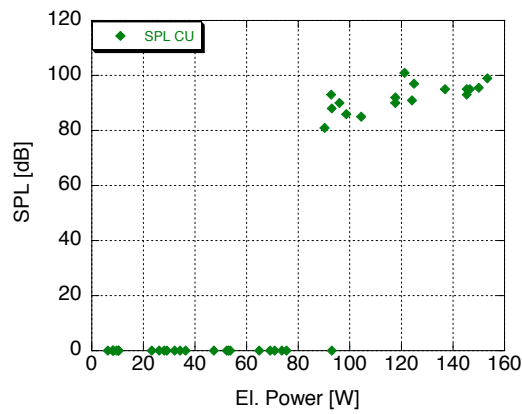
(b) Stainless



(c) Brass



(d) Aluminum

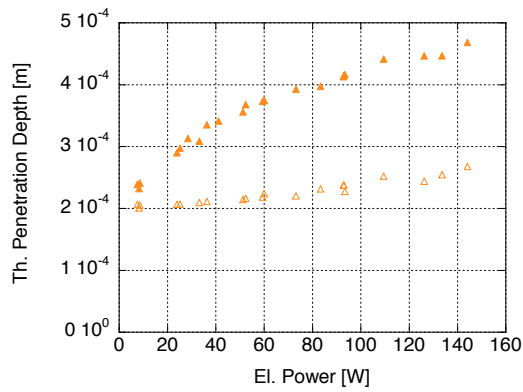


(e) Copper

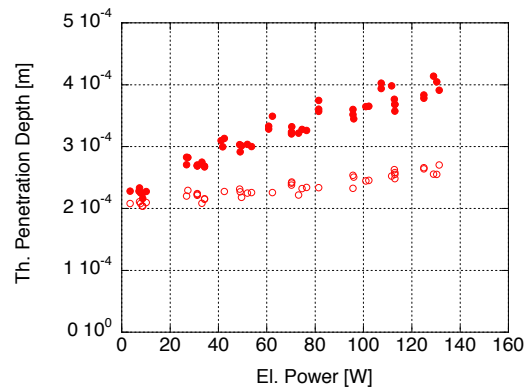
Figure 117: Sound pressure level achieved by each stack as a function of input power, ranging from materials with low thermal conductivity (a) to high thermal conductivity (e)

## **A.5 THERMAL PENETRATION DEPTH AS A FUNCTION OF INPUT POWER**

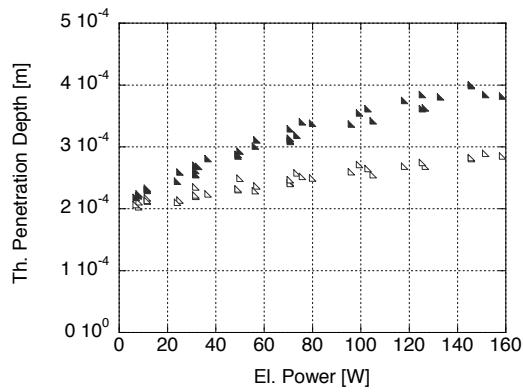
The thermal penetration depth of the working gas is temperature dependent. Thus, the operating condition of the stack changes. The data presented below illustrates this behavior.



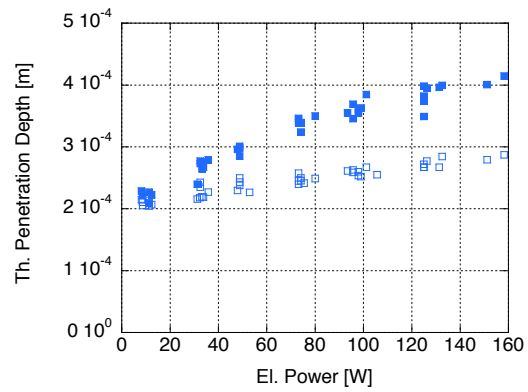
(a) Ceramic



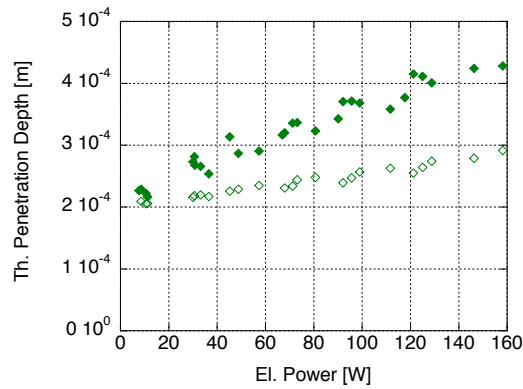
(b) Stainless



(c) Brass



(d) Aluminum



(e) Copper

Figure 118: Thermal penetration depth as a function of input power for each stack material, ranging from materials with low thermal conductivity (a) to high thermal conductivity (e)

## **A.6 RATIO OF CHANNEL SIZE AND THERMAL PENETRATION DEPTH AS A FUNCTION OF INPUT POWER**

The driving metric of a thermoacoustic device is the ratio of the thermal penetration depth and the channel size of the stack. As the thermal penetration depth is temperature dependent, the change of this relevant ratio must be investigated.

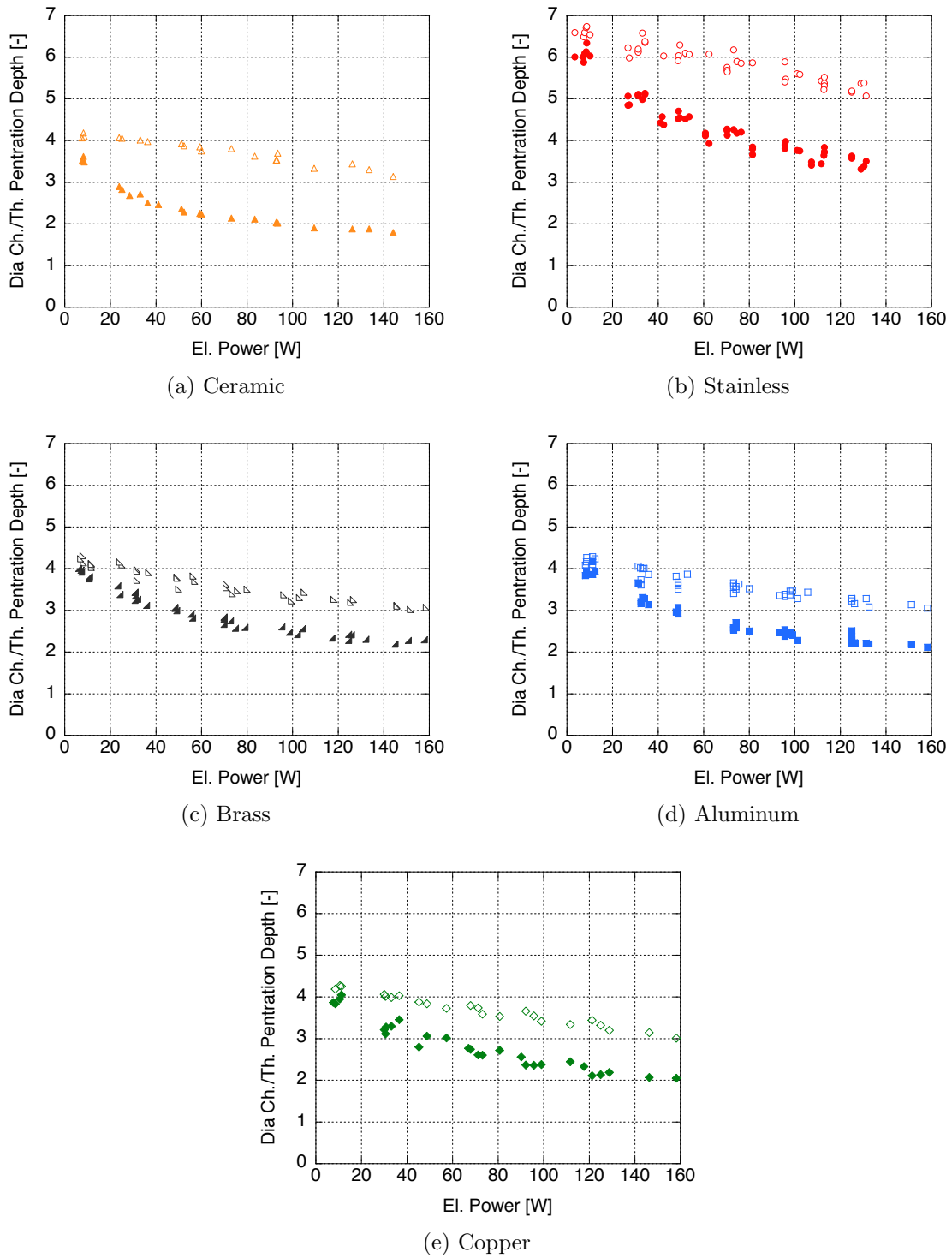


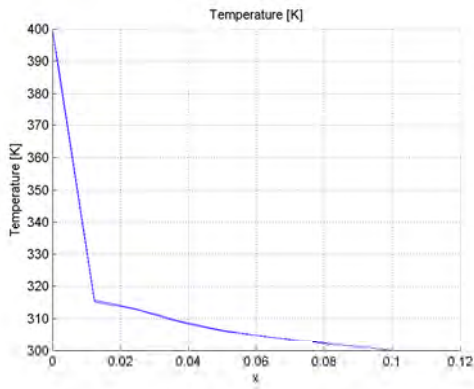
Figure 119: Ratio of the channel size and thermal penetration depth as a function of input power for each stack material, ranging from materials with low thermal conductivity (a) to high thermal conductivity (e)

## APPENDIX B

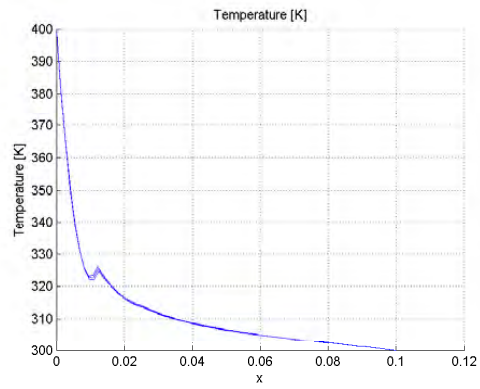
### ADDITIONAL PLOTS, OPTIMIZATION

#### B.1 TEMPERATURE DISTRIBUTIONS FOR DIFFERENT ELEMENT TYPES

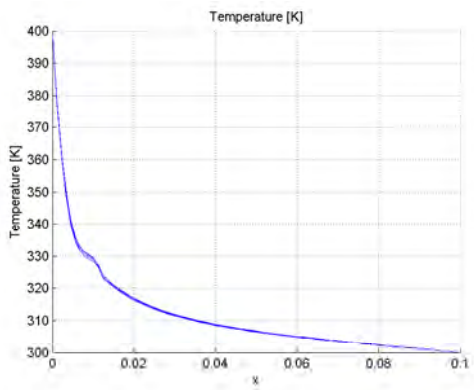
This figure illustrates the temperature trends across the stack assembly as a function of input power. This information is used for the calculation of thermal losses in Section [4.3](#)



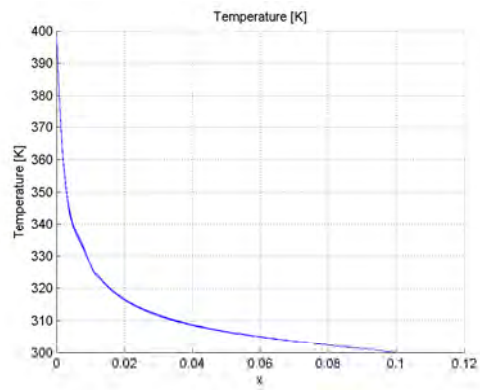
(a) Lagrange Linear



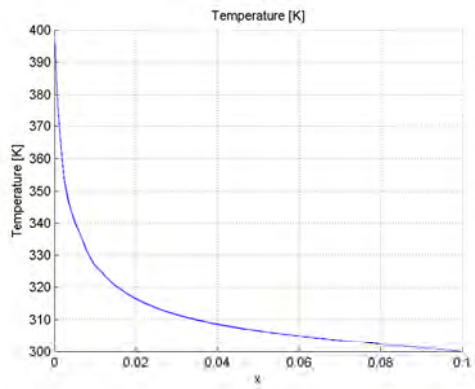
(b) Lagrange Quadratic (Default)



(c) Lagrange Cubic



(d) Lagrange Quartic

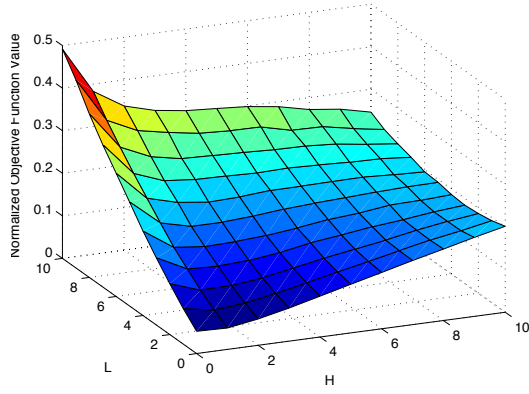


(e) Lagrange Quintic

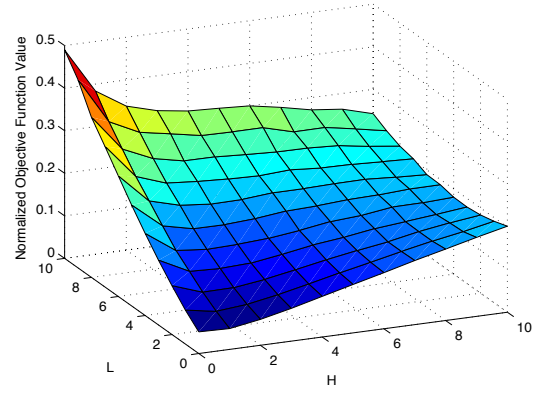
Figure 120: Illustration of the surface temperature distribution for a fixed domain size as a function of element type (Linear through quintic). Higher order elements minimize errors.

## B.2 PLOTS CORRESPONDING TO THE MATERIAL VARIATION

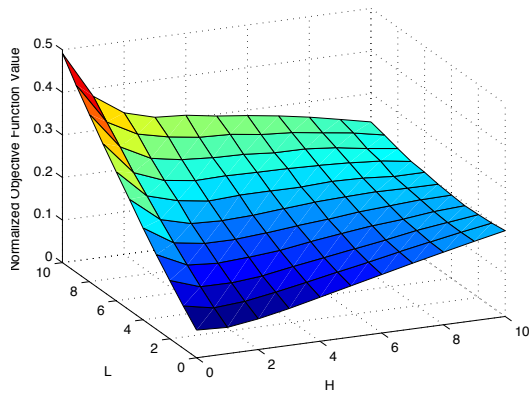
The following surface plots illustrate the effect of the variation of the material used for the calculations in COMSOL. This is a combination of all four objectives, with equal weights of 25%.



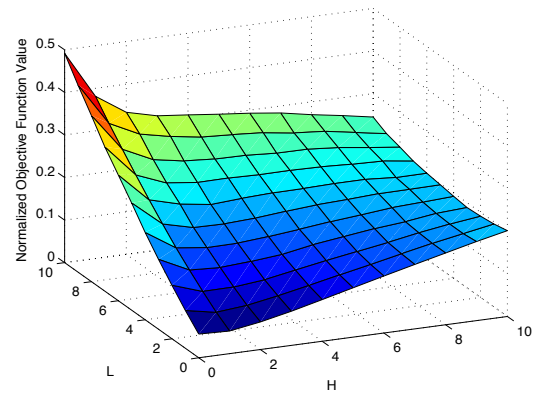
(a) Aluminium



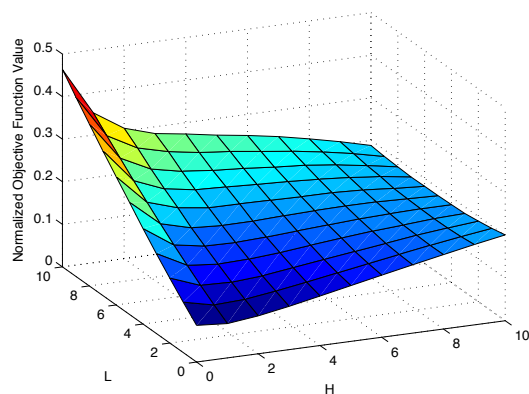
(b) Copper



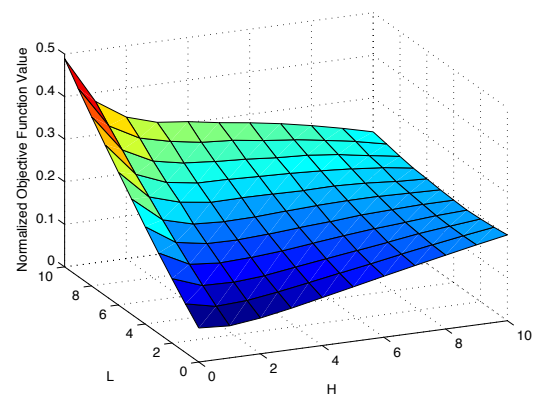
(c) Titanium



(d) Steel



(e) PMMA

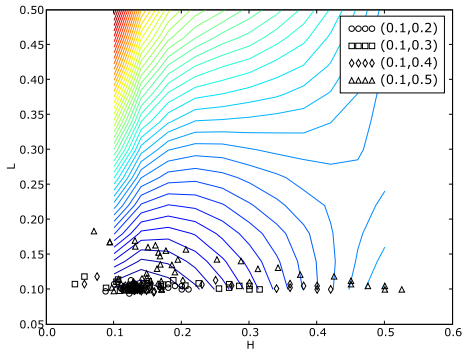


(f) Silicon Dioxide

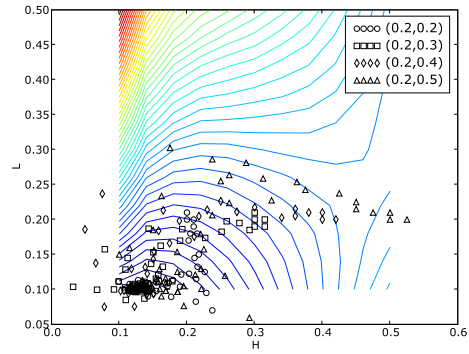
Figure 121: Variation of the stack material

### B.3 PLOTS SHOWING THE BEHAVIOR OF “FMINSEARCH”

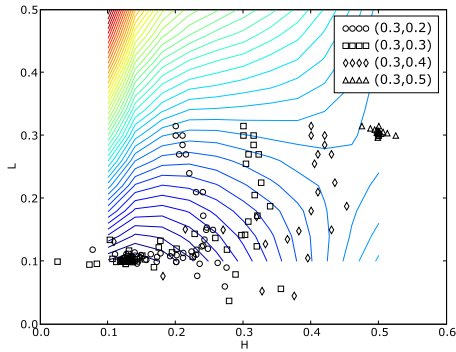
These plots illustrate the behavior of the optimizer for different starting points. Each of the five cases shows different starting points for a constant domain length  $L$ . The material used is PMMA, and the objective function is shown as a contour plot.



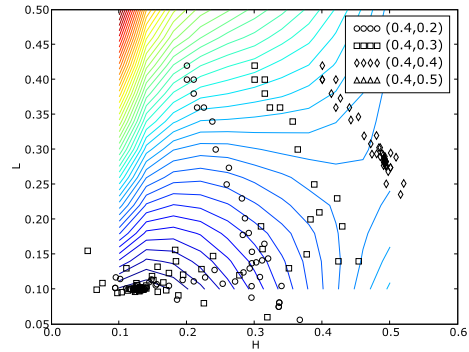
(a) Varying H with  $L = 0.1$



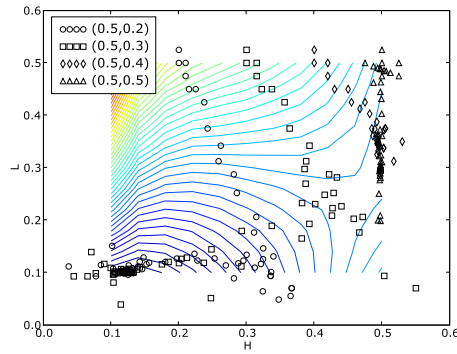
(b) Varying H with  $L = 0.2$



(c) Varying H with  $L = 0.3$



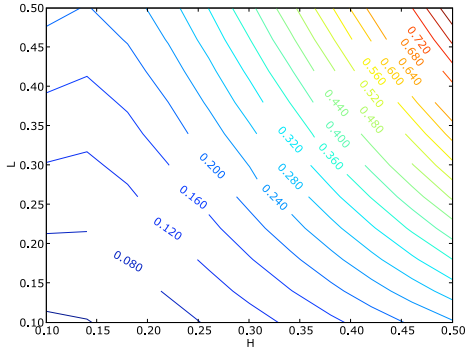
(d) Varying H with  $L = 0.4$



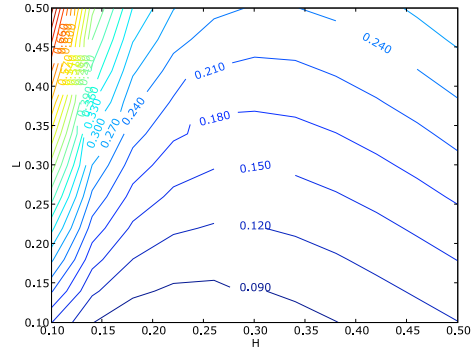
(e) Varying H with  $L = 0.5$

Figure 122: Variation of the starting points for constant L each (PMMA).

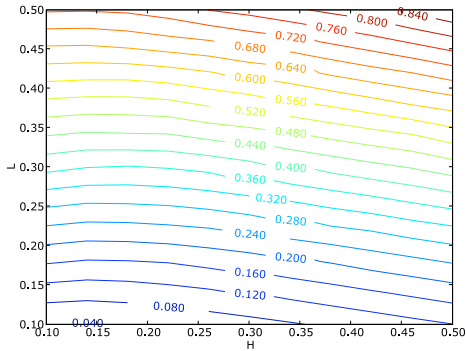
## B.4 VARIATION OF THE WEIGHTS FOR EACH OBJECTIVE



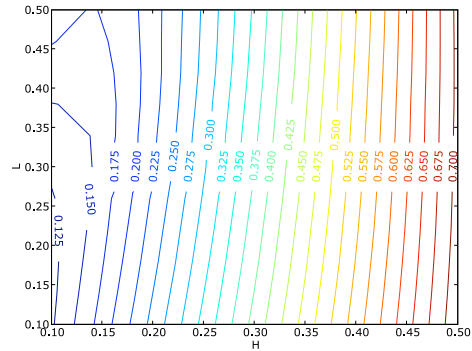
(a) Case 1: Emphasis on Power



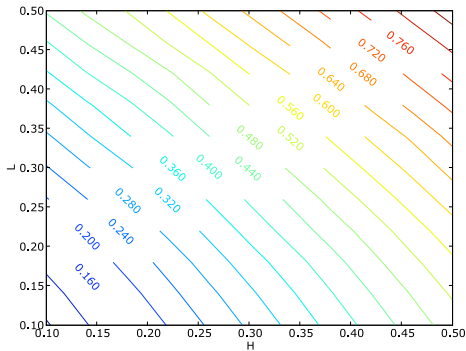
(b) Case 2: Emphasis on Resistance



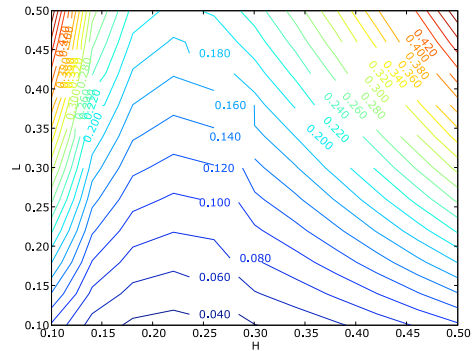
(c) Case 3: Emphasis on Convective Heat Flux



(d) Case 4: Emphasis on Conductive Heat Flux



(e) Case 5: Emphasis on Heat Loss



(f) Case 6: Emphasis on Power and Resistance

Figure 123: Variation of the Weights for each Objective, with case numbers corresponding to Table 24

## BIBLIOGRAPHY

- [1] S. L. Garrett, *Reinventing the engine*, Nature, **Vol. 339** pp. 303–305 (1999).
- [2] S. C. Kaushik, S. Kumar, *Finite time thermodynamic analysis of endoreversible Stirling heat engine with regenerative losses*, Energy, **Vol. 25** pp. 989–1003 (2000).
- [3] N. Kagawa, *Regenerative Thermal Machines*, International Institute for Refrigeration, Paris (2000).
- [4] G. W. Swift, S. Backhaus, *A resonant, self-pumped, circulating thermoacoustic heat exchanger*, Journal of the Acoustical Society of America, **Vol. 16 (5)** pp. 2923–2938 (2004).
- [5] A. C. Clarke, *Profiles of the Future: An Inquiry Into the Limits of the Possible*, Holt, Rinehart, and Winston, New York (1984).
- [6] N. Rott, *Damped and thermally driven acoustic oscillations in wide and narrow tubes*, Zeitschrift für angewandte Mathematik und Physik, **Vol. 20** pp. 230–243 (1969).
- [7] N. Rott, *Thermoacoustics*, Advances in Applied Mechanics, **Vol. 20** pp. 135–175 (1980).
- [8] P. H. Ceperley, *US Pat. No. 4114380* (1978).
- [9] P. H. Ceperley, *Gain and efficiency of a short traveling wave heat engine*, Journal of the Acoustical Society of America, **Vol. 77 (3)** pp. 1239–1244 (1985).
- [10] G. W. Swift, *Thermoacoustics: A unifying perspective for some engines and refrigerators*, Acoustical Society of America, Melville NY (2002).
- [11] J. H. Xiao, *Thermoacoustic heat transportation and energy transformation, Part 1: Formulation of the problem*, Cryogenics, **Vol. 35 (1)** pp. 15–19 (1995).
- [12] J. H. Xiao, *Thermoacoustic heat transportation and energy transformation, Part 2: Isothermal wall thermoacoustic effects*, Cryogenics, **Vol. 35 (1)** pp. 21–26 (1995).
- [13] J. H. Xiao, *Thermoacoustic heat transportation and energy transformation, Part 3: Adiabatic wall thermoacoustic effects*, Cryogenics, **Vol. 35 (1)** pp. 27–29 (1995).

- [14] P. H. Ceperley, *A pistonless Stirling Engine - The traveling wave heat engine*, Journal of the Acoustical Society of America, **Vol. 66 (5)** pp. 1508–1513 (1979).
- [15] S. Backhaus, G. W. Swift, *A thermoacoustic Stirling heat engine: Detailed Study*, Journal of the Acoustical Society of America, **Vol. 107 (6)** pp. 3148–66 (2000).
- [16] P. H. Ceperley, *US Pat. No. 4355517* (1982).
- [17] S. Backhaus, G. W. Swift, *A Thermoacoustic Stirling Heat Engine*, Nature, **Vol. 399** pp. 335–338 (1999).
- [18] Y. Ueda, T. Biwa, U. Mizutani, T. Yazaki, *Experimental studies of a thermoacoustic Stirling prime mover and its application to a cooler*, Journal of the Acoustical Society of America, **Vol. 72 (3)** pp. 1134–1141 (2003).
- [19] C. M. DeBlok, N. A. Hendrikus, J. V. Rijt, *US Pat. No. 6314740* (2001).
- [20] K. J. Bastyr, R. M. Keolian, *High-frequency thermoacoustic-Stirling heat engine demonstration device*, Acoustics Research Letters Online, **Vol. 4 (2)** pp. 37–40 (2003).
- [21] M. Poese, *An Evolution of Compact Thermoacoustic Refrigeration Devices*, Ph.D. thesis, Pennsylvania State University (2004).
- [22] T. Yazaki, A. Iwata, T. Maekawa, A. Tominaga, *Traveling Wave Thermoacoustic Engine in a Looped Tube*, Physical Review Letters, **Vol. 81 (15)** pp. 3128–3131 (1998).
- [23] D. L. Gardner, G. W. Swift, *A cascade thermoacoustic engine*, Journal of the Acoustical Society of America, **Vol. 114 (4)** pp. 1905–1919 (2003).
- [24] S. L. Garrett, *The power of sound*, American Scientist, **Vol. 88 (6)** pp. 516–526 (2000).
- [25] R. A. Hiller, G. W. Swift, *Condensation in a steady flow thermoacoustic refrigerator*, Journal of the Acoustical Society of America, **Vol. 108 (4)** pp. 1521–1527 (2000).
- [26] T. Yazakia, T. Biwa, A. Tominaga, *A pistonless Stirling cooler*, Applied Physics Letters, **Vol. 80 (1)** pp. 157–159 (2002).
- [27] R. Radebaugh, *Development of the Pulse Tube Refrigerator as an Efficient and Reliable Cryocooler*, Institute of Refrigeration (2000).
- [28] D. A. Russell, P. Weibulla, *Tabletop thermoacoustic refrigerator for demonstrations*, American Journal of Physics, **Vol. 70** (2002).
- [29] T. Jin, G. B. Chen, B. R. Wang, S. Y. Zhang, *Application of thermoacoustic effect to refrigeration*, Review of Scientific Instruments, **Vol. 74 (3)** pp. 677–679 (2003).
- [30] W. Dai, E. Luo, Y. Zhang, H. Ling, *A heat-driven thermoacoustic cooler capable of reaching liquid nitrogen temperature*, Applied Physics Letters, **Vol. 86** (2005).

- [31] K. Tang, R. Bao, G. B. Chen, Y. Qiu, L. Shou, Z. J. Huang, T. Jin, *Thermoacoustically driven pulse tube cooler below 60 K*, *Cryogenics*, **Vol. 47** pp. 526–529 (2007).
- [32] S. Vanapalli, M. Lewis, Z. Gan, R. Radebaugh, *120 Hz pulse tube cryocooler for fast cooldown to 50 K*, *Applied Physics Letter*, **Vol. 90** (2007).
- [33] J. J. Wollan, G. W. Swift, S. Backhaus, D. L. Gardner, *Development of Natural Gas Liquifier*, in *AIChE* (2002).
- [34] R. W. M. Smith, M. E. Poese, S. L. Garrett, R. S. Wakeland, *US Pat. No. 6725670* (2004).
- [35] R. W. M. Smith, M. E. Poese, R. S. Wakeland, S. L. Garrett, *US Pat. No. 7143856* (2006).
- [36] M. E. Poese, R. W. Smith, S. L. Garrett, R. van Gerwen, P. Gosselin, *Thermoacoustic refrigeration for ice cream sales*, in *Proceedings of 6<sup>th</sup> IIR Gustav Lorentzen Conference* (2004).
- [37] P. Kittel, *Ideal Orifice Pulse Tube Refrigerator Performance*, *Cryogenics*, **Vol. 32** pp. 843–844 (1992).
- [38] E. C. Luo, W. Dai, Y. Zhang, H. Ling, *Experimental investigation of a thermoacoustic-Stirling refrigerator driven by a thermoacoustic-Stirling heat engine*, *Ultrasonic*, **Vol. 44** pp. 1531–1533 (2006).
- [39] S. L. Garrett, *Resource Letter: TA-1: Thermoacoustic engines and refrigerators*, *American Journal of Physics*, **Vol. 72** (1) pp. 11–17 (2004).
- [40] J. C. Wheatley, G. W. Swift, A. Migliori, *The natural heat engine*, Los Alamos Science, **Vol. 14** pp. 2–33 (1986).
- [41] G. W. Swift, *Thermoacoustic Engines*, *Journal of the Acoustical Society of America*, **Vol. 84** (4) pp. 1145–1180 (1988).
- [42] C. Herman, Z. Travnicek, *Cool Sound: The future of refrigeration? Thermodynamic and heat transfer issues in thermoacoustic refrigeration*, *Heat and Mass Transfer*, **Vol. 42** pp. 492–500 (2006).
- [43] P. E. Phelan, J. Swanson, F. Chiriac, V. Chiriac, *Designing a mesoscale vapor-compression refrigerator for cooling high-power microelectronics*, *Thermal and Thermomechanical Phenomena in Electronic Systems (ITHERM'04)* (2004).
- [44] E. M. Benavides, *An analytical model of self-starting thermoacoustic engines*, *Journal of Applied Physics*, **Vol. 99** (2006).
- [45] E. M. Benavides, *Thermoacoustic nanotechnology: Derivation of a lower limit to the minimum reachable size*, *Journal of Applied Physics*, **Vol. 101** (2007).

- [46] P. Nika, Y. Bailly, F. Guerneur, *An integrated pulse tube refrigeration device with micro exchangers*, International Journal of Thermal Sciences, **Vol. 42** pp. 1029–1045 (2003).
- [47] P. Nika, Y. Bailly, F. Guerneur, *Thermoacoustics and related oscillatory heat and fluid flows in micro heat exchangers*, International Journal of Heat and Mass Transfer, **Vol. 48** pp. 3773–3792 (2005).
- [48] P. Nika, Y. Bailly, M. D. Labachellerie, J. C. Jeannot, J. D. Lalle, *Miniature pulse tube for the cooling of electronics devices* *L Functioning Principles and practical modeling*, Microscale Thermophysical Engineering, **Vol. 8** pp. 301–325 (2004).
- [49] O. G. Symko, *US Pat. No. 6574968* (2003).
- [50] O. G. Symko, E. Abdel-Rahman, Y. S. Kwon, M. Emmi, R. Behunin, *Design and development of high-frequency thermoacoustic engines for thermal management in microelectronics*, Microelectronics, **Vol. 35 (2)** pp. 185–191 (2004).
- [51] C. Tsai, R. L. Chen, C. L. Chen, J. DeNatale, *Micromachined Stack Components for Miniature Thermoacoustic Refrigerators*, Rockwell Scientific Corp. pp. 149–151 (2002).
- [52] O. Anderson, *Refrigeration in America*, JKennikat Press, Port Washington, NY (1972).
- [53] L. A. Schaefer, *Single Pressure Absorption Heat Pump Analysis*, Ph.D. thesis, Georgia Institute of Technology (2000).
- [54] M.-H. Kim, J. Pettersen, C. W. Bullard, *Fundamental process and system design issues in CO<sub>2</sub> vapor compression systems*, Progress in Energy and Combustion Science pp. 119–174 (2004).
- [55] S. O. Anderson, K. M. Sarma, K. N. Taddino, *Technology Transfer for the Ozone Layer*, Earthscan, London (2007).
- [56] US Department of Energy, *2007 Building Energy Data Handbook, Chapter 3.2*, <http://buildingsdatabook.eere.energy.gov/default.asp> (2007).
- [57] P. Weissler, *Cooling off Global Warming Potential*, SAE Automotive Engineering International, **Vol. 115 (10)** pp. 57–59 (2007).
- [58] American Society of Heating, Refrigeration and Air Conditioning Engineers (ASHRAE), *Standard 34-2004 Designation and Safety Classification of Refrigerants (ANSI Approved)* (2004).
- [59] R744.com, *Everything about R-744*, [www.r744.com/faq.php](http://www.r744.com/faq.php), as of 2/2009.
- [60] P. Weissler, *Consensus building on refrigerant type*, SAE Automotive Engineering International, **Vol. 116 (9)** pp. 30–32 (2008).

- [61] E. Baskin, E. S. Bayoglu, F. R. Delafield, *Performance of environmentally friendly CFC-12 replacements for refrigerators/freezers*, Tech. Rep. EPA/600/A-96/041, Environmental Protection Agency (1996).
- [62] P. S. ad Sath Aphornratana, S. Chunpaibulpatana, *A review of absorption refrigeration technologies*, Renewable and Sustainable Energy Reviews, **Vol. 5** pp. 343–372 (2001).
- [63] S. Garimella, *Innovations in energy efficient and environmentally friendly space-conditioning systems.*, Energy, **Vol. 28** pp. 1593–1614 (2003).
- [64] R. Wang, L. Wang, *Adsorption refrigeration- green cooling driven by low grade thermal energy*, Chinese Science Bulletin, **Vol. 50 (3)** pp. 193–204 (2005).
- [65] E. E. Anyanwu, *Review of solid adsorption solar refrigerator I: An overview of the refrigeration cycle*, Energy Conversion and Management, **Vol. 44** pp. 301–312 (2003).
- [66] E. E. Anyanwu, *Review of solid adsorption solar refrigerator II: An overview of the principles and theory*, Energy Conversion and Management, **Vol. 45** pp. 1279–1295 (2004).
- [67] S. L. Garrett, T. J. Hoffer, D. K. Perkins, *Thermoacoustic Refrigerators*, Refrigeration and Air Conditioning Technology Workshop (1993).
- [68] Alternative Fluorocarbons Environmental Acceptability Study (AFEAS), <http://www.afeas.org/tewi>.
- [69] A. McCulloch, P. M. Midgley, P. Ashford, *Releases of refrigerant gases (CFC-12, HCFC-22 and HFC-134a) to the atmosphere*, Atmospheric Environment, **Vol. 37** pp. 889–902 (2003).
- [70] L. Zoontjens, C. Howard, A. Zander, B. Cazzolato, *Feasibility Study of an Automotive Thermoacoustic Refrigerator* (2005).
- [71] G. W. Swift, S. N. Backhaus, D. L. Gardner, *US Pat. No. 6032464* (2000).
- [72] M. Weilenmann, A. Vasic, P. Stettler, P. Novak, *Influence of Mobile Air-Conditioning on Vehicle Emissions and Fuel Consumption: A Model Approach for Modern Gasoline Cars Used in Europe*, Environmental Science & Technology, **Vol. 39 (24)** pp. 9601–9610 (2005).
- [73] ASHRAE, *2002 ASHRAE Handbook, Refrigeration*, chapter 29.6 (2002).
- [74] C. R. Ferguson, A. T. Kirkpatrick, *Internal Combustion Engines, Applied Thermosciences*, John Wiley & Sons (2000).
- [75] T. J. Hendricks, J. A. Lustbader, *Advanced thermoelectric power system investigations for light-duty and heavy duty applications, Part 1*, in *Proceedings of the 21 International Conference on Thermoelectrics* (2002).

- [76] Energy Information Administration/Household Vehicles Energy Use, *Table A1. U.S. Number of Vehicles, Vehicle-Miles, Motor Fuel Consumption and Expenditures, 2001*, [www.eia.doe.gov/emeu/rtecs.../nhts\\_survey/2001/tablefiles/table-a01.pdf](http://www.eia.doe.gov/emeu/rtecs.../nhts_survey/2001/tablefiles/table-a01.pdf), as of 4/2008 (2001).
- [77] M. S. Bhatti, *Enhancement of R-134a Automotive Air Conditioning Systems*, in *SAE International Congress and Exposition* (1999).
- [78] US Census Bureau, *North American Transport in Figures, Section 4: Transportation, Energy, and the Environment*, <http://www.census.gov/econ/www/natf/Chap4.pdf>, as of 4/2008 (2000).
- [79] Environmental Protection Agency, *Emission Facts: Average Carbon Dioxide Emissions Resulting from Gasoline and Diesel Fuel (EPA420-F-05-001)*, <http://www.epa.gov/OMS/climate/420f05001.htm>, as of 4.2008 (2005).
- [80] Climate Leaders, U.S. Environmental Protection Agency, *Direct HFC and PFC Emissions from Use of Refrigeration and Air Conditioning Equipment*, climate Leaders Greenhouse Gas Inventory Protocol, Core Module Guidance (2007).
- [81] W. Schwarz, *Forecasting R-134a emissions from car air conditioning systems until 2020 in Germany (Translation of the German lecture)*, in *DKV Deutsche Kaelte-Klima-Tagung Bremen, 22.-24. November 2000*, Oeko-Recherche, Buero fuer Umweltforschung (2000).
- [82] Energy Information Administration, US Department of Energy, Office of Integrated Analysis & Forecasting, EI-81, *U.S. Carbon Dioxide Emissions from Energy Sources, 2006 Flash Estimate*, [www.eia.doe.gov/oiaf/1605/flash/pdf/flash.pdf](http://www.eia.doe.gov/oiaf/1605/flash/pdf/flash.pdf), as of 4/08 (2007).
- [83] ASHRAE, *1998 ASHRAE Handbook, Refrigeration*, chapter 29.1 (1998).
- [84] M. W. Thompson, A. A. Atchley, *Simultaneous measurement of acoustic and streaming velocity...LDA*, *Journal of the Acoustical Society of America*, **Vol. 117 (4)** pp. 1828–1838 (2005).
- [85] V. Kotsubo, P. Huang, T. C. Nast, *Observation of DC Flows in a Double Inlet Pulse Tube*, in *Cryocoolers 10*, Kluwer Academic/Plenum Publishers (1999).
- [86] J. R. Olson, G. Swift, *Acoustic Streaming in pulse tube refrigerators: Tapered Pulse Tubes*, *Cryogenics*, **Vol. 37 (12)** pp. 769–776 (1997).
- [87] V. Gusev, S. Job, H. Bailliet, P. Lotton, M. Bruneau, *Acoustic streaming in annular thermoacoustic prime-movers*, *Journal of the Acoustical Society of America*, **Vol. 108 (3)** pp. 934–945 (2000).

- [88] G. Penelet, V. Gusev, P. Lottona, M. Bruneaua, *Nontrivial influence of acoustic streaming on the efficiency of annular thermoacoustic prime movers*, Physics Letters A, **Vol. 351** pp. 268–273 (2006).
- [89] G. Swift, D. L. Gardner, S. Backhaus, *Acoustic Recovery of lost power in pulse tube refrigerators*, Journal of the Acoustical Society of America, **Vol. 105 (2)** pp. 711–724 (1998).
- [90] J. W. Strutt, B. Rayleigh, *The Theory of Sound*, Macmillan and Co. (1896).
- [91] J. P. Lee, P. K. and K. D. Timmerhaus, R. Radebaugh, *Higher Order Pulse Tube Modeling*, in *Cryogenics 9*, Plenum Press, New York (1996).
- [92] H. Bailliet, V. Gusev, R. Raspet, R. A. Hiller, *Acoustic streaming in closed thermoacoustic devices*, Journal of the Acoustical Society of America, **Vol. 110 (4)** pp. 1808–1821 (2001).
- [93] D. F. Gaitan, A. Gopinath, A. A. Atchley, *Experimental study of acoustic turbulence and streaming in a thermoacoustic stack*, Journal of the Acoustical Society of America, **Vol. 96** p. 3220 (1994).
- [94] T. Yazaki, A. Tominaga, *Measurement of sound generation in thermoacoustic oscillations*, in *Proceedings of the Royal Society - Mathematical, Physical and Engineering Sciences (Series A)* (1998).
- [95] W. P. Arnott, H. E. Bass, R. Raspet, *General formulation of thermoacoustics for stacks having arbitrarily shaped pore cross sections*, Journal of the Acoustical Society of America, **Vol. 60 (6)** pp. 3228–3237 (1991).
- [96] A. A. Atchley, H. E. Bass, T. J. Hoffer, H.-T. Lin, *Study of a thermoacoustic prime mover below onset of self-oscillation*, Journal of the Acoustical Society of America, **Vol. 91 (2)** pp. 734–743 (1992).
- [97] A. A. Atchley, *Standing wave analysis of a thermoacoustic prime mover below onset of self-oscillation*, Journal of the Acoustical Society of America, **Vol. 92 (5)** pp. 2907–14 (1992).
- [98] G. Mozurkewich, *Heat transfer from transverse tubes adjacent to a thermoacoustic stack*, The Journal of the Acoustical Society of America, **Vol. 110** p. 841 (2001).
- [99] A. J. Organ, *The Regenerator and the Stirling Engine*, Mechanical Engineering Publications Limited (1997).
- [100] N. Rott, *The influence of heat conduction on acoustic streaming*, Zeitschrift für angewandte Mathematik und Physik, **Vol. 25** pp. 417–421 (1974).
- [101] R.-L. Chen, C.-L. Chen, J. deNatale, *Study of a miniature thermoacoustic refrigerator*, in *Proceedings of IMECE2002* (2002).

- [102] D. G. Holmberg, G. S. Chen, H. T. Lin, A. M. Wo, *Thermal modeling and performance analysis of a thermoacoustic refrigerator*, Journal of the Acoustical Society of America, **Vol. 114 (2)** pp. 782–791 (2003).
- [103] R. S. Wakeland, R. M. Keolian, *Thermoacoustics with idealized heat exchangers and no stack*, Journal of the Acoustical Society of America, **Vol. 111 (6)** pp. 2654–2664 (2002).
- [104] J. R. Davis (editor), *ASM Specialty Handbook, Stainless Steel*, ASM International (1994).
- [105] J. R. Davis (editor), *Metals Handbook, Desk Edition, 2<sup>nd</sup> Edition*, ASM International (1998).
- [106] *Personal communication*.
- [107] H. D. Baehr, K. Stephan, *Wärme- und Stoffübertragung (transl: Heat and Mass Transfer)*, Springer, Heidelberg, 4 ed. (2004).
- [108] Y. Li, B. L. Minner, G. T.-C. Chiu, L. Mongeau, J. E. Braun, *Adaptive tuning of an electrodynamically driven thermoacoustic cooler*, Journal of the Acoustical Society of America, **Vol. 111 (3)** pp. 1251–1258 (2001).
- [109] K. Nam, S. Jeong, *Measurement of cryogenic regenerator characteristics under oscillating flow and pulsating pressure*, Cryogenics, **Vol. 43** pp. 575–581 (2003).
- [110] F. Jebali, J. V. Lubiez, M.-X. Francois, *Response of a thermoacoustic refrigerator due to the variation of the driving frequency and loading*, International Journal of Refrigeration, **Vol. 27** pp. 165–175 (2004).
- [111] H. K. Versteeg, W. Malalasekera, *An Introduction to Computational Fluid Dynamics, The Finite Volume Method, Second Edition*, Prentice Hall (2007).
- [112] C.-C. Hantschk, D. Vortmeyer, *Numerical Simulation of Self-Excited Thermoacoustic Instabilities in a Rijke Tube*, Journal of Sound and Vibration, **Vol. 277 (9)** pp. 758–763 (1999).
- [113] C.-C. Hantschk, D. Vortmeyer, *Numerical Simulation of Unsteady Interactions between Flow, Heat Conduction and Acoustics within Rijke Tube*, Chemical Engineering Technology, **Vol. 23 (3)** pp. 511–522 (2000).
- [114] J. A. L. a Nijeholt, M. E. Tijani, S. Spoelstra, *Simulation of traveling wave thermoacoustic engine using computational fluid dynamics*, Journal of the Acoustical Society of America, **Vol. 118 (4)** pp. 2265–2270 (2005).
- [115] L. Zoontjens, *Numerical Investigation of the Performance and Effectiveness of Thermoacoustic Couples*, Ph.D. thesis, School of Mechanical Engineering, The University of Adelaide (2008).

- [116] L. Zoontjens, C. Q. Howard, A. C. Zander, B. S. Cazzolato, *Numerical study of flow and energy fields in thermoacoustic couples of non-zero thickness*, International Journal of Thermal Sciences, **Vol. 48 (4)** pp. 733–746 (2009).
- [117] B. Thomas, D. Pittman, *Update on the evaluation of different correlations for the flowfriction factor and heat transfer of Stirling engine regenerators*, 35th Intersociety Energy Conversion Engineering Conference and Exhibit, **Vol. 1** pp. 76–84 (2000).
- [118] A. Atchley, T. Hoffer, M. Muzzerall, M. Kite, C. Ao, *Acoustically generated temperature gradients in short plates*, The Journal of the Acoustical Society of America, **Vol. 88** p. 251pp (1990).
- [119] N. Cao, J. R. Olson, G. W. Swift, S. Chen, *Energy Flux Density in a Thermoacoustic Couple*, Journal of the Acoustical Society of America, **Vol. 99 (6)** pp. 3456–3464 (1996).
- [120] A. Worlikar, O. Knio, R. Klein, F. Sicherheitstechnik, *Numerical simulation of a thermoacoustic refrigerator*, in *ESAIM: Proceedings*, Vol. 1, pp. 363–375 (1996).
- [121] A. S. Worlikar, O. M. Knio, R. Klein, *Numerical simulation of thermoacoustic refrigerator: II. stratified flow around the stack*, J. Comput. Phys., **Vol. 144 (2)** pp. 299–324 (1998).
- [122] E. Besnoin, O. M. Knio, *Numerical Study of Thermoacoustic Heat Exchangers in the Thin Plate Limit*, Numerical Heat Transfer; Part A: Applications, **Vol. 40** pp. 445–471 (2001).
- [123] E. Besnoin, *Numerical Study of Thermoacoustic Heat Exchangers*, Ph.D. thesis, Johns Hopkins University (2001).
- [124] H. Ishikawa, D. Mee, *Numerical investigations of flow and energy fields near a thermoacoustic couple*, The Journal of the Acoustical Society of America, **Vol. 111** p. 831 (2002).
- [125] D. Marx, P. Blanc-Benon, *Computation of the mean velocity field above a stack plate in a thermoacoustic refrigerator*, Comptes rendus-Mécanique, **Vol. 332 (11)** pp. 867–874 (2004).
- [126] D. Marx, P. Blanc-Benon, *Numerical simulation of stack-heat exchangers coupling in a thermoacoustic refrigerator*, AIAA Journal, **Vol. 42** pp. 1338–1347 (2004).
- [127] D. Marx, P. Blanc-Benon, *Numerical calculation of the temperature difference between the extremities of a thermoacoustic stack plate*, Cryogenics, **Vol. 45 (3)** pp. 163–172 (2005).
- [128] D. Marx, P. Blanc-Benon, *Computation of the temperature distortion in the stack of a standing-wave thermoacoustic refrigerator*, The Journal of the Acoustical Society of America, **Vol. 118** p. 2993pp (2005).

- [129] P. Blanc-Benon, D. Marx, *Nonlinear and edge effects in a thermoacoustic refrigerator*, in *AIP Conference Proceedings*, Vol. 838, p. 355 (2006).
- [130] A. Piccolo, G. Pistone, *Estimation of heat transfer coefficients in oscillating flows: The thermoacoustic case*, *Int. Journal of Heat and Mass Transfer*, **Vol. 49** pp. 1631–1642 (2006).
- [131] K. Tang, G. B. Chen, T. Jin, R. Bao, B. Kong, L. M. Qiu, *Influence of resonance tube length on performance of thermoacoustically driven pulse tube refrigerator*, *Cryogenics*, **Vol. 45** pp. 185–191 (2005).
- [132] J. R. Olson, G. W. Swift, *Energy Dissipation in oscillating flow through straight and coiled pipes*, *Journal of the Acoustical Society of America*, **Vol. 104** (1996).
- [133] D.-Y. Lee, S.-J. Park, S. T. Ro, *Heat Transfer in the thermally developing region of a laminar oscillating pipe flow*, *Cryogenics*, **Vol. 38 (6)** pp. 585–594 (1998).
- [134] P. H. in 't Panhuis, S. W. Rienstra, J. Molenaar, *Systematic Derivation of the Weakly Non-Linear Theory of Thermoacoustic Devices*, <http://alexandria.tue.nl/repository/books/608172>, as of December 2008.
- [135] J. R. Womersley, *Method for the calculation of Velocity, Rate of Flow and Viscous Drag in Arteries when the Pressure Gradient is Known*, *Journal of Physiology*, **Vol. 127** pp. 553–563 (1955).
- [136] J. Liu, S. L. Garrett, *Relationship between Nusselt number and the thermoviscous (Rott) functions*, *Journal of the Acoustical Society of America*, **Vol. 119 (3)** (2006).
- [137] M. R. Mackley, P. Stonestreet, *Heat Transfer and associated energy dissipation for oscillatory flow in baffled tubes*, *Chemical Engineering Science*, **Vol. 50 (14)** pp. 2211–2224 (1995).
- [138] A. Berson, M. Michard, P. Blanc-Benon, *Measurement of acoustic velocity in the stack of a thermoacoustic refrigerator using particle image velocimetry*, *Heat and Mass Transfer*, **Vol. 44 (8)** pp. 1015–1023 (2008).
- [139] X. Mao, Z. Yu, A. J. Jaworski, D. Marx, *PIV study of coherent structures generated at the end of a stack of parallel plates in a standing wave acoustic field*, *Experimental Fluids*, **Vol. 45** pp. 833–846 (2008).
- [140] V. John, *Large Eddy Simulation of Turbulent Incompressible Flows*, Springer (2004).
- [141] Fluent Inc., *Fluent 6.3 User's Guide* (2006).
- [142] V. Gusev, P. Lotton, H. Bailliet, S. Job, M. Bruneau, *Thermal wave harmonics generation in the hydrodynamical heat transport in thermoacoustics*, *The Journal of the Acoustical Society of America*, **Vol. 109** p. 84 (2001).

- [143] B. L. Minner, J. E. Braun, L. G. Mongeau, *Theoretical Evaluation of the Optimal Performance of a Thermoacoustic Refrigerator*, in *ASHRAE Transactions: Symposia*, Vol. 103, pp. 873–887 (1997).
- [144] M. Wetzel, *Experimental Investigation of a Single Plate Thermoacoustic Refrigerators*, Ph.D. thesis, Johns Hopkins University (1998).
- [145] L. Zoontjens, C. Q. Howard, A. C. Zander, B. S. Cazzolato, *Modelling and optimisation of acoustic inertance segments for thermoacoustic devices*, in *Proceedings of ACOUSTICS 2006* (2006).
- [146] M. E. H. Tijani, J. C. H. Zeegers, A. T. A. M. de Waele, *Design of thermoacoustic refrigerators*, *Cryogenics*, **Vol. 42** pp. 49–57 (2002).
- [147] M. N. Özisik, *Boundary Value Problems of Heat Conduction*, International Textbook Company (1968).
- [148] R. B. Statnikov, J. B. Matsusov, *Multicriteria Optization and Engineering*, Chapman & Hall (1995).
- [149] M. S. Bazraa, H. D. Sherali, C. M. Shetty, *Nonlinear Programming, Theory and Algorithms*, Wiley Interscience, Series in Discrete Mathematics and Optimization (1993).
- [150] J. A. Nelder, R. Mead, *A Simplex Method for Function Minimization*, *The Computer Journal*, **Vol. 7 (4)** pp. 308–313 (1965).
- [151] C. T. Kelley, *Iterative Methods for Optimization*, Society for Industrial and Applied Mathematics, Philadelphia (1999).
- [152] T. Bartz-Beielstein, *Experimental Research in Evolutionary Computation*, Springer Berlin Heidelberg (2006).
- [153] T. Kolda, R. Lewis, V. Torczon, *Optimization by Direct Search: New Perspectives on Some Classical and Modern Methods*, *SIAM Review*, **Vol. 45** pp. 385–482 (2004).
- [154] M. H. Wright, *Direct search methods: once scorned, now respectable.*, in *Proceedings of the 1995 Dundee Biennial Conference in Numerical Analysis*, Addison Wesley Longman, pp. 191–2008 (1996).
- [155] G. Wang, E. Goodman, W. Punch, *Toward the optimization of a class of black box optimization algorithms*, in *Ninth IEEE International Conference on Tools with Artificial Intelligence, 1997. Proceedings.*, pp. 348–356 (1997).
- [156] H. Kargupta, V. Hanagandi, D. E. Goldberg, *Unconstrained and Constrained Blackbox Optimization: The SEARCH Perspective*, in *SEARCH Perspective. Submitted in Indian Journal of Computer Science. LA-UR96*, pp. 6–5 (1996).

- [157] M. de Lemos, *Turbulence in porous media: modeling and applications*, Elsevier Science Ltd (2006).
- [158] I. Paek, J. E. Braun, L. Mongeau, *Characterizing heat transfer coefficients for heat exchangers in standing wave thermoacoustic coolers*, Journal of the Acoustical Society of America, **Vol. 118 (4)** pp. 2271–2280 (2005).